## *Specific heat measurements on chevrel phase materials exhibiting coexistence of superconductivity and magnetism*

Leigh, Nigel Royston

# Specific Heat Measurements on Chevrel Phase Materials Exhibiting Coexistence of Superconductivity and Magnetism



**Nigel Royston Leigh**

**A thesis submitted in partial fulfilment of the requirements for the degree of Doctor of Philosophy**

**Department of Physics**
**University of Durham**
**2001**

# Abstract

A probe for measuring the specific heat of superconductors at low temperatures and in high magnetic fields has been built and commissioned. The probe has been tested using the relaxation method on samples of copper and the accuracy of the data is 1.3 % between 5 K and 30 K, data taken using the long range pulse method has a resolution of 10 mK.

Specific heat measurements have been performed on members of the series $(Pb_{1-x}Cu_{1.8x})Mo_6S_8$, $(Sn_{1-x}Eu_x)Mo_6S_8$ and $(Pb_{1-x}M_x)Mo_6S_8$ where M = Gd and Eu, from 3 K up to 30 K and in magnetic fields up to 15 T. Additional results from resistivity, susceptibility, magnetisation, X-ray diffraction, transmission electron microscopy and electron dispersive X-ray measurements are also presented. These data have been compared to results from other authors and are analysed in terms of the BCS and GLAG theories of superconductivity and the magnetic properties of these materials.

The mean field model has been used to calculate numerically the magnetic contribution to the specific heat ($c_m$) of both ferromagnetic and antiferromagnetic systems as a function of temperature and applied field both above and below the ordering temperature. In addition an approximate analytic form for the magnetisation has been used to calculate $c_m$ above the ordering temperature. Expressions have been derived for the saturation value of the peak in $c_m$: $c_m^{sat} = 1.1245 n_{cell} R J/(J+1)$ and the temperature dependence of the peak with applied field: $\partial(\mu_0 H_{ext})/\partial T_{peak} = 6.540/g_J(J+1)$. They allow the simple calculation of the values of $J$ and $g_J(J+1)$ from specific heat data.

The magnetic contribution to the specific heat of the samples $(Sn_{0.65}Eu_{0.35})Mo_6S_8$ and $(Sn_{0.50}Eu_{0.50})Mo_6S_8$ have been modelled using these calculations and excellent agreement is found by considering the magnetic ions as free ions. The $(Pb_{0.70}Gd_{0.30})Mo_6S_8$ sample is accurately modelled by including an additional minority phase ($Gd_2S_3$). The approximate expressions have also been used to analyse data on high temperature superconductors producing values of $J$ and $g_J(J+1)$ consistent with a doublet ground state.

The properties of Chevrel phase materials have been determined as a function of doping level. The critical temperature is degraded by doping but an increase in the critical current density is observed in the series $(Pb_{1-x}Cu_{1.8x})Mo_6S_8$ for very low levels of doping. Increases of up to 28 % in the upper critical field, that are probably due to the compensation effect and an increase in the normal state resistivity, are also observed in the series $(Sn_{1-x}Eu_x)Mo_6S_8$ at high levels of doping and in the series $(Pb_{1-x}Gd_x)Mo_6S_8$ for low levels of doping.

# Declaration and Copyright

I hereby declare that the work contained within this thesis is my own original work and nothing that is the result of collaboration unless otherwise stated. No part of this thesis has been submitted for a degree or other qualification at this or any other university.



N. R. Leigh, August 2001

# Acknowledgements

Throughout the course of this study many people have provided invaluable assistance and I welcome this opportunity to express my gratitude.

First and foremost I would like to thank my supervisor, Dr D P Hampshire, for all of his guidance, support and unfailing enthusiasm during my Ph.D. Additionally I would like to express thanks to Dr Hampshire for many stimulating conversations about a wide variety of subjects and some invaluable advice when needed. I thank the University of Durham for providing financial support and Professors B K Tanner and M R Pennington for allowing me the use of the facilities in the Department of Physics.

Many other members of the Department of Physics have helped with technical support, in particular I thank David Stockdale for IT assistance, Phil Armstrong, George Teasdale, Steve Lishman and all the other members of the mechanical workshop and Mike Lee, Vicky Greener and Pauline Russell in the Audio-Visual group for their help. Norman Thompson, Davey Patterson and John Dobson have provided technical support in the laboratories and in the IT service I would like to thank Karen Brazier for answering many queries about Maple.

My colleagues in the Physics Department have provided much needed support, in particular Dr. Adrian Sneary, Simon Keys, Dan Read, Dr. Tom Hase and Dr. Ian Daniel have made my study very enjoyable, it has also been a pleasure to work with many others; Dr. John Clarke, Dr. Brian Fulthorpe, Dr. Najib Cheggour, Dr. D N Zheng, Dr. Hongjun Niu, Nicola Morley, David Taylor and George Carty.

Outside the Department I would like to thank the many friends I have come to know over the years and who have all made life a lot more bearable, in particular; Mike Walsh, Richard Cooke, Tom Marston, Max Britten, Steve Tregoning, John Holdsworth, Julie Nicholson and especially Lisa Alderton for her unfailing support.

Finally I would like to say a special thanks to my parents and family who have been so supportive over the years and without whom I would not have made it.

# Contents

# Chapter 1 - Introduction

Superconductivity is a fascinating area of science that has attracted vast amounts of research and produced many commercial applications. Some of the applications of superconducting technology that have become part of everyday life include magnetic resonance imaging (MRI) and nuclear magnetic resonance (NMR) technology. The fundamental properties of zero resistance and complete magnetic flux exclusion can lead to the observation of macroscopic quantum properties and also to the development of more specialised equipment. Much of the recent interest in superconducting materials has arisen due to the discovery of the high temperature superconductors (HTS) in the late 1980's that created the possibility for superconducting applications operating at liquid nitrogen temperatures. However present limitations of these HTS have promoted further research on other classes of superconductors that can compete with the HTS at lower temperatures and a more general interest in many of the presently unexplained properties of superconductors.

Chevrel phase materials are ceramic, isotropic, low temperature superconductors that have many interesting features due to their particular crystal structure. Discovered a decade before the HTS, research was initially focussed on the relatively high critical temperatures and the very high upper critical fields of a few members of this group. The low value of the critical current density ($J_c$) of these materials however limited their technological value and only recently have improvements on the fabrication of these materials produced wires that have values of $J_c$ close to the standard required by industry. Other research with these materials has concentrated on the possibilities of studying the interaction of superconducting and magnetic ordering within the same material. These two phenomena are generally mutually exclusive within the same material and the Chevrel phases are one of only a very small number of materials where the two types of ordering can interact.

This thesis is a study of the superconducting properties of the two Chevrel phase materials $PbMo_6S_8$ and $SnMo_6S_8$ when small metal ions or magnetic ions are substituted for the Pb or Sn ions in the unit cell. These two compounds have the highest superconducting properties of the large number of Chevrel phase compounds and the effect of substituting different metal ions in the lattice is generally observed as a degradation of the superconducting properties. The measured $J_c$ of these materials however is not a purely intrinsic property and is dependent on the bulk properties of the material. Doping with



small cations or magnetic cations can improve the superconducting properties at the grain boundaries of polycrystalline samples and therefore improve $J_c$. Chevrel phase compounds of the form $MMo_6S_8$ where M is a rare-earth ion display a great variety of magnetic and superconducting properties depending on the M ion. These compounds have superconducting properties that are generally much lower than either $PbMo_6S_8$ or $SnMo_6S_8$ and many display coexistence of both superconducting and magnetic ordering. We therefore study the effect of doping on the properties of these materials to determine if improvements in $J_c$ can be made with little or no degradation of the other key superconducting properties and to examine the coexistence of superconductivity and magnetism within these materials.

The primary method employed in this thesis to examine the properties of these materials is the specific heat measurement. The measured specific heat of a material can give information about the electronic, structural, superconducting and magnetic properties of the material and is therefore a very powerful tool. In particular specific heat measurements are an ideal way to study phase transitions within a material even from phases that do not constitute the main part of that material. Part of this thesis therefore details the design and commissioning of a probe to measure the specific heat of these materials at low temperatures and in high magnetic fields.

A significant part of this thesis is devoted to modelling the magnetic contribution to the specific heat capacity. There are various models of the interactions in a magnetically ordered system of which the simplest is the mean field model. This model is therefore used to calculate the magnetic contribution to the specific heat for both ferromagnetic and antiferromagnetic materials and to derive simple expressions that allow the important parameters to be determined from specific heat capacity data. The calculations are then used to model the magnetic contribution for the samples that we have measured and also to analyse data taken by other authors.

Chapter 2 of this thesis gives a basic introduction to the important theories and parameters that are used to discuss the superconducting and magnetic properties of materials. A review of the literature relevant to this work is presented in chapter 3. The information in this chapter summarises the important experimental results on the specific heat of normal materials, superconductors and magnetic materials, the structure and properties of Chevrel phase materials and finally the properties of magnetic

superconductors. In chapter 4 the mean field model of magnetic materials is used to derive a functional form for the magnetisation of materials and thermodynamic arguments are then used to calculate the specific heat capacity from the magnetisation as a function of applied field and temperature. A simplified function for the magnetisation is also used to derive the specific heat capacity and two approximate expressions are subsequently derived from this that allow comparison with experimental data. The accuracy of these approximations is then discussed in comparison to the results using the full functional form.

The design, construction and commissioning of a specific heat probe is detailed in chapter 6. The operating conditions of the system are outlined for two different techniques to measure the specific heat and results are presented on copper as a standard to determine the accuracy of the data obtained using this probe.

Specific heat measurements on six members of the series $(Pb_{1-x}Cu_{1.8x})Mo_6S_8$ are presented in chapter 6 along with the results of complementary measurements on these samples. The effect of substituting Cu ions into the unit cell on the superconducting properties of $PbMo_6S_8$ is then discussed in terms of the normal state properties of the materials and the BCS and GLAG theories of superconductivity. In chapter 7 the results of specific heat measurements on $SnMo_6S_8$ and $PbMo_6S_8$ doped with the magnetic ions Eu and Gd are presented. The specific heat data and data from complementary measurements are then discussed in terms of the normal state properties, the BCS and GLAG theories of superconductivity and the mean field model. The effect of doping with magnetic ions on the superconducting and magnetic properties of $SnMo_6S_8$ and $PbMo_6S_8$ is discussed and the magnetic contribution to the specific heat is compared with results calculated using the mean field model as detailed in chapter 4. Comparisons are then made using the approximate expressions derived in chapter 4 with similar data taken on high temperature superconductors containing rare-earth ions.

Chapter 8 presents some ideas for future work.

# *Chapter 2. – Introduction to Superconducting and Magnetic Materials.*

## 2.1 Introduction to Chapter 2.

A central theme in this thesis is the coexistence of superconductivity and magnetism and so this chapter presents an introduction to both superconducting and magnetic materials. Section 2.2 is a brief chronological history of the discovery of superconducting materials. Sections 2.3 and 2.4 describe the fundamental properties of superconductors and their magnetic properties. Section 2.5 outlines the basic thermodynamic relations that are important for analysis of magnetic and superconducting phenomena. The London, BCS and Ginzburg-Landau theories of superconductivity are outlined in sections 2.6, 2.7 and 2.8 respectively. The basic properties of magnetic ions are introduced in section 2.9 from an understanding of the effect of magnetic fields on the energy levels of atoms. The Heisenberg and Ising models of magnetic ordering are discussed in section 2.10 and the mean field theory in section 2.11. The chapter is concluded in section 2.12.

## 2.2 Brief History of Superconductivity.

In 1908 H. K. Onnes [1] succeeded in liquifiying Helium permitting a study of the properties of materials at very low temperatures. In 1911 [2] he observed that at about 4.2 K the resistivity of Mercury dropped abruptly to zero and so discovered the phenomenon of superconductivity. Many of the other elements are also superconducting below a characteristic critical temperature $T_c$. The transition to a superconducting phase is dependent on both the crystal structure and the chemical composition within a material. Many compounds and alloys are superconducting even when the constituent elements are not. Up until 1986 the highest critical temperature was 22.3 K for the alloy $Nb_3Ge$ [3], then Bednorz and Muller [4] discovered the Ba-La-Cu-O system with a $T_c$ above 30 K. Since then many copper-oxide systems (*cuprates*) have been fabricated that are superconducting. In 1987 Wu and Chu [5] discovered the Y-Ba-Cu-O system with a $T_c > 90$ K, the first to become superconducting above the boiling point of liquid nitrogen (77 K). To date the highest $T_c \sim 130$ K for the Hg-Ba-Ca-Cu-O system [6] and $T_c$'s > 150 K are reported for similar systems under high pressures [7].

## 2.3 Properties of Superconductors.

The two fundamental properties of superconductors below $T_c$ are zero resistance and perfect diamagnetism, called the *Meissner effect*. Experimentally an upper limit for the resistivity of the superconducting state has been determined, at approximately $10^{-23}$ Ωcm, at least 11 orders of magnitude lower than that of copper [3]. The Meissner effect is the total exclusion of a magnetic field from the bulk of the material below $T_c$. This effect distinguishes the superconductor from a perfect conductor which traps flux inside the bulk of the material rather than expelling it, if the material is cooled below $T_c$ in a magnetic field.

Application of an external current through the material or an external magnetic field can return the material to its normal state at temperatures less than $T_c$. The maximum current that can be passed through a superconducting material before a non-zero resistance can be detected is called the critical current density ($J_c$). The magnitude of $J_c$ is temperature dependent with a maximum value at T = 0 K. The maximum magnetic field up until which a material remains superconducting depends on the type of superconductor involved.

## 2.4 Type I and Type II Superconductors.

There are two classes of superconductors depending on their response to an applied magnetic field. Type I superconductors exhibit perfect diamagnetism up to a critical field $H_c$ when they return to the normal state. In the bulk of the material the net magnetic field is zero while in the Meissner state. Type II superconductors have a Meissner state up to a lower critical field $H_{c1}$. For applied fields greater than this and lower than an upper critical field $H_{c2}$, they exist in a *mixed state*. In this mixed state the magnetic field penetrates into the bulk of the superconductor in quantized amounts called *fluxons*. These fluxons are normal regions within the bulk of the superconducting material. Application of larger magnetic fields pushes more and more fluxons into the bulk of the material. When the applied field reaches the upper critical field the material has no superconducting regions remaining and returns to its normal state.

## 2.5 Thermodynamic Properties.

To characterise the thermodynamic state of a material in a magnetic field we use the Gibbs free energy ($G$). This function takes into account the internal energy ($U$), entropy ($S$), volume ($V$) and magnetization ($M$) of the system, as well as the effect of pressure ($P$), temperature ($T$) and applied field ($H$).

$$G = U - TS + PV - \mu_0 V \underline{M} \cdot \underline{H} \tag{2.1}$$

For a process at fixed temperature and pressure, with negligible volume change (as for most solids) we have an expression for the change in the Gibbs free energy with applied field.

$$dG(H,T) = -\mu_0 V \underline{M} \cdot d\underline{H} \tag{2.2}$$

The equation for the Gibbs free energy also gives a relation for the entropy ($S(\mathrm{JK^{-1}})$), in terms of the change in Gibbs energy at constant applied field.

$$S(T) = -\left(\frac{\partial G(H,T)}{\partial T}\right)_H \tag{2.3}$$

The *heat capacity* of a material ($C(\mathrm{JK^{-1}})$ at temperature $T$, is defined as the amount of heat ($\Delta Q$) required to raise the temperature of that material to a value $T + \Delta T$ in the limit that $\Delta T \rightarrow 0$. The *specific heat capacity* ($c(\mathrm{JK^{-1}gram^{-1}})$ is this quantity per unit mass.

$$c = \frac{C}{m} = \frac{1}{m} \lim_{\Delta T \to 0} \left(\frac{\Delta Q}{\Delta T}\right) \tag{2.4}$$

where $m$ is the mass of the material. The specific heat capacity depends on the state in which the measurement is performed. Different values of the specific heat capacity are measured for systems at constant pressure ($c_p$), constant volume ($c_v$), constant applied field strength ($c_H$) etc. For a reversible process at constant volume and constant applied field the first law of thermodynamics allows the specific heat to be related to the change in internal energy of the system.

$$c_{v,H} = \frac{1}{m}\left(\frac{\partial U}{\partial T}\right)_{v,H} \tag{2.5}$$

For solids most specific heat measurements are conducted at constant pressure and constant applied field strength. At low temperatures the difference between $c_{p,H}$ and $c_{v,H}$ for most solids is negligible (< 1%) and so we can take $c_{p,H} \approx c_{v,H}$ and only use the subscripts when distinctions are needed. For a reversible process we can also relate the specific heat capacity to the entropy at constant applied field.

$$c(T) = \frac{T}{m}\left(\frac{\partial S(T)}{\partial T}\right)_H \tag{2.6}$$

### 2.5.1 Specific heat of type I superconductors.

For a superconductor in the Meissner state $\underline{M} = -\underline{H}$ and in the normal state $\underline{M} = 0$. So if we assume (for a type I superconductor) a continuous Gibbs function through the superconducting transition we can evaluate the energy difference between the normal and superconducting states at a temperature $T$ and applied field $H$.

$$G_s(H,T) = G_n(T) - \frac{\mu_0 V}{2}\left(H_c^{\,2}(T) - H^2\right) \tag{2.7}$$

For applied fields $H < H_c$ the superconducting state is therefore energetically favourable. Use of Eqn. (2.3) and (2.6) allows the difference in the heat capacity to be determined.

$$C_s(T) = C_n(T) + \mu_0 VT\left(H_c(T)\frac{d^2H_c(T)}{dT^2} + \left(\frac{dH_c(T)}{dT}\right)^2\right) \tag{2.8}$$

At the superconducting transition the specific heat capacity is discontinuous with a corresponding change in the entropy of the system when $H_c \neq 0$, i.e. $T < T_c$. In 1934 Rutger derived an expression at $T = T_c$ for the specific heat capacity jump in zero applied field where $H_c(T_c) = 0$ [8].

$$C_s(T) - C_n(T) = \mu_0 VT_c\left(\frac{dH_c}{dT}\right)^2 \tag{2.9}$$

## 2.6 London Theory of Superconductivity.

In 1935 the London brothers [9] proposed a phenomenological theory of the electrodynamics of a superconductor. The theory describes the two basic properties of superconductivity by means of two equations relating the total magnetic field ($\underline{B}$), the electric field ($\underline{E}$) and the superconducting current ($\underline{J}_s$) but makes no attempt to explain the superconducting mechanism.

$$\underline{E} = \mu_0 \lambda_L^{\,2} \frac{\partial}{\partial t}\underline{J}_s \tag{2.10}$$

$$\underline{B} = -\mu_0 \lambda_L^{\,2} \nabla \wedge \underline{J}_s \tag{2.11}$$

where

$$\lambda_L^{\,2} = \frac{m^*}{\mu_0 n_s e^*} \tag{2.12}$$

The first London equation (2.10) describes the zero resistivity state where a constant electric field will constantly accelerate the charge carriers, number density $n_s$, effective mass $m^*$ and effective electronic charge $e^*$. In comparison Ohms law describes an electric field that keeps the charge carrier velocity constant against the resistance of the material. On substitution of the second London equation (2.11) into Maxwell's equation $(\nabla \wedge \underline{B} = \mu_0 \underline{J}_s)$ the Meissner state is described.

$$\nabla^2 \underline{B} = \frac{1}{\lambda_L^{\,2}} \underline{B} \tag{2.13}$$

Equation (2.13) gives a solution that decays exponentially from the surface into the interior of the material and so leads to value of $\underline{B} = 0$ inside the bulk of the material. A magnetic field is then screened from the interior of the material by currents that flow on the surface of the material within a small layer called the *London penetration depth* ($\lambda_L$).

This model assumes spatial variations of $\underline{J}_s$ are small and no variation in $n_s$ with field or current intensity. The limitations of the London theory became apparent when trying to model the mixed state of a superconductor or the destruction of superconductivity due to a critical field or critical current density.

## 2.7 BCS Microscopic theory.

In 1957 Bardeen, Cooper and Schrieffer [10] published a microscopic theory of superconductivity (BCS theory). To date this is the only theory to successfully describe how a superconducting state is formed on a microscopic scale. The basis of the theory is that the normal ground state of an electron gas is unstable with respect to the formation of a system of correlated electron pairs called *Cooper pairs*. Cooper showed in 1956 [11] that electrons will become bound together as a pair if a positive attraction exists between two electrons, no matter how small that attraction. This can be thought of as the exchange of a virtual phonon through the lattice. An electron moving through the lattice polarizes the ions due to its electrical charge. The change in polarization of the lattice interacts with a second electron causing a net positive attraction between two. In certain materials this positive attraction overcomes the Coulomb repulsion between the electrons producing a lower energy state, the superconducting state. The characteristic distance over which the two electrons in a Cooper pair are linked is the BCS coherence length ($\xi_{BCS}$), of the order $10^3$ Å. Each Cooper pair in the superconducting state has a total linear momentum of zero

and so the two individual electrons have equal and opposite momentum. The stability of any Cooper pair is intimately linked to all the other Cooper pairs and consequently the BCS superconducting state is a highly correlated electron system.

Excitation of any Cooper pair can only occur as an excitation of the whole system, requiring an enormous amount of energy, due to the correlation between all the pairs in that region. The binding energy of a Cooper pair then becomes the minimum energy required to excite the electron system, splitting a Cooper pair into two normal electrons. The band structure for the material then has an energy gap between the paired, lower energy state and the two single-electron states and is often denoted $2\Delta$.

In a normal material the scattering of electrons off the lattice is mainly responsible for the resistance of the material. In a superconductor this scattering energy is smaller than the binding energy of the Cooper pair and so the pair passes through the lattice without interacting with it, i.e. with zero resistance.

The strength of the electron-electron interaction in a Cooper pair depends on the phonon frequency of the lattice. Heavier ions in the lattice produce lower frequency phonons. This reduces the strength of the interaction and so lowers the transition temperature of the material. This dependence of $T_c$ on the mass of the ions in the lattice is called the isotope effect.

The BCS theory deals with systems where the Cooper pairs are weakly coupled to the lattice and where the spatial variation in the BCS order parameter is small. Some of the elements and many other alloys deviate from the BCS predictions because the electron-phonon coupling is not in the weak limit assumed in BCS theory. The predictions made in the BCS theory are however the first quantitative understanding of superconductivity and are very successful when compared to experimental data. Two of the predictions from BCS theory relate to the specific heat capacity of a superconductor in zero applied field. The low temperature form of the electronic contribution to the specific heat capacity should have an exponential temperature dependence

$$\frac{c_{es}}{\gamma T_c} = a\exp\left(-b\frac{T_c}{T}\right) \tag{2.14}$$

where $a = 8.5$ and $b = 1.44$ for $2.5 < T_c / T < 6$ [10]. At the transition the discontinuity in the specific heat is given by:

$$\frac{c_{es}(T_c) - \gamma T_c}{\gamma T_c} = 1.43 \tag{2.15}$$

The high-$T_c$ superconductors have a superconducting mechanism that maybe non-BCS like, although it is still thought to involve the pairing of electrons. The exact nature of the mechanism involved is a controversial subject and many theories have been suggested.

## 2.8 Ginzburg-Landau Theory.

In 1950 V. Ginzburg and L. Landau [12] published another phenomenological theory which has been extremely successful in describing many superconducting properties. The theory is based upon a second order phase transition from the normal to superconducting state which is characterised by a complex order parameter $\Psi(\underline{r}) = |\Psi(\underline{r})|e^{i\theta}$. The physical interpretation of $\Psi$ is that it represents the density of superelectrons $n_s = |\Psi(\underline{r})|^2$.

The Gibbs free energy of the material due to the kinetic energy of the charge carriers, the response to an applied field ($\underline{H}$) and the condensation energy of the superelectrons, is considered close to the transition temperature.

$$G_s[\Psi] = G_n + \frac{1}{V}\int d^3\underline{r}\left[\frac{1}{2m}(-i\hbar\nabla - 2e\underline{A})\Psi^*(i\hbar\nabla - 2e\underline{A})\Psi + \left(\frac{1}{2\mu_0}\right)B^2(\underline{r}) - \mu_0\underline{H}(\underline{r})\cdot\underline{M}(\underline{r}) + \alpha|\Psi|^2 + \frac{1}{2}\beta|\Psi|^4\right] \tag{2.16}$$

By minimising this equation with respect to variations in $\Psi$ and in the vector potential $\underline{A}$ ($\underline{B} = \nabla \wedge \underline{A}$) we obtain the two Ginzburg-Landau equations which can be solved analytically only in a few special cases.

$$\frac{1}{2m}(-i\hbar\nabla - 2e\underline{A})^2\Psi + \alpha\Psi + \beta|\Psi|^2\Psi = 0 \tag{2.17}$$

$$\mu_0\underline{J} = -\frac{i\hbar e}{m}(\Psi^*\nabla\Psi - \Psi\nabla\Psi^*) - \frac{4e^2}{m}\underline{A}|\Psi|^2 \tag{2.18}$$

Solving these two equations under appropriate conditions leads to the introduction of the two fundamental length scales of superconductivity, the *coherence length* ($\xi$) and the *penetration depth* ($\lambda$), also used in the London theory. The coherence length is the characteristic length over which $\Psi(\underline{r})$ varies appreciably and the penetration depth, is the length over which an external field decays inside the bulk of a superconductor in the Meissner state. The London equations can be derived from the second Ginzburg-Landau equation (2.18).

One of the great successes of this theory is the prediction of the observed mixed state of the superconductor. By considering the surface tension between a homogeneous state (superconducting or normal) and a mixed state in a magnetic field, they were able to show that there were two classes of superconductors determined by a parameter $\kappa = \lambda/\xi$. The first class is more stable in the Meissner state than it would be by formation of the mixed state. The second class is unstable in the Meissner state, spontaneously forming regions of normal material within the bulk of the superconductor that enclose magnetic flux. Materials with a value of kappa for which $\kappa < 1/\sqrt{2}$ are type I superconductors and materials for which $\kappa > 1/\sqrt{2}$ exhibit type II behaviour.

In 1957 A. Abrikosov [13] solved the Ginzburg-Landau equations for a type II superconductor. He determined that the form of the mixed state, inside the bulk of the superconductor would be that of a square lattice of tubes of magnetic flux (normal regions), each containing one flux quantum of value $\Phi_0 = h / 2e = 2.07 \times 10^{-5}$ Wb. These fluxons have a radius equal to the coherence length and the decay of the field from the fluxon into the superconducting region is again characterised by the penetration depth. In 1964 Kleiner et al [14] found a lower energy solution to Abrikosov's work, predicting a triangular arrangement of fluxons, which is the most commonly experimentally observed state.

In 1959 Gor'kov [15] showed that the Ginzburg-Landau equations can be derived from BCS theory providing a theoretical justification of their use for temperatures close to the critical temperature.

## 2.9 Magnetic properties of materials.

The magnetic properties of materials are generally a result of the interaction of an applied magnetic field strength ($\underline{H}(Am^{-1})$), with the spin and orbital angular momenta of the electrons within a material. The effects of the interaction of the applied field with the nuclear spins of an atom are much smaller and are ignored. In metallic materials the conduction electrons are dissociated from the lattice sites and have separate orbital and spin components. It can be shown that in many cases the magnetic response of these electrons is also negligible. Magnetic atoms are those that have an incomplete shell of electrons in addition to a partially or fully filled (outer) valence shell. In these atoms this lower electron shell will have a net dipole moment that is unaffected by the transfer of valence electrons such as in an ionic crystal or a molecule. The response of an electron, or of the net dipole

moment of an atom to an applied field is called the *magnetic moment* ($\underline{m}(\mathrm{Am}^2)$). Quantum mechanically, for an isolated atom of energy state $E_n$ in a uniform magnetic field $\underline{H}$, the magnetic moment is the change in the energy state as a function of the applied field.

$$\mu_0 \underline{m} = -\frac{\partial E_n(H)}{\partial \underline{H}} \tag{2.19}$$

We can then define the net magnetic moment per unit volume or *magnetization* ($\underline{M}(\mathrm{Am}^{-1})$), by $\underline{M} = \underline{m}/V$. At a temperature $T$ in thermal equilibrium, the magnetization density is the thermal equilibrium average of the magnetization density of each excited state.

$$\underline{M}(\underline{H},T) = \frac{\sum_n \underline{M}_n(\underline{H}) e^{-E_n/k_B T}}{\sum_n e^{-E_n/k_B T}} \tag{2.20}$$

where

$$\mu_0 \underline{M}_n(\underline{H}) = -\frac{1}{V}\frac{\partial E_n(H)}{\partial \underline{H}} \tag{2.21}$$

Using Maxwell-Boltzmann statistics for distinguishable particles we can define the magnetic Helmholtz free energy $F$ [16].

$$e^{-F/k_B T} = \sum_n e^{-E_n(H)/k_B T} \tag{2.22}$$

This allows Eqn. (2.21) to be written in its thermodynamic form.

$$\mu_0 \underline{M} = -\frac{1}{V}\frac{\partial F}{\partial \underline{H}} \tag{2.23}$$

Any material can then be classified by the dimensionless *magnetic susceptibility* ($\chi$).

$$\chi = \frac{\partial \underline{M}}{\partial \underline{H}} = -\frac{1}{\mu_0 V}\frac{\partial^2 F}{\partial H^2} \tag{2.24}$$

We also can define the net field ($\underline{B}$) at any point in a material in terms of the thermodynamic field strength ($\underline{H}$) and the magnetization of the material ($\underline{B} = \mu_0(\underline{H} + \underline{M})$).

### 2.9.1 Total magnetic response. Diamagnetism.

To determine the total energy change of an atom we consider the interaction of the magnetic field with both the total spin ($\underline{S}$) and total orbital angular momentum ($\underline{L}$) of the atom. These interactions with the applied field produce a change in energy, represented by field-dependent terms in the Hamiltonian operator of the system. In calculating the total spin and orbital angular moment of the atom we consider only the contribution of incomplete electron shells, since a filled electron shell has a resultant spin and orbital

angular component of zero. Perturbation theory then allows the change in energy levels ($\Delta E_n$) to be calculated to second order from the Hamiltonian operator.

$$\Delta E_n = \mu_B \mu_0 \underline{H} \cdot \langle n | \underline{L} + g_0 \underline{S} | n \rangle + \sum_{n \neq n'} \frac{\left| \langle n | \mu_B \mu_0 \underline{H} \cdot (\underline{L} + g_0 \underline{S}) | n' \rangle \right|^2}{E_n - E_n'} + \frac{\mu_0^2 e^2}{8m} H^2 \langle n | \sum_i (x_i^2 + y_i^2) | n \rangle \tag{2.25}$$

where $\mu_B$ is the Bohr magneton equal to $9.27 \times 10^{-24}$ $JT^{-1}$ and m and e are the fundamental electronic mass and charge respectively. We can note that the first term of this energy shift is almost always the dominant term.

Molecules that have no net dipole moment also have resultant total orbital angular momentum and spin values of zero. The first two terms in Eqn. (2.25) therefore vanish and the energy shift due to an applied field is then just given by the third term. In thermal equilibrium the most probable energy state for the atom is the ground state ($E_0$) and the energy shift of the ground state determined from Eqn. (2.25) is positive. On applying a magnetic field the material therefore has a *diamagnetic* response, that is the induced magnetization opposes the applied field. Materials that are diamagnetic such as copper, gold and sodium chloride have a negative susceptibility of about $(-10^{-5})$ – $(-10^{-6})$. Superconductors are perfectly diamagnetic in the Meissner state ($\underline{M} = -\underline{H}$) and have a susceptibility of -1.

### 2.9.2 Paramagnetism.

Materials that have atoms with incomplete electron shells have a *paramagnetic* response. In zero applied field the atomic dipoles are randomly orientated. On application of a magnetic field the first term in Eqn. (2.25) does not vanish and is the dominant term. This leading term favours alignment of the dipoles parallel to the applied field producing a positive susceptibility of typically $10^{-4}$ – $10^{-3}$ at room temperature. Thermal activation disrupts alignment of the ions with the applied field and so paramagnetic ions have a susceptibility that is inversely proportional to temperature. In atoms that have an electron shell one short of being half-filled the leading term in Eqn. (2.25) vanishes but the second (paramagnetic) term does not. A balance between the second and (diamagnetic) third term in the equation then determines the response of the atom.

### 2.9.3 Curie's Law.

The ground state of an isolated atom in zero field which does not have a total electronic angular momentum value ($\underline{J} = \underline{L} + \underline{S}$) equal to zero (i.e. paramagnetic), will be $(2J+1)$-fold degenerate. Application of a magnetic field lifts this degeneracy and we are left with $2J+1$ low lying energy levels. If the separation of the first excited multiplet from the zero-field multiplet is large compared to $k_B T$, such as at low temperatures, then only the lowest $2J+1$ states will contribute appreciably to the free energy. Under these circumstances we can write the first term of the energy shift due to a magnetic field (2.25) as $\Delta E_n = \underline{\mu} . \mu_0 \underline{H}$ where $\underline{\mu} = -g_J \mu_B \underline{J}$ and $g_J$ is the Lande $g$-factor.

$$g_J = \frac{1}{2}\frac{[J(J+1)+L(L+1)-S(S+1)]}{J(J+1)} + \frac{g_s}{2}\frac{[J(J+1)+S(S+1)-L(L+1)]}{J(J+1)} \qquad (2.26)$$

The electronic $g$-factor ($g_s$) is approximately equal to 2.

Equation (2.22) allows calculation of the free energy ($F$).

$$e^{-F/k_B T} = \sum_{J_z=-J}^{J} e^{-g_J \mu_0 \mu_B \underline{J}\cdot\underline{H}/k_B T} = \frac{e^{g_J \mu_B \mu_0 H(J+1/2)/k_B T} - e^{-g_J \mu_B \mu_0 H(J+1/2)/k_B T}}{e^{g_J \mu_B \mu_0 H/2k_B T} - e^{-g_J \mu_B \mu_0 H/2k_B T}} \qquad (2.27)$$

The magnetization ($\underline{M}$) and susceptibility ($\chi$) of the material then follow from Eqn.'s (2.23) and (2.24), where $N$ is the number of magnetic ions in volume $V$.

$$\chi = \frac{\partial \underline{M}}{\partial \underline{H}} = -\frac{N}{\mu_0 V}\frac{\partial^2 F}{\partial H^2} = \frac{N}{\mu_0 V} g_J \mu_B J \frac{\partial (B_J(y,J))}{\partial H} \qquad (2.28)$$

where $$B_J(y,J) = \frac{2J+1}{2J}\coth\left(\frac{2J+1}{2J}y\right) - \frac{1}{2J}\coth\left(\frac{1}{2J}y\right) \qquad (2.29)$$

with $y = g_J \mu_B \mu_0 H/k_B T$. Equation (2.29) is called the *Brillouin* function. For most fields and temperatures $y$ is small and so $\coth(y)$ can be expanded as $\coth(y) \approx 1/y + y/3$. The resultant form of the susceptibility is known as Curie's law, determined by the *Curie* constant ($C$).

$$\chi = \frac{N}{V}\frac{p_{eff}^2 \mu_B^2}{3k_B T} = \frac{C}{T} \qquad (2.30)$$

with the *effective Bohr magneton number* defined as $p_{eff} = g_J[J(J+1)]^{1/2}$.

### 2.9.4 Ferromagnetism, antiferromagnetism and ferrimagnetism.

Two other classes of magnetic materials occur in paramagnetic materials where neighbouring magnetic ions interact with each other as well as the applied field. In the majority of cases the dominating interaction between neighbouring ions is the electron-electron interaction which tends to be larger than any dipole-dipole interaction or spin orbit coupling. This interaction leads to a spontaneous ordering of the magnetic dipoles relative to each other, even in zero field, below a characteristic temperature ($T_m$). If the magnetic ions align parallel to each other such as in Fe, Ni or Co, the material has a net bulk magnetization called the *spontaneous magnetization* and the ordered state is described as *ferromagnetic*. These materials often have regions inside the material called *domains*, in which all the ions are aligned parallel but in a different orientation from a neighbouring domain. Ferromagnetic materials in their ordered state can often have very large susceptibilities of $10^3$-$10^4$ due to movement of these domain walls. More commonly the ions align antiparallel to each other such as in Mn, Cr or FeO giving a total bulk magnetization of zero and the ordered state is described as *antiferromagnetic*. In materials where alignment is antiparallel but the magnitudes of the magnetization in opposing directions are not equal, the bulk magnetization is non-zero and the ordered state is described as *ferrimagnetic*. Above the ordering temperatures all these classes of material return to a paramagnetic state.

## 2.10 Heisenberg and Ising models of magnetically ordered systems.

In a system where the magnetic ions interact with each other we need to take into account the electrostatic and dipolar interactions when calculating any of the properties of the system. If we consider a simple 2-electron system in zero field, i.e. two hydrogen atoms, which has a four-fold degenerate ground state when the atoms are well separated. In a certain regime the atoms are close enough to interact and split the four lowest energy states but the probability of exciting higher energy states is still very small. The general state of the system can then be expressed as a linear combination of these four lowest states and we can construct an operator, called the *spin Hamiltonian*, whose eigenfunctions give the corresponding spin states of the system and therefore the energy states. For a system of $N$ magnetic ions in zero field, all of which interact only weakly, we can define the spin Hamiltonian simply as the 2-electron case summed over all pairs [16].

$$H^{\text{spin}} = -\sum J_{ij} \underline{S}_i \cdot \underline{S}_j \tag{2.31}$$

This Hamiltonian is known as the *Heisenberg Hamiltonian* and the $J_{ij}$'s are the exchange coupling constants between pairs. The Heisenberg model assumes that the magnetic moment of each ion is spatially localized and that there is negligible overlap with the wavefunction of the conduction electrons. Furthermore only interactions between nearest magnetic neighbours are considered in this model and interactions between magnetic ions that are next-nearest neighbours or further away, are assumed to be negligible.

The *Ising model* is a simplified version of the Heisenberg model. Due to either an anisotropic exchange interaction or an anisotropic coupling of the magnetic moments the spins of the ions can only lie in either the $+z$ or $-z$ direction [16].

$$H^{\text{Ising}} = -\sum J_{ij} \underline{S}_i^z \cdot \underline{S}_j^z \tag{2.32}$$

Using a statistical form for the temperature dependence of the energy levels of the spin Hamiltonian, the partition function can then be derived and consequently various thermodynamic properties. In general calculating and using either the Heisenberg or Ising Hamiltonian or indeed any other model for interacting magnetic ions is an incredibly difficult task even with very simplified models. Exact solutions using these models have been achieved for both one [17] and two dimensional lattices [18] in the Ising model, but as yet no complete solution exists for either a three dimensional Ising system, or any of the one, two or three dimensional lattices in the Heisenberg model. To calculate thermodynamic properties for the unsolved systems, approximate solutions using series expansions are commonly used in the temperature region of interest. Many other theories relating to particular types of lattice, including the effects of next nearest neighbours or in particular temperature regimes have also been proposed. A lot of these theories start from either the Heisenberg or Ising models however and do not in general give any significant qualitative improvements over the whole temperature [16].

One of the successful predictions using the Heisenberg model in three dimensions is of *magnons* or *spin-waves* at very low temperatures by Bloch in 1932 [19]. The ground state of a ferromagnetic or antiferromagnetic system has all the spins lined respectively parallel or antiparallel. Low lying excitations are sufficient to cause a perturbation along a line or ring of adjacent ions that is equivalent in total to a single spin reversing its direction. These perturbations are quantized in their dispersion relation, relating the frequency (i.e. energy) of the spin-wave to its wave-vector. Higher excitations at low but finite temperatures can

then be regarded as a superposition of spin waves with different wave vectors. Calculation of the internal energy of the system and hence the magnetic contribution to the specific heat capacity then proceeds from the dispersion relation, giving $c_m \propto T^{3/2}$ for ferromagnets and $c_m \propto T^3$ for antiferromagnets [20].

The various thermodynamic quantities of ordered systems are better described in the region of the critical temperature by scaling laws. Near to the critical temperature ($T_m$) the approximate solutions for thermodynamic properties yield power law expansions which can be reduced to functions of only a small number of unknowns [21]. The magnetic contribution to the specific heat capacity in the region of the transition can be described by an inverse power-law singularity.

$$c_m \sim A(T - T_m)^{-\alpha} \text{ for } T > T_m \tag{2.33}$$

$$c_m \sim A'(T - T_m)^{-\alpha'} \text{ for } T < T_m \tag{2.34}$$

Theoretical models propose that $\alpha = \alpha'$ and that within any subset of magnetic materials with the same structural and quantum parameters the value of $\alpha$ will be constant.

## 2.11 Mean Field Theory.

In 1907 P. Weiss published a theory of the ferromagnetic transition called the mean (or molecular) field theory. Although this theory predates the Heisenberg and Ising models, the theoretical treatment of the mean field model is justified in terms of the quantum mechanical formalism of the Heisenberg model. The theory is quite simplistic and has therefore many failings, it does however give a reasonable quantitative description of many magnetic characteristics and is very widely used as a starting point for more sophisticated theories.

If we consider a simple, periodic (Bravais) lattice of magnetic ions at sites $\underline{R}$ in an applied field, we can describe the low-lying excitations of the system by a ferromagnetic Heisenberg Hamiltonian (2.31). The Hamiltonian includes the interaction of the electron spins with both the applied field ($\underline{H}$) and the dipolar field ($\lambda_D \underline{M}$) produced by the neighbouring atoms as well as the electron-electron interaction. The electron-electron exchange interaction $J(\underline{R} - \underline{R}') = J(\underline{R}' - \underline{R}) \geq 0$ is positive for ferromagnetic materials and so

favours parallel alignment of neighbouring spins.

$$H^{spin} = -\frac{1}{2}\sum_{\underline{R}\underline{R}'} \underline{S}(\underline{R})\cdot\underline{S}(\underline{R}')J(\underline{R}-\underline{R}') - g\mu_B H\sum_{\underline{R}} S_z(\underline{R}) - g\mu_B\lambda_D M\sum_{\underline{R}} S_z(\underline{R})$$

$$H^{spin} = -\sum_{\underline{R}} \underline{S}(\underline{R})\cdot\left(\sum_{\underline{R}\neq\underline{R}'} J(\underline{R}-\underline{R}')\underline{S}(\underline{R}') + g\mu_B \underline{H} + g\mu_B\lambda_D \underline{M}\right) \tag{2.35}$$

The mean field approximation assumes that each spin has the same average value $\langle\underline{S}(\underline{R})\rangle = V\underline{M}/Ng\mu_B$ and so we can therefore describe the atom as having an energy shift just due to an *effective field* ($\underline{H}_{eff}$), with electrostatic exchange interaction $\lambda_{exc}$.

$$\underline{H}_{eff} = \underline{H} + \lambda_{exc}\underline{M} + \lambda_D\underline{M} \tag{2.36}$$

$$\text{where } \lambda_{exc} = \frac{1}{g\mu_B}\sum_{\underline{R}'} J(\underline{R}-\underline{R}')\underline{S}(\underline{R}') = \frac{1}{g\mu_B}\langle\underline{S}(\underline{R})\rangle\sum_{\underline{R}} J(\underline{R}) = \frac{V}{N}\frac{\underline{M}}{(g\mu_B)^2}J_0 \tag{2.37}$$

In some materials $\lambda_{exc}\underline{M}$ or $\lambda_D\underline{M}$ is negligible at certain temperatures and so the effective field can be simply represented by $\underline{H}_{eff} = \underline{H} + \lambda\underline{M}$.

In an ordered material the $\lambda\underline{M}$ term is a collective response from the rest of the ions. As ordering begins on a few lattice sites the magnetization becomes larger, promoting further ordering of the ions through the exchange interaction $\lambda$. In an antiferromagnet we can consider two interpenetrating sublattices, A and B, in which all of the ions within one sublattice are aligned parallel to each other but antiparallel to the other sublattice. If we further assume that only nearest neighbour interactions are important then for an ion in sublattice A, $\underline{H}_{eff,A} = \underline{H} - \lambda\underline{M}_B$, in sublattice B, $\underline{H}_{eff,A} = \underline{H} - \lambda\underline{M}_B$, and $\underline{M} = \underline{M}_A + \underline{M}_B$. The calculated bulk susceptibility for both ferromagnets and antiferromagnets then has a Curie-like temperature dependence above the ordering temperature, called the *Curie-Weiss* law.

$$\chi = \frac{C}{T \pm \theta_{CW}} \tag{2.38}$$

In general we define the Curie-Weiss constant as $\theta_{CW} = -\lambda C$, for $\chi = C/(T + \theta_{CW})$, with $\lambda$ positive for a ferromagnetic material and negative for an antiferromagnetic material. The ferromagnetic ordering temperature (Curie temperature) can be very high e.g. 1043 K for iron. The antiferromagnetic ordering temperature (Néel temperature) is at $T_m = |\theta_{CW}|$ and is generally below room temperature e.g. α-Mn at 100 K.

Below the ordering temperature in zero applied field, mean field theory gives a contribution to the specific heat from the spontaneous magnetization of the ordered system. By considering the energy of an individual spin due to its alignment with the molecular

field inside the material we can calculate the total magnetic contribution to the internal energy per unit volume of a system of $N$ ions.

$$U_{\text{vol}} = -\int_0^{M_s} \underline{M} \cdot d\underline{B} = -\int_0^{M_s} \mu_0 \lambda \underline{M} \cdot d\underline{M} \tag{2.39}$$

where $M_S$ is the *saturation magnetization*, the value of $M$ at $T = 0$ K in zero field. Using Eqn. (2.5) we can then evaluate the magnetic contribution to the heat capacity per unit volume in zero field [22].

$$C_{\text{m(vol)}} = \left(\frac{\partial U_{\text{vol}}}{\partial T}\right)_{H=0} = \frac{-3N\text{k}_\text{B}(-\theta_{CW})}{2VM_s^2} \frac{J}{(J+1)} \left(\frac{\partial (M^2)}{\partial T}\right)_{H=0} \tag{2.40}$$

## 2.12 Conclusions.

In this chapter we have introduced some of the fundamental ideas behind the magnetic, superconducting and thermodynamic properties of materials. The London and Ginzburg-Landau phenomenological theories of superconductivity have been summarised and related to the BCS microscopic theory. The Ginzburg-Landau and BCS theories form the basis of any understanding of experimental work on superconducting materials. We have also outlined the mean field theory for ferromagnetic and antiferromagnetic materials and the Heisenberg and Ising models of magnetic systems. These models provide a basis for the analysis of magnetic phase transitions and the effect of magnetic ions in superconductors.

# *Chapter 3- Review of specific heat measurements in the literature.*

## 3.1 Introduction for chapter.

This chapter provides a review of the vast body of research pertinent to this thesis. The specific heat measurements presented in subsequent chapters have been conducted on Chevrel phase materials doped with magnetic ions. Analysis on the normal, superconducting and magnetic contributions to the total measured specific heat, are all required and so this review introduces the major topics of each of these sections in turn. A significant part of this chapter is also devoted to the Chevrel phase materials providing an outline of why these materials are of both technological and fundamental interest to the scientific community.

Specific heat measurements have a unique ability to reveal fundamental changes that occur within a material. Since the measured heat capacity of a material has contributions from all constituent parts within the material, factors that affect any of these contributions such as structural, magnetic or superconducting transitions are all visible in the specific heat. The experimental value is an average volumetric response from the sample that is not limited by microstructural properties in the same way that transport measurements are.

Sections 3.2, 3.3 and 3.4 outline the lattice, electronic and nuclear contributions to the heat capacity of a normal, non-magnetic material at low temperatures. From consideration of the distribution of energy levels for the conduction electrons, the lattice electrons and the nuclei, expressions can be derived with leading terms $A_1T$, $A_3T^3$ and $DT^{-2}$ respectively, for the separate contributions to the heat capacity. Analysis of experimental data using these theories allow important material properties such as the Sommerfeld constant ($\gamma$) or the Debye temperature ($\theta_D$) to be determined from the constants $A_1$ and $A_3$. These values and others which can then be calculated, such as the density of states $N(E)$, are fundamental to many solid state theoretical models.

Section 3.5 introduces the specific heat of superconductors. The change in specific heat of the material through the phase transition from the normal state is due to a change in the contribution of the conduction electrons. Comparisons are made with the BCS theory and deviations from this are shown to have several possible explanations including strong coupling and gap anisotropy. Ginzburg-Landau theory is compared to measurements on type II superconductors and various theoretical extensions are introduced that include the temperature dependencies of the upper critical field, kappa and the size of the specific heat

jump at the transition. The upper critical is very important technologically and can be determined along with the lower critical field, the thermodynamic critical field and kappa from calorimetric data. The theories of Maki and WHH take into account paramagnetic effects in both the normal and superconducting states using the parameters $\alpha$ and $\lambda_{so}$. This provides a means of fitting the experimentally determined temperature dependencies of $B_{c2}$ and $\kappa$ and estimating the value of $B_{c2}(0)$.

Section 3.6 reviews the structural, normal state and superconducting properties of the Chevrel phase superconductors and some of the typical fabrication routes available. The peculiar structure of these materials produces many interesting properties such as relatively high critical temperatures, very high upper critical fields and coexistence of superconductivity and magnetism. The structural variations affecting these parameters are discussed and the relevant theoretical expressions for data analysis on these materials are outlined. Low critical current densities in these materials limit their technological application and a brief discussion of some of the reasons for this are presented. A short review of some important differences of the high temperature superconductors, which also have great technological potential, are then presented in section 3.7.

In section 3.8 the specific heat of the Ising, Heisenberg model and mean field theory are compared. These three models provide the basis for any understanding of magnetic ordering in a material although due to their complexity, power law expansions and scaling functions are often used for analysing data, particularly in the critical region. Analysis of specific heat data allows the magnetic ordering temperature ($\theta_{cw}$) and the dimensionality of the magnetic exchange interaction to be determined. Expressions for the approximations for the specific heat are given and some of the other possible magnetic contributions to the heat capacity are reviewed.

Section 3.9 discusses the interplay of superconductivity and magnetism of both ferromagnetic and antiferromagnetic superconductors. This subject is still not fully understood but measurements on the nature of the coexistence region and the effect of magnetic ordering on the upper critical field provide important information. The important role of the Chevrel phases in this area of research is outlined, which due to their particular structure exhibit more examples of coexistence than any other system. Finally section 3.10 concludes.

## 3.2 Lattice specific heat.

In 1819 Dulong and Petit made the first measurements of specific heat at room temperature and concluded that the specific heat of any material seemed to be a constant [23]. Measurements on materials at lower temperatures however, showed that the specific heat actually dropped as the temperature was lowered. At room temperature the specific heat of a material is almost entirely due to the lattice and Einstein later proved in 1908 [24] that this lattice contribution drops rapidly with temperature as confirmed by experiment. The lattice specific heat is the excitation of a distribution of phonons in the lattice at a particular temperature. These phonons are considered as discrete vibrational modes of the atoms in the lattice about their equilibrium position. Each mode of vibration requires a specific excitation energy, dependent on the potential energy of the ions away from their equilibrium position. Counting the number of excitations becomes the principle method of calculating the lattice specific heat. Consideration of only long-wavelength, harmonic, acoustic modes gives an approximation for the lattice contribution ($c_L$) to the total specific heat capacity at low temperatures, in terms of odd powers of $T$ above $T^3$ [25].

$$c_L \approx A_3 T^3 + A_5 T^5 + A_7 T^7 + A_9 T^9 + \ldots. \tag{3.1}$$

### 3.2.1 Debye model.

The Debye lattice approximation [26] is the simplest representation of the frequency spectra of a crystal lattice and essentially treats the lattice as an isotropic elastic continuum. Phonon dispersion is neglected and the total number of harmonic modes is limited, providing a lower bound for the minimum wavelength to be considered. The resulting form for the specific heat reduces to a single cubic term at low temperatures, in accord with (3.1) and gives a better fit to experimental data than the Einstein model. The lattice contributions are characterised by a Debye temperature ($\theta_D$) which ranges between 70 K and 600K for most solids [27, 28] and is defined by the pre-factor of the cubic term in $c_L$ when measured in $JK^{-1}mole^{-1}$.

$$A_3 T^3 = \frac{12}{5}\pi^4 R\left(\frac{T}{\theta_D}\right)^3 \tag{3.2}$$

The Debye temperature is the approximate temperature below which the high frequency vibrations begin to freeze out and no longer contribute to $c_L$, leading to a rapid reduction in $c_L$ with temperature. Experimental data in the Debye approximation should have a single value of $\theta_D$, so all data sets would scale onto a universal curve. In practice an effective

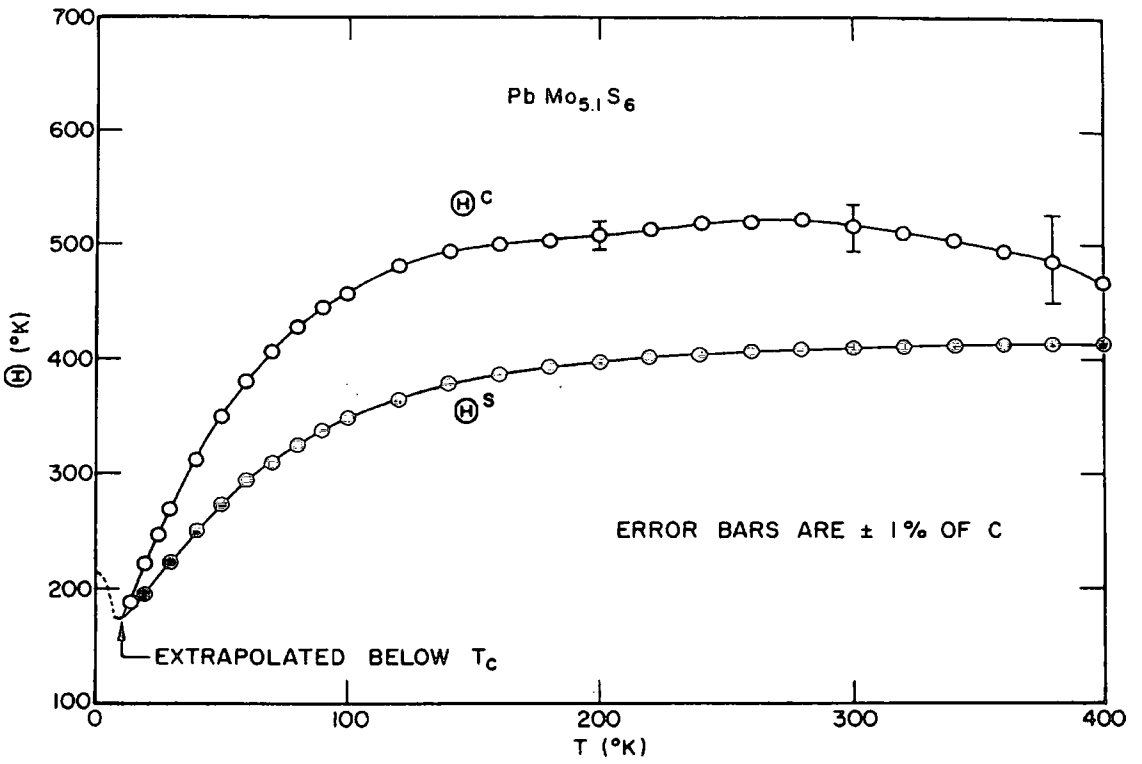


**Figure 1. $\theta_D$ as a function of $T$ for $PbMo_6S_8$, determined from measurements of the lattice specific heat ($\Theta^c$) and entropy ($\Theta^s$) [29].**

Debye temperature, which varies with temperature, is defined by introducing higher order ($T^5$, $T^7$ etc) terms in the expression for $c_L$ when fitting to experimental data. The original Debye temperature is then equivalent to measuring the slope of $c_L/T$ vs $T^2$ as $T \rightarrow 0$ K and is defined as $\theta_D(T = 0\ \text{K}) = \theta_0$. Generally the initial effect of phonon dispersion above the lowest temperatures (~ 1 - 5 K) produces a positive deviation from $T^3$ behaviour (in higher powers of $T$) since phonons are then more easily excited at a given frequency than in the non-dispersive case. The value of $\theta_D$ is therefore smaller than its corresponding value at lower temperatures, has minimum value at a temperature of about $\theta_0/6$ to $\theta_0/8$ and then increases to a constant value above about $\theta_0/2$ [28] as shown in Fig. 1. Other anomalous behaviour of $\theta_D$ has been observed which can be explained by negative deviations from $T^3$ behaviour [30-32].

Experimentally $\theta_D$ can be determined by measurements of the specific heat or of the elastic constants of the phonons using slow neutron or x-ray scattering at an effective temperature of $T \sim 5\text{x}10^{-4}$ K [28]. Measurement of the elastic constants of the phonons gives the inter-planar and hence inter-atomic force constants in what is called a *force*

*constant model* of the frequency spectrum. Both calorimetric and elastic measurements give values of $\theta_D$ which are similar for most metals to within 1-2 % [28], elastic measurements being a better approximation of $\theta_0$. The agreement between the two techniques is generally better for calorimetric data taken as $T \rightarrow 0$ K, especially when nuclear, magnetic or electronic contributions to the total heat capacity can be ignored such as in copper or gold [28]. Alloys such as $Cu_3Au$, have also been measured [33, 34] and the agreement between the two techniques is again reasonable. Impurities in pure metals can have anomalous contributions to the heat capacity. Effects due to heavy impurity atoms such as in dilute alloys, have been shown to produce localised, low frequency [35-37] modes that can have a large contribution to the low temperature heat capacity [38]. Measurements on various alloys [39-42] have found qualitative agreement with theoretical predictions of these localised modes.

### 3.2.2 Phonon density of states.

In principle, the determination of $c_L$ is just a case of counting the phonon modes of the lattice and their respective energies as a function of temperature. Much effort has been put in over the years into trying to model and measure the frequency of lattice vibrations, the *phonon density of states*. More detailed theories of lattice vibrations including anharmonic vibrations, non-periodic lattices and anisotropic crystals are generally too complex to yield solutions, but experiments involving neutron scattering and simple three dimensional models of lattice harmonics now yield the phonon spectra with reasonable accuracy. Perturbations of these basic lattice harmonics are used to explain effects at higher temperatures but can only be solved in a few cases. Measurement of an "excess" specific heat is often attributed to anharmonic terms and theories of thermal expansion and thermal conductivity can only be described in anharmonic terms [25]. Near to the melting point different approaches are needed due to additional anharmonic and/or lattice vibrations present in the solid, as the melting point is approached [20].

Figure 2 shows the specific heat of $PbMo_6S_8$ as a function of temperature and the total lattice contribution calculated from various contributions (labelled *a*, *b* and *c*) to the phonon density of states. The experimental value is larger than the calculated value at high temperatures due to anharmonic and electronic contributions and a simplified model of the lattice.

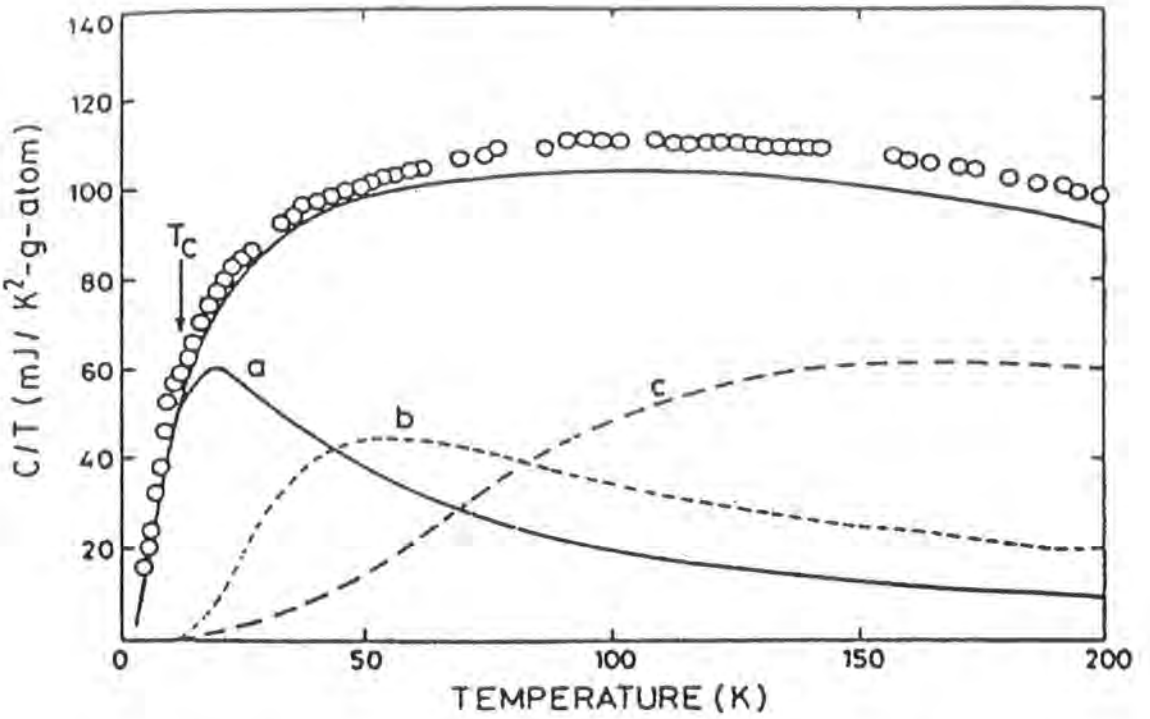


**Figure 2. Measured $c$ / $T$ as a function of $T$ for $PbMo_6S_8$ (open circles) with the total calculated value (solid line) from three contributions (a, b and c) with different Debye temperatures** [43].

## 3.3 Electronic specific heat

In a metal the valence electrons can be considered as an *electron gas*. This describes an electron system where the electrons are not bound to the lattice sites and do not interact with each other. In 1927 Sommerfeld [44] proposed that this electron system would obey the Pauli exclusion principle which limits only one particle to any quantum state. The gas is then correctly described in terms of Fermi-Dirac statistics. The contribution of the specific heat from the electron gas ($c_e$) is then determined by the number of electrons in each energy level, the *electron density of states* ($N(E)$). Using Fermi-Dirac statistics at temperatures much less than the characteristic Fermi temperature ($T_F \sim 10^4 - 10^5$ K for a metal) this summation can be expanded in a series of odd powers of $T$ [45] where the coefficients are determined by $N(E)$.

$$c_e \approx A_1 T^1 + A_3 T^3 + A_5 T^5 + \ldots . \qquad (3.3)$$

For most solids the Fermi-Dirac distribution means that only electrons with energies comparable to the Fermi energy ($E_F$) can contribute to the summation. This reduces the

power series to just the first linear term or the first two terms, if the density of states fluctuates rapidly near the Fermi energy at higher temperatures [45].

The problem of determining $N(E_F)$ is a difficult problem if all electron-electron and electron-lattice interactions are taken into account. In the electron gas model we have a system of unbound electrons which do not interact with each other except through the Pauli exclusion principle. If we further take electrons as *free* electrons, that is they see no potential from the lattice and move as free particles, the determination of $N(E_F)$ is straightforward. The resultant linear term for the electronic heat capacity has a coefficient called the *Sommerfeld constant* $\gamma$.

$$\gamma T = \tfrac{1}{3}\pi^2 k_B^2 N(E_F) T \tag{3.4}$$

### 3.3.1 Effective electron mass.

Experimental evidence shows that all metals have a linear electronic contribution to the heat capacity at low temperatures although the measured value of $\gamma$ is often larger than the theoretical value from the free electron model ($\gamma_0$). The difference between the observed value of $\gamma$ and $\gamma_0$ due to the effect of different electron interactions is described by an *effective mass* ($m^*$). The ratio of effective mass to electron mass ($m^*/m_e$) is then defined as the ratio $\gamma / \gamma_0$ [20]. Due to the very small contribution of the electronic specific heat to the total heat capacity (~ 1% at room temperature) the linear dependence is only significant at very low temperatures. A "Debye plot" of $c / T$ vs $T^2$ is frequently used to determine the coefficients of the electronic and lattice contributions to the heat capacity in the liquid helium range. Typical values of $\gamma$ for most simple metals and alloys are between 1 and 15 $mJK^{-2}mole^{-1}$ [27, 28].

Materials which have a ratio of $m^*/m_e$ significantly greater than one are clearly poorly approximated by the free electron model where no electron interactions are taken into account. Methods for including electron interactions generally rely on several approximations. Typically the electron-phonon and direct electron-electron interactions are ignored and the electron is considered to move in an average periodic field produce by the ions and the other electrons. The form of the periodic potential chosen then determines the electron band structure for that material. The alkali metals (Li, Na, K, Rb and Cs) with one valence electron per atom have a nearly constant parabolic density of states and therefore the electronic specific heat is linear [20]. Polyvalent metals such as Be, Mg, Hg, Al, Tl and Pb have more complicated Fermi surfaces due to a higher number of valence electrons,

producing a larger electron density and expanding the Fermi surface. Large fluctuations of $N(E_F)$ can then appear giving a more complex function for the electronic contribution to the heat capacity. The transition metals have deep valence electrons in the d-band which are more localised to their parent ions than the outer s-band valence electrons. The d-states contribute a large density of states producing a peak in the total density of states [46]. If the Fermi energy coincides with this peak the value of $\gamma$ will be very large and will decrease rapidly as the temperature is raised.

### 3.3.2 Electron-phonon interactions.

The calculated *band structure density of states* ($n_b(E_F)$) is generally not large enough to account for the observed value of $\gamma$ [47-49]. The difference is attributed to enhancement effects of the electron-phonon and direct electron-electron (Coulomb) interactions. These two effects are assumed to be additive and are represented by the phonon and coulomb enhancement factors $\lambda$ and $\lambda_c$. For comparison with experiment we define the *band effective mass* ($m_b$) so that the ratio of $m_b/m_e$ is equal to the ratio of $n_b(E_F)$ to the corresponding free electron density of states [50, 51]. The magnitude of $\lambda_c$ is similar to the uncertainty in $\lambda$ except for the alkali metals and is therefore usually ignored [51]. For pure metals the agreement with the experimental values for $m^*$ is quite good within the accuracy of the values of $m_b$ and $\lambda$ [20].

### 3.3.4 Rigid band model for alloys.

For dilute alloys we can use the *rigid-band model*. This model assumes that by adding impurity atoms into a *host* lattice the value of $z$ (valence electron/atom ratio) is changed but the band structure is not. This assumption is reasonably good for impurity atoms of near atomic number which do not change the crystal structure of the host lattice. By changing the impurity atom and therefore $z$ we can measure the band density of states at different Fermi energies and hence the structure of $n_b(E_F)$ of the pure metal in the region of the Fermi energy. For many of the transition metal alloys the change in $\gamma$ with $z$ is represented well by the rigid band model [27, 52] but for non-transition metal alloys the changes are much smaller and not as clearly defined in terms of this model. Many explanations for the different behaviour of these non-transition metal alloys have been suggested but as yet there is little agreement in either the theoretical or the experimental dependence of $\gamma$ with $z$ [28].

Those alloys that have a superconducting transition can be analysed more accurately since for strongly coupled superconductors the electron-phonon coupling can be determined by electron tunnelling measurements [53]. In these alloys the quantitative change of $\gamma$, and therefore $\lambda$, with $z$ is in agreement with the rigid band model [28].

## 3.4 Nuclear specific heat.

The presence of an external magnetic field, an electric field gradient (i.e. in a non-cubic crystal) or an effective hyperfine magnetic field can lift the degeneracy of the nuclear energy levels. This splitting of the energy levels leads to a contribution to the heat capacity that is a maximum at temperatures of the order of the energy splitting. This characteristic temperature is generally less than 1 K and so in this region the nuclear contribution can dominate over other contributions to the heat capacity, although at temperatures above 1 K the nuclear contribution has little effect. In most measurements only the high temperature tail of this nuclear contribution is observed and can be approximated by a power series in $T^{-1}$ below $T^{-2}$ [54]. The coefficients of this expansion are determined by the moments of the energy levels.

$$c_{\text{nuc}} \approx D_2 T^{-2} + D_4 T^{-4} + D_6 T^{-6} + \ldots\ldots \tag{3.5}$$

## 3.5 Specific heat and critical fields of superconductors.

Keesom and Kok made the first measurements of a specific heat jump at the superconducting transition of tin in 1932 [55]. Similar measurements were subsequently made for thallium in 1934 [56-58] and again for tin in an applied field in 1938 [59]. In the majority of measurements analysis of data gives values of $\gamma$ and $\theta_D$ from the normal state specific heat. Data in the normal state below $T_c$ is obtained by the application of a magnetic field and allows measurement of $\gamma$ and $\theta_D$ to the lowest temperatures that approach the free electron values. From the value of $\gamma$ the value of $N(E_F)$ can be determined allowing band structure calculations and the variation of $T_c$ with electron band densities to be calculated [60].

To describe the superconducting state thermodynamically, we split the superconducting state into an electronic ($c_{es}$) and a lattice contribution ($c_{ls}$). In general we assume that the lattice is unchanged by the transition to the superconducting state and so we can equate the superconducting state lattice contribution to the normal state lattice contribution ($c_{ln}$).

$$c_s = c_{es} + c_{ls} = c_{es} + c_{ln} \tag{3.6}$$

This assumption which is used in the BCS microscopic theory is justified by specific heat measurements on metallic elements [61-65] that have shown within the experimental accuracy that $c_{ln}$ and $c_{ls}$ are the same.

### 3.5.1 Electronic specific heat of superconductors.

The electronic contribution to the superconducting specific heat was originally thought to have the form $aT^3$. This cubic dependence was in accordance with the empirical observation of a parabolic temperature dependence of the thermodynamic critical field for most type I superconductors [66]. By 1954 experimental resolution was sufficient to reveal an exponential temperature dependence of $c_{es}$ from measurements of vanadium by Corak et al [67]. This observed dependence was one of the important experimental observations that led to the development of the BCS theory in 1957 [10]. The prediction of a superconducting energy gap leads directly to an exponential temperature dependence of $c_{es}$

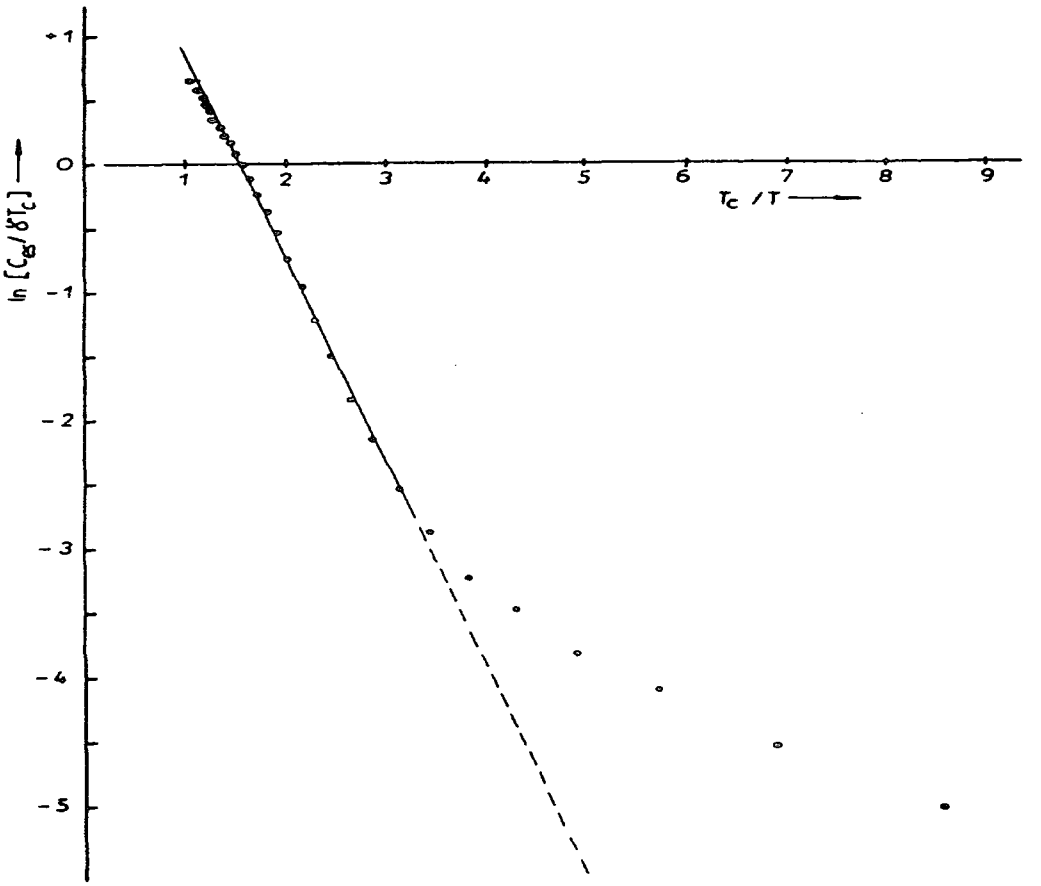


**Figure 3. $\ln(c_{es} / \gamma T_c)$ versus $T_c / T$ for $PbMo_6S_8$ [68].**

for temperatures much less than the critical temperature [10]. Measurements on many of the metallic elements [62-64, 69-72] confirm an exponential temperature dependence of $c_{es}$ for some temperature region below $T_c$. In general the coefficients $a$ and $b$ in the exponential plots from these measurements deviate from the BCS predicted values of $a$ = 8.5 and $b$ = 1.44 by as much as 50%, although this is not surprising considering the approximations made in the BCS theory. At very low temperatures ($T_c / T > \sim 4$) a positive deviation from a simple exponential is often observed even though accurate data at these temperatures is difficult to obtain [28]. Figure 3 shows the exponential behaviour of the electronic contribution to the specific heat in the superconducting state of $PbMo_6S_8$ for $1 < T_c / T < 3$ and a positive deviation at lower temperatures.

### 3.5.2 Thermodynamic critical field.

Specific heat data can also be used to calculate the temperature dependence of $H_c$ from thermodynamic relations, Eqn. (2.9). BCS theory predicts a negative deviation of $H_c$ from a parabolic dependence [10] and data show similar trends to the BCS prediction for many of the elements [62-64, 71-75]. Data on mercury [76] and lead [77, 78] however, both exhibit a positive deviation and niobium lies between both sets [79].

### 3.5.3 Deviations from BCS theory.

In 1959 Anderson [80] noted that for a pure superconductor an anisotropic energy gap would produce deviations from a simple exponential temperature dependence of $c_{es}$. A sufficient concentration of impurities, such as in alloys, should also "smear" out the anisotropy such that $c_{es}$ would be a function of a single average energy gap. The effect of the impurities on the energy gap anisotropy and the critical temperature of a pure (weak-coupling) superconductor was studied by Markowitz et al [81]. Clem [82] followed on from Markowitz et al and determined the effect of energy gap anisotropy on other properties of a pure superconductor including the specific heat and critical field. The effects of anisotropy on thermodynamic parameters such as the specific heat jump at $T_c$, are small even if the gap anisotropy is large since they rely on excitation energies of order of the energy gap. The probability of excitation at these energies is appreciable for all directions and so an average angular anisotropy determines the bulk thermodynamic response. If the energy gap varies over the Fermi surface, then $c_{es}$ will be the sum of different exponential functions and so functions with small energy gaps will dominate at

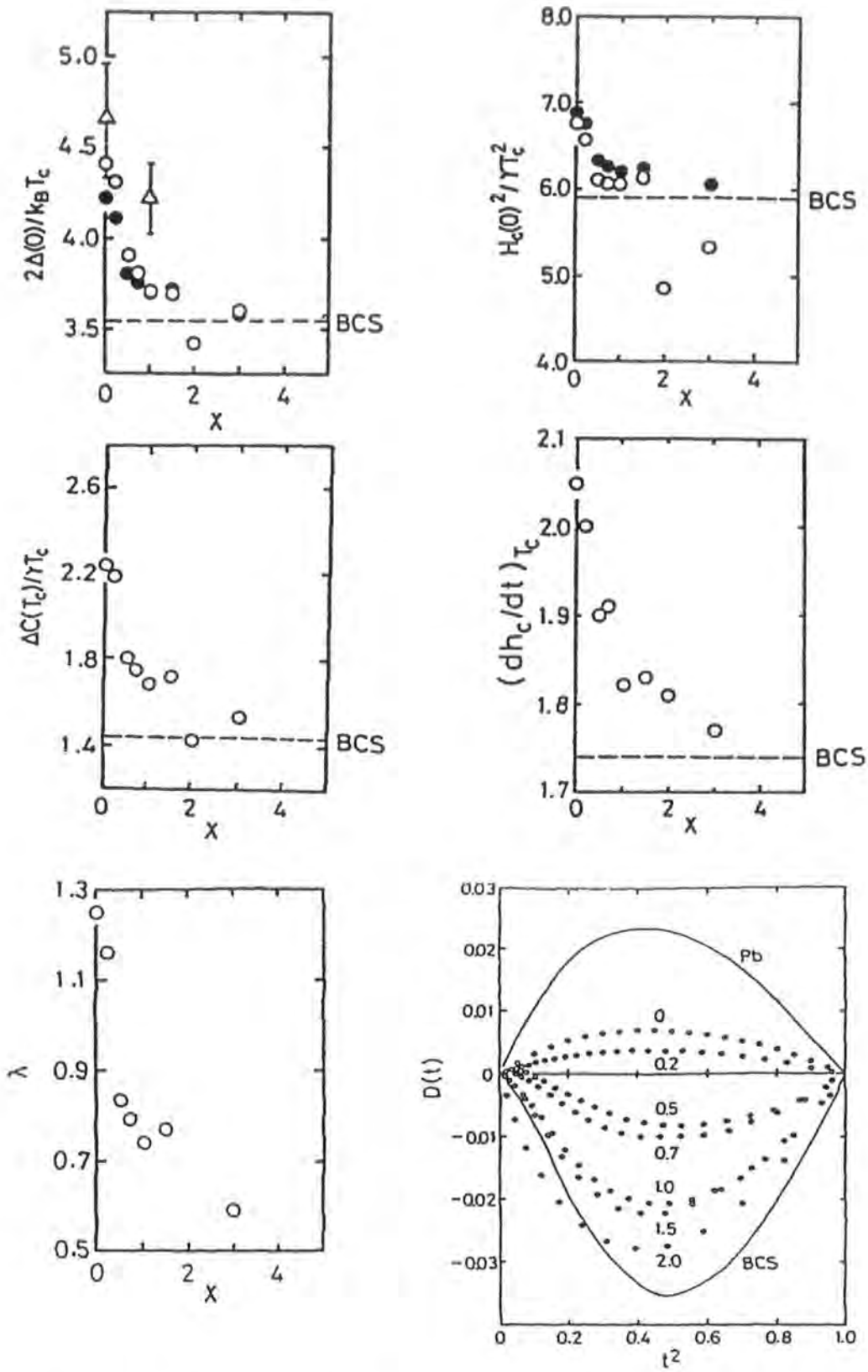


**Figure 4. Variations from the weak coupling predictions of BCS theory as a function of concentration $x$ determined from specific heat data on $MoSe_{8-x}S_x$ [83].**

low temperatures producing a positive deviation from a simple BCS exponential [82]. Measurements on aluminium alloyed with maganese [84] illustrate the effect of alloying on the energy gap anisotropy. By increasing the alloying level to 0.49 at % or greater, $b$ increases from a value in agreement with Clem's model to the BCS value, independent of any further increase in impurity concentration.

Strong coupling superconductors have a large ratio of $\Delta_0/k_BT_c$ low values of $\theta_D$ and large values of $\lambda$ [85, 86]. The energy gap of these superconductors is poorly approximated by a constant value at the Fermi surface as in the BCS theory of weak coupling superconductors. These strong coupling effects lead to deviations from the BCS predictions and more complicated expressions for thermodynamic properties such as the critical field, entropy and specific heat [85-87]. Figure 4 shows data calculated from specific heat measurements on the series $MoSe_{8-x}S_x$ and typical deviations from BCS theory due to strong coupling. As the composition changes from $Mo_6Se_4S_4$ to $Mo_6Se_8$ the calculated values of $\Delta c(T_c)/\gamma T_c$, $2\Delta(0)/k_BT_c$, $H_c(0)^2/\gamma T_c^2$ and $(dh_c/dt)_{Tc}$ increase from the BCS predictions of 1.43, 3.52, 5.95 and 1.73 respectively and the value of $\lambda$ is also increased. The deviation of $H_c(T)$ from a parabolic law also increases across this series from a large negative value, for $Mo_6Se_4S_4$, as predicted by BCS theory to a positive value for $Mo_6Se_8$. These deviations are opposite to that due to the anisotropy of the energy gap [82] and so separating the two effects experimentally can be difficult.

In some cases, the deviations of $c_{es}$ from a simple exponential form cannot be attributed to either energy gap anisotropy or to strong coupling mechanisms, although extreme anisotropy of the energy gap could be responsible [74]. A number of transition metals, Nb [88], V [73, 88] and Ta [88] exhibit positive deviations that are often characteristic of a secondary exponential form. These results are in qualitative agreement [88, 89] with the existence of a second energy gap due to inter-band (s- and d-band) scattering [90, 91] in the transition metals. Since $c_{es}$ is extremely sensitive to impurities this large deviation is reduced for samples of lower purity [88] and approaches that of a single energy gap in the dirty limit where the electron mean free path is very short. The presence of an excess linear term in $c_{es}$ at low temperatures in V [73], $Nb_3Sn$ [92, 93] and $V_3Si$ [94] can also be explained by a second energy gap. If this secondary energy gap is sufficiently small compared to the first, then its contribution to $c_{es}$ is linear and dominates at the lowest temperatures.

### 3.5.4 Type II superconductors.

The Ginzburg-Landau theory of superconductivity was extended by Abrikosov and Gor'kov, as outlined in Chapter 2, and is collectively known as GLAG theory. This theory identified a second type of superconductor characterised by a value of the Ginzburg-Landau parameter $\kappa > 1/\sqrt{2}$ and a lower ($B_{c1}$) and upper critical field ($B_{c2}$). Measurements on $V_3Ga$ [95, 96], V-5 at. % Ta [97] and titanium alloys [98] showed bulk superconducting transitions from specific heat data in magnetic fields well above the thermodynamic critical field. This confirmed that the existence of high-field superconductivity was a bulk property rather than a localised effect due to dislocations.

Niobium, vanadium and molybdenum are elemental type II superconductors that have values of $\kappa$ only just greater than $1/\sqrt{2}$. Most type II superconductors are alloys and generally have a very short electron mean path due to impurity scattering. This leads to an increase of $\lambda_L$, a reduction of $\xi$ and therefore values of $\kappa >> 1$. Gor'kov [99] and subsequently Goodman [100] derived a relation for $\kappa$ of an alloy which directly relates it to physically measurable variables and the value of kappa of the pure metal ($\kappa_0$). Conventionally we represent $\kappa$ as the sum of an intrinsic or "clean" component and an extrinsic or "dirty" component. Physically these two components are defined by the electron mean free path ($l$) and the coherence length of the pure superconductor ($\xi_0$). The clean limit corresponds to $l >> \xi_0$ and the dirty limit to $l << \xi_0$.

$$\kappa = \kappa^c + \kappa^d \tag{3.7}$$

$$\kappa_0 = \kappa^c = 0.957\ \lambda_{L(0)} / \xi_0 \tag{3.8}$$

$$\kappa^d = 23.7 \times 10^6\ \rho_n \gamma_v^{1/2} = 0.720\ \lambda_{L(0)} / l \tag{3.9}$$

where $\rho_n$ is the normal state resistivity ($\Omega$m), $\gamma_v$ is the coefficient of the normal state electronic specific heat per unit volume ($JK^{-2}m^{-3}$) and $\lambda_{L(0)}$ is the London penetration depth (m) at $T = 0$ K.

### 3.5.5 GLAG theory.

The original GLAG theory was applicable for a general mean free path length but only at temperatures close to $T_c$. Subsequently a considerable amount of work went into extending the theory to lower temperature regimes. Gor'kov derived an expression for the temperature dependence of $B_{c2}$ in the clean limit [101]. Maki and de Gennes [102-104]

extended the GLAG theory to the whole temperature range in the dirty limit. Hefland et al [105, 106] included s-wave scattering of impurities to derive the complete temperature and purity dependence of $B_{c2}$ for low upper critical fields ($B_{c2} < 5$ T). Work by Maki et al [107] and Caroli et al [108] focussed on the slope of the magnetisation in both clean and dirty limits respectively and later Eilenberger included the effects of p-wave scattering for both arbitrary temperature and impurity concentration [109].

### 3.5.6 Temperature dependence of kappa.

In extending the GLAG theory Maki introduced three temperature dependent parameters $\kappa_1(T)$, $\kappa_2(T)$ and $\kappa_3(T)$ to replace the original Ginzburg-Landau parameter $\kappa$. These parameters are a feature of all extensions to the GLAG theory and in the dirty limit they are defined by [110]:

$$\kappa_1(T) = \frac{B_{c2}(T)}{\sqrt{2}B_c(T)} \tag{3.10}$$

$$\left(\frac{dM}{dH}\right)_{\mu_0 H_{c2}} = \frac{1}{\beta_A(2\kappa_2^2 - 1)} \tag{3.11}$$

$$B_{c1} = \sqrt{2}B_c(T)(\ln\kappa_3(T)/2\kappa_3) \tag{3.12}$$

where $\beta_A$ is the Abrikosov flux-lattice factor and is equal to 1.16 for a triangular lattice. Measurements of the upper critical field, the slope of the magnetisation and the lower critical field are therefore needed to determine the temperature dependencies of these three parameters. The generalised versions of the GLAG theory require that $\kappa_1(T_c) = \kappa_2(T_c) = \kappa_3(T_c) = \kappa$ at the critical temperature. This result is confirmed to within a few percent by Kinsel et al using magnetisation measurements on alloys of bismuth in indium [111] and similarly on Nb [75] and V [112]. At $T = 0$ K Maki's theory gives

$$\kappa_{10} = \kappa_{20} = 0.784\kappa_{30} = 1.20\kappa^d \tag{3.13}$$

where the subscript "$_0$" refers to the value at $T = 0$ K.

A series of experiments on various niobium titanium alloys by Feitz and Webb [113] allowed the temperature dependencies of $\kappa_1(T)$ and $\kappa_2(T)$ to be compared with the various theories. Doping niobium with different levels of titanium provides the complete range of the electron mean free path length from clean to dirty limits, while the basic superconducting parameters e.g. $B_c(T)$ and $T_c$, remain nearly constant. The work on this series showed that the temperature dependencies of the Maki parameters were not described

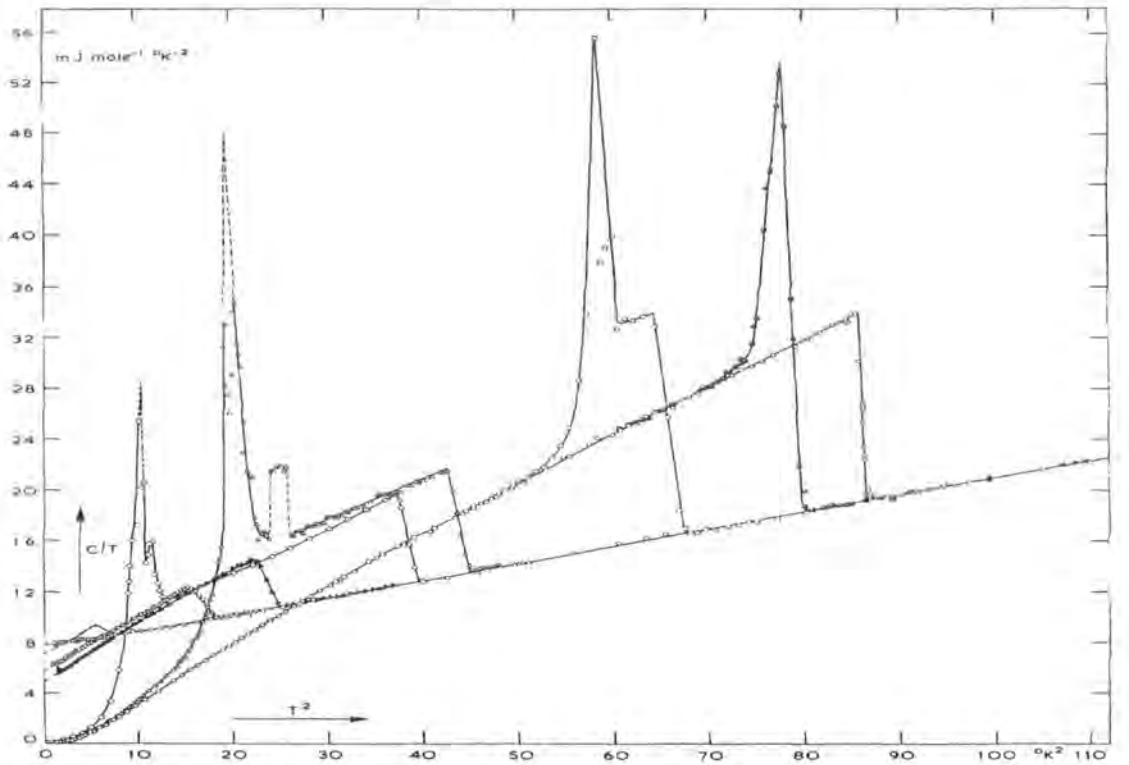


**Figure 5.** $c$ / $T$ **as a function of** $T^2$ **of unannealed niobium wires in various applied magnetic fields** [75].

satisfactorily by any one theory although many of the general features were correct.

### 3.5.7 Orbital upper critical field.

Combining Eqn. (3.10) and the BCS expression for the thermodynamic critical field at $T$ = 0 K ($H_c^2(0) = 5.95\ \gamma T_c^2$) we get an expression for the value of the upper critical field in the dirty limit, measured at $T = 0$ K [110].

$$\mu_0 H_{c20}^{*d} = 3.06 \times 10^3\ \rho_n \gamma_v T_c \qquad (3.14)$$

This is often referred to as the *orbital* critical field and labelled with an asterisk to distinguish it from the measured upper critical field. Only the effect of the applied field on the electron orbits is taken into account in the breaking of the Cooper pairs.

### 3.5.8 Specific heat of type II superconductors.

The phase transitions of a type II superconductor in a magnetic field, produce anomalies in the specific heat [114]. Figure 5 shows specific heat data on unannealed niobium wires in applied magnetic fields $\mu_0 H < B_{c1}$, $B_{c1} < \mu_0 H < B_{c2}$ and $\mu_0 H > B_{c2}$, from which the transitions to the mixed and normal state can be clearly be seen. Extensive calorimetric

studies have been carried out on the mixed state of many superconductors in an attempt to determine the various superconducting parameters [75, 93, 94, 112, 115-122]. The change in the specific heat anomalies at $B_{c2}(T)$ and $B_{c1}(T)$ with applied magnetic field, along with calculation of $B_c(T)$ and Eqn.'s (3.10) and (3.12), allow the temperature dependencies of $\kappa_1(T)$ and $\kappa_3(T)$ to be determined [75]. The magnitude of the specific heat jump $\Delta C$ at the transition from the mixed to the normal state, can be related to the slope of the magnetisation [96] and therefore $\kappa_2(T)$ by Eqn. (3.11) [112, 115, 116]. Calculated temperature dependencies of $\kappa_1$ and $\kappa_2$ from both specific heat and magnetisation data vary and although the qualitative features agree with theory the quantitative details are generally inconsistent [75, 112, 114, 115, 122].

| Intrinsic | Dirty | |
|---|---|---|
| | $B_{c2}(0) < \sim 5$ T | $B_{c2}(0) > \sim 5$ T |
| $\kappa_2 > \kappa_1 > \kappa_3 > \kappa$ | $\kappa_3 > \kappa_1 \approx \kappa_2 > \kappa$ | $\kappa_3 > \kappa_1 > \kappa > \kappa_2$ |

**Table 1. Qualitative relationships between Ginzburg-Landau parameters for temperatures less than $T_c$** [114].

In the Meissner state the formal description of a type II superconductor is the same as for a type I superconductor. The specific heat in a weak magnetic field $\mu_0 H < B_{c1}(0)$ follows exactly the zero field specific heat until the transition to the mixed state is approached as shown in Fig. 5 [119, 120]. At the temperature which corresponds to the transition to the mixed state $B_{c1}(T)$, the specific heat goes through a second order transition and often exhibits a large peak [119, 120]. In the mixed state the specific heat ($c_m$) is larger than the zero field value until a temperature $T_c(H) < T_c(H = 0)$ is reached where there is a discontinuity in $c_m$ as the sample enters the normal state [119, 120]. Caroli et al [123] predicted for pure, large $\kappa$, type II superconductors that low energy excitations near to a flux line would produce a linear temperature dependence in $c_m$ at low temperatures, which is proportional to the number of flux lines in the bulk. More detailed calculations [124-126] have confirmed this and some include higher order terms in the expression for $c_m$. Experimental data shows evidence for both linear and cubic terms that are proportional to the applied field but they are not conclusive [75, 94, 112, 118, 119].

The specific heat transitions at $B_{c1}(T)$ and $B_{c2}(T)$ have been extensively studied. The transition at $B_{c1}(T)$ can be influenced by irreversible flux motion and so depends on

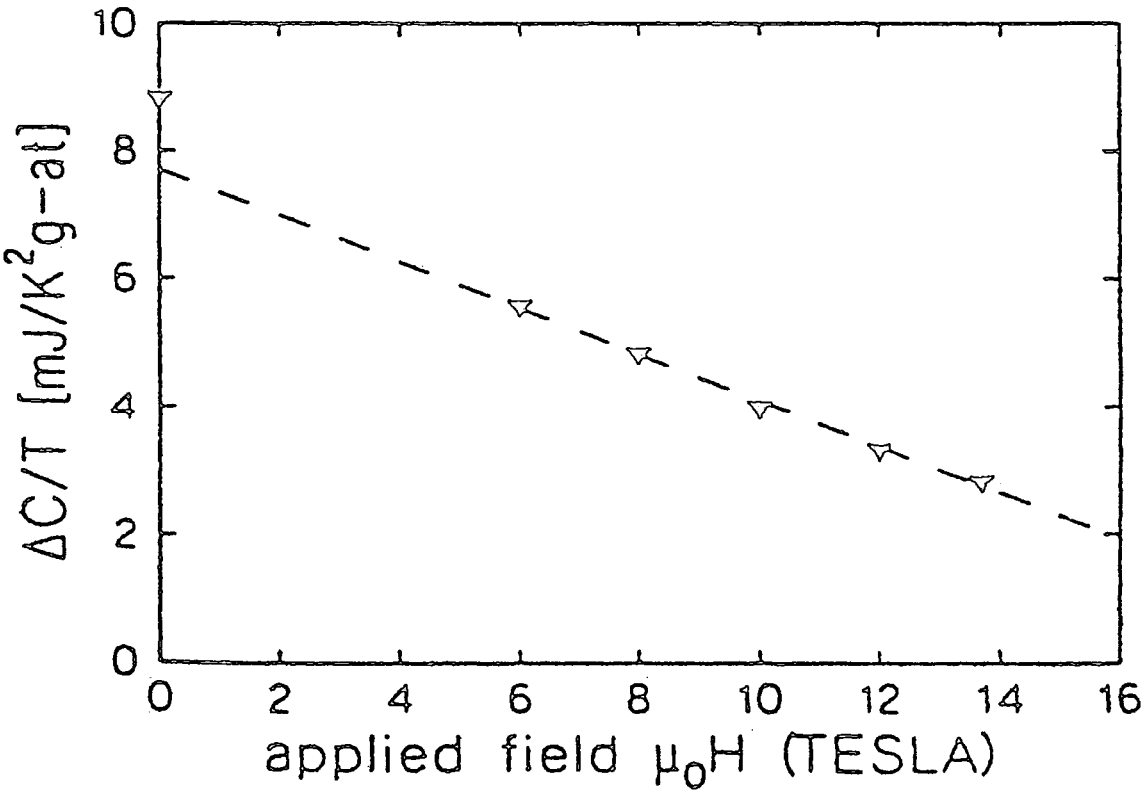


**Figure 6. $\Delta c/T$ versus $H$ for $PbMo_6S_8$ from Cors et al showing the field dependence of the size of the specific heat jump [127].**

whether the sample is cooled in a magnetic field or in zero field [75, 112, 115, 116, 119, 120, 122], however for pure, clean specimens the transition approaches an ideal λ-type anomaly and is reversible in behaviour [114, 115]. The transition at $B_{c2}(T)$ is also reversible and less affected in its nature by impurities [114]. The magnitude of the jump in the specific heat at $B_{c2}(T)$ is in good agreement with theory [97, 115] and follows a $T^3$ dependence [75, 112, 117] as proposed by Vijfeijken [126] and a similar temperature dependence by Maki [124].

(Maki)
$$\frac{c_m - c_n}{T_s} = \frac{1}{\left[2\kappa_2^2(T)-1\right]\beta}\left(\frac{dB_{c2}}{dT}\right)^2 \tag{3.15}$$

(Vijfeijken)
$$\frac{c_m - c_n}{\gamma T_s} = \frac{c_s - c_n}{\gamma T_c}\left[\frac{1}{1-\left(1/2\kappa^2\right)ln\,\kappa}\right]\left(\frac{T_s}{T_c}\right)^2 \tag{3.16}$$

### 3.5.9 Pauli paramagnetism and spin orbit coupling.

It was recognised by Chandrasekhar [128] and Clogston [129] that inclusion of the normal state Pauli paramagnetism of the conduction electrons, would in principle set an

upper limit on the magnitude of the upper critical field. In the original GLAG theory where Pauli paramagnetism is ignored, the free energy in the superconducting state ($g_s$) is increased by application of a magnetic field whereas the normal state free energy ($g_n$) remains constant. The free energy of the superconducting state becomes equal to the free energy of the normal state at a field $B_{c2}^*$ (orbital critical field) and the superconductivity is destroyed. If Pauli paramagnetism is taken into account in the normal state but the response of the superconductor to the applied field is ignored, then $g_n$ decreases with increasing magnetic field whereas $g_s$ remains constant. The normal state free energy becomes equal to $g_s$ in a first order transition at the Clogston field ($B_p$) – also called the pure paramagnetic limit.

$$B_{p0} = 1.84\ T_c \text{ Tesla} \tag{3.17}$$

If the response of the superconductor to the applied field is included the upper critical field ($B_{c2}$) transition should be first rather than second order and occur at the intersection of a reducing $g_n$ and an increasing $g_s$ i.e. below the lower of $B_{c2}^*$ and $B_p$. Maki studied the effect of the normal state Pauli paramagnetism on the temperature dependence of $\kappa_1$, $\kappa_2$ and $B_{c2}$ of alloys. He introduced a new parameter $\alpha$ which describes the amount by which the original GLAG (non-paramagnetic) result ($B_{c20}$*) is reduced by the effect of paramagnetic limiting and provided an estimate for $B_{c20}$ [104, 110].

$$\alpha = \sqrt{2}(B_{c20}^* / B_{p0}) \tag{3.18}$$

$$\Rightarrow B_{c20} = \frac{B_{c20}^*}{\sqrt{1+\alpha^2}} = \frac{B_{c20}^* B_{p0}}{\sqrt{2B_{c20}^{*\,2} + B_{p0}^{\,2}}} \tag{3.19}$$

where $B_{c20}$ is the (Clogston) paramagnetically limited upper critical field at $T = 0$ K and $\alpha$ can be calculated from either normal ($\alpha_n$) or superconducting state data ($\alpha_s$).

$$\alpha_s = 0.523\mu_0(-dH_{c2}/dT)_{T_c} \tag{3.20}$$

$$\alpha_n = 2.37\times10^3 \rho_n \gamma_v \tag{3.21}$$

and

$$\alpha_s = \alpha_n = \alpha \tag{3.22}$$

Comparison of Maki's prediction with experiment showed that it underestimated the upper critical field for many alloys [110, 130]. Subsequent theories introduced the idea of a superconductive-state paramagnetism, due to spin-orbit induced spin-flip scattering (or spin orbit scattering) which would compensate for the normal state paramagnetism and increase $B_{c2}$. The theories of Maki [131] and Werthamer et al (WHH theory) [132] both proposed that spin orbit scattering could decouple the spins of a Cooper pair while still maintaining a

net spin of zero for the pair. Zeeman splitting of the spin states due to a magnetic field then becomes possible without breaking the Cooper pair and so leads to a paramagnetic superconducting state. Spin orbit scattering offsets the effect of the normal state paramagnetism, raises the value of $B_{c2}$ and leads to a second order transition to the normal state. For extreme type II superconductors, $\kappa >> 10$, paramagnetic effects in the superconducting state become important and a large spin orbit scattering frequency can push $B_{c20}$ above $B_{p0}$ and approach the original GLAG estimate $B_{c20}^*$. Magnetisation measurements by Hake [133, 134] on various extreme type II alloys revealed a crossover from a diamagnetic to a paramagnetic mixed superconducting state i.e. from $M/H < 0$ to $M/H > 0$ at an applied field $\mu_0 H < B_{c2}$. At the upper critical field there was a reversible second order transition from the paramagnetic mixed state to the paramagnetic normal state, confirmed also with specific heat measurements by Barnes et al [135]. Evaluation of $\kappa_1(T)$ and $\kappa_2(T)$ from both of these measurements gave qualitative agreement with the predictions of Maki and WHH theory in the dirty limit.

To characterise the effect of spin orbit scattering on the experimentally determined upper critical field ($B_{c2}$) Maki introduced the parameter $\beta_m$.

$$\beta_M^2 \equiv \alpha^2 \left( \frac{3\Delta_{00}}{\hbar} \right) \tau_{so} = \frac{18\mu_B^2 c}{v_F^2 e\hbar} \left( \frac{\tau_{so}}{\tau_{tr}} \right) B_{c20}^* \tag{3.23}$$

where $\Delta_{00}$ is the BCS half energy gap at $T = 0$ K, $\tau_{so}$ is the spin orbit relaxation time, $\tau_{tr}$ is the electron transport scattering relaxation time and $v_F$ is the Fermi velocity. This led to a set of general formulae in the dirty limit for the temperature dependencies of $\kappa_1$, $\kappa_2$ and the upper critical field in terms of the reduced parameters $t = T / T_c$, $h^*(t,\beta_M) = 0.68\ B_{c2}(t) / B_{c20}^*$ and $h_{c2}(t) = B_{c2}^*(t) / B_{c20}^*$ where:

$$\kappa_1(t,\beta_M)/\kappa^d = 1 + (0.119 - 0.361\beta_M^2)(1-t) \quad \text{for } t \cong 1 \tag{3.24}$$

$$\kappa_{21}(t,\beta_M^2)/\kappa^d = 1 + (0.105 - 0.722\beta_M^2)(1-t) \quad \text{for } t \cong 1 \tag{3.25}$$

and

$$h^*(t,\beta_M) = \frac{1.36 h_{c2}(t)}{1 + \left(1 + \beta_M^2 h_{c2}(t)\right)^{1/2}} \tag{3.26}$$

From calorimetric or magnetisation measurements the experimental forms of $\kappa_1(t)$ and $\kappa_2(t)$ (or equivalently $h^*(t)$) can be determined as outlined in section 3.5.8. By taking $\beta_M$ as a free parameter, plots of $\kappa_1(t)$ and $\kappa_2(t)$ allow a best-fit value of $\beta_M$ to be determined.

WHH theory derived the functional from of the upper critical field in terms of the parameters

$$\lambda_{so} = 2\hbar / 3\pi k_B T_c \tau_{so} \tag{3.27}$$

and
$$\left(\pi^2/4\right)\bar{h}(t) = \frac{B_{c2}}{\left(dB_{c2}/dt\right)_{t=1}} \equiv \frac{\bar{h}}{\left(-d\bar{h}/dt\right)_{t=1}} \equiv h^*(t) \tag{3.28}$$

which in the dirty limit is equivalent to the parameter $h^*(t)$ in Maki's theory. The temperature dependence of the upper critical field is then given by

$$ln\left(\frac{1}{t}\right) = \sum_{n=-\infty}^{n=+\infty}\left[\frac{1}{|2n+1|} - \frac{1}{|2n+1| + \bar{h}/t + \dfrac{\left(\alpha\bar{h}/t\right)^2}{|2n+1| + \left(\bar{h}+\lambda_{so}\right)/t}}\right] \tag{3.29}$$

This dependence shows that a reduction of the normal state Pauli paramagnetism ($\alpha \rightarrow 0$) is equivalent, for non-zero $\alpha$, to an increase in the spin orbit scattering frequency ($\lambda \rightarrow \infty$) and therefore $B_{c20}$ approaches $B_{c20}^*$. For strong spin orbit scattering (i.e. non-paramagnetically limited) we can estimate the orbital critical field at $T$ = 0 K in the dirty limit from the WHH relations [110, 136].

$$h^*\left(t=0, \lambda_{so}=\infty\right) = B_{c20}^* / \left(-dB_{c2}/dt\right)_{t=1} = 0.693 \tag{3.30}$$

therefore
$$B_{c20}^* = 0.693 T_c \left(\frac{-dB_{c2}}{dT}\right)_{T_c} \tag{3.31}$$

In the clean limit the constant 0.693 is replaced by the value 0.726. WHH theory is derived in the regime where $\tau_{so} >> \tau_{tr}$ and with this assumption also predicts that the spin orbit scattering frequency should scale with the atomic number as $Z^4$. Neuringer et al [137] who measured titanium alloyed with different transition metals confirmed a $Z^4$ dependence of $\lambda_{so}$ and an order of magnitude agreement for the estimated values of $\tau_{so}$.

### 3.5.10 Comparison with experimental results.

Several comparisons of experimental results with the predicted temperature dependencies of $B_{c2}$, $\kappa_1$ and $\kappa_2$ by Maki and WHH theory, have been conducted on superconducting alloys [134, 137, 138]. The predicted values of $h^*$ from both theories are found to be in reasonable agreement with each other [134]. To compare the experimental data with both theories $\alpha$ is calculated from either the normal state or superconducting data close to $T_c$ and then $\lambda_{so}$ is chosen to give the best fit between the theoretical curves and the data for $T << T_c$.

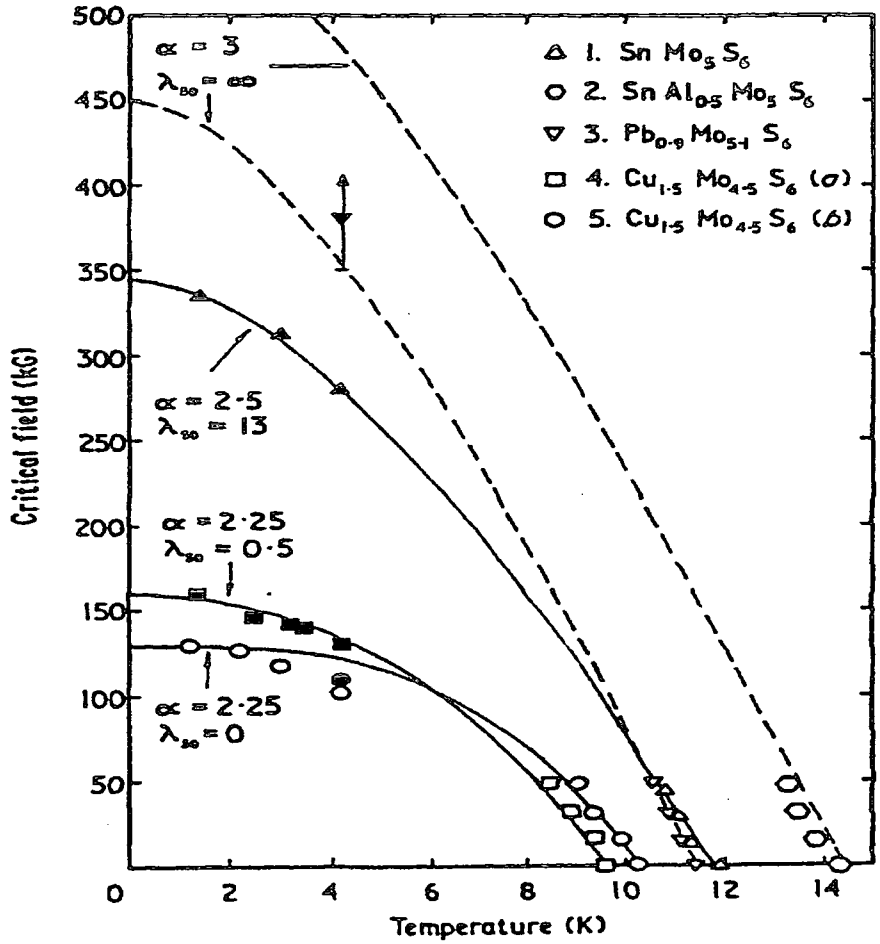


**Figure 7. $H_{c2}$ versus $T$ for various Chevrel phases with WHH and Maki fitting as described in the text [139].**

Figure 7 shows typical data on some Chevrel phase compounds with the corresponding fitting from the theories of WHH and Maki. Generally agreement with the theory is reasonable although the detailed shape is not correct and furthermore the choice of $\lambda_{so}$ required to fit the data is sometimes unphysical, often changing from the fitting of one parameter to another [134]. In particular, results by Neuringer et al [137] found that the upper critical field of Ti-52 at.% Ta was actually above the non-paramagnetic limiting value (equivalent to $\alpha = 0$ (Maki) or $\lambda_{so} = \infty$ (WHH)), leading to an unphysical value of $\tau_{so} \rightarrow 0$. Similar results by Orlando et al [140] found that there was no Pauli paramagnetic limiting in $Nb_3Sn$.

Several theories have tried to account for the various discrepancies from the WHH-Maki theories. Effects due to strong-coupling corrections, impurity scattering and anisotropy of

the electron-phonon interaction have all been considered. Orlando et al [140, 141] and Beasley et al [142] considered the combined effect of electron-electron interaction, electron-phonon interaction, spin fluctuations and strong coupling. These effects can be of considerable importance for transition metal alloy superconductors where strong coupling and electron-phonon corrections become important. In the case of $Nb_3Sn$ these additional effects led to an increase of the Clogston field ($B_p$), allowing fitting of the results to WHH theory for a finite value of $\lambda_{so}$. However the resulting value of $\tau_{so} \cong \tau$ (the electron transport relaxation time in the absence of any scattering mechanisms) from their fit violated the limitations of the original WHH theory which required that $\tau_{so} >> \tau$. Schopohl and Scharnberg [143] re-examined the WHH theory in 1981 and recalculated values for $B_{c2}$ that were larger than in the original work. This brought any estimate from WHH theory immediately closer to the non-paramagnetic limit, allowing non-infinite values of $\lambda_{so}$ to be used in fitting data where previously $\lambda_{so} = \infty$ had been required. They also further extended the range of validity of WHH theory to any arbitrary value of $\tau_{so} / \tau$, justifying the approach of Orlando et al.

For bulk samples with strong spin orbit scattering, Fischer showed that the upper critical field can be simply described by a correction to the orbital critical field [144].

$$H_{c2}(T) = H^{*}_{c2}(T) - 0.022\frac{\alpha}{\lambda_{so}T_c}H^{2}_{c2}(T) \qquad (3.32)$$

This correction arises from the interaction of the conduction electron spins with the applied field. It can therefore be seen that for high fields ($T << T_c$) the correction term is significant but as we approach $T_c$ its effect is negligible. In particular as we approach $T_c$ then $B_{c2}$ approaches zero and the derivative $dB_{c2}/dT$ becomes equal to $dB_{c2}^{*}/dT$. Data for superconductors with strong spin orbit scattering can therefore be analysed close to $T_c$ just in terms of the orbital critical field with paramagnetic effects only becoming important well below the transition temperature.

## 3.6 Chevrel phases.

The Chevrel phases were discovered in 1971 by Chevrel and co-workers [145]. They attracted the interest of the superconductivity community in 1972 when Matthias et al [146] discovered several members to be superconducting at relatively high temperatures (8 – 14 K). Interest was further stimulated as more of these superconducting phases were fabricated and many were also found to be extremely high-field superconductors with upper

critical fields in excess of 30 T [139, 147-149]. At this time technological systems were well developed using materials such as $Nb_3Sn$, $Nb_3Al$ and Nb-Ti with critical temperatures between 9 – 18 K and upper critical fields at $T = 0$ K between 14 and 30 T. High-field magnet systems were gradually being pushed to higher and higher fields as a better understanding of the material properties and the fabrication processes of these superconductors were established. The upper critical fields of these materials however, limit the maximum possible fields that these magnet systems could ever reach. For the next generation of high-field magnet systems operating significantly above 20 T, new high field superconductors such as the Chevrel phases were, and still are needed.

The Chevrel phases are ternary compounds with the unit cell comprised of three elements in the stoichiometric ratio $M_xMo_6X_8$, where M is a metal ion and X is a chalcogen (S, Se or Te). So far there are about 160 different compounds and solid solutions of the same type of structure with the majority being sulphides or selenides [150]. These compounds fall into two different types depending on the metal ion M. The first class occurs when M is a small cation and the value of $x$ then varies continuously between two limits e.g. $Cu_xMo_6S_8$, $1.8 \leq x \leq 4$. The second class occurs when M is a large cation, in which case $x$ is either well defined or takes a value in a very narrow homogeneity domain e.g. $Pb_xMo_6S_8$, $0.9 \leq x \leq 1$ [150]. At present the two compounds with the most favourable superconducting properties for high-field design are $PbMo_6S_8$ with $T_c \sim 15$ K and $B_{c2}(0) \sim 60$ T and $SnMo_6S_8$ with $T_c \sim 14 - 14.5$ K and $B_{c2}(0) \sim 35$ T.

In 1975 Fischer et al [151] fabricated the series $REMo_6S_8$ (RE = rare earth ion) and in 1976 Shelton et al [152] fabricated the corresponding $REMo_6Se_8$ series. Virtually all the members of both series were superconducting, a result surprising due to the large percentage (~ 7 at.%) of magnetic ions in the system. Previous studies had shown that only a very small percentage of magnetic ions are required to destroy superconducting ordering in a material [153, 154]. In general the rare-earth selenide phases were found to have higher $T_c$'s ( ~ 5 – 11 K) than their sulphide equivalents ( ~ 1 – 9 K). The relatively high critical temperatures of both series together with various physical properties indicated a weak interaction between the magnetic ions and the superconducting ordering. Studies such as this confirmed that the superconductivity in these Chevrel phases resides in $Mo_6X_8$ clusters and is only weakly dependent on the interaction between the M ion and these clusters. This spatial separation of the superconductivity from a regular lattice of metal ions led to many investigations about the possibility of coexistence of superconductivity

and magnetism in these materials. In 1977 the first of many Chevrel phase compounds were discovered to exhibit simultaneous superconductivity and long range antiferromagnetic ordering [155, 156].

### 3.6.1 Structure and chemistry of Chevrel phases

Nearly all the Chevrel phases have a hexagonal-rhombohedral structure, space group R3. This near cubic unit cell has a rhombohedral angle close to 90° and sides of length ~ 6.5 Å for the sulphides and ~ 6.7 Å for the selenides. The structure can be viewed as a system of stacked $Mo_6X_8$ units within a regular lattice of M ions. The $Mo_6X_8$ unit is a slightly distorted cube with the chalcogen atoms sitting on the corners and the Mo atoms sitting slightly outside the middle of the faces. These $Mo_6X_8$ units do not lie parallel to the unit cell vectors but are turned by an angle of about 27° around the ternary axis. This arrangement means that the corner chalcogen of one unit lies directly opposite the molybdenum atom at the face center of an adjacent unit providing close links between the two. The intercluster Mo-Mo distance is about 3.10 - 3.60 Å and larger than the intracluster Mo-Mo distance of about 2.65 - 2.80 Å. This arrangement leaves vacant channels running along the rhombohedral axes with cavities in between certain neighbouring chalcogen atoms. The largest cavity is located at the three-fold axis in between two $Mo_6X_8$ units and is the principle site for the M ion.

Chevrel phases with a large cation such as Pb, Sn and the rare earth elements allow one metal ion per unit cell as shown in Fig. 8 and have a rhombohedral angle between 88 - 90°. For small cations such as Cu, Zn, Ni or Li the unit cell can accommodate more than one metal ion in several sites depending on the particular cation involved. The unit cell is then more distorted than for large cations with the rhombohedral angle between 93 - 95° and can often favour a transition to a triclinic structure. In both cases the addition of the M ion acts to stabilise the binary $Mo_6X_8$ structure and changes the intercluster Mo-Mo bond length. If the ionic radii of the metal ion is increased (e.g. as M changes from La to Lu), an increase in the intercluster Mo-Mo bond length, a corresponding decrease in the rhombohedral angle and an overall increase in the unit cell volume is observed [157]. The intracluster Mo-Mo distance however is not significantly altered, confirming that the $Mo_6X_8$ clusters are tightly bound and can be physically treated separately from the metal ion. It has been shown however, that the slight change in the intracluster bond length is related to the number of valence electrons on the $Mo_6X_8$ cluster that is determined by the charge transfer from the

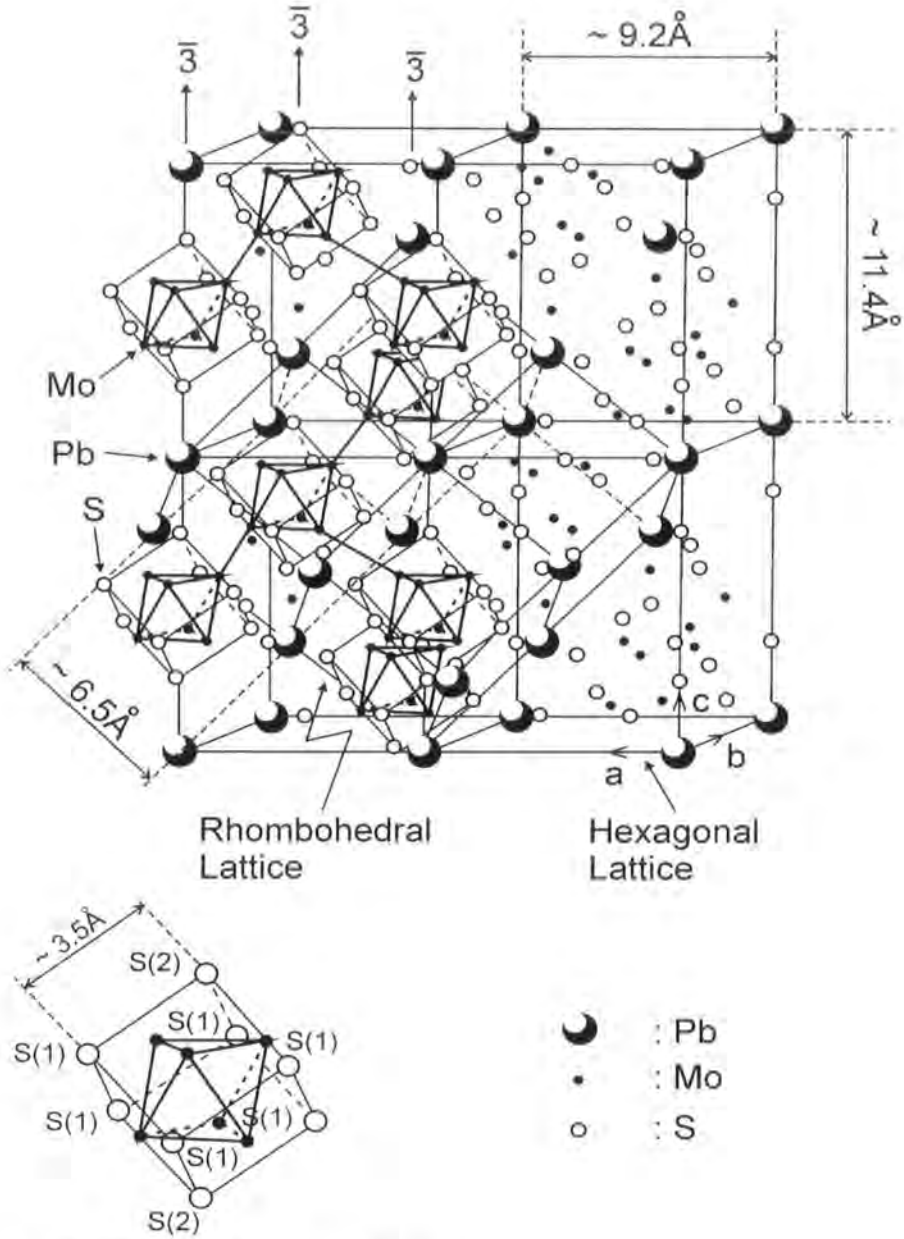


**Figure 8. Chevrel phase structure.**

metal ion [158].

Solid solutions of the chalcogens $M_xMo_6X_{8-y}X'_y$ and of the metal ions $M_{1-x}M'_xMo_6X_8$ can also generally be made if the two respective end compounds exist. If one of the compounds does not exist there is often a domain of solubility around the existing compound.

### 3.6.2 Preparation of bulk samples and single crystals.

Preparation of polycrystalline samples is generally done by solid state reaction of the three starting elements (M, Mo and X) or particularly if M is volatile, by reacting

molybdenum with the pre-sintered metal chalcogenide ($M_xX_y$). All material handling and reactions are done in a dry, oxygen free atmosphere. Oxygen contamination can degrade superconducting properties by replacing some of the sulphur atoms in the $Mo_6X_8$ cluster [159]. The materials are ground thoroughly together in the appropriate stoichiometric ratio to form a homogenous mix and then placed in a molybdenum, alumina or boron nitride crucible. This crucible should be previously outgassed at elevated temperature to prevent contamination from the crucible walls with the powder. Reaction procedures typically involve several sinterings of the mixture at intermediate temperatures (400 - 700°C) with subsequent regrindings to from the binary precursors M-X and/or Mo-X. Finally the powder is sintered at 1000 - 1200°C for several days to form the ternary phase. If rare earths are involved, subsequent reactions for shorter periods are needed at about 1500°C to ensure the ternary phase has formed [150, 160]. Reactions around 1500°C can also be performed on other large cation compounds such as $PbMo_6S_8$ and $SnMo_6S_8$ to increase the homogeneity of the final compound and minimise impurity phases [161].

Typical grain sizes from these fabrication routes are about 2 μm and 5 μm for samples reacted at about 1200°C and 1500°C respectively [162]. Bulk samples with larger grain sizes often have significant porosity and poor intergrain connectivity that can severely degrade the critical current density. To fabricate samples with a smaller grain size a different technique can be used [163]. Here the Chevrel phase is fabricated with a small cation (e.g. Cu, Li, Ni) and then treated with an aqueous solution of HCl. The M cation reacts with the acid and is removed from the $Mo_6X_8$ lattice. A large cation such as Pb can then be directly inserted into the lattice at temperatures between 450°C and 700°C that can easily be obtained industrially. The resulting ternary phase has a superconducting transition temperature comparable to that obtained by conventional synthesis but the grain size is much smaller, typically < 3000 Å.

Preparation of single crystals requires melting of the pre-sintered ternary phase at temperatures between 1600 - 1900°C, depending on the metal ion involved. The starting composition can be melted in the correct stoichiometric ratio or preferably a non-stoichiometric mix for rare-earth compounds. The addition of extra molybdenum or metal-chalcogenide position the starting composition in a region of the phase diagram which minimises the formation of competing binary phases e.g. $Mo_2S_3$ in $PbMo_6S_8$ [164-166].
Due to the very high temperatures used and therefore high reactivity of the chalcogenide, special consideration is needed of the crucible to be used. The mixture is usually melted at

high temperature for a short period of time, either in a sealed or open crucible under argon and then cooled slowly to allow optimum crystal growth. The resulting product typically contains many crystals of the ternary phase imbedded in a metal-chalcogenide crust. Alcohol-acid solutions are used to dissolve the crust and crystals of varying size up to as much as $5mm^3$ can be obtained [150].

The techniques of hot pressing and hot isostatic pressing (HIPing) of samples are used to increase the density and connectivity between grains of a polycrystalline sample. Hot pressing of samples by applying uniaxial pressure is limited by sulphur losses and consequent degradation of the superconducting properties [167, 168]. HIP'ing of samples is performed at elevated temperatures and at pressures up to 2000 bar under an inert gas such as argon. The melting temperature of the steel used to encase the samples limits the maximum reaction temperature to about 950°C. Studies on hot-pressed $PbMo_6S_8$ have shown that temperatures above 1000°C are required to fully densify the material [167]. Improved fabrication processing however, particularly in Chevrel phase wires have produced near fully dense samples when HIP'ed at 900 - 950°C with significant increases in the critical current density over un-HIP'ed samples [169-171].

### 3.6.3 Structural properties.

The influence of the M ion on the $Mo_6X_8$ band structure determines most of the varied structural and electronic properties of the Chevrel phases [172]. The transfer of valence electrons from metal ions to the Mo-Mo bonds within the $Mo_6X_8$ block increases the number of valence electrons available for bonding. Calculations suggest that the formation of the $Mo_6^{2+}$ octahedron requires 24 valence electrons to form 12 covalent metal-metal bonds. However the Chevrel phases generally have less than 24 valence electrons in the $Mo_6$ octahedron. In particular, the $Mo_3S_4$ phase has the greatest deficiency in the sulphide system of 4 valence electrons and the most distorted octahedron [158]. Additional charge transfer from a metal cation stabilises the structure causing the octahedron to contract and become more regular [158]. Ions such as Pb or Sn, with valence +2 produce a total of 22 valence electrons per cluster and the highest transition temperatures. The octahedral distortion is a minimum when four valence electrons are transferred from the metal ion(s) although the superconductivity of the $Mo_6X_8$ cluster is severely depressed as this limit is approached. In the copper system, $Cu_xMo_6S_8$, increasing the number of copper ions produces four different modifications of the rhombohedral phase at low temperatures [173].

The effect of increasing charge transfer is seen in the change of transition temperature of the stable phases; from 5.6 K for $x$ = 1.2, to 11 K and then 6.4 K for $x$ = 1.8 and $x$ = 3.2 respectively and finally with $x$ = 4 the phase is non-superconducting.

Band structure calculations on $PbMo_6S_8$ and $PbMo_6Se_8$ show that in the region of the Fermi level the Mo-*d* bands are the major contribution to the density of states [174-176]. These calculations also show that the 3*p* levels are all occupied, verifying that sulphur has the valence –2 in agreement with measured S-S distances of 3.56 Å within the $Mo_6S_8$ cluster. These calculations are strong evidence for the superconductivity in Chevrel phases being primarily due to the Mo-*d* bands. The Fermi level is situated just above a narrow Mo-*d* energy band which due to its $d(x^2-y^2)$ symmetry and the large intercluster Mo-Mo distance is highly localised to the $Mo_6$ octahedron. The localised nature of the energy bands closest to the Fermi surface indicates a short coherence length in the material. This is confirmed by the characteristic high upper critical field, which is inversely related to the coherence length.

### 3.6.4 Physical and electrical properties.

Density of states values, determined from specific heat and susceptibility measurements are typically a factor 2-3 lower than found in the A15 compounds such as $Nb_3Sn$. Specific heat measurements give phonon-enhanced density of states values of around 1 state (eV-atom spin)$^{-1}$ that are about twice as high as those found from susceptibility measurements or band structure calculations for strong coupling superconductors [172]. The Fermi level in divalent compounds such as $SnMo_6S_8$ and $PbMo_6S_8$ is thought to lie near a peak in the density of states [172]. This peak explains the comparatively large $T_c$ of these compounds compared to trivalent compounds such as $LaMo_6S_8$ and $LuMo_6S_8$. The addition of a third valence electron to the $Mo_6X_8$ block shifts the Fermi level to a minimum in the density of states and so lowers the transition temperature. Magnetisation measurements show a temperature dependent susceptibility for divalent compounds and a temperature independent susceptibility for the trivalent compounds that is consistent with this positioning of the Fermi level [172]. In the selenides the situation is different with a density of states at the Fermi level being larger for trivalent compounds than for divalent ones [150]. This gives some understanding for the higher critical temperatures of the rare earth selenides compared to their sulphide counterparts. The measured susceptibility of high temperature Chevrel phases ($PbMo_6S_8$, $LaMo_6Se_8$) vary by a factor 1.3 – 1.5 from 20

K to room temperature [172, 177] and measurements on single crystals also show an anisotropy of about 40% in the susceptibility. For rare earth Chevrel phases the susceptibility at high temperatures is well described by a Curie-Weiss law with a magnetic moment given by the theoretical free ion value [151, 177, 178]. At low temperatures strong deviations from the paramagnetic behaviour may occur due to both crystal field effects and magnetic ordering [177, 178].

The normal state resistivity of Chevrel phases shows a pronounced deviation from linearity above ~ 50 K similar to that observed in the A15 compounds [150]. This deviation is common regardless of whether the sample is polycrystalline, thin film or a single crystal and is also observed in rare earth phases [150]. The low temperature resistivity and particularly the residual resistivity are both strongly dependent on the sample preparation and quality. So far there is no general consensus for the explanation of the temperature dependence of the resistivity, particularly due to the variation in sample properties on preparation [150]. The residual resistivity is in general very high even in single crystals and of the order 0.2 mΩcm [179]. This indicates that the low temperature mean free path is very short in these materials and estimates from data on $Cu_xMo_6S_8$ give a value of about 30 – 40 Å [180].

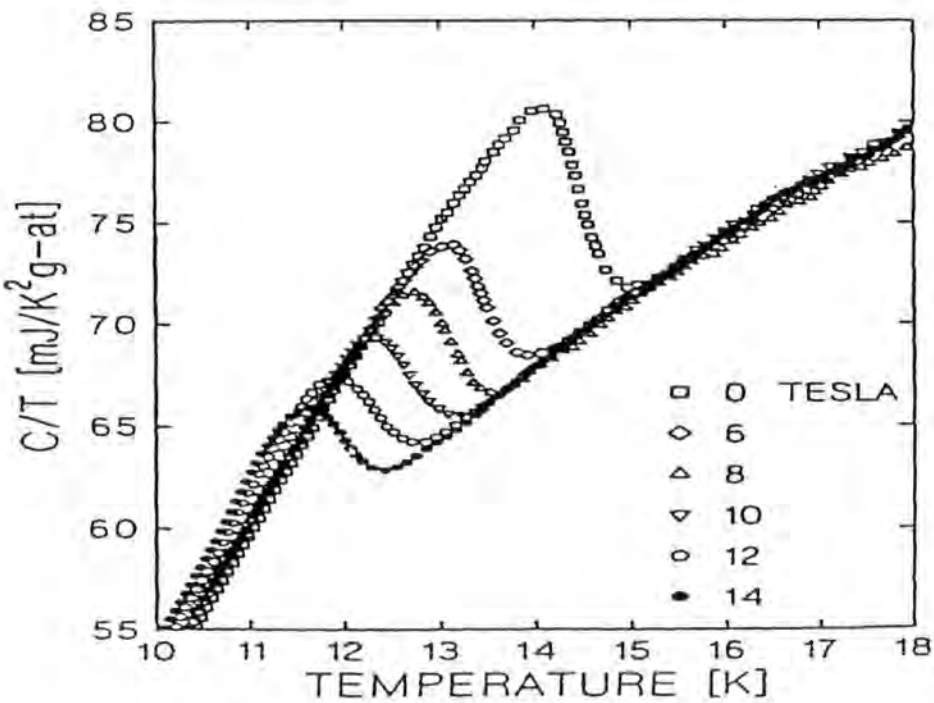


**Figure 9.** ***c/T*** **versus** ***T*** **for PMS in magnetic fields up to 14 T [127].**

Specific heat measurements and inelastic neutron diffraction measurements have been carried out on a number of the Chevrel phases [29, 43, 83, 127, 181-183], an example of specific heat data taken on a $PbMo_6S_8$ sample is presented in Fig. 9.

| MATERIAL | $T_c$ (K) | $\gamma$ ($mJK^{-2}mole^{-1}$) | $B_{c2}(0)$ (T) | $\Delta c / T_c$ ($mJK^{-2}mole^{-1}$) |
|---|---|---|---|---|
| $PbMo_6S_8$ [183] | 14.3 | 97.5 | 56 | - |
| $PbMo_6S_8$ [127] | 14.5 | - | 55 | 132.1 |
| $PbMo_6S_8$ [68] | 13.7 | 125 | 55 | - |
| $PbMo_6S_8$ [184] | 11.5 | - | 54 | 62.6 |
| $SnMo_6S_8$ [68] | 11.4 | 84 | 37 | 104 |
| $Cu_{1.8}Mo_6S_8$ [185] | 10.7 | 63 | - | - |
| $Mo_6Se_8$ [83] | 6.34 | 47.2 | 9.4 | 107.6 |
| $Mo_6Se_5S_3$ [83] | 2.59 | 35.1 | < 6.0 | 53.7 |

**Table 1. Parameters derived from specific heat measurements on Chevrel phases.**

The measured specific heat values vary according to sample preparation and quality as indicated in table 1. Generally the Sommerfeld constant ranges from about 20 - 100 $mJK^{-2}mole^{-1}$ and for $PbMo_6S_8$ the effective Debye temperature varies from around 200 K at 4.2 K to 400 K at room temperature, as shown in Fig. 1 [29]. At the superconducting jump the specific heat is about 1 $mJK^{-1}mole^{-1}$ and the size of the jump is typically around 10 – 15 % of the absolute value [127]. There is also evidence of a linear term in the mixed state of $PbMo_6S_8$ due to the normal cores of the fluxons [183]. The measured phonon density of states for several compounds are in general agreement with calculations based on a molecular crystal model where the $Mo_6X_8$ is a tightly bound unit weakly coupled to other units and the M ion [43]. The dispersion curves measured for $PbMo_6S_8$ and $SnMo_6S_8$ are relatively flat up to about 50 meV with a minimum at about 18 meV [186]. The modes above this minimum are associated with the 'hard' internal modes of the $Mo_6X_8$ unit and below this with the 'soft' external modes. At about 5 meV there is a sharp peak that is absent in $Mo_6Se_8$ but not in $PbMo_6Se_8$, $PbMo_6S_8$ or $SnMo_6S_8$ and is consequently associated with an Einstein-type mode of the M ion [186, 187].

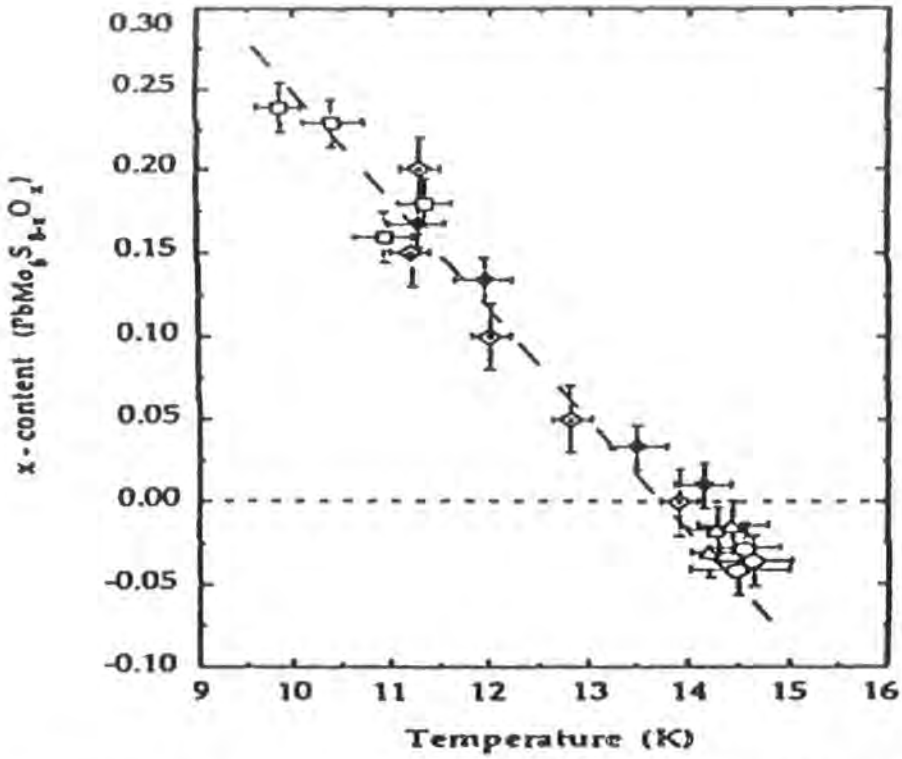


**Figure 10. Oxygen content as a function of $T_c$ for $PbMo_6S_{8-x}O_x$ samples with various preparation procedures [162].**

### 3.6.5 Superconducting critical temperature.

Quantitative discussion of the superconducting and normal state properties of Chevrel phase materials is greatly hampered, as shown in Fig. 10, by the large variation of results in the literature. Effects of stoichiometry and impurities, in particular oxygen, are the main factors responsible for the variation in reported superconducting parameters [159, 161]. Furthermore different types of measurements such as resistivity, susceptibility or specific heat are affected in different ways by the sample preparation and quality. $PbMo_6S_8$ which has the highest critical temperature of the Chevrel phases at ~ 15 K in good quality samples, has been reported by different groups with critical temperatures ranging between 11 K to 15 K [162, 183, 184].

Qualitative analysis however can be performed on these materials by using BCS theory with strong-coupling corrections. An equation for the transition temperature of strongly coupled superconductors using BCS theory was proposed by McMillan [188] and subsequently modified by Allen and Dynes [189].

$$T_c = \frac{f_1 f_2 \langle \omega_{log} \rangle}{1.20} exp\left( - \frac{1.04(1+\lambda)}{\lambda - \mu^* - 0.62\lambda\mu^*} \right) \quad (3.33)$$

where $$\langle \omega_{log} \rangle = \exp\left( \frac{2}{\lambda} \int_0^{\alpha} \frac{d\omega}{\omega} \alpha^2(\omega) F(\omega) \ln(\omega) \right) \quad (3.34)$$

$\lambda$ and $\mu^*$ represent the electron phonon interaction and Coulomb repulsion respectively, $F(\omega)$ is the phonon density of states, $\alpha^2(\omega)$ is the electron phonon coupling strength and $f_1$ and $f_2$ are correction factors important only when $\lambda >> 1$. Despite the crucial role of phonons in determining the transition temperature, the phonon density of states is only known approximately for a few compounds [186] and no experimental values for $\alpha^2(\omega)$ are known. To estimate a value for $\langle \omega_{log} \rangle$ we note that at the high frequency end of the spectrum $\alpha^2(\omega)$ is expected to decrease and therefore these internal modes of the $Mo_6X_8$ cluster should be less significant to the superconductivity. The low frequency modes are associated with the external modes of the cluster and therefore with the M ion. The large distance between the M ion and the $Mo_6X_8$ cluster and the large difference in $T_c$ between $PbMo_6S_8$ (~ 15 K) and $PbMo_6Se_8$ (~ 4 K), which have essentially the same low frequency phonon spectra, indicate that these modes are also of little significance [187]. The external modes centred at $\langle \omega_{log} \rangle$ = 12 meV are therefore generally taken as those most responsible for the superconductivity. Taking a value for $\mu^*$ as 0.1, values of $\lambda$ can then be calculated for the various Chevrel phases. Fradin et al [29] found a net linear correlation between $\lambda$ and the band density of states at the Fermi level ($N_{BS}(0)$). This correlation shows that the electronic density of states is more important than the details of the phonon spectrum in understanding the variation of $T_c$ between compounds.

The M ion affects both the inter-cluster Mo-Mo distances and the charge transfer to the $Mo_6X_8$ cluster. Correlation between the volume of the unit cell (i.e. $d(\text{Mo-Mo})_{inter}$) and the transition temperature have been observed in a number of series [151, 152, 190, 191]. A smaller cation reduces the unit cell volume broadening the widths of the bands at the Fermi surface. The density of states is then reduced and a corresponding decrease in the critical temperature is observed. Shelton et al [192] directly changed the volume of a variety of Chevrel phases by applying pressure and showed that generally there is a strong decrease in $T_c$ with increasing pressure, in accordance with the above correlation. The effect of charge transfer, as outlined in the preceding section, is observed by comparing compounds with divalent ions compared to trivalent ions. In the sulphide series the divalent compounds

have a higher density of states and corresponding transition temperatures, although exceptions are common [172]. Exact comparisons between compounds is difficult however since changing the metal ion changes both the unit cell volume and the charge transfer and so generally there is a combination of both effects.

The properties of the sulphide, selenide and telluride series are in general quite different. The main factor thought to be responsible for these differences is the effective valency of the chalcogen [172]. This variation contributes to a change in the position of the bands at the Fermi level from one chalogen compound to another. Solid solutions of the type $M_yMo_6S`_{8-x}S``_x$ have been fabricated [83, 193-195] and show a decrease in $T_c$ when one chalcogen is replaced by another due to a destruction of the symmetry in these compounds. Similar solid solutions where the chalcogen is replaced by a halogen (e.g. Br, I) have also been studied [196]. Increases in $T_c$ compared to the parent compound in these compounds are attributed to no symmetry breaking and charge transfer effects.

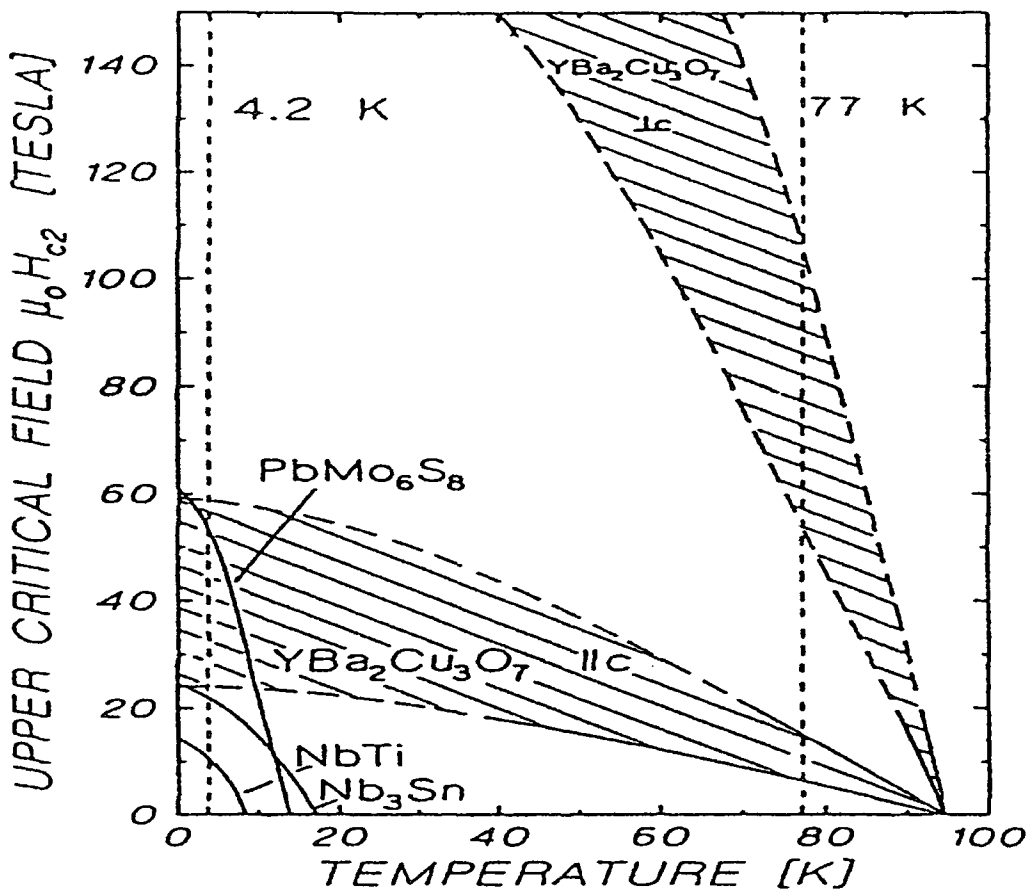


**Figure 11. Upper-critical-fields of technologically important materials** [150].

### 3.6.6 Superconducting upper critical field.

Many of the Chevrel phases have high upper critical fields and until the discovery of the high temperature superconductors some of the members exhibited the highest critical fields ever reported (e.g. $PbMo_6S_8$, $B_{c2}(0) > 50$ T) [139]. Figure 11 illustrates the upper critical fields of technologically important materials including the Chevrel phases. Since direct measurements of these very high critical fields are beyond the reach of conventional d.c. magnet systems pulsed field techniques must be used when $T << T_c$. Due to the relatively short measurement time however errors can become significant in these measurements. Estimates of $B_{c2}(0)$ can be made using WHH theory, from extrapolation of the initial slope $dB_{c2}/dT$ determined from conventional resistivity, susceptibility or specific heat measurements. The transition widths however even in single crystals can be as much as 10% of the critical field itself producing large variations in estimates of $B_{c2}(0)$ [172]. The effects of sample quality and stoichiometry can also be significant on both measured and extrapolated values and so careful analysis is needed.

The values of $B_{c2}(0)$ in these materials are typically a factor of 2 – 2.5 higher than the calculated Clogston paramagnetic limit $B_{p0}$. This paramagnetic limit is therefore clearly not a true limit in these materials, mainly due to strong spin-orbit coupling of the two states forming the Cooper pair [197]. The resulting superconducting paramagnetic susceptibility leads to an increase of the paramagnetic limit ($B_p$) as described in section 3.5.9. Fischer has shown that in the limit of strong spin orbit scattering of impurities ($\lambda_{so} >> 1$) the increased paramagnetic limit may be expressed as [172]:

$$B_p = 1.33\sqrt{\lambda_{so}}B_{p0} \tag{3.35}$$

Since we must have $B_{c2} < B_p$ a lower limit can be calculated of $\lambda_{so} > 4$ for these materials. This indicates that spin orbit coupling effects are important and in particular for very large $\lambda_{so}$, the critical field will essentially be the orbital critical field and not influenced by paramagnetic effects. Furthermore when $\lambda_{so} >> 1$ and $T \rightarrow T_c$ the slope $(dB_{c2}/dT)_{Tc} = (dB_{c2}^*/dT)_{Tc}$, as outlined in section 3.5.10, this justifies consideration of only orbital effects in this temperature region. Using the fitting procedure outlined in section 3.5.10 of the temperature dependence of $B_{c2}$, WHH theory allows a better determination of $\lambda_{so}$. Values calculated using this procedure are typically very high, $\lambda_{so} > 10$ [172], but there is evidence that the presence of strong coupling or anisotropy effects could lead to large

errors from this fitting [198, 199]. Measurements on $SnMo_6S_8$ and $PbMo_6S_8$ containing magnetic ions provide values of $\lambda_{so} \approx 8$ [200].

A plot of the measured values of $(dB_{c2}/dT)_{Tc}$ versus $\gamma$ for many of these compounds reveals a linear correlation [172] as expected from eqn (3.14). This equation is obtained for a dirty superconductor with no Pauli paramagnetic limiting, whereas for a clean superconductor a highly non-linear fit would be expected. The gradient of the linear relation then gives a value for the residual resistivity of about 0.22 mΩcm that is close to that obtained in single crystals [179]. Estimates of the coherence length at $T \rightarrow 0$ from values of $B_{c2}$ and $N_{BS}(0)$ show that for $PbMo_6S_8$ $\xi_0 \approx 30$ Å and for $LaMo_6S_8$ $\xi_0 \approx 200$ Å [201]. Values of the mean free path however are estimated at 20 – 30 Å showing that whereas $LaMo_6S_8$ is a very dirty superconductor, $PbMo_6S_8$ is between the dirty and clean regimes [180]. Nevertheless it seems that the majority of Chevrel phases can be considered as dirty superconductors where the upper critical field is essentially the orbital critical field with small paramagnetic corrections [172]. The very large values of the upper critical field are a consequence of the molecular structure that leads to a short coherence length and a short mean free path.

Measurements on single crystals of $PbMo_6S_8$, $PbMo_6Se_8$, $Cu_{1.8}Mo_6S_8$ and $SnMo_6Se_8$ reveal an anisotropy in $B_{c2}$ of about 15% [202, 203]. This anisotropy is one of the reasons for deviations from WHH theory and the broad transitions observed in polycrystalline samples. Theory however predicts a nearly cubic symmetry in the band structure and so the origin of the measured anisotropy is not clearly understood.

### 3.6.7 Superconducting critical current.

The most important parameter for technologically viable materials is the critical current density $J_c$. Although many Chevrel phase materials have upper critical fields that are easily large enough for high-field applications the $J_c$ values fall below the required levels of about $5 \times 10^9$ $Am^{-2}$ at 20 T and 4.2 K. The main problem in the production of high-$J_c$ wires comes from the granularity of the fabricated materials. Grain boundaries are necessary for high critical currents in these materials since they act as pinning sites for the fluxons. However due to the relatively short coherence length of Chevrel phase materials (~ 30 - 40 Å), grain boundaries with poor superconducting properties can prevent the transfer of the supercurrent from grain to grain [204, 205]. Large intergrain porosity and degraded superconducting properties at the grain boundaries have been two major factors preventing

production of large critical current carrying wires. Estimates of the maximum intragrain critical current density for $PbMo_6S_8$ of $10^{10}$ $Am^{-2}$ at 4.2 K and 20 T and flux penetration measurements with small ac fields confirming that $J_c > 10^{10}$ $Am^{-2}$ at 4.2 K and 5 T [206] show that these materials do have industrial potential. The highest reported values so far are for HIP'ed wires of the quaternary $(Pb,Sn)Mo_6S_8$ that have $J_c$ values of $7x10^8$ $Am^{-2}$ at 4.2 K and 14T [207]. The addition of Sn suppresses the formation of non-superconducting $MoS_2$ at the grain boundaries [208] while HIP'ing of the wire reduces porosity by improving the connectivity between the grains [171]. The magnet potential of these wires has been shown in the production of both multifilamentary and monocore wires and small three layer coils fabricated using $PbMo_6S_8$ [209].

## 3.7 High temperature superconductors.

Since their discovery in 1986 an enormous amount of effort has gone into studying and developing high-temperature-superconductors (HTS). The high transition temperatures (~ 92 K for $YBa_2Cu_3O_{6+\delta}$ and ~ 95 K for $Bi_2Sr_2CaCu_2O_{8+\delta}$) and extremely high critical fields ($B_{c2}(0) > 150$ T for $B$ // c-plane for $YBa_2Cu_3O_7$) have made them natural candidates for many superconducting applications. Extreme anisotropy however, that for example reduces $B_{c2}(0) \sim 50 - 60$ T for $B \perp$ c-plane ($YBa_2Cu_3O_7$) and problems with fabricating high critical current carrying wires have so far limited their use. Vast amounts of specific heat [210, 211] and other types of data have been collected on HTS and so this section will serve only to point out some of the main differences in the specific heat of HTS from the low temperature superconductors. Due to the large international effort on these materials the quality and reproducibility of samples is continually being improved. Many results therefore from measurements in the first five or ten years have now been superseded and so when reviewing the literature care is needed.

Due to the high temperatures involved, the electronic contribution to the total specific heat of HTS near to $T_c$ is very small, typically less than 3% of the total heat capacity [210]. This presents problems in making accurate calorimetric measurements of the superconducting transition and any subsequent subtraction to analyse the superconducting contribution. Accessing the normal state at temperatures significantly below $T_c$ by the application of a magnetic field is also difficult due to their very high upper critical fields. Intrinsic properties such as an extremely short coherence length (~ 5 Å) that is comparable to the lattice parameters, mean that the effect of small-scale defects are enhanced compared

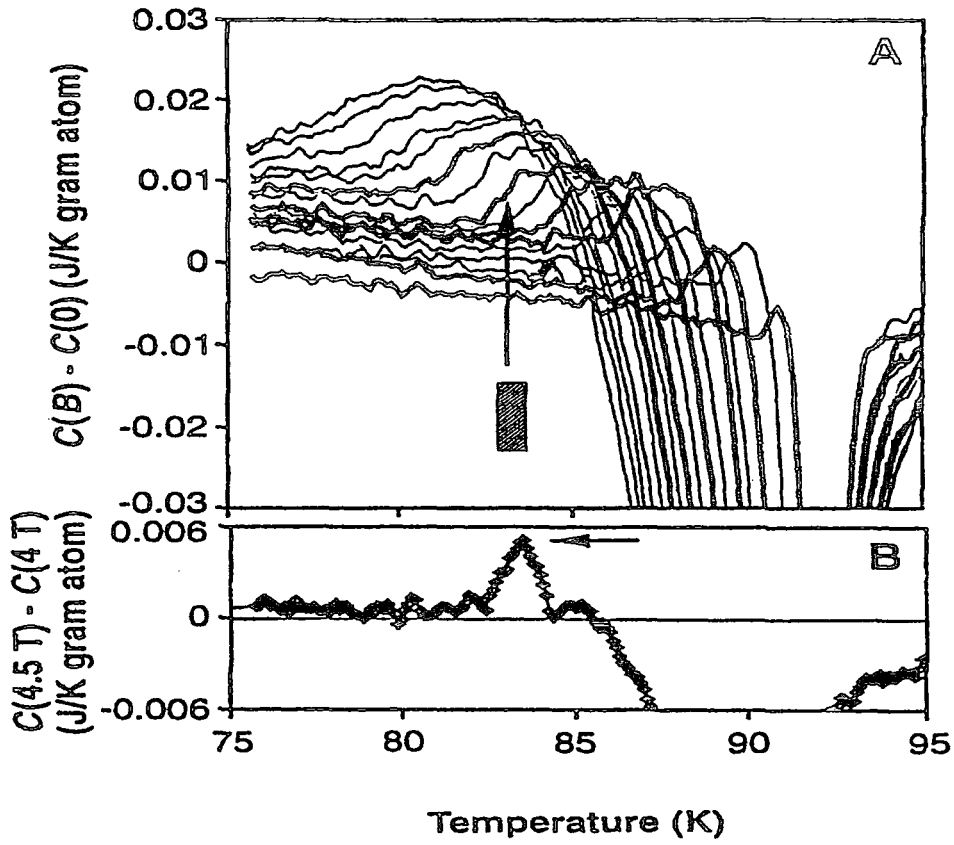


**Figure 12. Vortex melting observed in specific heat measurements on $YBa_2Cu_3O_{6.94}$ in large magnetic fields [213].**

to low temperature superconductors [211]. Additionally temperature fluctuations within the material on the scale of the coherence length then become important, especially in determining the shape of the specific heat jump at $T_c$ [212].Values of the Debye temperature and the Sommerfeld constant have been determined from normal state data and lie between 200 - 400 K and 3 – 15 $mJK^{-2}mole^{-1}$ respectively for the majority of HTS [3]. At very low temperatures (~ 1 K) the majority of HTS exhibit an upturn in zero field $c/T$ data due to the electronic magnetic moments ordering [211]. Subtraction of this low temperature upturn leaves a non-zero value at $T = 0$ K that is the intercept of a frequently observed linear term in the zero field specific heat. The coefficient of this linear term is called the residual Sommerfeld constant and has a value generally < 0.5 $mJK^{-2}mole^{-1}$ although this becomes larger with impurities [210]. The origin of this low temperature linear term is unclear and research is targeted at determining whether it is an intrinsic property of HTS or due to imperfections and incomplete superconducting transitions within the material.

Vortex melting has also been observed in the HTS by specific heat measurements [213] as shown in Fig. 12 by the excess heat capacity in applied magnetic fields below the superconducting transition.

There is much evidence that the superconducting mechanism in HTS is not the same as for the low temperature superconductors [212]. Application of BCS theory to any results from HTS then becomes difficult to justify. In particular there is no strong evidence for either an exponential dependence of $c_{es}$ or a characteristic sharp discontinuity in the specific heat at $T_c$ in the HTS [210]. The width of the specific heat anomaly at $T_c$ is generally very broad ($\Delta T \sim 2$ - 10 K) even for high quality single crystals [212]. Variations in the shape of the specific heat transition between samples due to imperfections and additional effects of fluctuations and strong electron-phonon coupling have further complicated study of the specific heat anomaly. Recent work has shown that the HTS can be characterised by the parameter $k_F\xi$, where $k_F$ is the Fermi wave number [212]. As $k_F\xi$ changes so does the type of superconductivity, from a BCS type superconductor with $k_F\xi \sim 2$ to a 3D-*XY* or Bose-Einstein condensate superconductor for $k_F\xi < 1/\pi$. The different shapes of specific heat anomalies then become intrinsic properties of the superconductor depending on the type of superconductivity involved.

In low temperature superconductors the electron-phonon coupling strength, characterised by the parameter $\lambda$, is essentially temperature independent for $T < T_c$. In HTS the temperature dependence of $\lambda$ (and therefore $\gamma$) is significant and modifies the temperature dependence of $c_{es}$ [211]. Strong coupling effects are especially evident near to $T_c$ in both the magnitude of the specific heat jump which can reach $\Delta c/c_e \sim 4$ - 5 (compared to 1.43 from BCS theory) [3] and the shape of the curve for $T < T_c$ [211]. Tunneling experiments give values of $2\Delta/k_BT_c \approx 8 - 12$ for $Bi_2Sr_2CaCu_2O_8$ [214], much larger than the strong coupling BCS superconductors ($2\Delta/k_BT_c \approx 4 - 5$) also suggesting extreme strong coupling in HTS. Comparison of band structure calculations with experimental values of $\gamma$ however, gives small values of $\lambda$ that are incompatible with such strong coupling effects [211]. These results are taken as evidence for a non-phonon mechanism in HTS.

## 3.8 Magnetic specific heat.

In 1907 P Weiss [215] published a mean field model to describe ferromagnetic ordering in materials. Subsequent work by Neel in 1932 [216] and Landau in 1933 [217] extended

this mean field theory to antiferromagnetic materials as well. Comparison with experimental data however showed that these simplified models failed to give even a qualitatively accurate description of the majority of available data. Statistical treatments of the atomic interactions by Ising in 1925 [17] and Heisenberg in 1928 [218] using quantum mechanics, provided a more rigorous treatment of the problem. The two models of Heisenberg and Ising (treated using the Heisenberg formalism) are the basis of the understanding of magnetic ordering within materials but they are applicable only for insulating materials or those that have no overlap between the conduction electrons and the magnetic moments. Due to the complexity of the statistics deriving exact solutions of either model is a formidable task and has only been completed in a few cases.

Ising provided an exact solution for a one-dimensional lattice of the Ising type in his original paper [17]. Bloch introduced the concept of spin waves for a Heisenberg system at low temperatures in 1930/32 [19], allowing quantitative predictions for temperatures well below the ordering temperature. After developments in the theory of

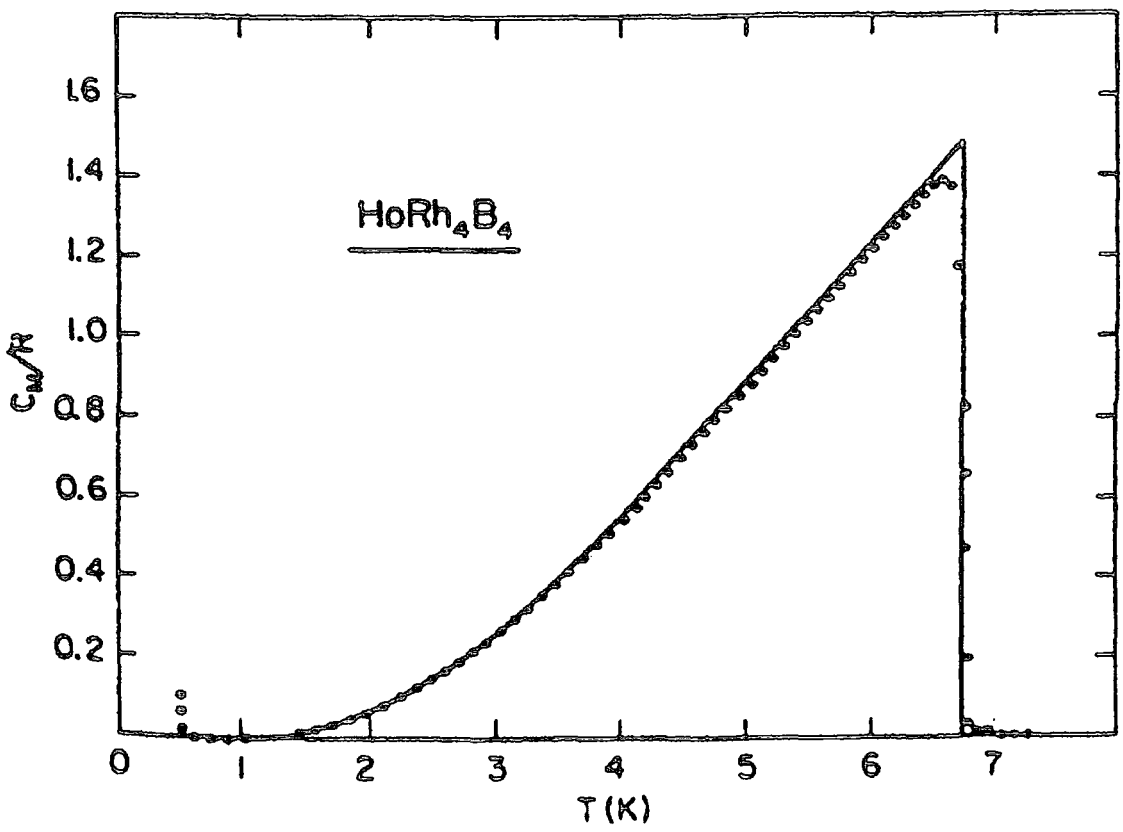


**Figure 13. Experimentally determined magnetic contribution to the specific heat $c_M/R$, as a function of temperature for $HoRh_4B_4$ (solid circles) and mean-field prediction (solid line)** [219].

long-range order in materials [220], Bethe [221] developed the theory of short range ordering allowing an improved approximation of the Ising model. The two dimensional Ising model was solved exactly by Onsager in 1944 [18] for a quadratic lattice, providing the only other exact solution of either Ising or Heisenberg models to date. Despite the failure of obtaining exact solutions, use of approximations and series expansions have provided quantitative predictions of both Ising and Heisenberg models enabling very accurate comparison with experimental data [222]. Monte Carlo simulations have also been used to investigate the nature of the critical region.

### 3.8.1 Comparison of Ising, Heisenberg models and the mean field theory.

The vast body of research on magnetic materials includes many examples of systems that can be approximated to a greater or lesser degree by the models of Heisenberg or Ising [223]. In general the mean field theory although a useful comparison is applicable to very few materials due to its failure to take into account fluctuations, spin waves and short range order in a material. Fisher showed in 1967 that the mean field theory is exact in the limiting case of long range order within a material, where each ion interacts with the other ions over a range $r$, as $r \rightarrow \infty$ [224]. In such a situation each ion has an infinite number of equivalently interacting neighbours and so any ion only sees the averaged field of all the other ions. One example of a real material which acts as a model mean field ferromagnet is $HoRhB_4$ [219], although the reason for its lack of short range order is unclear. Figure 13 shows the experimental values of the specific heat of $HoRh_4B_4$ and the predicted values from mean field theory for an $S = ½$ ferromagnet. Very close agreement with theory is found for the specific heat, spontaneous magnetisation and resistivity even up to the critical temperature. Short range order in a magnetic material occurs because the interaction range between magnetic ions of real systems is finite. The effect of short range order on the response of the system depends critically on the dimensionality of the lattice involved [225]. Short range order effects are most significant for one dimensional systems where there is a complete absence of long range order for any non-zero temperature [17, 226, 227]. As the lattice dimension is increased, the effects of short range order are reduced, although for the Heisenberg model short range order effects in a two dimensional system still prevent any long range order manifesting itself for $T > 0$ K [226].

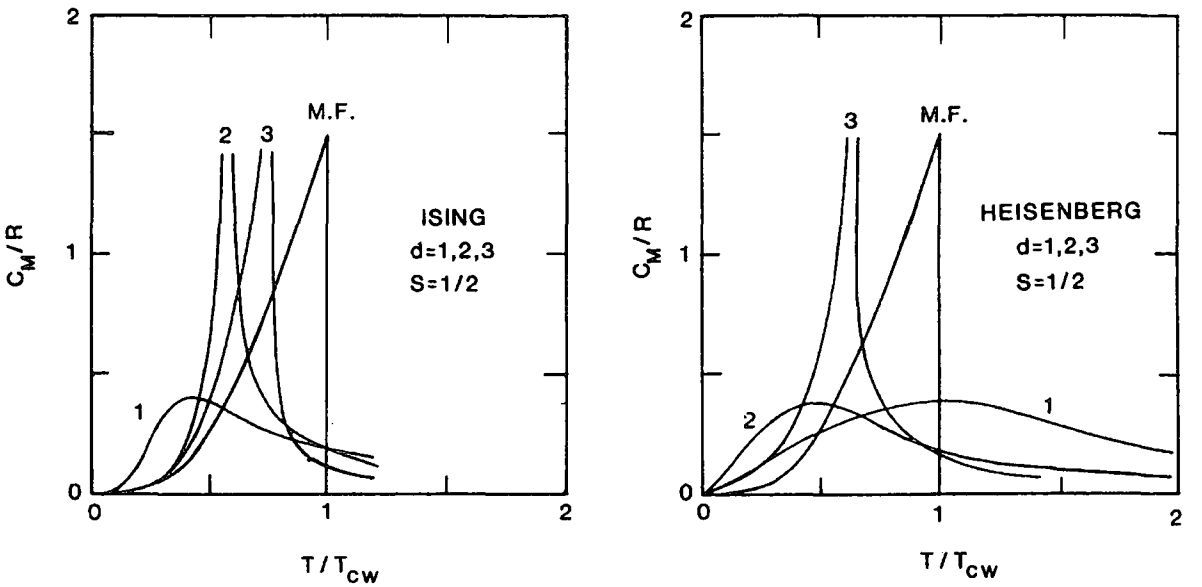


**Figure 14. Calculated magnetic contribution to the specific heat ($c_M$) as a function of $T$ for Ising and Heisenberg models of 1,2 and 3 dimensions and the mean field theory (M.F.)** [223].

Calculations of $c_m$ in Fig. 14 [223], show that short range ordering lowers the temperature of the transition to long range order, characterised by a singularity in $c_m$, below that of the mean field theory ($T_m = \theta_{CW}$) and produces a 'tail' in $c_m$ for $T > T_m$ above the peak. This high temperature 'tail' is observed experimentally [228] but cannot be accounted for by mean field theory which has no ordering above $T_m = \theta_{CW}$. Studies of the critical parameters as a function of the total spin ($S$) of the magnetic ions, show that lowering $S$ also enhances the effects of short range order [229]. Deviations from the mean field theory therefore become more significant as both the dimensionality of the lattice and the total spin of the magnetic ions are reduced. Nevertheless the mean field theory is found to be remarkably successful in describing the overall properties of materials with three dimensional lattices and we shall only consider theories and materials of this dimensionality.

### 3.8.2 Ising model.

The Ising model was originally developed to consider systems of only spin $S = ½$, allowing only either parallel or antiparallel orientations to the applied field [17]. Extensions allow arbitrary value of $S$ to be considered and so the Ising model corresponds to the case of extreme magnetic anisotropy since there is only an interaction between the $z$

components of the spins [225]. Specific heat measurements on $ZnF_2$, $MnF_2$, $FeF_2$, $NiF_2$ and $CoF_2$ by Stout et al [228] clearly show a deviation from antiferromagnetic mean field theory and comparisons with antiferromagnetic spin wave theory show a qualitative agreement in accord with an Ising type material. Calculations of the series expansions by Domb et al [222, 230] on various types of three dimensional lattices, gave expressions for the specific heat and susceptibility of the Ising model for temperatures above and below $T_m$. Further extensions in 1961 [231] and new analytical techniques [232, 233] provided additional accuracy of the approximations particularly in the region of the transition.

In 1962 Domb et al [229] considered the effect of varying the value of $S$ and deduced that the peak in the specific heat at the transition would become considerably sharper as $S$ is increased. Essam et al [234] provided a series expansion for the Ising model diamond lattice that converged right up to the critical point allowing very accurate determinations of both specific heat and spontaneous magnetisation. Various improvements of computing power and analysis over the following years yielded more accurate solutions both above [235] and below the critical point [236]. Consideration of interactions with next nearest neighbours and further by Domb et al [237] showed that the dimension and number of nearest neighbours are more significant in determining the critical parameters than lattice type. The finer details of the critical point were shown however to be unchanged from those determined by including just nearest neighbour interactions.

Specific heat data on $CoCs_3Cl_5$ [238], $DyAlO_3$ [239], $Tb(OH)_3$ [240], $CoRb_3Cl_5$ [241] and $DyPO_4$ [242] have all been compared to the expansions outlined above. Good agreement of the data both above and below the critical point is found although comparisons with theories for the asymptotic form close to $T_m$ are inconclusive due to experimental limitation as $T \rightarrow T_c$. In 1972 Sykes et al [243] gave a complete description of the specific heat in zero field for $T_m \leq T \leq \infty$, for face-centred cubic, body centred cubic and simple cubic lattices. The behaviour close to the critical point is described asymptotically by a power law with an exponent $\alpha \approx 1/8$ independent of lattice type.

For example the face-centred-cubic lattice is given by:

$$\frac{c}{R} = 1.089\left((1-t')^{-1/8} - 1 - \frac{1}{8}t'\right) + \left(-0.0140t'^2 - 0.0031t'^3 + 0.0005t'^5 + 0.0002t'^6\right) \quad (3.36)$$

where

$$t' = \frac{T_m}{T} \quad (3.37)$$

and R is the molar gas constant.

### 3.8.3 Heisenberg model.

Calculations for the Heisenberg model are generally more difficult and series expansions are slower to converge so that approximations for these models tend to be less accurate [225]. Dyson [244, 245] derived the low temperature expansion of the specific heat due to spin-waves for a three dimensional ferromagnetic Heisenberg system, which accounts well for the observed properties up to temperatures $T < 0.5T_m$. Above the Curie temperature series expansions were initially derived by Rushbrooke et al [246-248] and Domb et al [230] for the specific heat and susceptibility with subsequent work [233] studying the critical region. The effect of increasing $S$ increases the sharpness of the high temperature tail, similar to the Ising model, although the general sharpness is less than for the Ising model with the Heisenberg series for $S = \infty$ being comparable to the Ising series for $S = ½$ [229]. Dalton et al [249] studied the effect of introducing interactions with next nearest neighbours and Domb et al [237] extended this work to include further neighbours. Perhaps the most extensive calculations have been performed by Baker et al [250] for $T > T_m$ on face-centred cubic, body centred cubic and simple cubic lattices for the $S = ½$ Heisenberg model. Analysis of the series expansions indicates that the peak in $c_m$ in the three dimensional Heisenberg model actually remains finite even though the derivative on either side is infinite and so the curve displays a sharp cusp. For example in zero field the specific heat as calculated by Baker for a face-centred-cubic lattice is:

$$\frac{c}{R} = \left(\frac{T_m}{T}\right)^2 \left[1.206 - 0.966\left(1 - \frac{T_m}{T}\right)^{0.20}\right] \quad \text{for } 0.70 < T_c / T < 0.95 \tag{3.38}$$

where R is the molar gas constant.

Specific heat data on EuS [251-253], $CuM_2X_4.2H_2O$ [254] and EuO [255] have been compared to expressions for Heisenberg ferromagnets with good agreement. Similarly specific heat data on $MnF_2$ [256], $RbMnF_3$ [257] and (Nd,Dm,Er)GaG [258] show good agreement with antiferromagnetic Heisenberg models although analysis of both ferromagnetic and antiferromagnetic materials is often hindered due to the rounding of the peak in $c_m$ [253, 257, 258].

The behaviour of specific heat data in the region of the critical point is hypothesised to belong to a scaling law whereby only two variables are needed to describe the data above and below $T_m$ [259]. Furthermore a consequence of the scaling law is the concept of universality, that states for a given class of materials with the same dimension and effective

number of spin degrees of freedom, the exponents of the scaling law will all be the same. Specific heat data on the three dimensional Heisenberg ferromagnets, iron, nickel, EuO and some Cu salts, support this hypothesis to a reasonable accuracy.

### 3.8.4 Other magnetic contributions.

If a system is essentially an independent collection of magnetic ions, the energy levels of the system will often have a degenerate energy level that is split on application of a magnetic field. If the splitting of the energy levels is comparatively small then both levels can be excited. The specific heat will then exhibit a characteristic peak due to the lifting of this degeneracy called a *Schottky anomaly*, at a temperature below about $0.5T_\Delta = 0.5\Delta / k_B$ where $\Delta$ is the energy separation of the levels [20]. For temperatures $T << T_\Delta$ the specific heat increases with temperature as $c_{sch} \sim \exp(-a / T)$ and for temperatures $T >> T_\Delta$ the specific heat increases with temperature as $T^{-2}$. Generally the splitting of energy levels and therefore the temperature regime involved is very low.

In systems which are nearly-ferromagnetic the exchange interaction strongly enhances the paramagnetic susceptibility producing spin fluctuations or critically damped spin waves [20]. The effect of spin fluctuations is to enhance the effective mass of the conduction electrons and so the electronic specific heat at low temperatures can be given approximately by $c_e = \gamma T + \alpha (T / T_s)^3 \ln (T / T_s)$, where $T_s$ is a temperature characteristic of the spin fluctuation energy.

## 3.9 Coexistence of magnetism and superconductivity.

Magnetic and superconducting ordering are not generally observed in the same material at the same time. Ginzburg noted in 1957 [260] that the interaction of magnetic ions with a superconducting system would in most cases destroy the superconducting state. If the effective field produced by the magnetic ions is larger than the critical field of the material (as for most type I superconductors) than the interaction breaks up the Cooper pairs. Matthias et al [153, 154] introduced magnetic impurities into superconductors to study the interplay of the two phenomena. The results showed that only very small levels of impurities were required to destroy the superconducting state suggesting that the exchange interaction between the conduction electrons and the localised magnetic moments was responsible. Abrikosov and Gor'kov then went on to propose a theory of paramagnetic

impurities in superconductors in 1961[261] that described the reduction in $T_c$ with increasing concentration of impurities.

Attempts to find materials where the two phenomena could coexist mainly concentrated on doping magnetic ions into superconductors. The very small level of impurities needed and the random distribution of these impurities in the host lattice presented many problems. In particular, distinguishing between clustering and short range order effects and the effect of long range magnetic order on superconductivity was very difficult. The discovery of the Chevrel phases and later the rare earth rhodium borides ((RE)$Rh_4B_4$) [262] provided ideal systems where the interplay of superconductivity and magnetism could be studied. Both systems have a regular lattice of metal ions spatially separated from superconducting clusters. If the metal ion is a rare earth element then the localised $4f$ electrons responsible for the magnetic behaviour have virtually no interaction with the conduction electrons of the clusters responsible for the superconductivity.

The HTS are an example of a system where magnetic ions in one layer are spatially separated from adjacent superconducting layers. This extreme decoupling of the rare earth ions from the conduction electrons means that the magnetic ions have virtually no effect on the superconducting properties. The (RE)$Ba_2Cu_3O_7$ system has a $T_c$ around 90 K which is virtually independent of the rare earth ion involved [263].

More recently Nagarajan et al [264] discovered a system of layered intermetallic rare-earth transition metal borocarbides (RE)$Ni_2B_2C$. These compounds also displayed both superconducting and magnetic properties and have been the subject of much recent investigation.

### 3.9.1 Upper critical field.

In a magnetic superconductor the destruction of superconductivity results from not only the interaction of the applied field with the conduction electron orbits and spins, but also due to the scattering and polarisation effects of the magnetic ions. The exchange interaction between the localised magnetic moments and the conduction electrons can be written as [263].

$$H_{ex} = \left(\frac{1}{N}\right)\sum J(S_i s) \tag{3.39}$$

where $J$ is the exchange integral, $S_i$ is the spin of the $N$ localised moments and $s$ is the spin of the conduction electrons. When the magnetic spins align and produce a non-zero

magnetisation either as a result of an external field or magnetic ordering, then the exchange interaction corresponds to an *effective exchange field* ($H_J$) acting on the conduction electrons.

$$H_J = \frac{xJ_{ex}\langle S_z \rangle}{g_e \mu_B} = \left( \frac{J_{ex}}{g g_e N \mu^2} \right) M(H,T) \tag{3.40}$$

where $x$ is the concentration of magnetic impurities and $M(H,T)$ is the magnetisation. Fischer derived the form of the effect on the upper critical field of the exchange field and the magnetic scattering as well as those mechanisms already described in Eqn. 3.32 [144, 203].

$$\begin{aligned} H_{c2}(T) = {} & H^*_{c2}(T) - M(H_{c2},T) - 3.56\lambda_m H^*_{c2}(0) \\ & - 0.22(\alpha/\tau_{so}T_{c0})[H_{c2}(T) + M(H_{c2},T) + H_J(H_{c2},T)]^2 \end{aligned} \tag{3.41}$$

where $\lambda_m$ describes the effect of magnetic scattering. The form of this equation allows most of the differing temperature dependencies of $H_{c2}(T)$ to be explained. A peak in $H_{c2}$ at non-zero temperature is related to the gradual polarisation of the conduction electron spins

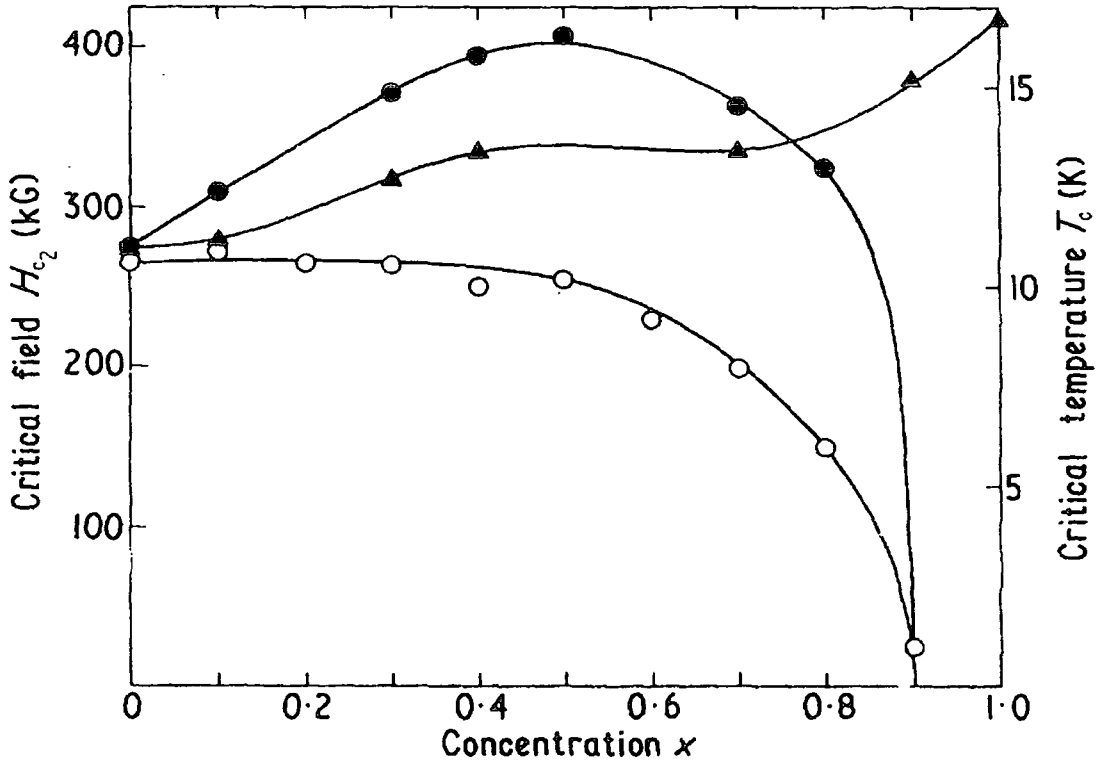


**Figure 15. Upper critical field (solid circles) and transition temperature (open circles) of series $Sn_{1.2(1-x)}Eu_xMo_{6.35}S_8$ as a function of $x$ and upper critical field (solid triangles) of series $Sn_{1.2(1-x)}Pb_xMo_{6.35}S_8$ [200].**

and therefore a rapid increase in $H_J$ as $T$ is lowered [263]. The onset of magnetic ordering produces a maximum in the susceptibility and therefore an increase in $H_{c2}$ corresponding to a decrease in $M(H,T)$ at lower temperatures. If magnetic ordering occurs at temperature lower than a peak in $H_{c2}$ due to polarisation of electron spins the resulting $H_{c2}(T)$ curve will exhibit a minimum at $T_m$. However not all of the anomalous $H_{c2}(T)$ behaviour can be explained with Eqn. (3.46) and other explanations including additional pair breaking parameters [263] or partial gapping of the Fermi surface in the antiferromagnetic state have been proposed [265].

### 3.9.2 Compensation effect.

In 1962 Jaccarino and Peter [266] proposed that a *compensation effect* could occur in superconductors that have ferromagnetic elements or impurities in the lattice. The interaction of the exchange field ($H_J$) between the magnetic ions and the conduction electrons polarises the electron spins, preventing superconductivity from occurring if $\mu_0 H_J > B_{c2}$. However in certain materials $H_J$ is negative and so polarises the spins of the conduction electrons in the opposite orientation to those of the magnetic ions. In these materials if an external field is applied of the same order of magnitude as $H_J$, then it will oppose $H_J$ and cancel the polarisation of the electron spins. Providing therefore that the orbital critical field is larger than the paramagnetic limit of the material [144], superconductivity can be induced at a field larger than the normal upper critical field. Another effect of this compensation is on the temperature dependence of $H_{c2}$, for bulk samples Fischer showed a pronounced upwards curvature of $H_{c2}(T)$ would be observed for temperatures close to $T_c$ [144]. An example of the compensation effect was noted in the pseudoternary system $Sn_{1.2(1-x)}Eu_xMo_{6.35}S_8$ fabricated by Fischer et al [200]. Figure 15 shows the upper critical field at $T = 0$ K of the pure $Sn_{1.2}Mo_{6.35}S_8$ sample increases from 27.5 T to 40 T when half of the tin ions were replaced by europium ions, with superconductivity being destroyed at a concentration of $x = 0.9$.

### 3.9.3 Ferromagnetic superconductors.

Due to the direct competition between the superconducting and ferromagnetic ordering on the spins of the conduction electrons very few examples of ferromagnetic superconductors have been found. The ternary compounds Gd, Tb and $HoRh_4B_4$ exhibit ferromagnetic order but not superconductivity and only $HoMo_6S_8$ and $ErRh_4B_4$ exhibit both

superconducting and ferromagnetic transitions [150]. The ferromagnetic ordering in these compounds destroys the superconductivity in zero field at a temperature $T_{c2}$ well below the temperature at which superconductivity first occurs upon cooling the material down, $T_{c1}$. Resistivity measurements by Fertig et al [267] on $ErRh_4B_4$ and Ishikawa et al [268] on $HoMo_6S_8$ were the first to show a transition to a zero resistance state at $T_{c1}$ followed by a reappearance of the resistivity at a lower temperature $T_{c2}$, called *reentrant resistivity*. In $ErRh_4B_4$ $T_{c1}$ and $T_{c2}$ occur at 8.7 K and 0.92 K respectively and in $HoMo_6S_8$ at 2.0 K and 0.6 K. Magnetisation measurements for $T_{c1} > T > T_{c2}$ on both $ErRh_4B_4$ [269] and $HoMo_6S_8$ [270] show that the upper critical field is anisotropic and that in $ErRh_4B_4$, as $T_{c2}$ is approached the mixed state disappears and the superconductor becomes type I, due to a decrease in $\lambda_L$ and therefore $\kappa$ [271, 272].

The transition at $T_{c2}$ is hysteretic in these compounds with the magnetic transition actually occurring at a slightly higher temperature than $T_{c2}$. The region for $T_{c2} < T < T_m$ has been shown to exhibit the coexistence of superconducting and magnetic ordering by neutron diffraction measurements [273-275], whereas below $T_{c2}$ the superconductivity is destroyed. The nature of the coexistence phase has been extensively studied and numerous theoretical models have been suggested [271, 276-278]. Due to the coupling of the two phenomena, either the magnetic order is uniform in space and the superconducting state is oscillating or the superconducting state remains uniform and forces the ferromagnetic ordering to be oscillatory [263]. Experimental evidence from neutron scattering has

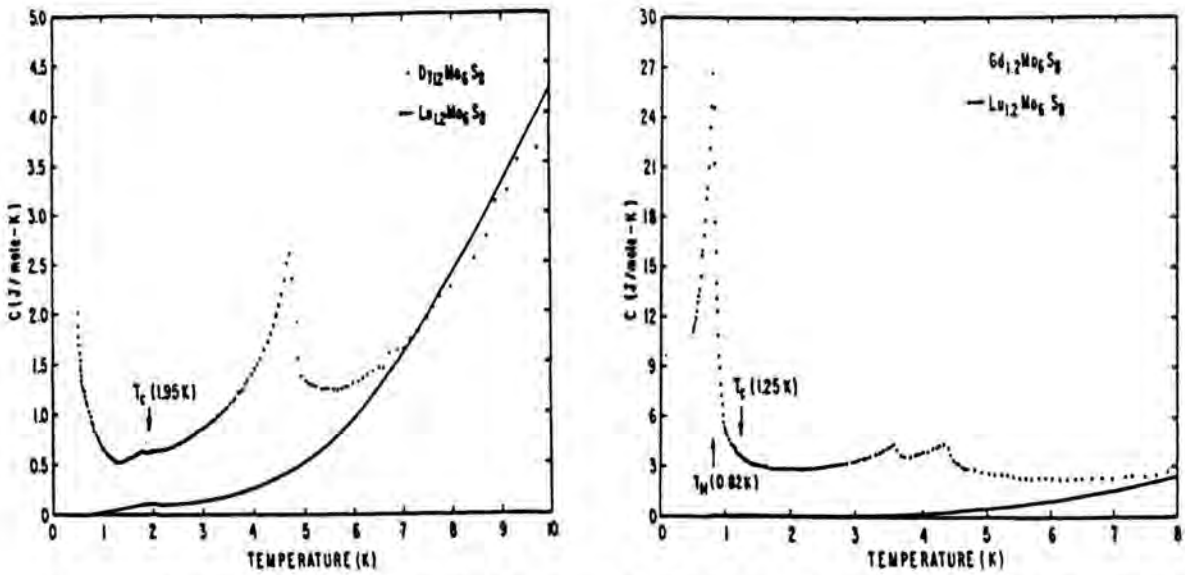


**Figure 16. Specific heat of $GdMo_6S_8$ and $DyMo_6S_8$ compared with isostructural $LuMo_6S_8$ showing excess magnetic contributions** [182].

confirmed oscillatory magnetic states in both compounds with a wavelength of the order 100 Å to 1000 Å [273, 275]. The question of whether this oscillatory ferromagnetic state is due to the exchange interaction between the rare earth ions or due to the electromagnetic coupling between the two phenomena is still open [263, 276].

The value of the resistivity below $T_{c2}$ is significantly lower than the resistivity above $T_{c1}$ and this has been interpreted as the fact that a small fraction of the sample remains superconducting down to $T = 0$ K. Several authors have investigated this effect [279, 280] and have attempted to determine whether it is a bulk effect or whether superconductivity just occurs along the walls between ferromagnetic domains.

### 3.9.4 Antiferromagnetic superconductors.

The coexistence of superconductivity and antiferromagnetism does not have the intrinsic problem of ferromagnetic ordering providing that the antiferromagnetic period is much shorter than the superconducting coherence length [281]. The coexistence of both phenomena however modifies the superconducting state, although generally the material remains superconducting down to the lowest temperatures and so the coexistence region is comparatively large. Many of the (RE)$Mo_6S_8$, (RE)$Mo_6Se_8$, (RE)Rh4B4 and (RE)$Ni_2B_2C$ order antiferromagnetically at sufficiently low temperatures and the first observation of coexistence was in compounds Dy, Tb and $ErMo_6S_8$ [155]. The onset of antiferromagnetic ordering produces an anomaly in the temperature dependence of the upper critical field and the application of a large enough applied field, produces a reentrant state in the resistivity that is not seen in zero applied field [155]. Upper critical field values for the (RE)$Mo_6S_8$ and (RE)$Mo_6Se_8$ compounds are generally less than 1 T and neutron diffraction and susceptibility measurements indicate the effective Bohr magneton value in these compounds is close to the free ion value [150]. Neutron scattering experiments on $DyMo_6S_8$ by Moncton et al [282] confirmed antiferromagnetic ordering at 0.4 K and identified the ordered state as composed of spins parallel within the plane and alternating between the planes. Specific heat measurements on $Er_xMo_6Se_8$ [156], $Gd_{1.2}Mo_6Se_8$ [283], $NdMo_6X_8$ [284], $Tb_{1.2}Mo_6S_8$, $Gd_{1.2}Mo_6S_8$ and $Dy_{1.2}Mo_6S_8$ [182] show anomalies at $T_{c1}$ and characteristic lambda-type anomalies at $T_m$. Figure 16 shows the specific heat of $Gd_{1.2}Mo_6S_8$ and $Dy_{1.2}Mo_6S_8$ compared to that of isostructural $Lu_{1.2}Mo_6S_8$ indicating the excess contribution to the heat capacity from the magnetic ions. For $Gd_{1.2}Mo_6S_8$ the entropy calculated from the specific heat was nearly equal to the value obtained assuming a

free ion model, however for other members the entropy values are lower indicating effects due to the crystal field.

The rare-earth rhodium borides have $T_{c1}$ values up to about 11 K and upper critical fields below 1 T. Nd, Sm, Tm, and $HoRh_4B_4$ have all shown coexistence of antiferromagnetism and superconductivity with many interesting features [263]. In $NdRh_4B_4$ ($T_{c1}$ = 5.3 K) application of a field above 0.3 T produces a reentrant phase in the resistivity at 1.31 K followed by a sharp drop again at 0.89 K [285]. Specific heat data shows two lambda type anomalies at these temperatures and the antiferromagnetic nature is confirmed by neutron diffraction [286]. Many of the antiferromagnetic superconductors exhibit complex magnetic states that can be formed at different temperatures and evidence for these phase transitions are observed as anomalies in the specific heat that cannot be identified with secondary phases.

The (RE)$Ni_2B_2C$'s are a system of layered intermetallic rare earth transition metal borocarbides with $T_c$'s up to 16.5 K and magnetic transitions in the same compounds up to 8.5 K [287]. One exceptional case is the compound $DyNi_2B_2C$ that has a magnetic transition at 10.3 K *above* the superconducting transition at 6.2 K. These compounds have upper critical field values below 10 T and effective bohr magneton values from susceptibility measurements in agreement with free ion values [288]. A lot of research has been conducted on these materials revealing many interesting features, including the possibility of a weak ferromagnetic superconducting state in $ErNi_2B_2C$ at temperatures below the antiferromagnetic superconducting state observed in both specific heat and magnetisation data [289].

## 3.10 Conclusions.

In this chapter we have reviewed the relevant theoretical and experimental research on the specific heat of magnetic superconductors and the Chevrel phase superconductors. Starting from a normal, non-magnetic material the specific heat has been divided into contributions from the lattice, the conduction electrons and the atomic nuclei. The parameters $\gamma$ and $\theta_D$ can be determined from normal state specific heat data, typically using a plot of $c/T$ versus $T^2$, and provide important of the material properties.

The specific heat of superconductors has been considered in the context of the BCS and Ginzburg-Landau theories of superconductivity. Additional theories of WHH and Maki have been outlined which allow the temperature dependence of the upper critical field,

kappa and the size of the specific heat jump to be modelled and provide estimates for $B_{c2}(0)$. The lower critical field and the thermodynamic critical field can also be determined from calorimetric data although they have less technological significance.

Chevrel phase superconductors are candidates for high field magnet systems due to their comparatively high upper critical fields and transition temperatures. Some of the main properties of these materials have been discussed in terms of their peculiar structure summarised and a comparison has been given with the properties of high temperature superconductors. The main reason for the limited technological use of these materials is given as a fabrication problem rather than an intrinsic limitation.

The final part of this review has looked at the models of magnetic materials and the interplay of magnetic and superconducting ordering. The three most important models of magnetic ordering, the Ising, Heisenberg and the mean field models have been compared and the resulting form of the heat capacity presented in each case. Analytical expressions which are used to study the behaviour of the heat capacity in the region of the critical point are presented and allow the ordering temperature to be accurately determined.

Materials in which superconductivity and magnetism coexist are rare and the Chevrel phases are perhaps the most versatile system available for detailed study. Theories of the nature of the coexisting states have been introduced and experimental evidence for both ferromagnetic and antiferromagnetic superconductivity outlined. The temperature dependence of the upper critical field and the compensation effect in ferromagnetic superconductors has been discussed in terms of the additional pair breaking effect of the magnetic ions.

# *Chapter 4 – Calculation of the magnetic contribution to the specific heat of Chevrel phase compounds containing rare-earth ions.*

## 4.1 Introduction.

The magnetic contribution to the specific heat of magnetic materials ($c_m$) arises from the interaction of the energy levels of the electrons of the magnetic ions with both the applied field and with the electrons from neighbouring ions. In the region of a magnetic phase transition the contribution to the specific heat from the magnetic ions can often dominate the total specific heat, particularly at low temperatures where both the lattice and electronic contributions are both dropping rapidly towards zero. The effect of this large magnetic contribution can hide other features in the specific heat making them difficult to analyse and can also produce a significant paramagnetic contribution to the specific heat for temperatures above a magnetic phase transition [182]. Calculation of the magnetic contribution enables the model of the magnetic interaction to be compared with a real system, the important magnetic parameters such as $T_M$ and $p_{eff}$ to be determined and subtraction of the magnetic contribution to allow the remaining contributions to the specific heat to be analysed.

Chevrel phase materials can contain magnetic ions either in a ternary phase $M_xMo_6X_8$ or with another (typically) non-magnetic ion (M′) in a pseudo-ternary phase $M'_yM_xMo_6X_8$. The magnetic ternary phases generally have superconducting transition temperatures of less than 10 K whereas the pseudo-ternary phases can have a transition temperature up to that of the parent $M'_yMo_6S_8$ compound (e.g. ≤ 15 K for $PbMo_6S_8$), depending on the proportion of magnetic ions included [150]. In either case the Chevrel phase crystal structure ensures that the magnetic ions are sufficiently far apart that the exchange interaction is relatively weak. This relatively weak interaction is characterised by magnetic ordering temperatures of typically less than 2 K and values of the effective Bohr magneton number for these materials that are close to that of the free ions [150]. In this situation we can then treat the system of magnetic ions in the 'Mean field' formalism and expect little of the effects characterised by either an Ising or Heisenberg system of ions. The small temperature region in which the material exhibits both superconducting and magnetic phase transitions is a region of great interest due to the interplay between these two competing interactions.

Specific heat measurements are therefore the ideal way to study the effects of both of these phenomena and also to determine the important material parameters.

Section 4.2 outlines the theoretical derivation of the specific heat capacity of a system of magnetic ions from thermodynamic arguments in both ferromagnetic and antiferromagnetic cases. The calculation of the magnetisation, ordering temperature and the zero field contribution to the specific heat capacity are determined separately and then combined to form the complete description of the specific heat. The results of the calculations, using the computer software Maple, are presented in section 4.3 in terms of the magnetisation, Gibbs free energy and specific heat as a function of both field and temperature. An approximate form for $c_m$ above the ordering temperature is derived in section 4.4 along with two simple expressions for analysis in the high temperature limit. These approximate expressions are compared to the results of the previous calculations and the chapter is then concluded in section 4.5.

## 4.2 Theory.

### 4.2.1 Calculation of the magnetization – ferromagnetic case.

In the mean field model each ion in a cylindrical material, lying parallel to the applied field, sees an *effective field* ($B^*$) due to the applied field ($\mu_0 H_{ext}$), the self-field from the material ($\mu_0 M$), and an electrostatic interaction from the neighbouring ions ($\mu_0 \lambda^* M$).

$$B^* = \mu_0 \left( H_{ext} + M + \lambda^* M \right) \tag{4.1}$$

The magnetization per unit volume ($M$) of the material can then be expressed as:

$$M = n_v J g_J \mu_B B_J \left( y, J \right) \tag{4.2}$$

where
$$B_J \left( y, J \right) = \frac{2J+1}{2J} coth\left( \frac{2J+1}{2J} y \right) - \frac{1}{2J} coth\left( \frac{1}{2J} y \right) \tag{4.3}$$

is called the *Brillouin function*, $n_v$ is the number of magnetic ions per unit volume and

$$y = J g_J \mu_B B^* / k_B T \tag{4.4}$$

where $T$ is the temperature, $k_B$ is the Boltzmann constant, $J$ is the total electronic angular momentum, $\mu_B$ is the Bohr magneton, and $g_J$ is the Lande $g$-factor defined by:

$$g_J = \frac{1}{2} \frac{\left[ J(J+1) + L(L+1) - S(S+1) \right]}{J(J+1)} + \frac{\left[ J(J+1) + S(S+1) - L(L+1) \right]}{J(J+1)} \tag{4.5}$$

where $L$ and $S$ are respectively the total orbital angular momentum and the total spin of the atom. If we define a *saturation magnetisation* as

$$M_s = n_v g_J \mu_B J \tag{4.6}$$

then we can write two equations for the ratio $M / M_s$ as a function of $y$, which in turn is a function of the applied field and temperature.

$$\frac{M}{M_s} = B_J(J, y) \tag{4.7}$$

and

$$\frac{M}{M_s} = y\left(\frac{n_v k_B T}{\mu_0(\lambda^* + 1)M_s^2}\right) - \frac{H_{ext}}{(\lambda^* + 1)M_s} \tag{4.8}$$

In zero field the two functions of $M / M_s$ defined in Eqn.'s (4.7) and (4.8) intersect at a critical temperature ($T_M^F$) such that the gradient of these two functions at $y = 0$ are equal. In the low field regime $B_J(J , y) \approx y\ (J + 1) / 3J$ and so we can define the gradient of this function as $y \rightarrow 0$ as

$$\frac{\partial B(J, y)}{\partial y} = \frac{(J+1)}{3J} = \frac{n_v k_B T_M^F}{\mu_0(\lambda^* + 1)M_s^2} \tag{4.9}$$

The temperature at which the material spontaneously magnetizes in zero field is then given by:

$$T_M^F = (1 + \lambda^*)C \tag{4.10}$$

where

$$C = \frac{n_v p_{eff}^2 \mu_B^2 \mu_0}{3k_B} \tag{4.11}$$

and

$$p_{eff}^2 = g_J^2(J(J+1)) \tag{4.12}$$

For non-superconducting magnetic materials the self-field term is generally much smaller than the electrostatic term i.e. $\lambda^* >> 1$ and so $T_M^F \approx \lambda^* C$, for magnetic superconductors such as the Chevrel phases however these two terms are of the same order of magnitude and so both need to be included.

For simplicity of notation we define $\alpha = Jg_J\mu_B(1 + 1 / 2J)$ and $\beta = Jg_J\mu_B(1 / 2J)$ and so the equation for the magnetisation (Eqn. 4.2) can be rewritten as

$$M = n_v\left[\alpha \coth\left(\frac{\alpha\mu_0\left(H_{ext} + M + \left(\frac{T_M^F}{C} - 1\right)M\right)}{k_B T}\right) - \beta \coth\left(\frac{\beta\mu_0\left(H_{ext} + M + \left(\frac{T_M^F}{C} - 1\right)M\right)}{k_B T}\right)\right] \tag{4.13}$$

In the general case of arbitrary field and temperature Eqn. (4.13) allows the magnetization, through the Brillouin function, to be expressed as a function of the variables $J$, $L$, $S$, $n_v$, the ordering temperature ($T_M^F$), the applied field ($\mu_0 H_{ext}$) and the absolute temperature ($T$). For a given rare-earth ion the values of $J$, $L$ and $S$ can be determined from Hund's rules and $n_v$ can be determined from the stoichiometry and the lattice parameters of the compound. If a value of the ordering temperature ($T_M^F$) can be determined from specific heat or susceptibility measurements the magnetization can then be calculated as a function of applied field and temperature.

### 4.2.2 Calculation of the magnetisation – antiferromagnetic case.

In the antiferromagnetic case we consider two interpenetrating sublattices A and B, where at $T = 0$ K the magnetic ions within each sublattice are all aligned parallel with each other and antiparallel to the ions in the other sublattice. For each sublattice the magnetisation is given as:

$$M_A = n_{v(A)} J g_J \mu_B B_{J(A)}(J, y_A) \tag{4.14}$$

$$M_B = n_{v(B)} J g_J \mu_B B_{J(B)}(J, y_B) \tag{4.15}$$

If we take the effective field at a particular ion as the sum of the applied field ($\mu_0 H_{ext}$), the self-field of the material ($\mu_0 M_A + \mu_0 M_B$) and an electrostatic interaction from only the nearest neighbour ions ($\mu_0 \lambda_A^* M_A$ or $\mu_0 \lambda_B^* M_B$) where $\lambda_A^* = \lambda_B^*$, then $B_A^*$ and $B_B^*$ are given by:

$$B_A^* = \mu_0 (H_{ext} + M_A + M_B + \lambda^* M_B) \tag{4.16}$$

$$B_B^* = \mu_0 (H_{ext} + M_A + M_B + \lambda^* M_A) \tag{4.17}$$

Using the definitions of $M_s$ ($M_s = n_{v(Total)} g_J \mu_B J$), $C$ and $p_{eff}$ as in Eqn.'s (4.11) and (4.12) and noting that $n_{v(A)} = n_{v(B)} = (n_{v(Total)} / 2)$ i.e. half the total number of ions, we can write $M_A / M_s$ as a function of $y$.

$$\frac{M_A}{M_s} = \frac{1}{2} B_{J(A)}(J, y_A) \tag{4.18}$$

and

$$\frac{M_A}{M_s} = y_A \left( \frac{n_v k_B T}{\mu_0 M_s^2} \right) - \left( \frac{(1+\lambda^*) M_B + H_{ext}}{M_s} \right) \tag{4.19}$$

In zero field, $M_A = - M_B$ and in the low field field regime both $B_{J(A)}(J , y_A) \approx y_A (J + 1) / 3J$ and $B_{J(B)}(J , y_B) \approx y_B (J + 1) / 3J$. This allows us to determine the ordering temperature

($T_M^{AF}$) by equating the gradient of $M_A / M_s$ as a function of $y_A$, determined from both Eqn. (4.18) and Eqn. (4.19), as $y \rightarrow 0$.

$$\frac{\partial\left(\frac{B(J,y)}{2}\right)}{\partial y} = \frac{1}{2}\frac{(J+1)}{3J} = \frac{n_v k_B T_M^{AF}}{\mu_0(-\lambda^*)M_s^2} \tag{4.20}$$

The ordering temperature is then given by:

$$T_M^{AF} = -\frac{\lambda^* C}{2} \tag{4.21}$$

Comparing Eqn.'s (4.10) and (4.21) we can see there is a difference from standard textbook analysis which does not explicitly include both the self-field and electrostatic terms in the equations for the magnetisation.

Using the definitions of $\alpha$ and $\beta$ as before, we can rewrite Eqn.'s (4.14) and (4.15) as:

$$M_A = \frac{n_{v(Total)}}{2}\left[\alpha\coth\left(\frac{\alpha\mu_0\left(H_{ext}+\left(1-\frac{2T_M^{AF}}{C}\right)M_B+M_A\right)}{k_B T}\right)-\beta\coth\left(\frac{\beta\mu_0\left(H_{ext}+\left(1-\frac{2T_M^{AF}}{C}\right)M_B+M_A\right)}{k_B T}\right)\right] \tag{4.22}$$

$$M_B = \frac{n_{v(Total)}}{2}\left[\alpha\coth\left(\frac{\alpha\mu_0\left(H_{ext}+\left(1-\frac{2T_M^{AF}}{C}\right)M_A+M_B\right)}{k_B T}\right)-\beta\coth\left(\frac{\beta\mu_0\left(H_{ext}+\left(1-\frac{2T_M^{AF}}{C}\right)M_A+M_B\right)}{k_B T}\right)\right] \tag{4.23}$$

So if a value of the ordering temperature ($T_M^{AF}$) can be determined from specific heat data and $n_{v(Total)}$ can be determined from the structure of the material, then the simultaneous Eqn.'s (4.22) and (4.23) can be solved numerically to give the magnetisation of both A and B sublattices for arbitrary applied field and temperature.

### 4.2.3 Calculation of the specific heat.

To determine the magnetic contribution to the specific heat for either a ferromagnetic or antiferromagnetic material, we have to consider the change in the Gibbs free energy per unit volume due to the total magnetization per unit volume ($M$) of the material.

$$G = U - TS - \mu_0 H_{ext} M \tag{4.24}$$

Here $U$ is the internal energy per unit volume, $T$ is the temperature, $S$ is the entropy per unit volume, and $\mu_0 H_{ext}$ is the applied field. For any reversible process we can consider the change in internal energy given by the change in heat flow into the system minus the total work done by the system, as given by the expression:

$$dU = dQ - dW = TdS - \sum XdY \tag{4.25}$$

where $X$ is an external variable (e.g. pressure, applied field etc.) and $dY$ is the corresponding change in the internal variable $Y$ (e.g. volume, magnetization etc.). For a magnetic solid only the change in magnetization due to the applied field is physically significant [290], hence if we ignore demagnetization factors and the effect of the applied field on free space ($\mu_0 H_{ext} dH_{ext}$) then Eqn. (4.25) becomes:

$$dU = TdS + \mu_0 H_{ext} dM \tag{4.26}$$

and so substituting Eqn. (4.26) into Eqn. (4.24) the change in Gibbs energy is given by:

$$dG = -SdT - \mu_0 M dH_{ext} \tag{4.27}$$

At constant applied field strength we can then define the entropy ($S$):

$$S = -\left(\frac{\partial G}{\partial T}\right)_{H_{ext}} \tag{4.28}$$

and at constant temperature we can define the magnetization ($M(H_{ext},T)$):

$$\mu_0 M = -\left(\frac{\partial G}{\partial H_{ext}}\right)_T \tag{4.29}$$

So given the magnetization we can calculate the Gibbs free energy from Eqn. (4.27).

$$G(H_{ext},T) = G(0,T) + \left[-\int_0^{H_{ext}} \mu_0 M dH_{ext}\right]_T \tag{4.30}$$

and we explicitly include the zero field contribution ($G(0,T)$). The heat capacity per unit volume ($C_{vol}$) can then be calculated from the Gibbs free energy using Eqn. (4.28).

$$C_{vol} = T\left(\frac{\partial S}{\partial T}\right)_{H_{ext}} = -T\left(\frac{\partial^2 G}{\partial T^2}\right)_{H_{ext}} = -T\frac{\partial^2}{\partial T^2}\left(G(0,T) + \left[-\int_0^{H_{ext}} \mu_0 M dH_{ext}\right]_T\right) \tag{4.31}$$

i.e.
$$C_{vol} = C_{vol}(0,T) - T\frac{\partial^2}{\partial T^2}\left[-\int_0^{H_{ext}} \mu_0 M dH_{ext}\right]_T \tag{4.32}$$

The term $C_{vol}(0,T)$ represents the heat capacity due to the spontaneous alignment of the magnetic ions in zero applied field at temperatures below the ordering temperature. The

specific heat capacity is then calculated by simply dividing $C_{vol}$ by the density of the material.

### 4.2.4 Spontaneous magnetization – Ferromagnetic case.

In the mean field theory in zero applied field, the magnetisation only becomes non-zero for temperatures less than the ordering temperature ($T_M^F$). The magnetic ions spontaneously align in zero applied field as the temperature of the system drops below $T_M^F$. Below the ordering temperature therefore the lowest energy state is that with all of the spins aligned parallel. At higher temperatures the thermal energy disrupts this alignment, however applying an external field will offset this disruption and so the energy of the system in zero field, at temperatures $0 < T < T_M^F$, is larger than that of the system at the same temperature in an applied field.

In a system of ferromagnetic ions the effective field at an ion inside the material is $B^* = \mu_0(H_{ext} + \lambda^* M + M)$ (Eqn. 4.1) which in zero field reduces to $B^* = \mu_0(1 + \lambda^*) M$. The internal energy per unit volume of the system due to the magnetisation will then be given by:

$$U^F(0,T) = -\int_0^{B^*} \underline{M} \cdot d\underline{B}^* = -\int_0^{M} \mu_0(1+\lambda^*)\underline{M} \cdot d\underline{M} = -\frac{1}{2}\mu_0(1+\lambda^*)M^2 \qquad (4.33)$$

Since $(1 + \lambda^*) = T_M^F / C$ (Eqn. 4.10) and we have (Eqn. 4.6) $M_s = n_v g_J \mu_B J = M$ ($T = 0$ K) we can then calculate the heat capacity per unit volume in zero applied field ($C^F_{vol}(0,T)$) [22, 291].

$$C^F_{vol}(0,T) = \left(\frac{\partial U^F(0,T)}{\partial T}\right)_{H=0} = \frac{-\mu_0 T_M^F}{2C}\frac{\partial M^2(0,T)}{\partial T} = \frac{-3k_B n_v T_M^F}{2M_s^2}\frac{J}{(J+1)}\frac{\partial M^2(0,T)}{\partial T} \qquad (4.34)$$

### 4.2.5 Spontaneous magnetization – Antiferromagnetic case.

In an antiferromagnetic system the magnetic ions also spontaneously align below the ordering temperature ($T_M^{AF}$). The exchange interaction between neighbouring ions however is negative and thus neighbouring ions align in opposite directions to each other. In zero applied field the effective field at an ion in sublattice A is given by $B_A^* = \mu_0(H_{ext} + \lambda^* M_B + M_A + M_B) = \mu_0\lambda^* M_B$, since $M_A = - M_B$, and similarly the effective field at an ion in sublattice B is $B_B^* = \mu_0(H_{ext} + \lambda^* M_A + M_B + M_A) = \mu_0\lambda^* M_A$. The internal energy per unit

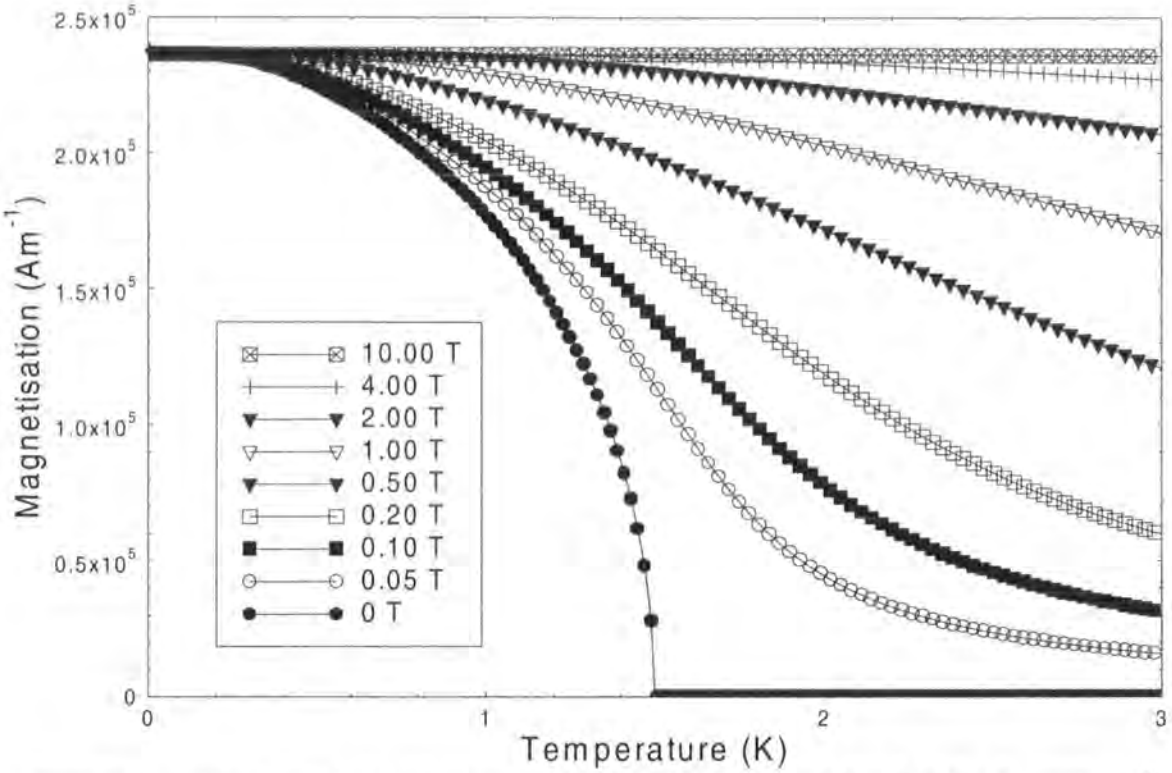


**Figure 1. The magnetisation as a function of temperature for $GdMo_6S_8$ with $T_M^F$ = 1.5 K and in applied fields from 0 T to 10 T.**

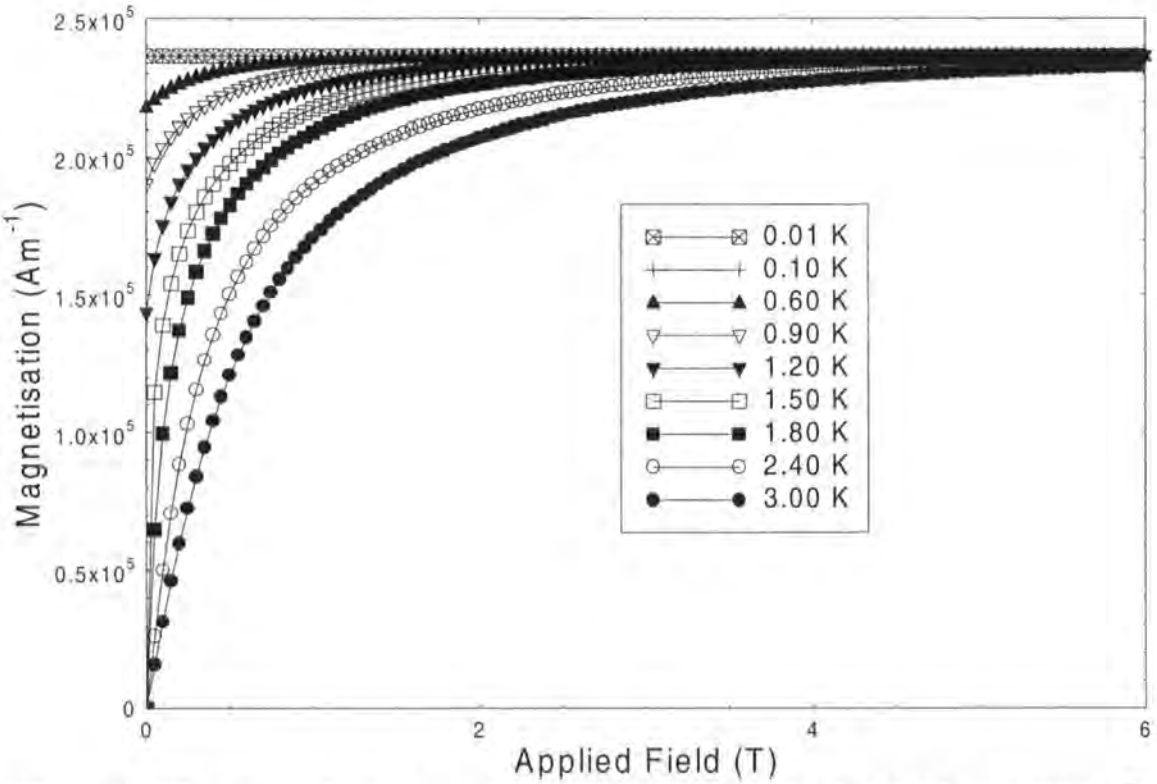


**Figure 2. The magnetisation as a function of applied field for $GdMo_6S_8$ with $T_M^F$ = 1.5 K and for temperatures from 0.01 K to 3.00 K.**

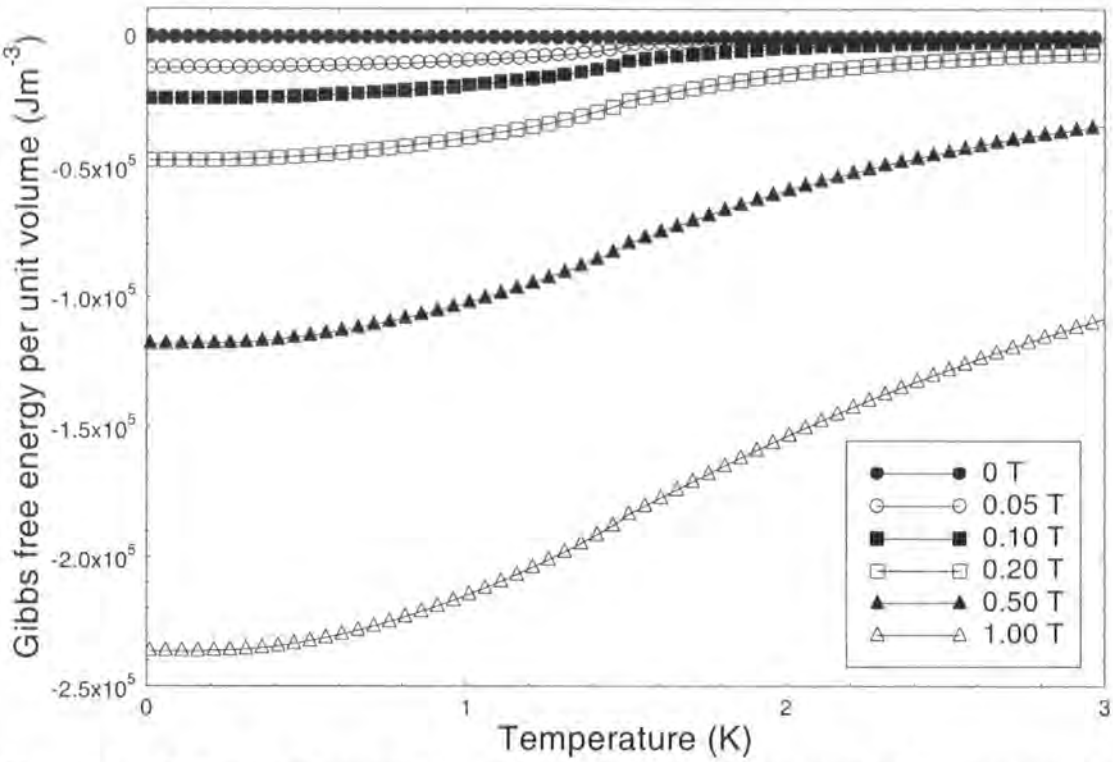


**Figure 3. Gibbs free energy per unit volume as a function of temperature for $GdMo_6S_8$ with $T_M^F$ = 1.5 K in applied fields from 0 T to 1 T.**

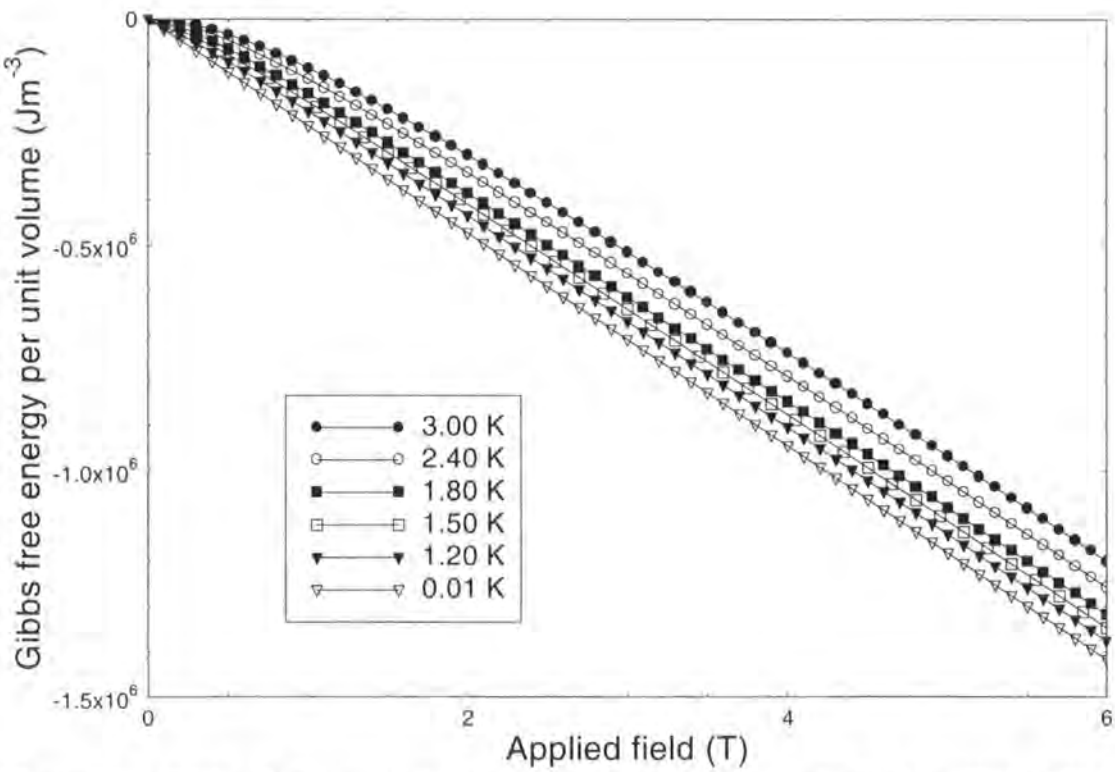


**Figure 4. Gibbs free energy per unit volume as a function of applied field for $GdMo_6S_8$ with $T_M^F$ = 1.5 K and for temperatures from 0.01 K to 3.0 K.**

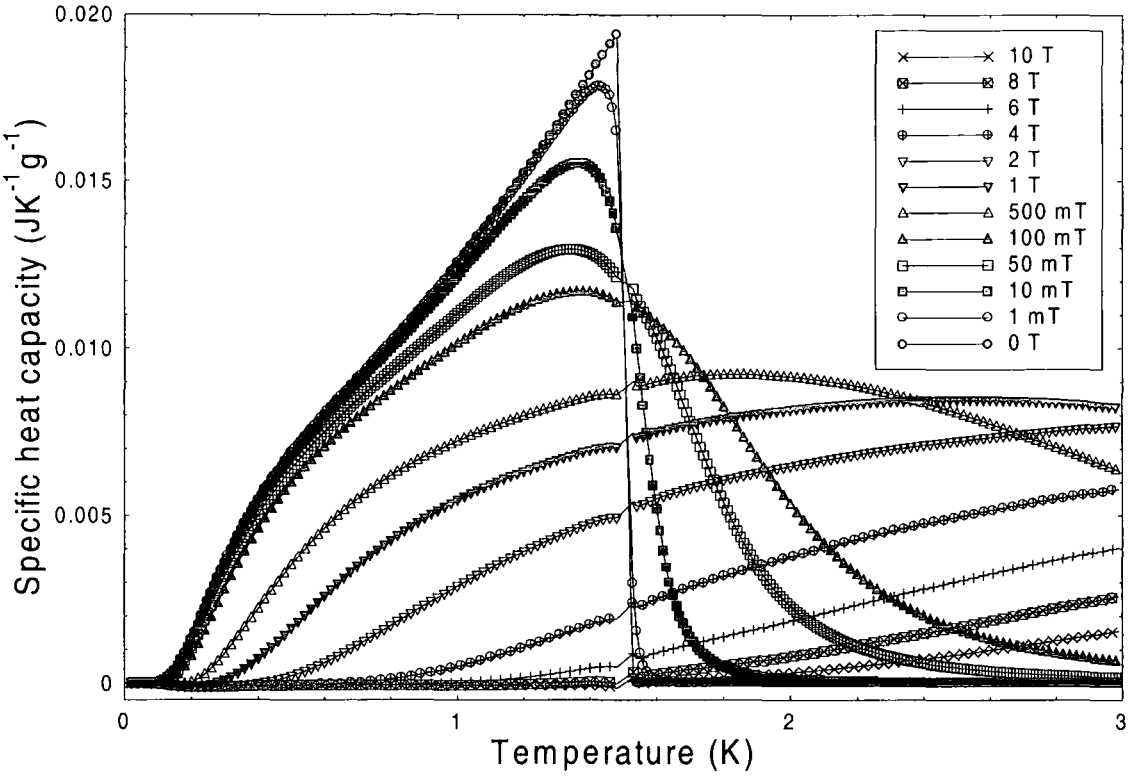


**Figure 5. Specific heat capacity as a function of temperature for $GdMo_6S_8$ with $T_M^F$ = 1.5 K in applied fields from 0 T to 10 T.**

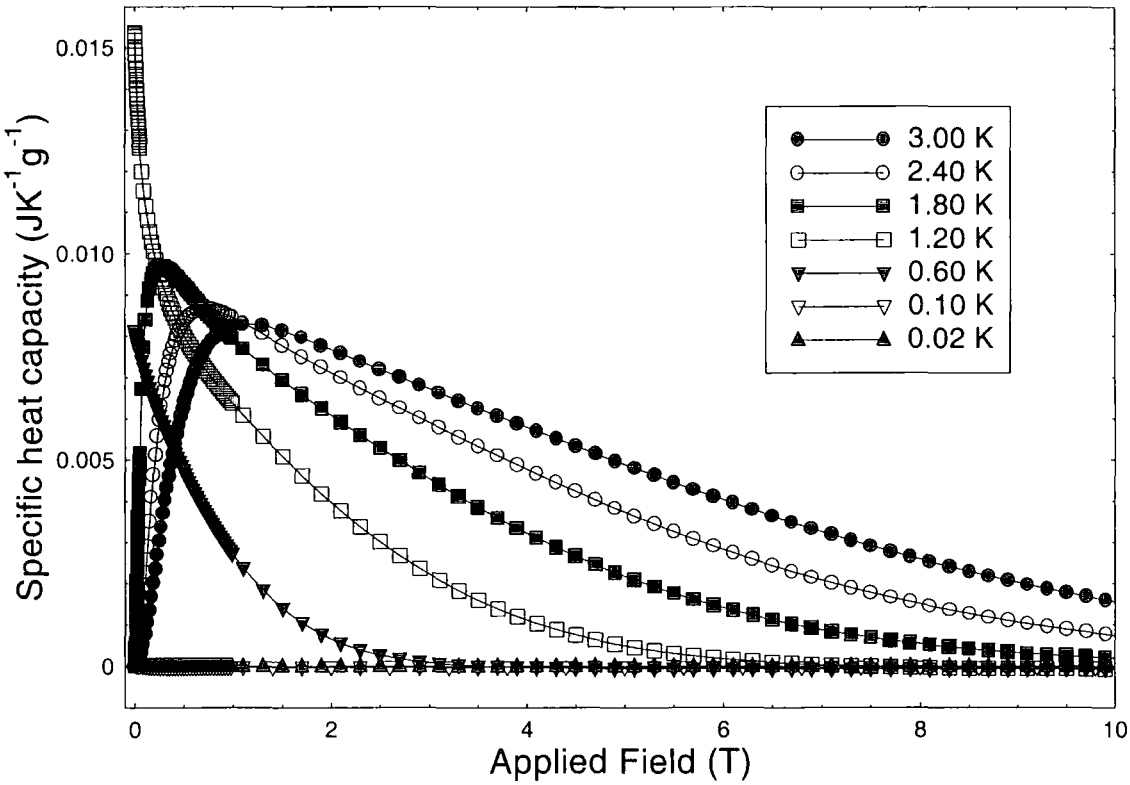


**Figure 6. Specific heat capacity as a function of applied field for $GdMo_6S_8$ with $T_M^F$ = 1.5 K and for temperatures from 0.02 K to 3.0 K.**

volume associated with the zero field magnetisation of the system can then be determined by considering the energy of the ions on both sublattice A and sublattice B.

$$U^{AF}(0,T)=\int_0^{B_A^*} M_A dB_A^* + \int_0^{B_B^*} M_B dB_B^* = \mu_0\lambda^* \int_0^{M_B} M_A dM_B + \mu_0\lambda^* \int_0^{M_A} M_B dM_A \qquad (4.35)$$

therefore $$U^{AF}(0,T)=\frac{\mu_0\lambda^*}{2}\left(M_A^2+M_B^2\right)=\mu_0\lambda^* M_A^2 \qquad (4.36)$$

Since $\lambda^* = -2T_M^{AF} / C$ (Eqn. 4.21) and we have (Eqn. 4.6) $M_s = n_v g_J \mu_B J = 2M_A$ ($T = 0$ K) we can then calculate the heat capacity per unit volume in zero applied field ($C^{AF}_{vol}(0,T)$).

$$C_{vol}^{AF}(0,T)=\left(\frac{\partial U^F(0,T)}{\partial T}\right)_{H=0} = \frac{-2\mu_0 T_M^{AF}}{C}\frac{\partial M_A^2(0,T)}{\partial T} = \frac{-6k_B n_v T_M^{AF}}{M_s^2}\frac{J}{(J+1)}\frac{\partial M_A^2(0,T)}{\partial T} \qquad (4.37)$$

We can also note that since $4M_A^2(0\ ,\ T) = M_F^2(0\ ,\ T)$, where $M_F$ is the equivalent value of the magnetisation in the ferromagnetic case for the same parameters, then we have:

$$C_{vol}^{AF}(0,T)=C_{vol}^{F}(0,T) \qquad (4.38)$$

## 4.3 Results of calculations.

The magnetic contribution to the specific heat is calculated in both ferromagnetic and antiferromagnetic cases for the compound $GdMo_6S_8$ with a unit cell size of $(6.5Å)^3$, values of $J = S = 7/2$ and $L = 0$ (the free ion values for Gd) and an arbitrary choice of ordering temperature of 1.5 K.

### 4.3.1 Ferromagnetic case ( $T_M^F$ = 1.5 K).

Taking $T_M^F$ = 1.5 K we can numerically solve the equation for the magnetization (Eqn. 4.13) as a function of applied field and temperature using the computer program Maple. Figures 1 and 2 show the results of the calculations for the magnetisation as a function of both field and temperature (Eqn. 4.13). Figures 3 and 4 show the calculated Gibbs free energy as a function of both field and temperature (Eqn. 4.30) and Fig.'s 5 and 6 show the corresponding values of the specific heat capacity as a function of both field and temperature (Eqn.'s 4.32 and 4.34). Although both the magnetisation and the Gibbs free energy are both smooth functions of temperature the gradient of the magnetisation as a function of temperature changes very rapidly for low fields in the region of $T_M^F$ and discontinuously for the zero field trace at $T_M^F$. The effect of this rapid change in gradient is observed as a deviation in the resultant (non-zero field) data for the specific heat capacity

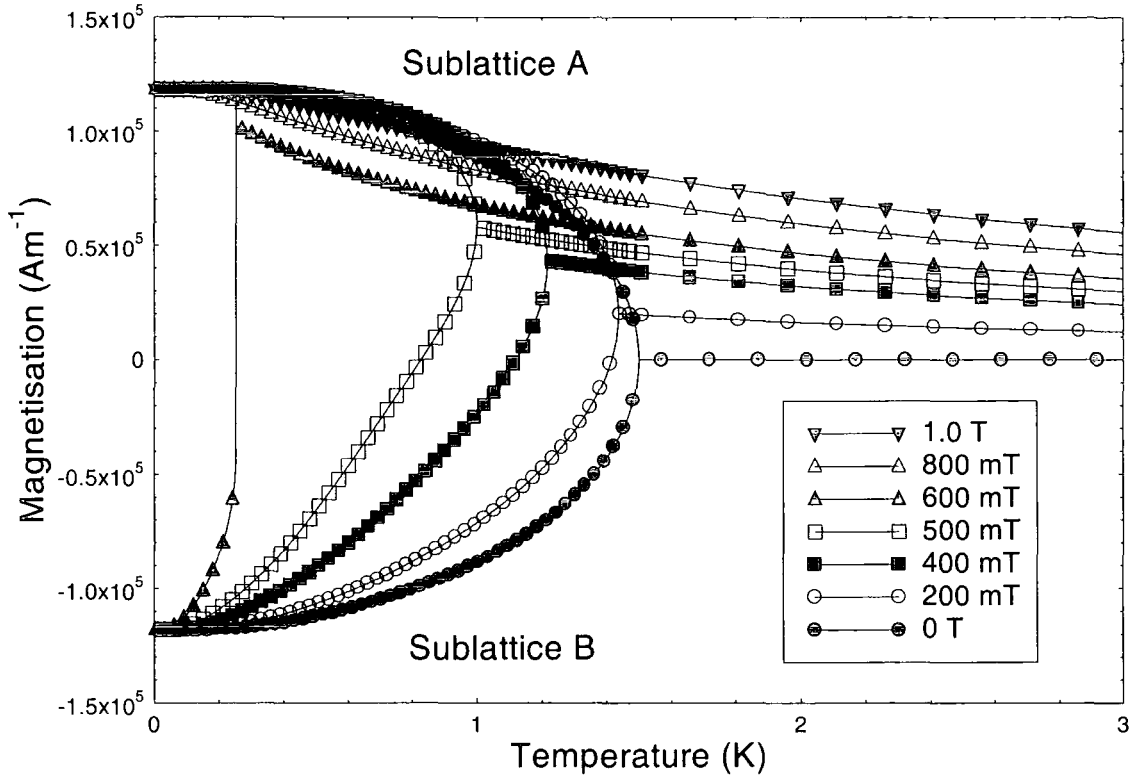


**Figure 7. The magnetisation for sublattices A and B as a function of temperature for $GdMo_6S_8$ with $T_M^{AF}$ = 1.5 K and in applied fields from 0 T to 1 T.**

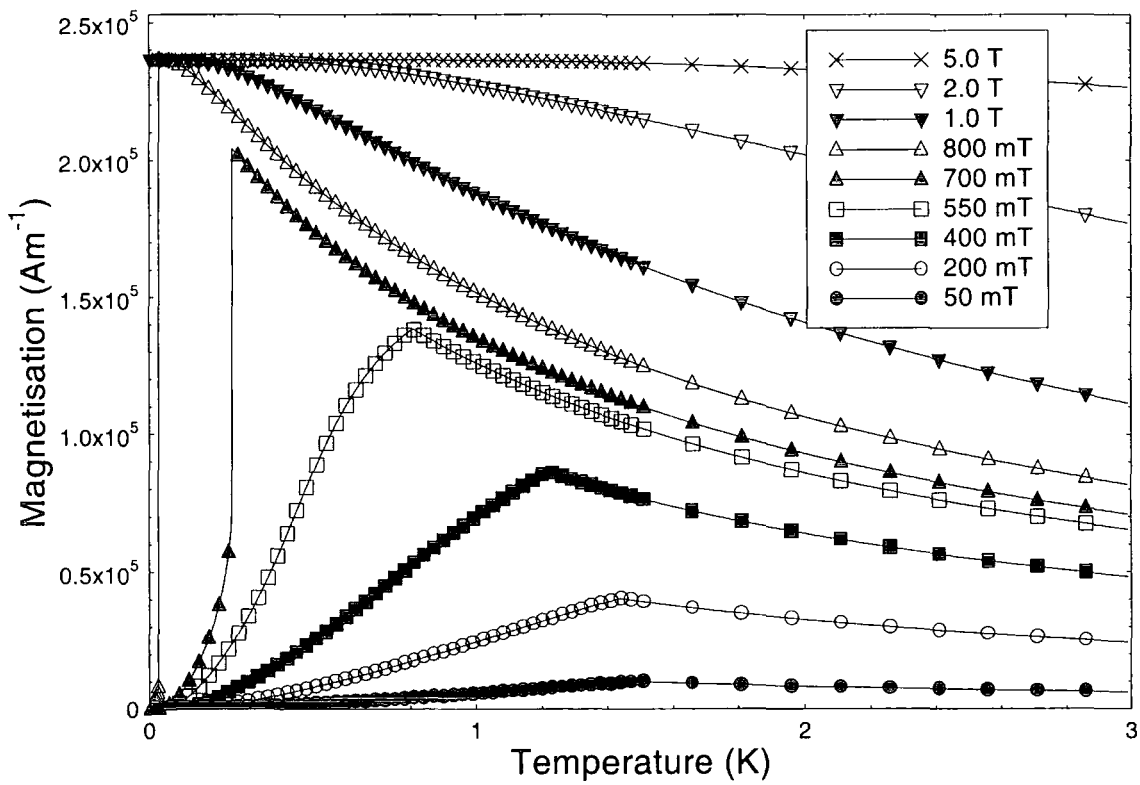


**Figure 8. The total magnetisation as a function of temperature for $GdMo_6S_8$ with $T_M^{AF}$ = 1.5 K and in applied fields from 0 T to 5 T.**

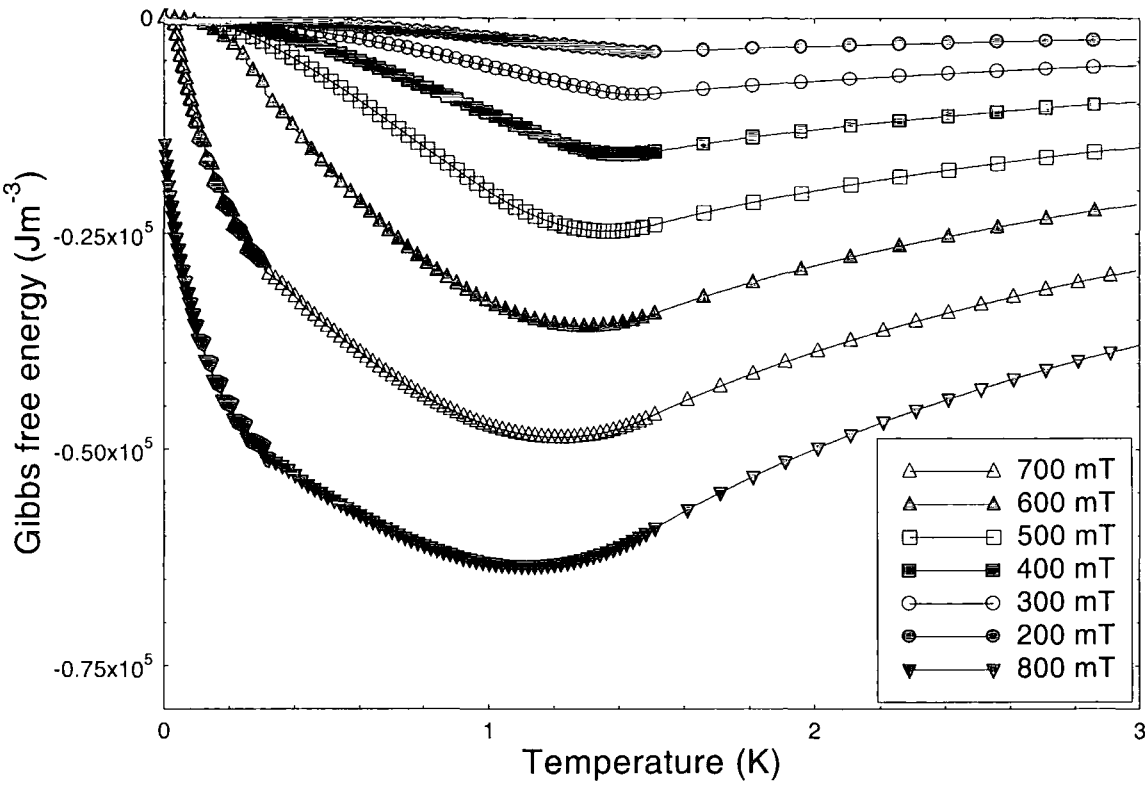


**Figure 9. Gibbs free energy per unit volume as a function of temperature for $GdMo_6S_8$ with $T_M^{AF}$ = 1.5 K in applied fields from 0 T to 800 mT.**

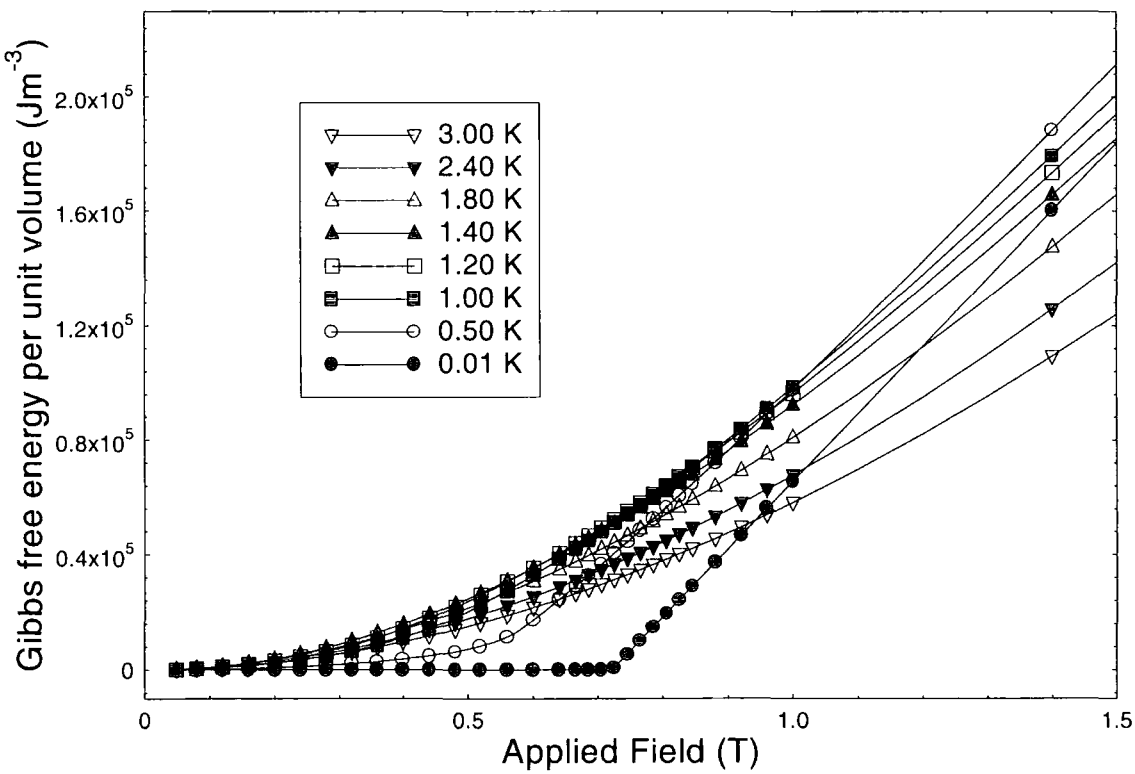


**Figure 10. Gibbs free energy per unit volume as a function of applied field for $GdMo_6S_8$ with $T_M^{AF}$ = 1.5 K and for temperatures from 0.01 K to 3.0 K.**

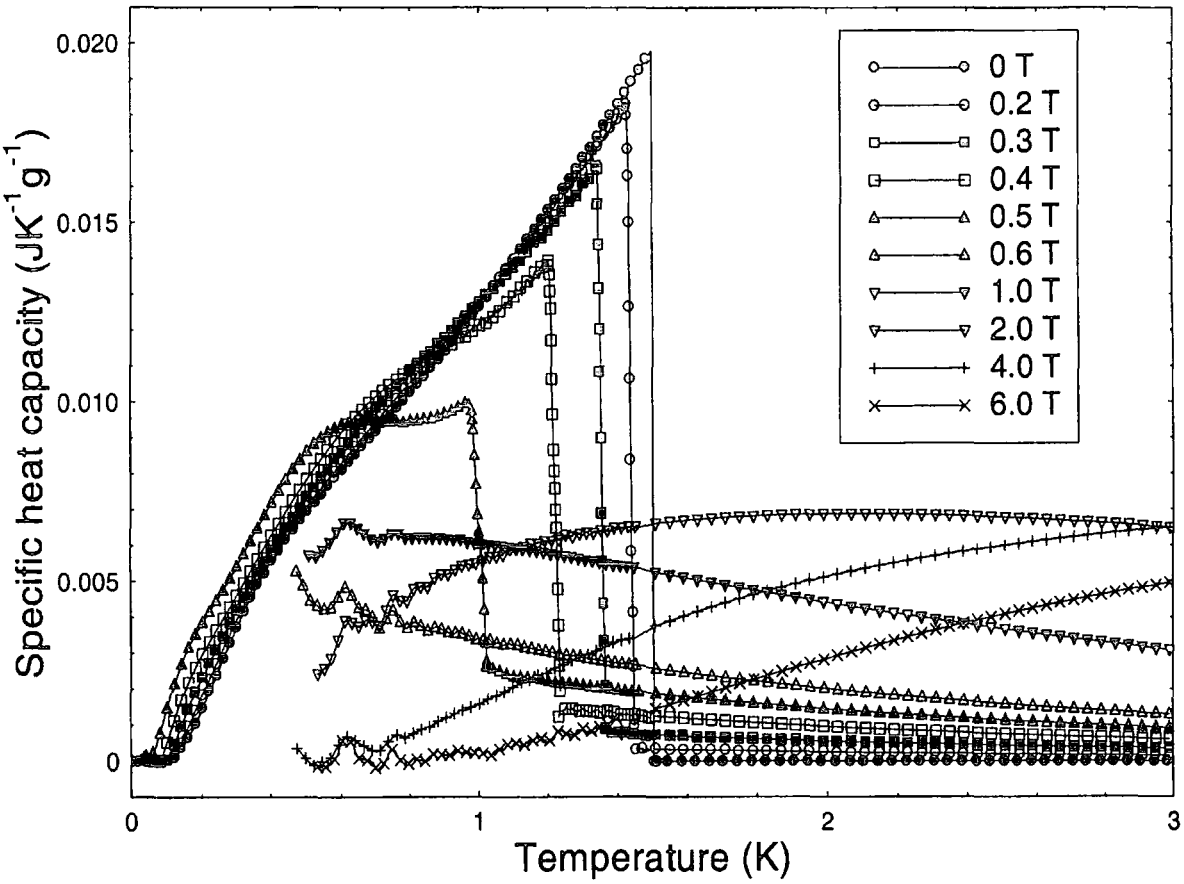


**Figure 11. Specific heat capacity as a function of temperature for $GdMo_6S_8$ with $T_M^{AF}$ = 1.5 K in applied fields from 0 T to 6 T.**

in the region of $T_M^F$. Taking a larger number of low field traces in the computation of the magnetisation reduces the size of this deviation but is however computationally demanding. The data presented in Fig. 5 shows that the anomaly in the in-field traces have been reduced to a extent that only the points within 0.03 K of $T_M^F$ are affected and that the specific heat is otherwise a smooth function of both temperature and applied field (Fig. 6). The points of largest deviation within this region have been omitted from Fig. 5 for clarity.

### 4.3.2 Antiferromagnetic case ($T_M^{AF}$ = 1.5 K).

Taking $T_M^{AF}$ = 1.5 K the two equations for the magnetisation of the sublattices A and B (Eqn.'s 4.22 and 4.23) are solved simultaneously using the computer program Maple. Figures 7 and 8 show the results of the calculations for the magnetisation of both sublattices and the total magnetisation as a function of temperature. Figures 9 and 10 show the total

Gibbs free energy as a function of both field and temperature and Fig. 11 shows the specific heat capacity as a function of temperature.

In zero applied field the A and B sublattices are equal and oppositely orientated giving a resultant total magnetisation of zero for any temperature. Fig. 7 shows that in a magnetic field, applied in the same direction as the (saturated) ions in sublattice A, the magnetisation of sublattice B is reduced and that of sublattice A increased as the applied field is increased. The total magnetisation therefore exhibits a peak at a temperature less than the ordering temperature ($T_M^{AF}$) in zero applied field that is then reduced in temperature as the applied field is increased, as shown in Fig. 8. For temperatures above this peak the material behaves paramagnetically and the magnetisation of both sublattices are equal and orientated in the same direction. At a field of about 740 mT the effective ordering temperature of the material is less than 2 mK (the lowest temperature use in these calculations) and so the material behaves paramagnetically for all non-zero temperatures. As the applied field is increased towards 740 mT the gradient on the low temperature side of the peak in the magnetisation becomes extremely sharp and fewer points are calculated in this region (e.g. 700 mT trace in Fig. 8). This leads to a discontinuity in the Gibbs free energy, as shown in Fig. 9 for the 700 and 800 mT traces below 0.4 K, at each temperature that corresponds to peak in the magnetisation at these relatively high fields. Since the Gibbs free energy at a field $\mu_0 H_{ext}$ is calculated as the integral at a fixed temperature from zero field up to $\mu_0 H_{ext}$ each discontinuity then becomes included in the computation of the Gibbs free energy of any field larger than that field where the discontinuity occurred. Taking the differential of the Gibbs free energy in the region of these discontinuities leads to a large, non-physical, oscillatory region in the specific heat of all the fields greater than about 550 mT and for temperatures less than ~ 0.6 K. The data for fields above 500 mT and below 0.6 K has therefore not been included in Fig. 11 for clarity, although even at 0.6 K there is still a large scatter evident for the high field data.

For temperatures between 0.6 K and 1.5 K a similar effect to the above is seen due to the peaks in the magnetisation at fields $0 < \mu_0 H_{ext} < 550$ mT. Integrating a finite number of magnetisation traces at different applied fields give a smooth Gibbs free energy trace as seen in Fig. 9 at low fields. The gradient of this function however is not smooth with a small discontinuity at each temperature where a peak has occurred in the magnetisation at lower fields. The Gibbs free energy and both the first and second differentials of this

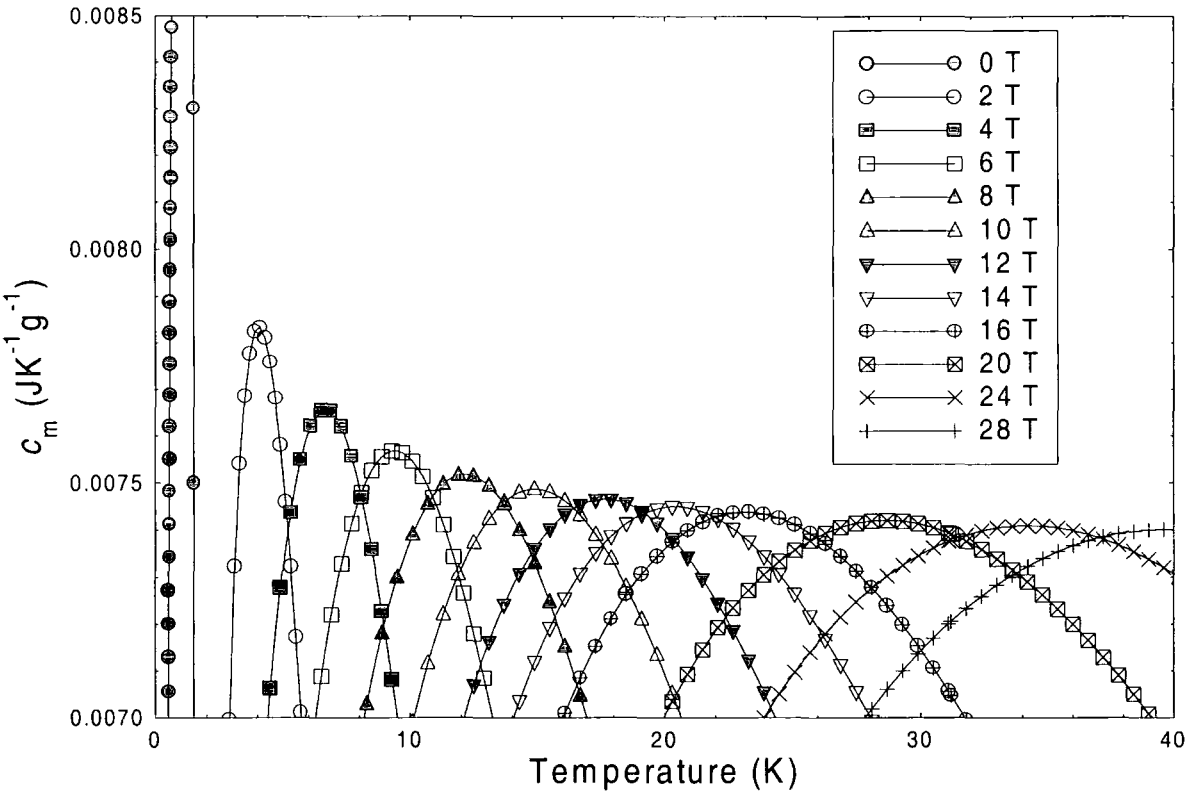


**Figure 12.** $c_m$ **as a function of temperature for various applied fields above the ordering temperature for a ferromagnetic** $GdMo_6S_8$ **with** $T_M^F$ **= 1.5 K.**

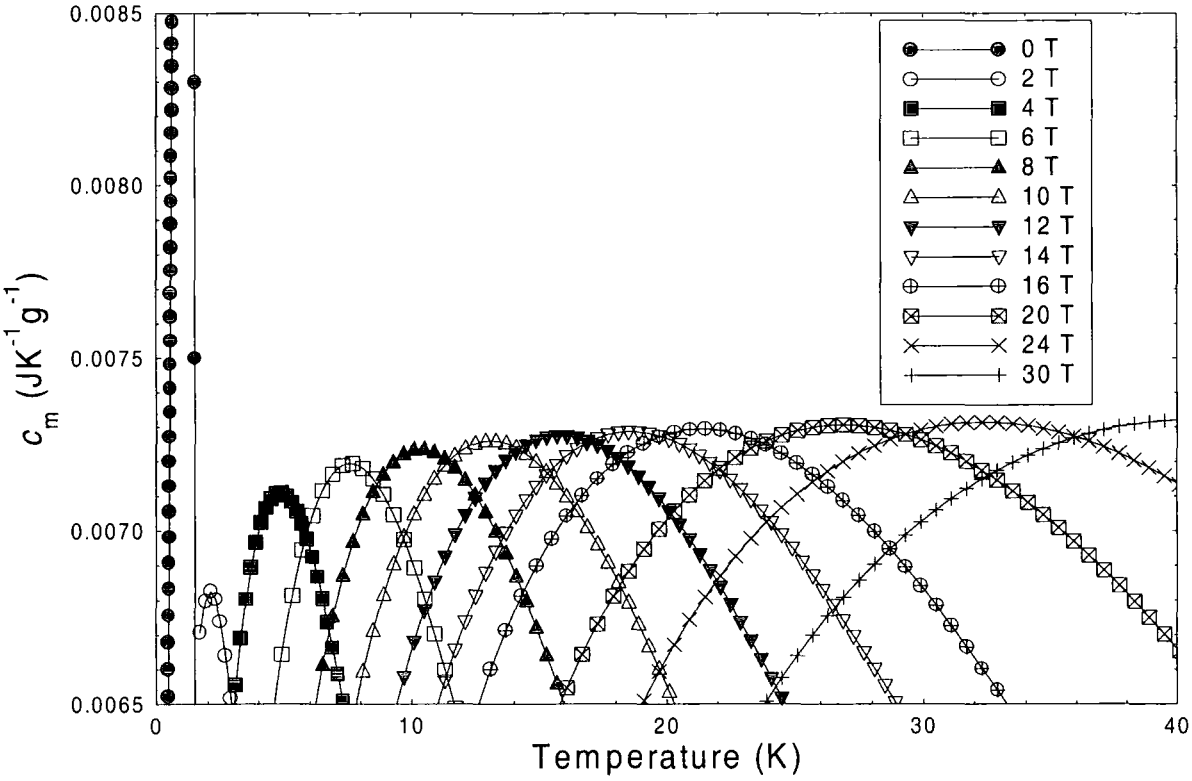


**Figure 13.** $c_m$ **as a function of temperature for various applied fields above the ordering temperature for an antiferromagnetic** $GdMo_6S_8$ **with** $T_M^{AF}$ **= 1.5 K.**

function are therefore smoothed up to 1.5 K for each field using a window of about 40 mK, to produce the data in Fig. 11. The effect of this smoothing produces a region between 1.45 K and 1.50 K where data has to be omitted, however as can be seen in Fig. 11 the magnitude and curvatures of the specific heat on either side of this region are in good agreement. Above 1.5 K the specific heat does not require any smoothing and can be calculated accurately with a much smaller density of points. The region where the material behaves paramagnetically can therefore be determined accurately for all fields down to temperatures as low as 0.6 K. The large peak in the specific heat that corresponds to the magnetic ordering of the material can also be determined accurately for fields up to about 550 mT.

Using a much larger density of both field traces and temperature points the two effects described above could be reduced and possibly even eradicated. The increase in computation time demanded however would be significant.

### 4.3.3 High temperature behaviour of $c_m$.

Figures 12 and 13 show the magnetic contribution to the specific heat capacity (calculated from Eqn. 4.32) as a function of temperature for constant applied field and for $T > T_M$ in both ferromagnetic and antiferromagnetic cases. At any fixed field, the specific heat exhibits a peak ($c_{m(peak)}$) at a temperature above $T_M$. This peak arises due to the competition between ordering of the ions due to the applied field and thermal disorder. At low temperatures the thermal energy of the magnetic ions is small and so they are preferentially aligned parallel to the applied field. A small change in temperature has little effect on this preferential alignment at these temperatures and so $c_m$ ($= dU_m / dT$) $\rightarrow 0$ as $T \rightarrow 0$. At sufficiently high temperatures the ions are randomly orientated with respect to the applied field to such a degree that small changes in the temperature have little effect on this disordered state and so $c_m$ ($= dU_m / dT$) $\rightarrow 0$ as $T \rightarrow \infty$. At some intermediate temperature a small change in temperature will therefore have a maximum effect on the alignment of the ions with respect to the applied field and so produce a maximum in $c_m$ [20]. Furthermore as the applied field is increased larger temperatures are required to significantly disrupt the preferential alignment of the ions and so the temperature at which $c_{m(peak)}$ occurs is also larger.

From Fig.'s 12 and 13 we can see that the calculated temperature of $c_{m(peak)}$ is strongly dependent on the applied field but the magnitude of $c_{m(peak)}$ is only weakly dependent on the applied field. At fields between 2 T and 7.5 T in the antiferromagnetic case, the temperature of $c_{m(peak)}$ changes from 1.5 to 6 times the zero field ordering temperature but the magnitude of the peak only changes from 35 % to 36.5 % of the zero field peak value. For fields from 7.5 T to 340 T the temperature of $c_{m(peak)}$ then changes from 6 to 260 times the zero field ordering temperature however the magnitude of $c_{m(peak)}$ increases to only 37 % of the zero field peak.

The magnitude of $c_{m(peak)}$ increases with applied field in the antiferromagnetic case but decreases with increasing applied field in the ferromagnetic case. Inspection of this field dependence can therefore indicate the nature of the magnetic ordering in the material. The magnitude of $c_{m(peak)}$ has been determined in both ferromagnetic and antiferromagnetic cases for fields up to 80 T and in both cases the value of $c_{m(peak)}$ appears to converge to the same saturation value ($c_m^{sat}$).

## 4.4 An approximate form for $c_m$ above the ordering temperature.

In order to analyse experimental specific heat data where any of the parameters $J$, $L$, $S$, $n_v$ and $T_M^F$ / $T_M^{AF}$ are not known, an approximate form for the specific heat is required that allows the determination of some or all of the above parameters without rigorous calculation. In the mean field model above the zero field ordering temperature ($T_M$) the material behaves paramagnetically and so the magnetisation can be approximated in terms of the saturation magnetisation ($M_s$), applied field strength ($\mu_0 H_{ext}$) and temperature ($T$).

$$M = M_s \tanh\left(K(T)H_{ext}\right) \tag{4.39}$$

where for a fixed value of $T$, $K(T)$ is a constant. Differentiating Eqn. (4.39) with respect to $H_{ext}$ at constant $T$ and taking the low field limit:

$$\chi' = \frac{\partial M}{\partial H_{ext}} = \frac{M_s K(T)}{\cosh^2\left(K(T)H_{ext}\right)} \approx M_s K(T) \tag{4.40}$$

since $\cosh(K(T)H_{ext}) \rightarrow 1$ as $H_{ext} \rightarrow 0$.

If we assume the susceptibility has a Curie-Weiss temperature dependence with Curie-Weiss constant $\theta$, then from Eqn. (4.40):

$$K(T) = \frac{\chi'}{M_s} = \frac{1}{M_s}\frac{CH_{ext}}{(T-\theta)} \tag{4.41}$$

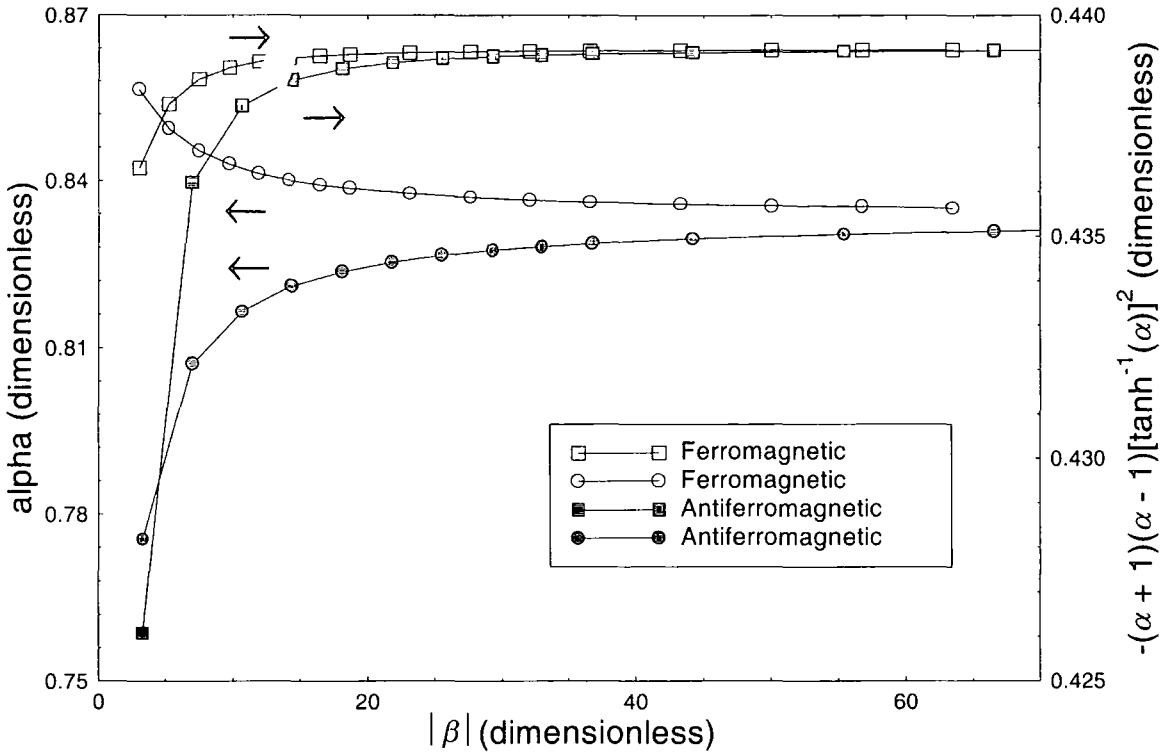


**Figure 14. $\alpha$ and the function $-(\alpha + 1)(\alpha - 1)[\tanh^{-1}(\alpha)]^2$ evaluated at $c_{m(peak)}$ as a function of $|\beta|$ for ferromagnetic and antiferromagnetic $GdMo_6S_8$ with $T_M^F$ = 1.5 K using the approximate form for $c_m$.**

and substituting back into Eqn. (4.39).

$$M = M_s \tanh\left(\frac{CH_{ext}}{M_s(T-\theta)}\right) \tag{4.42}$$

Using Eqn. (4.2) for the magnetisation in the ferromagnetic case and Eqn.'s (4.13) and (4.14) for the magnetisation of the sublattices A and B in the antiferromagnetic case then the low field susceptibility can be determined in both cases.

Ferromagnetic: $$\chi'^{F} = \frac{C}{(T - C(1+\lambda^*))} = \frac{C}{(T - T_M^F)} \tag{4.43}$$

Antiferromagnetic: $$\chi'^{AF} = \frac{C}{(T - C(1+\lambda^*/2))} = \frac{C}{(T - C + T_M^{AF})} \tag{4.44}$$

and so in Eqn. (4.42) $\theta = T_M^F$ in the ferromagnetic case and $\theta = (C - T_M^{AF})$ in the antiferromagnetic case. In the special case that $C > T_M^{AF}$, $\theta$ is positive and the material behaves ferromagnetically. Following the procedure outlined in section 4.2.3, the specific heat per unit volume is calculated from the magnetisation by integrating with respect to $H_{ext}$

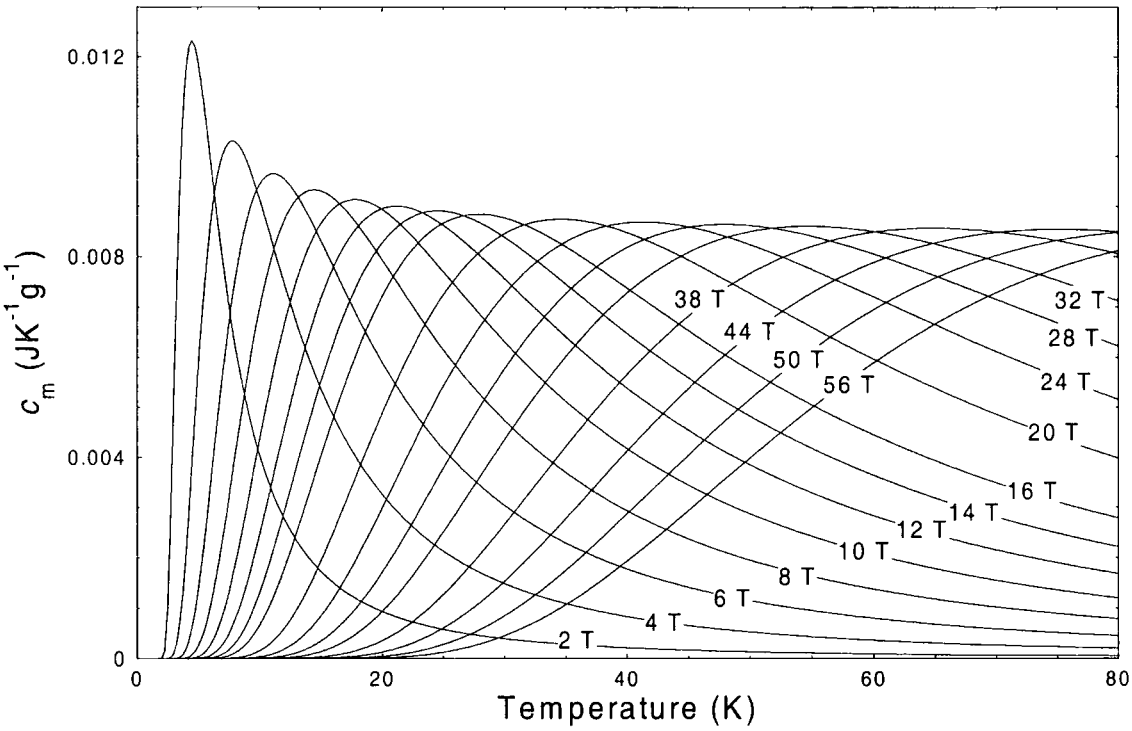


**Figure 15.** $c_m$ **for various applied fields above the ordering temperature determined from the approximate function (Eqn. 4.48) for ferromagnetic** $GdMo_6S_8$ **with** $T_M^F = 1.5$ **K,** $J = 3.5$, $g_J = 2.0$ **and** $n_v = 3.64 \times 10^{27}$ **m**$^{-3}$.

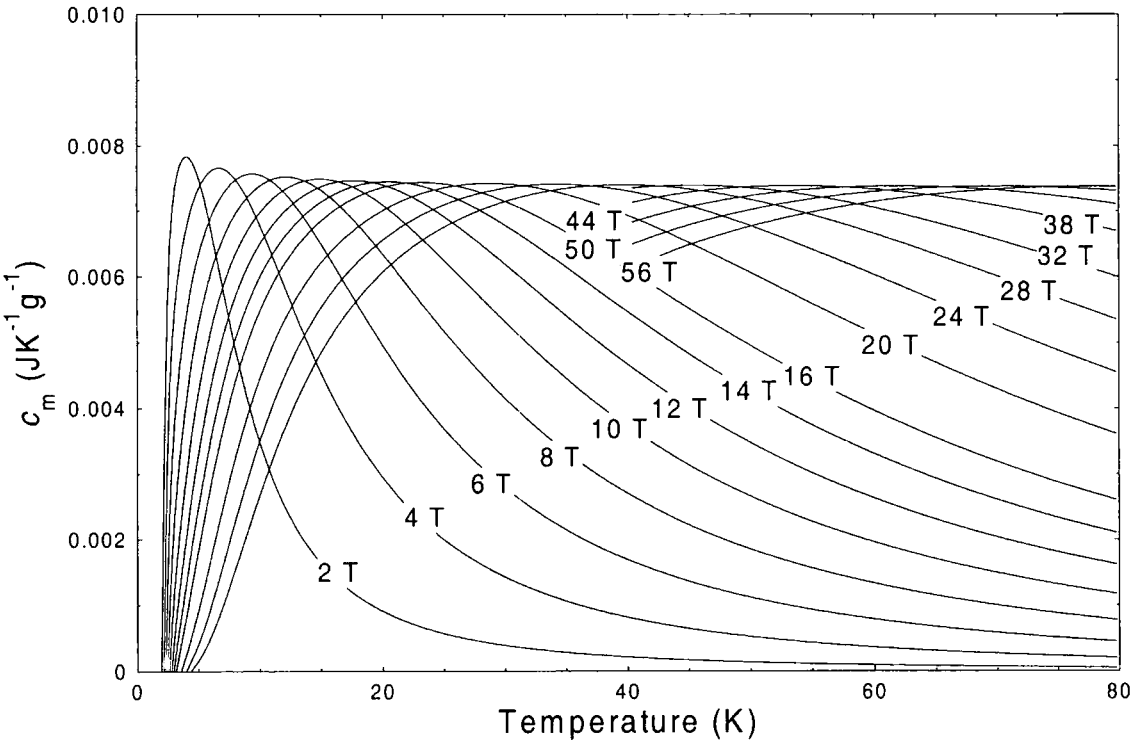


**Figure 16.** $c_m$ **for various applied fields above the ordering temperature determined from the rigorous calculation (Eqn. 4.32) for ferromagnetic** $GdMo_6S_8$ **with** $T_M^F = 1.5$ **K,** $J = 3.5$, $g_J = 2.0$ **and** $n_v = 3.64 \times 10^{27}$ **m**$^{-3}$.

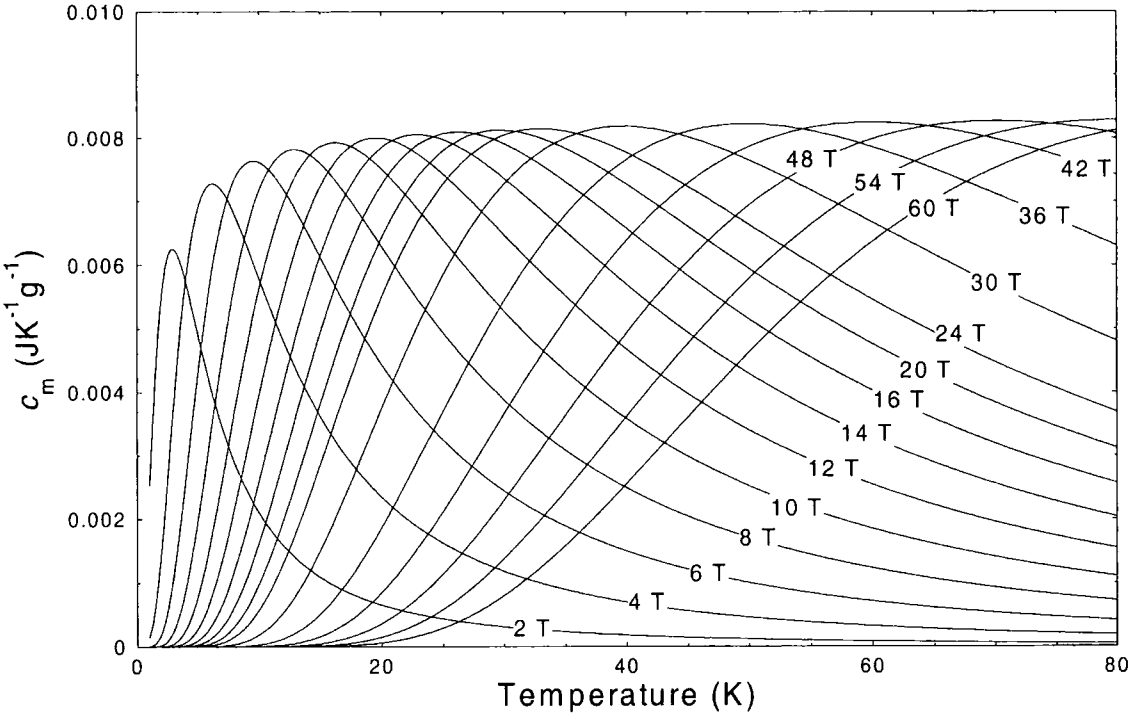


**Figure 17.** $c_m$ **for various applied fields above the ordering temperature determined from the approximate function (Eqn. 4.48) for antiferromagnetic** $GdMo_6S_8$ **with** $T_M^{AF}$ **= 1.5 K,** $J$ **= 3.5,** $g_J$ **=2.0 and** $n_v = 3.64 \times 10^{27}$ **m$^{-3}$.**

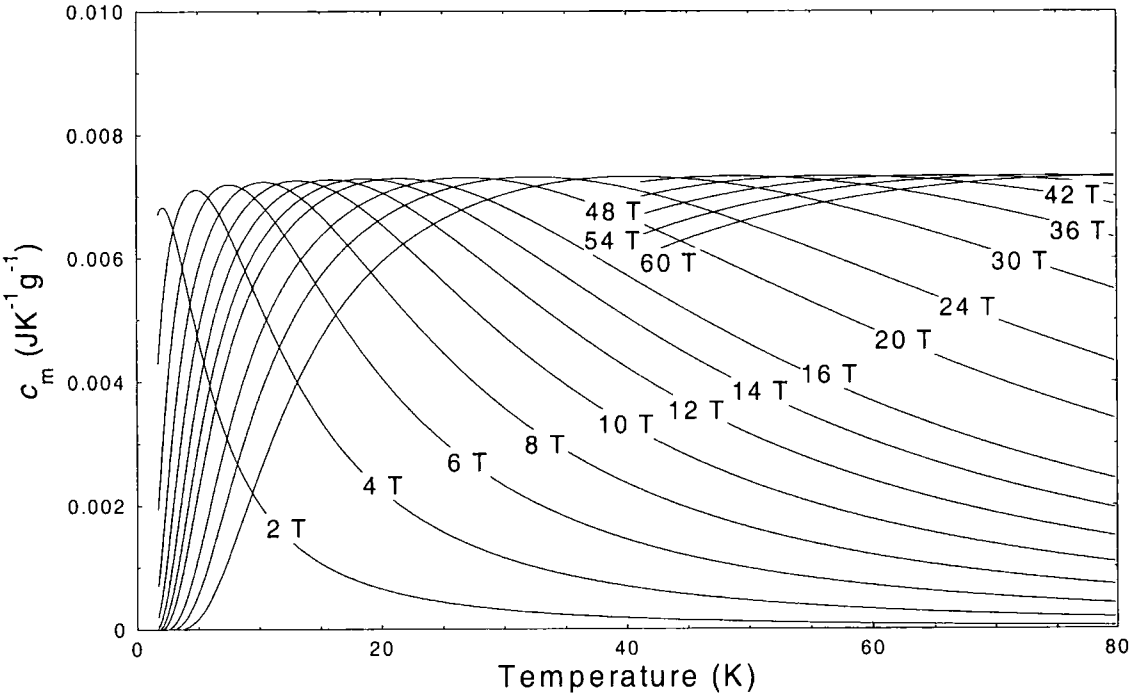


**Figure 18.** $c_m$ **for various applied fields above the ordering temperature determined from the rigorous calculation (Eqn. 4.32) for antiferromagnetic** $GdMo_6S_8$ **with** $T_M^{AF}$ **= 1.5 K,** $J$ **= 3.5,** $g_J$ **= 2.0 and** $n_v = 3.64 \times 10^{27}$ **m$^{-3}$.**

at constant temperature, then differentiating twice with respect to $T$ at constant applied field and finally multiplying the result by $-T$.

$$c_{m(vol)} = \frac{-\left[\tanh\left(\frac{CH_{ext}}{M_s(T-\theta)}\right)+1\right]\left[\tanh\left(\frac{CH_{ext}}{M_s(T-\theta)}\right)-1\right]C\mu_0 H_{ext}^2 T}{(T-\theta)^3} \tag{4.45}$$

In the high temperature limit this expression gives:

$$\underset{T\to\infty}{c_{m(vol)}} \approx \frac{C\mu_0 H_{ext}^2 T}{(T-\theta)^3} \alpha \frac{H_{ext}^2}{T^2} \tag{4.46}$$

in agreement with models of $c_m$ used by other authors [292]. Substituting $\alpha = \tanh(CH_{ext} / M_s(T - \theta)$ and therefore $H_{ext} = M_s(T - \theta) \tanh^{-1}(\alpha) / C$ and noting that since $M_s = n_v J g_J \mu_B$ (Eqn. 4.6) and $C = n_v \mu_B^2 \mu_0 p_{eff}^2 / 3k_B$ (Eqn. 4.11) we get:

$$M_s^2 = \frac{3k_B n_v C}{\mu_0}\left(\frac{J}{J+1}\right) \tag{4.47}$$

and therefore $$c_{m(vol)} = \frac{-[\alpha+1][\alpha-1][\tanh^{-1}\alpha]^2 3k_B n_v T}{(T-\theta)}\left(\frac{J}{J+1}\right) \tag{4.48}$$

Finally we substitute $T = \beta\,\theta$, where for high ordering temperatures, $\beta$ is a positive number in the ferromagnetic case and a negative number in the antiferromagnetic case.

$$c_{m(vol)} = \frac{-[\alpha+1][\alpha-1][\tanh^{-1}\alpha]^2 3k_B n_v \beta J}{(\beta-1)(J+1)} \tag{4.49}$$

this gives an approximate equation for $c_m$ for both ferromagnetic and antiferromagnetic materials, which is a function of $\alpha$, $\beta$, $J$ and $n_v$.

By noting the temperature at which $c_{m(peak)}$ occurs for each field we can determine the temperature dependence of $\alpha$. Figure 14 shows the temperature dependence of $\alpha$ and the function $-(\alpha + 1)(\alpha - 1)[\tanh^{-1}(\alpha)]^2$ when evaluated at $c_{m(peak)}$ in both ferromagnetic and antiferromagnetic cases using the approximate form (Eqn. 4.49). The value of the function $-(\alpha + 1)(\alpha - 1)[\tanh^{-1}(\alpha)]^2$ in both cases changes by less than 5 % from 2 to 50 times the Curie-Weiss constant and saturates at high temperatures at a value of ~ 0.4392.

### 4.4.1 Comparison of approximate form for $c_m$ with rigorous calculation.

To compare the results for $T > T_M$ from the rigorous calculation (Eqn. 4.32) with the approximate expression in Eqn. (4.48), both functions are used to calculate $c_m$ as a function of temperature and applied field up to ~ 80 K and ~ 60 T. Figures 15 and 16 show the

results in the ferromagnetic case and Fig.'s 17 and 18 the corresponding results in the antiferromagnetic case. These figures show that the data calculated using the simplified function (Eqn. 4.49) in Fig.'s 15 and 17 is in good agreement with the data calculated using the full functional form for $M(H,T)$ (Eqn. 4.32) in Fig.'s 16 and 18. The main discrepancy between the sets of data is the value of $c_{m(peak)}$, which when calculated at each field using the approximate function is larger in both temperature and magnitude than the corresponding results of the rigorous calculation. The general trend in the magnitude of $c_{m(peak)}$ however is to decrease in the ferromagnetic case and increase in the antiferromagnetic case as the applied field is increased. At high fields $c_{m(peak)}$ reaches a saturation value ($c_m^{sat}$) in both Fig.'s 15 and 17 in agreement with the data in Fig.'s 16 and 18. The value of $c_m^{sat}$ from the approximate function is ~ 12 % larger in both ferromagnetic and antiferromagnetic cases than the value of $c_m^{sat}$ obtained from the rigorous calculations.

When analysing experimental specific heat data we can take advantage of this saturation in the peak value of $c_m$ for $T > T_M$. If $T >> \theta$, then the ratio $\beta / (\beta - 1) \approx 1$ and from Fig. 14 the value of the function $-(\alpha + 1)(\alpha - 1)[\tanh^{-1}(\alpha)]^2$ evaluated at $c_{m(peak)}$ also reaches a constant value. We can therefore make the substitution:

for $T >> \theta$

$$A = \frac{-[\alpha+1][\alpha-1][\tanh^{-1}\alpha]^2 3\beta}{(\beta-1)} \tag{4.50}$$

where A is a dimensionless number, and so we can write:

$$c^{sat}_{m(vol)} = Ak_B n_v \frac{J}{(J+1)} \tag{4.51}$$

In units of $JK^{-1}mole^{-1}$ Eqn. (4.51) becomes:

$$c^{sat}_{m} = A\frac{k_B n_v m_{mol}}{\rho}\frac{J}{(J+1)} \tag{4.52}$$

where $\rho$ is the density and $m_{mol}$ is the molar mass of the compound. For an ideal sample the density is related to the molar mass and the unit cell volume ($V_{cell}$).

$$\rho = \frac{m_{mol}}{N_A V_{cell}} \tag{4.53}$$

where $N_A$ is Avagadro's number. Since $n_v = n_{cell} / V_{cell}$ where $n_{cell}$ is the number of magnetic ions per unit cell we therefore have a very simple expression for the saturation value of $c_{m(peak)}$ for temperatures far above the ordering temperature.

$$c^{sat}_{m} = A\frac{n_{cell} R J}{(J+1)} \tag{4.54}$$

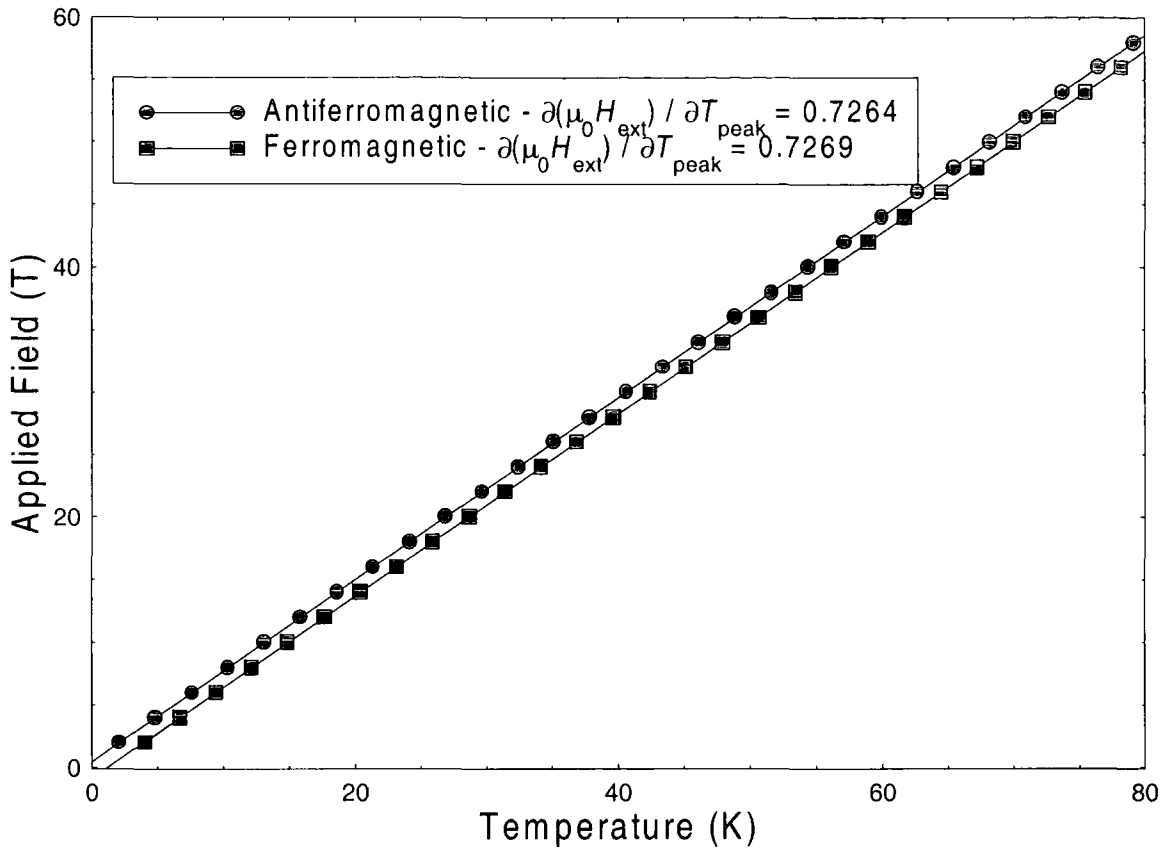


**Figure 19. Applied field as a function of temperature at $c_{m(peak)}$ determined from the rigorous calculations (Fig.s 16 and 18) for both ferromagnetic and antiferromagnetic cases.**

where $R = k_B N_A = 8.3145$ $JK^{-1}mole^{-1}$ is the molar gas constant. A value of A = 1.286 can be determined from the data calculated using the approximate function in Fig.'s 15 and 17 and a value of A = 1.1245 from the data calculated using the full functional form of $M(H,T)$ in Fig.'s 16 and 18. These values are chosen such that the value of $c_m^{sat}$ is equal to the saturation value of $c_{m(peak)}$ in the high temperature limit. The value of $c_{m(peak)}$ in both ferromagnetic and antiferromagnetic cases is assumed to converge to $c_m^{sat}$, although due to the computation time involved the rigorous calculations have only been checked up to 80 T.

Further calculations have been completed using the full functional form of $M(H,T)$ for the magnetic ions $Ce^{3+}$ and $Dy^{3+}$, rather than $Gd^{3+}$. These ions were chosen because they have respectively the smallest and largest Bohr magneton values in the rare-earth series. The equivalent values of A determined from the data for $Ce^{3+}$ and $Dy^{3+}$ are 1.0279 and 1.2035 respectively. We therefore chose the value of A = 1.1245 determined from the rigorous calculations for $Gd^{3+}$ as an average value across the series. Using this value of A

in Eqn. (4.54) and the values of $c_m^{sat}$ from these further calculations, values of $J$ are determined for $Ce^{3+}$ and $Dy^{3+}$ as 2.46 and 4.97 respectively. The free ion values are 2.5 for $Ce^{3+}$ and 7.5 for $Dy^{3+}$ and so we conclude that this analysis becomes more inaccurate in the high $J$ limit as the term $J / (J + 1)$ in Eqn. (4.54) approaches unity.

The magnitude of the error involved in using Eqn. (4.54), with A = 1.1245, for temperatures where $c_{m(peak)}$ is not in the saturation region is determined from Fig.'s 16 and 18. The data in these figures is analysed at $T \sim 60$ K, $T \sim 12$ K and $T \sim 3$ K, this corresponds to values of $\beta = 40$, 8 and 2 in the ferromagnetic case and $\beta = -66.5$, - 13.3 and – 3.3 in the antiferromagnetic case. Using $n_{cell} = 1$ and $m_{mol} = 989.402$ gmole$^{-1}$ for $GdMo_6S_8$ we can use Eqn. (4.54) at the above values of $\beta$ to estimate $J$ from the values of $c_{m(peak)}$ in Fig.'s 16 and 18. Conversely we can then use the correct value of $J = 3.5$ in Eqn. (4.54) to estimate values of $c_{m(peak)}$ at the values of $\beta$ specified above. From the ferromagnetic data in Fig. 16 the estimated values of $J$ are respectively < 1 %, ~ 10 % and ~ 50 % larger than the correct value. Conversely the estimated values of $c_{m(peak)}$ are respectively 0.6 %, 2 % and 8 % larger than the data in Fig. 16. Repeating these calculations for the antiferromagnetic data in Fig. 18, the estimated values of $J$ are < 0.1 %, ~ 5 % and ~ 20 % smaller than the correct value and the estimates of $c_{m(peak)}$ are < 0.1 %, ~ 1 % and ~ 5 % smaller than the data in Fig. 18.

Using the fact that $c_{m(peak)}$ saturates at high temperatures, we can derive an expression for the change in the temperature of $c_{m(peak)}$ with field from the approximate form for $M(H,T)$ (Eqn. 4.42). From Eqn. (4.47) we can note that:

$$\frac{C}{M_s} = \frac{g_J (J+1) \mu_B \mu_0}{3k_B} \tag{4.55}$$

and

$$\alpha = \tanh\left( \frac{CH_{ext}}{M_s (T - \theta)} \right) \tag{4.56}$$

In the high temperature limit the value of $\alpha$ saturates (Fig. 14). We can therefore look at the field dependence of the temperature of $c_{m(peak)}$ in this limit.

$$\frac{\partial(\mu_0 H_{ext})}{\partial T_{peak}} = \tanh^{-1}(\alpha) \frac{M_s}{C} \approx \tanh^{-1}(\alpha) \frac{3k_B}{g_J (J+1) \mu_B} \tag{4.57}$$

So in the high temperature limit this gives:

$$\frac{\partial(\mu_0 H_{ext})}{\partial T_{peak}} = \frac{A^*}{g_J (J+1)} \tag{4.58}$$

where $A^* = 5.335$ using the approximate form for $c_m$. Using the data from the rigorous calculations in both ferromagnetic and antiferromagnetic cases (Fig.'s 16 and 18 respectively) the temperature of $c_{m(peak)}$ for each applied field is determined and the results are presented in Fig. 19. The data in both cases lie on a straight line for all temperatures allowing the gradient to be determined from a linear fit to the data and an average value of $A^* = 6.540$ to be calculated. Values of $A^*$ of 6.234 and 7.414 can also be determined from rigorous calculations using respectively $Ce^{3+}$ and $Dy^{3+}$ ions instead of $Gd^{3+}$ ions. We therefore chose $A^* = 6.540$ from the rigorous calculations using $Gd^{3+}$ ions, as an average value across the rare-earth series. Using $A^* = 6.540$ in Eqn. (4.58) and values of $\partial(\mu_0 H_{ext} / \partial T)$ determined from the data for the $Ce^{3+}$ and $Dy^{3+}$ ions, $g_J(J + 1)$ is calculated for these ions as 3.15 and 10.0 respectively. These values are in reasonable agreement with the free ion values of 3.0 ($Ce^{3+}$) and 11.3 ($Dy^{3+}$).

Simply noting the temperature at which $c_{m(peak)}$ occurs for different applied fields can therefore give an estimate for $g_J(J + 1)$ for the material. This approximation is independent of the fraction of the material that contributes to $c_m$ and is therefore a useful tool for investigating mixed phase materials or magnetic impurity phases.

## 4.5 Conclusions.

The magnetic contribution to the specific heat capacity of a model $GdMo_6S_8$ system has been calculated as a function of both applied magnetic field and temperature in both the ferromagnetic and antiferromagnetic cases using an ordering temperature of 1.5 K. A mean field model has been used to develop the equations for the magnetisation since Chevrel phase materials that contain magnetic ions exhibit magnetic properties that are characteristic of this model. Thermodynamic arguments are used to calculate the ordering temperature, the zero field contribution to the specific heat and therefore the total magnetic contribution to the specific heat from the magnetisation. The calculations rely on computer software to numerically solve the equations for the magnetisation of the material. The resulting values of $M(H_{ext},T)$ can then be manipulated to give both the Gibbs free energy and the specific heat capacity.

The calculated specific heat data in the ferromagnetic case are smooth functions of both applied field and temperature apart from a small window (~ 0.03 K) close to the zero field ordering temperature. This window arises from the sharp change in the magnetisation close

to the ordering temperature in low fields and can be reduced even further by increasing the computation time. In the antiferromagnetic case the summation of the magnetisation of the two sublattices A and B lead to peaks in the total magnetisation that become discontinuities for $GdMo_6S_8$ at fields between 550 mT and 740 mT due to the finite number of temperature points used. The calculated specific heat capacity of $GdMo_6S_8$ where both the applied field is greater than 550 mT and the temperature is below $0.4T_M^{AF}$ is unreliable. The data for temperatures between $0.4T_M^{AF}$ and $T_M^{AF}$ for all fields has to be smoothed. The resulting data however clearly show the change in the ordering temperature as a function of applied field up to 550 mT and the magnetic contribution to the specific heat capacity for all fields down to temperatures as low as $0.4T_M^{AF}$.

Finally an approximate function has been derived for $c_m$ at temperatures above the zero field ordering temperature ($T_M$) that has the same general temperature and field dependence as the rigorous calculations. Visible in the data calculated using both the approximate and rigorous functional forms is a peak in the specific heat ($c_{m(peak)}$) above $T_M$ for any applied field. This effect is due to competition between the alignment of the magnetic ions with the applied field and thermal disorder. The magnitude of $c_{m(peak)}$ for $T > T_M$ increases with increasing applied field in the antiferromagnetic case and decreases with increasing applied field in the ferromagnetic case. At high fields in both ferromagnetic and antiferromagnetic cases the magnitude of $c_{m(peak)}$ saturates and an expression for this saturation value ($c_m^{sat}$) is given in terms of the number of magnetic ions per unit cell and $J$:

$$c_m^{sat} = 1.1245 \frac{n_{cell} R J}{(J+1)}$$

The value of the constant in this equation depends on the magnetic ion used in the calculations. The value of 1.1245 is therefore chosen as an average value across the rare-earth series as determined from calculations with $Ce^{3+}$, $Gd^{3+}$ and $Dy^{3+}$ ions. In the high $J$ limit however the $J / (J + 1)$ term approaches unity and the accuracy when using this equation is reduced.

By comparing this expression to the results of the rigorous calculation, the accuracy of using the expression for $c_m^{sat}$ to determine the value of either $J$ or $c_{m(peak)}$ has been determined as better than 10 % ($J$) or 2 % ($c_{m(peak)}$) at high temperatures ($\beta > 10$). At lower temperatures the deviation between approximate form and rigorous calculation increases, when $\beta \sim 2$ the error reaches approximately 50 % in calculating $J$ and approximately 10 % in calculating $c_{m(peak)}$.

A second expression has also been derived from the approximate form for $M(H,T)$, that relates the change in temperature of $c_{m(peak)}$ with applied field to the value of $g_J(J + 1)$ for the material:

$$\frac{\partial(\mu_0 H_{ext})}{\partial T_{peak}} = \frac{6.540}{g_J(J+1)}$$

The value of the constant in this equation is again chosen as an average value across the rare-earth series as determined from calculations using $Ce^{3+}$, $Gd^{3+}$ and $Dy^{3+}$ ions. Using this value of the constant $g_J(J + 1)$ tends to be underestimated in the high $J$ limit and overestimated in the low $J$ limit. This simple expression is independent of the fraction of the material that contributes to $c_m$, relying only on the positions of the peaks in $c_m$ and is therefore ideal for studying mixed phase samples or magnetic minority phases.

# *Chapter 5 –Measurement technique and experimental design.*

## 5.1 Introduction.

Specific heat measurements give a bulk response from a sample. The measured response has contributions from all the constituent parts of the material and so is ideal to study phase changes. Measurements can be made at any temperature, in magnetic fields and for any type or size of material providing appropriate considerations are taken into account, both in the experimental system and the measurement technique. The specific heat probe in Durham was originally developed by S. Ali [293] using the heat pulse and a.c. methods to measure the specific heat of superconductors in high magnetic fields. Limitations on the absolute accuracy using this probe and a new magnet insert with a smaller bore size, prompted the construction of a new probe using the relaxation and long range methods to perform the measurements.

Section 5.2 briefly outlines the heat pulse and a.c. techniques for specific heat measurement that were used in the original probe and provides examples of the data taken. In the new probe the relaxation method and long range pulse are used and the details of these techniques and the general principles of specific heat measurement are presented in section 5.3. The design and construction of the new probe is presented in 5.4, this takes into account sample size, the size limitations of the probe and the need for accurate temperature control. Calculations to determine the optimum working conditions for the probe are presented in section 5.5. The calibration and commissioning of the probe is detailed in section 5.6 using measurements on copper as a standard. The absolute accuracy of the data is established and the addenda contribution that has to be subtracted from all subsequent measurements is determined. The final operating procedure for the probe is outlined in section 5.7. This includes the mounting of the sample, the precooling conditions and the detailed running conditions for both relaxation and long range methods. The chapter is concluded in section 5.8.

## 5.2 Preliminary specific heat measurements.

The Durham specific heat probe was originally developed by S. Ali [293] using the *heat pulse* and *a.c.* non-adiabatic methods. Both techniques were run successively using the same sample and system to provide both accuracy (heat pulse) and sensitivity (a.c.).

### 5.2.1 Heat pulse method.

The heat pulse method, originally developed by Bachmann in 1972 [294], consists of applying a short heat pulse to the sample and then monitoring the temperature decay back to the original temperature. The decay curve is extrapolated back to give the maximum temperature rise ($\Delta T$) that would have occurred in adiabatic conditions. Using the definition in Eqn. (2.4), the heat capacity can then be determined:

$$C = \frac{\Delta Q}{\Delta T} = \frac{I^2 R_H \Delta t}{\Delta T} \tag{5.1}$$

where $I$ is the pulse current (A) through the heater of resistance $R_H$ ($\Omega$) and $\Delta t$ is the duration of the pulse (s). This method gives very accurate results provided that the characteristic time for the sample to thermally equilibrate is much smaller than the characteristic time for the heat leak away from the sample.

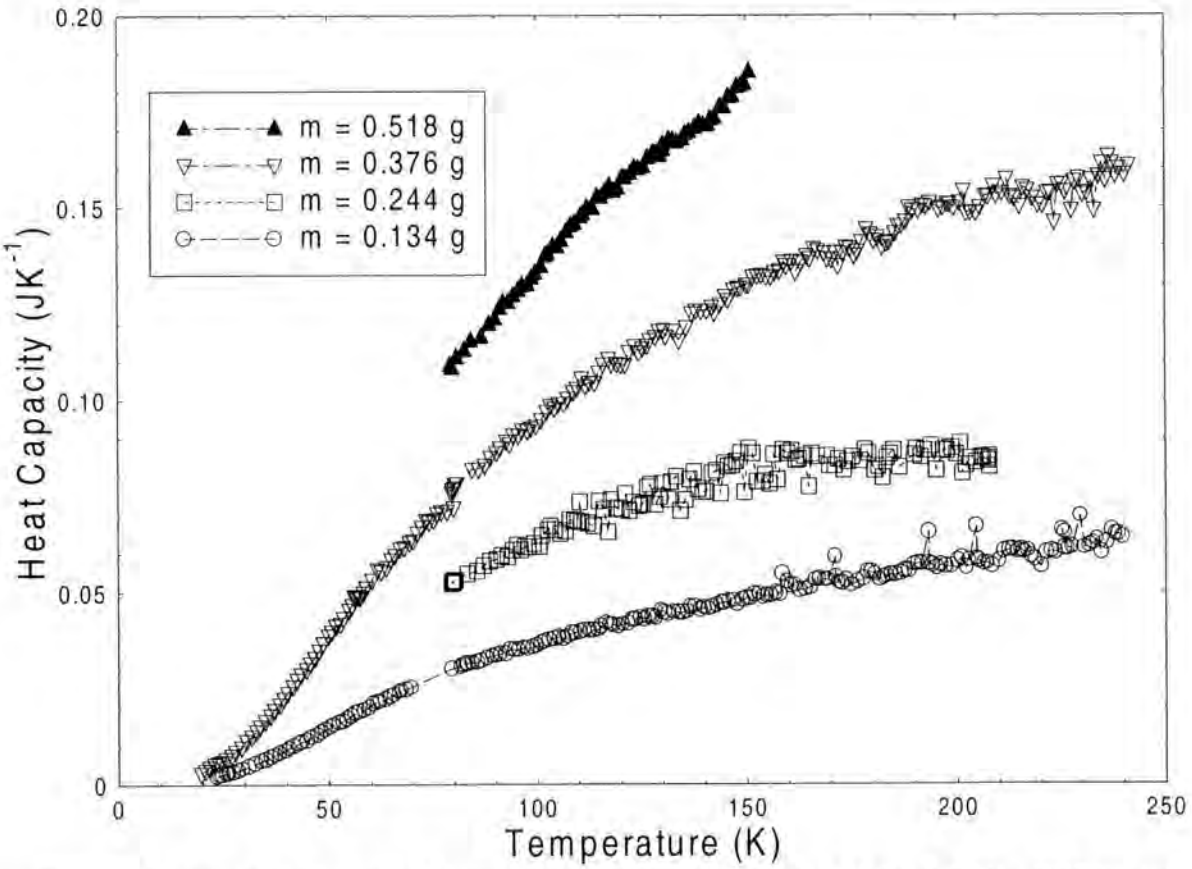


**Figure 1. Heat capacity of four copper samples, mass 0.134g, 0.244g, 0.376g and 0.518g as a function of temperature using the heat pulse method.**

Figure 1 shows the measurements taken on four copper samples of different masses from 10 K to 150 K from which the accuracy of the data were was determined as < 10% at 15 K and < 5 % at 150 K.

### 5.2.2 A.c. method.

The a.c. technique was developed by Sullivan and Seidel in 1968 [295] and is excellent for measuring very small changes in heat capacity. The technique uses a lock in amplifier to input an a.c. power at frequency $f$ and then to detect the subsequent temperature oscillation at the second harmonic. The heat capacity is then given by

$$C = \frac{\sqrt{2}}{8\pi f}\left(\frac{V_{in}^2}{R_H}\right)\frac{I_{thm}}{V_{rms}}\frac{dR_{thm}}{dT} \tag{5.2}$$

where $I_{thm}$ and $dR_{thm}/dT$ are the excitation current (A) and sensitivity ($\Omega K^{-1}$) of the thermometer respectively, $V_{in}$ and $R_H$ are the r.m.s. input voltage (V) and resistance ($\Omega$) of the heater and $V_{rms}$ is the measured a.c. voltage (V) across the thermometer.

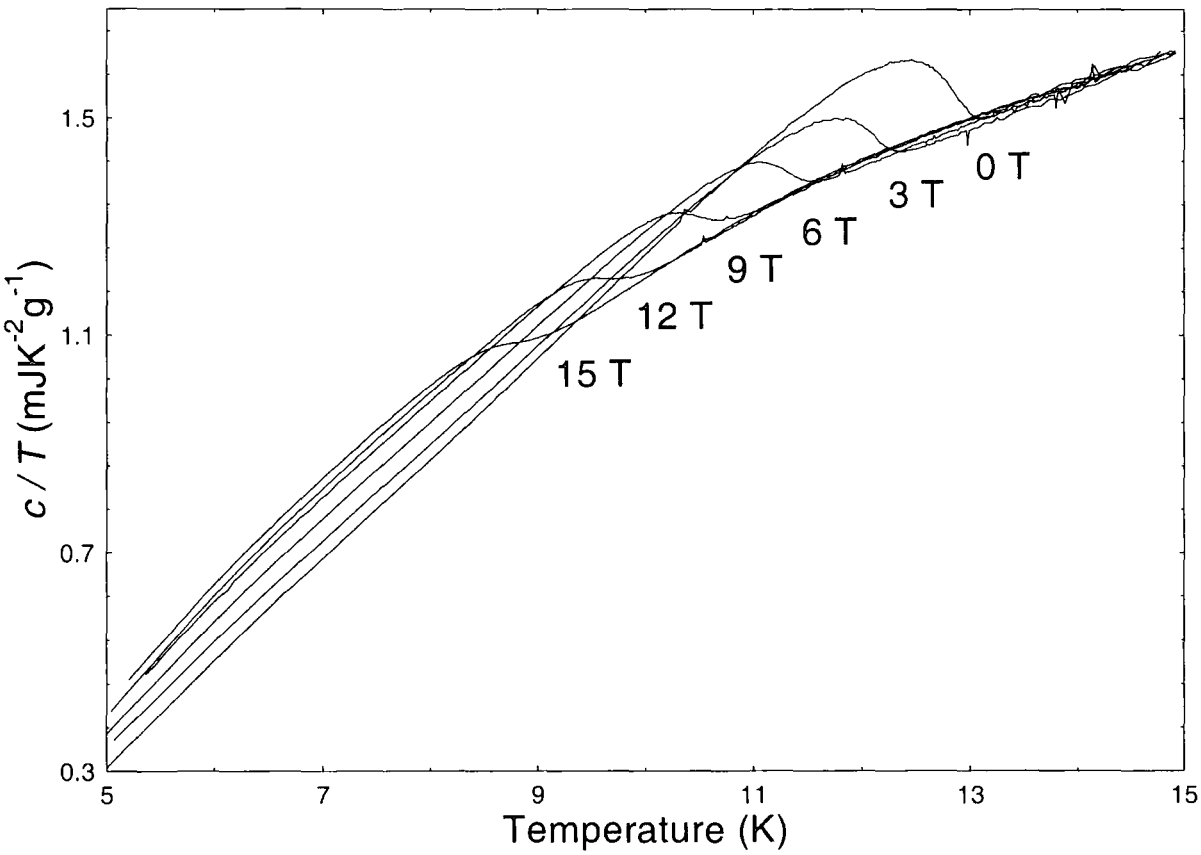


**Figure 2. Specific heat capacity divided by temperature, of $SnMo_6S_8$ as a function of temperature in applied magnetic fields up to 15 T.**

Figure 2 shows measurements taken on a sample of $SnMo_6S_8$ in magnetic fields up to 15 T. This technique gives superb resolution in the measurement of the heat capacity, however the absolute values differ from those of the heat pulse method by as much as 50 %. The use of smaller samples than in previous measurements [293] has increased the resolution but decreased the accuracy of the data.

### 5.2.3 Limitations of the original probe.

The advantage of using these two techniques is the combination of both accuracy and sensitivity. These preliminary measurements however, show that scaling of the a.c. traces onto those of the heat pulse method produces data with excellent sensitivity but insufficient accuracy (< 10 %) in the temperature range of interest. These techniques were therefore discarded and two different techniques employed.

## 5.3 Principles of specific heat measurement.

There are a number of established techniques to measure the specific heat of solids at low temperatures [296]. All of these techniques rely on the same measurement principle of applying heat energy into a sample and monitoring the temperature response. In order to make accurate measurements both the energy input and the subsequent temperature response needed to be precisely determined. Typically the heat energy is provided by joule heating of a resistance wire or a known semiconductor, thus requiring the resistance of the heater and the input current to be known. A thermometer

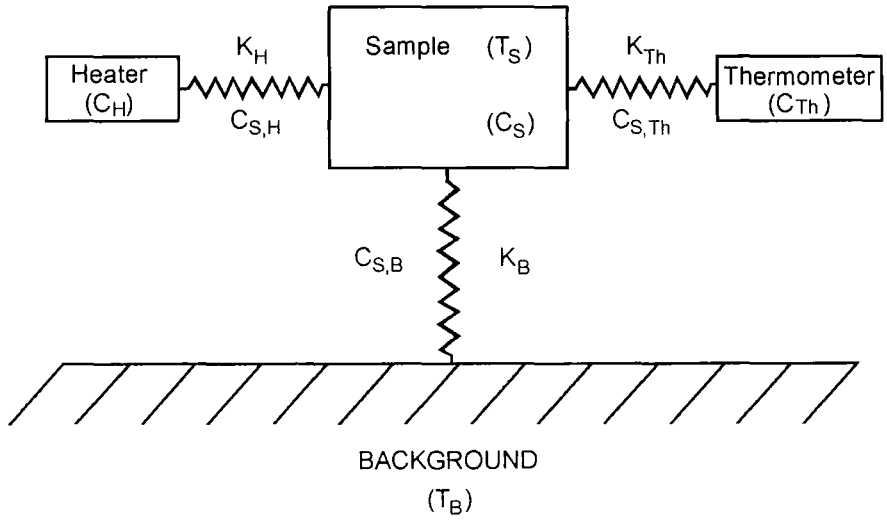


**Figure 3. Typical setup for non-adiabatic specific heat measurement.**

with sufficient sensitivity in the temperature range of interest and known magnetic field dependence is then used to monitor the temperature response.

Specific heat measurements require the sample to be isolated from the surroundings, typically by evacuating the sample chamber and minimising conduction paths to the sample [296]. This condition ensures that if the sample mass and the extra contributions to the measured heat capacity due to the system (addenda) are known, the specific heat of the material can be determined. Adiabatic methods of measuring the specific heat require total isolation from the surroundings but rely on heat switches to change the temperature of the sample and are less accurate for small samples.

Non-adiabatic methods are better suited to small samples [297] and have a weak thermal link from an otherwise isolated sample to a background of fixed temperature, as shown in Fig. 3. The thermal link allows the temperature of the sample to be altered and is normally well characterised. The samples we have measured have small heat capacities due to their size and so non-adiabatic methods have been employed.

In the previous section (5.2) the heat pulse and a.c. techniques were outlined. Efforts to improve the low temperature accuracy of the original probe using these two techniques were unsuccessful. Two other non-adiabatic methods, the *relaxation technique* and *long range method*, were therefore used to give the required accuracy and sensitivity.

### 5.3.1 Relaxation method.

The relaxation method is a variation of the heat pulse method [297]. The input power is incremented from a fixed value ($P_1$) corresponding to steady state temperature ($T_1$), to a higher value ($P_2$). The subsequent temperature rise to a secondary steady state temperature ($T_2$) is monitored giving a characteristic time constant that is a measure of the heat capacity of the sample.

In the measurement, the sample has a thermometer and heater attached to the sample as indicated in Fig. 3 and a thermal link to a background of fixed temperature ($T_B$) provided typically by a liquid cryogen. The thermal links between the sample and heater and the sample and thermometer are assumed to have a thermal conductivity much greater than the thermal link between the sample and background. If this condition is met, the sample, thermometer and heater can be considered to be in thermal equilibrium during the entire measurement.

At the start of the measurement the sample is in thermal equilibrium with its surroundings. The input power ($P_1$) required to keep the sample at temperature ($T_1$) is therefore equal to rate of heat loss to the surroundings ($dQ/dt$).

$$P_1 = \frac{dQ}{dt} \tag{5.3}$$

therefore

$$I_1^2 R_1 = \frac{\kappa A}{L}(T_1 - T_B) \tag{5.4}$$

where $I_0$ is the steady state current (A) through the heater, $R_1$ is the resistance ($\Omega$) of the heater at temperature $T_1$ and $\kappa$, $A$ and $L$ are respectively the thermal conductivity ($Wm^{-1}K^{-1}$), cross sectional area ($m^2$) and length (m) of the thermal link between the sample and the background.

On incrementing the input power (i.e. for an *up* pulse) the system is no longer in thermal equilibrium and the temperature of the system rises until the rate of heat loss is once more equal to the input power ($P_2$). From the definition of $C$ ($C = \Delta Q / \Delta T$ as $\Delta T \rightarrow 0$), if the temperature difference ($\Delta T_{21} = T_2 - T_1$) between the final and initial temperatures is small, so that $C$ does not vary appreciably over the temperature step we can make the approximation

$$C_{up} = \frac{\Delta Q}{\Delta T_{21}} \approx \frac{dQ}{dT} = \frac{dQ/dt}{dT/dt} \tag{5.5}$$

and therefore

$$C_{up}\frac{dT}{dt} = \frac{dQ}{dt} \tag{5.6}$$

The rate of heat loss of the system ($dQ/dt$) in non-equilibrium conditions is determined by the difference between the input power and the heat leak down the thermal link.

$$C_{up}\frac{dT}{dt} = I_2^2 R(T) - \frac{\kappa A}{L}(T - T_B(T)) \tag{5.7}$$

where we use $R(T)$ and $T_B(T)$ since the resistance of the heater is temperature dependent and the temperature of the background may drift during the measurement. If we take the temperature dependencies of $R(T)$ and $T_B(T)$ to be approximately linear over a small temperature region then we can make the following substitutions:

$$R(T) = R_1 + \Delta T\frac{\partial R}{\partial T} = R_1 + (T - T_1)\frac{\partial R}{\partial T} \tag{5.8}$$

$$T_B(T) = T_B + \Delta T\frac{\partial T_B}{\partial T} = T_B + (T - T_1)\frac{\partial T_B}{\partial T} \tag{5.9}$$

Using these expressions we can expand Eqn. (5.7) and define $P_1 = I_1^2 R_1$, $P^* = I_2^2 R_1$, $B = \kappa A / L$, $D = I_2^2 \, \partial R / \partial T$ and $E = \partial T_B / \partial T$.

$$C_{up} \frac{dT}{dt} = P^* + DT - DT_1 - BT + BT_B + BET - BET_1 \tag{5.10}$$

$$\Rightarrow \quad C_{up} \frac{dT}{dt} = -(B - E - BE)\left[ T - \left( \frac{P^* - DT_1 + BT_B - BET_1}{B - D - BE} \right) \right] \tag{5.11}$$

We can then rearrange this equation and assuming that $\partial R / \partial T$ and $\partial T_B / \partial T$ are constant over the small temperature increment, we can integrate from $T = T_1$ to $T$ and from $t = 0$ to $t$.

$$ln\left[ \frac{T(B - D - BE) - (P^* - DT_1 + BT_B - BET_1)}{T_1 B - P^* - BT_B} \right] = \frac{-(B - D - BE)}{C} t \tag{5.12}$$

From Eqn. (5.4) we know that in steady state conditions $P_1 = B\,(T_1 - T_B)$. Substituting this into the denominator in Eqn. (5.12) and rearranging we find the time dependence of the temperature of the sample.

$$T(t) = \left( \frac{P^* - DT_1 + BT_B - BET_1}{B - D - BE} \right) - \left( \frac{P^* - P_1}{B - D - BE} \right) exp\left[ -\frac{(B - D - BE)}{C_{up}} t \right] \tag{5.13}$$

Defining the characteristic time constant of the exponential decay ($\tau_{up}^{sys}$) as

$$\tau_{up}^{sys} = \frac{C_{up}}{(B - D - BE)} = \frac{C_{up} L}{\kappa A}\left[ 1 - \left( \frac{L}{\kappa A} \right) I_2^2 \frac{\partial R}{\partial T} - \frac{\partial T_B}{\partial T} \right]^{-1} \tag{5.14}$$

We can rewrite Eqn. (5.13) more simply.

$$T(t) = \frac{\tau_{up}^{sys}}{C_{up}}(P^* - DT_1 + BT_B - BET) - \frac{\tau_{up}^{sys}}{C_{up}}(P^* - P_1) exp\left[ -\frac{t}{\tau_{up}^{sys}} \right] \tag{5.15}$$

The boundary conditions imply that when $t \rightarrow \infty$ then $T\,(t \rightarrow \infty) \rightarrow T_2$,

$$\Rightarrow \quad T_2 = \frac{\tau_{up}^{sys}}{C_{up}}(P^* - DT_1 + BT_B - BET_1) \tag{5.16}$$

and similarly when $t = 0$, $T\,(t = 0) = T_1$,

$$\Rightarrow \quad T_1 = \frac{\tau_{up}^{sys}}{C_{up}}(P^* - DT_1 + BT_B - BET_1) - \frac{\tau_{up}^{sys}}{C_{up}}(P^* - P_1) \tag{5.17}$$

Substituting Eqn. (5.16) into (5.17)

$$T_1 = T_2 - \frac{\tau_{up}^{sys}}{C_{up}}(P^* - P_1) \tag{5.18}$$

and we can then determine the heat capacity of the sample from Eqn. (5.18).

$$C_{up} = \frac{(P^* - P_1)\tau_{up}^{sys}}{\Delta T_{21}} = \frac{(I_2^2 - I_1^2)R_1\tau_{up}^{sys}}{\Delta T_{21}} \tag{5.19}$$

Performing the same calculation for a *down* pulse (i.e. $P_2 \rightarrow P_1$ and $R_2 \rightarrow R_1$) and defining $P^{**} = I_1^2 R_2$, we obtain the result:

$$C_{down} = \frac{(P_2 - P^{**})\tau_{down}^{sys}}{\Delta T_{21}} = \frac{(I_2^2 - I_1^2)R_2\tau_{down}^{sys}}{\Delta T_{21}} \tag{5.20}$$

where $$\tau_{down}^{sys} = \frac{C_{down}}{(B + D - BE)} = \frac{C_{down}L}{\kappa A}\left[1 + \left(\frac{L}{\kappa A}\right)I_1^2\frac{\partial R}{\partial T} - \frac{\partial T_B}{\partial T}\right]^{-1} \tag{5.21}$$

Since the heat capacity is independent of the measurement we have $C_{up} = C_{down}$. However, experimental error in the determination of $\tau^{sys}$ and $R$ can produce different values of $C$ from an up and down pulse over the same temperature increment and so at least one up and one down pulse need to be measured to give an average value of $C$.

$$C_{avg} = \frac{(I_2^2 - I_1^2)R_1\tau_{up}^{sys}}{\Delta T_{21}} + \frac{(I_2^2 - I_1^2)R_2\tau_{down}^{sys}}{\Delta T_{21}} = \frac{(I_2^2 - I_1^2)}{\Delta T_{21}}\frac{(R_1\tau_{up}^{sys} + R_2\tau_{down}^{sys})}{2} \tag{5.22}$$

So assuming that $\partial R / \partial T$ and $\partial T_B / \partial T$ are linear over a small temperature increment, the characteristic exponential rise or decay in temperature can be analysed to give both the time constant of the system to the background and the heat capacity of the system.

Using the relaxation method an accuracy of better than 1% can be achieved for small samples. Optimised results are produced when the temperature step is small and the characteristic time constant for the sample to reach thermal equilibrium is much faster than the system time constant, defined in Eqn. (5.14).

### 5.3.2 Long range method.

This method was introduced by Forgan et al in 1980 [298] and provides a continuous measurement of the heat capacity in contrast to the relaxation method that produces discrete points. The method is similar to the small step relaxation method but a much larger temperature step, of 5 - 10 Kelvin, is used. The sample is held in thermal equilibrium at a temperature ($T_1$) by an input power ($P_1$). The input power is then reduced by a large amount to a secondary value ($P_2$) and the corresponding temperature decay is measured. The heat capacity and thermal conductivity of the thermal link are no longer constant

during the measurement, so we consider a point in time during the temperature decay and construct the equation for the heat loss from the system.

$$\frac{dQ}{dt} = C(T)\frac{dT}{dt} = -\frac{A\kappa(T)}{L}(T - T_B(T)) + I_2^2 R(T) \tag{5.23}$$

In this situation the rate of heat loss down the thermal link is greater than the power input from the heater. Rearranging Eqn. (5.20) we have an equation for the temperature dependence of the heat capacity of the sample.

$$C(T) = -\frac{dt}{dT}\left[\frac{A\kappa(T)}{L}(T - T_B(T)) - I_2^2 R(T)\right] \tag{5.24}$$

The ratio $dt/dT$ is determined from the measured temperature decay curve, the term $I_2^2R(T)$ is determined by the equivalent resistance decay curve and the term $(A\kappa(T) / L)(T - T_B(T))$ is determined in thermal equilibrium from the input power (Eqn. (5.4)). During the small step relaxation method, the sample is in thermal equilibrium at the start of each measurement and so provides a calibration of the heat loss as a function of temperature.

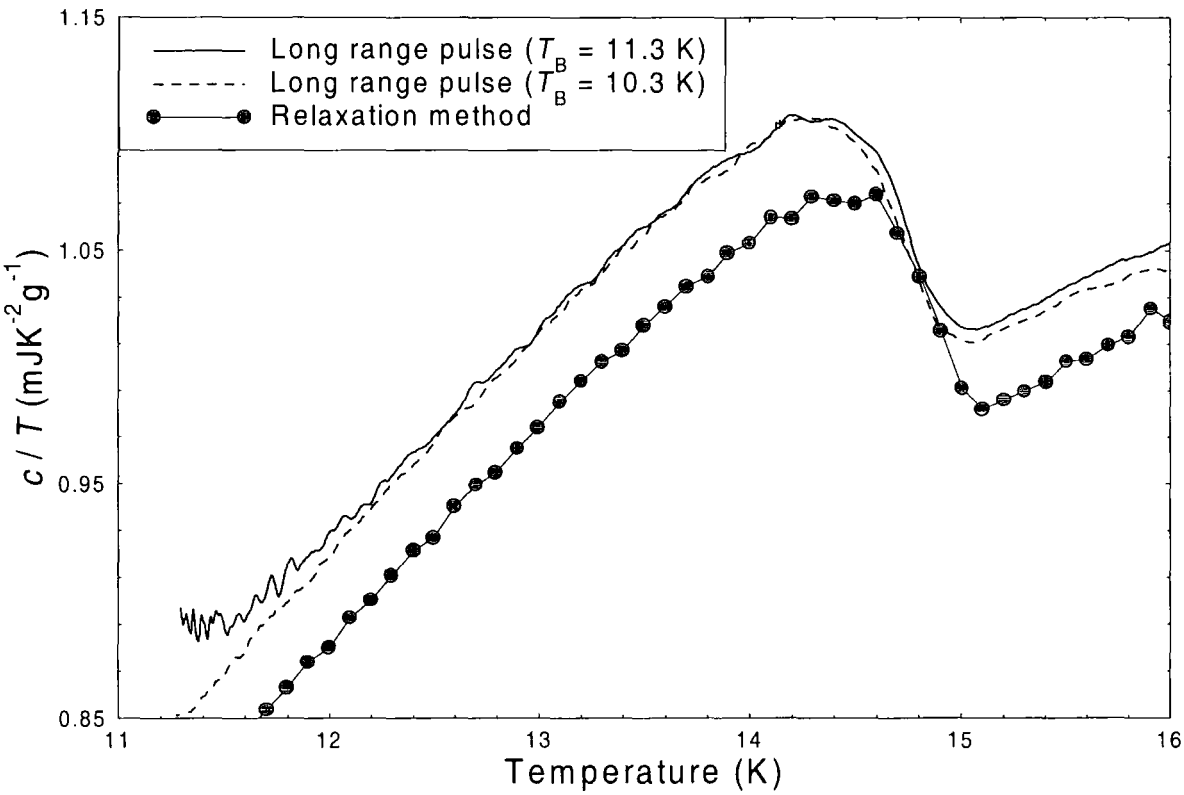


**Figure 4. $c$ / $T$ as a function of temperature for $PbMo_6S_8$ in zero applied field measured by the relaxation method and long range pulse technique with different base temperatures ($T_B$).**

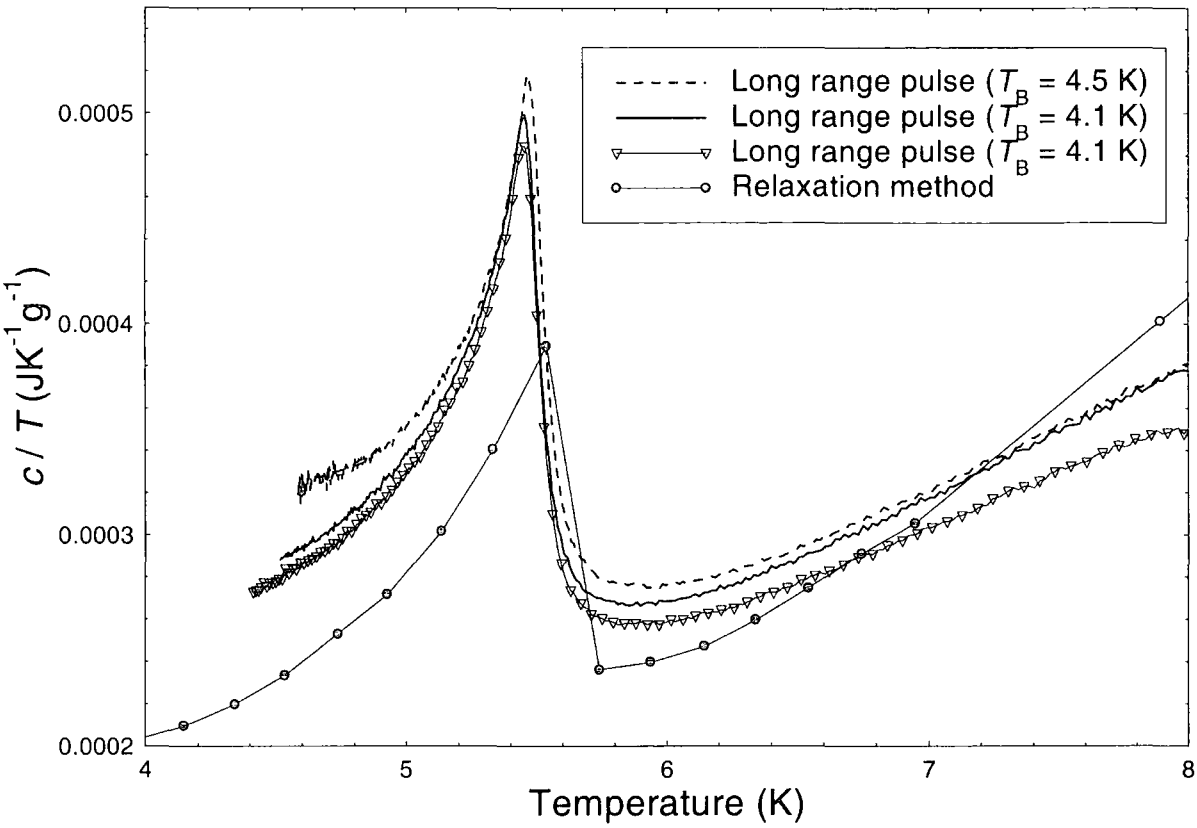


**Figure 5.** ***c / T*** **as a function of temperature for $(Pb_{0.90}Gd_{0.10})Mo_6S_8$ in zero applied field, measured by the relaxation method and long range pulse technique with different base temperatures ($T_B$).**

Curve fitting this calibration curve then produces a continuous measure of the value of $(A\kappa(T) / L)(T - T_B(T))$ or equivalently of $P_1(T) = I_1^2R(T)$. The advantage of this method is that the background temperature ($T_B$) does not need to be determined and the ratio of $A\kappa(T) / L$ is accurately determined *in situ* providing the two methods are run successively.

The long range method gives a continuous readout of the heat capacity and is therefore a very sensitive method for studying small or sudden changes in $C$. The accuracy of this method however, is dependent on the previously measured relaxation method and an appropriate curve fitting of the point by point calibration for $P_1(T)$.

### 5.3.3 Comparison between techniques.

Figures 4 and 5 show a comparison between the long range pulse and the relaxation method. The data in Fig. 4 are taken on a sample of $PbMo_6S_8$ and show the superconducting transition at about 15 K, whereas the data in Fig. 5 show the magnetic transition of a sample of $(Pb_{0.90}Gd_{0.10})Mo_6S_8$ at about 5.5 K. The accuracy of the relaxation

method at ~ 1 % is well documented, however the need for an accurately determined temperature step during the measurement limits the temperature resolution to about 100 mK. Figures 4 and 5 show that the long range method has a better temperature resolution of about 10 mK but the magnitude of the specific heat values are accurate to only 20 %.

The data taken using the long range pulse in Fig. 4 differ from the relaxation method in both the magnitude of the specific heat values and the temperature of the specific heat transition. We attribute this difference to an uncertainty in the term $T_B(T)$ in the equation for the specific heat of the long range method. Changes in the background temperature during the course of the measurement are unlikely to be the same in both the dynamic (long range) and steady state (relaxation) regimes as assumed in the derivation of $C$ for the long range method. Figure 5 however, shows long range data that are measured over a temperature range much closer to the background temperature and exhibit a much smaller temperature error compared to the relaxation data. This indicates that the change in the background temperature ($T_B(T)$) is much smaller at 5.5 K than that at temperatures above 10 K and is similar to the steady state regime.

Measurements taken using the long range pulse with different base temperatures, as shown in Fig,'s 4 and 5, produce data with slightly different values of both the heat capacity and the temperature of the prominent features. The difference in heat capacity is attributed to small changes in the background temperature from one pulse to another and the difference in temperature is attributed to the rate at which the temperature of the system is changing at that point. The temperature of the features in the long range pulse data in both Fig.'s 4 and 5, is closer to the data in the steady state measurement when the base temperature is higher and the temperature of the system is then not changing as rapidly. We suggest that the most accurate measurements are therefore taken with a base temperature that is as close as possible to the temperature region of interest.

The long range method is therefore a useful technique for determining the temperature of magnetic or superconducting transitions but only over small temperature ranges close to the background. The temperature resolution of this technique is much better than the relaxation method, however the accuracy of the specific heat values is significantly worse.

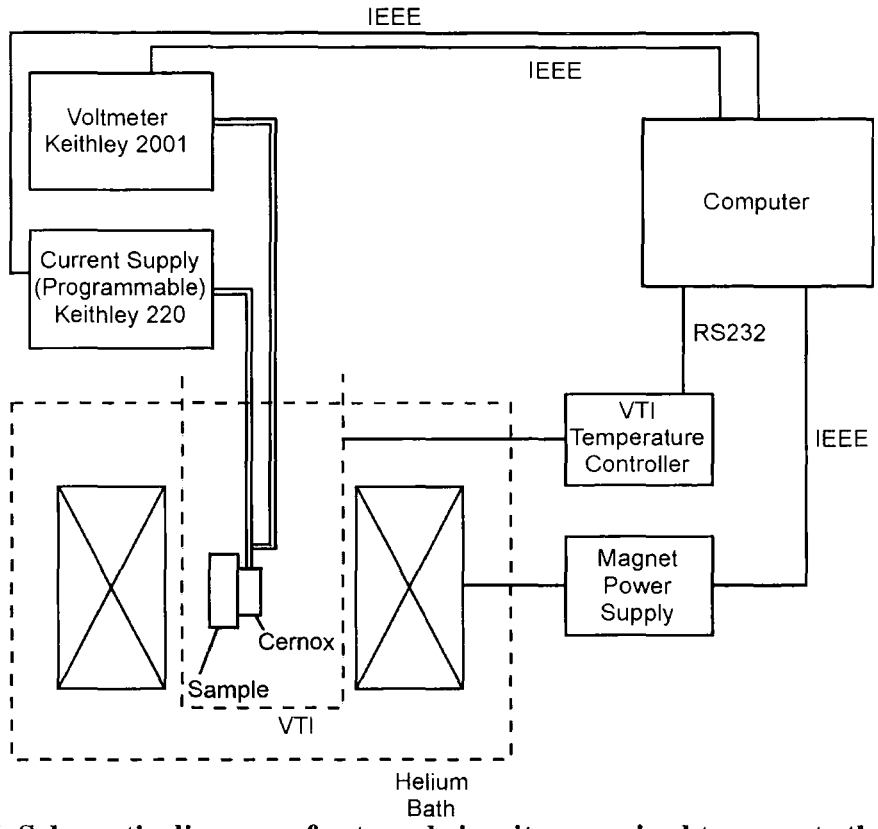


**Figure 6. Schematic diagram of external circuitry required to operate the $c_p$ probe.**

## 5.4 Construction of a specific heat probe.

This section describes the design and construction of a probe to measure the specific heat capacity of type II superconductors at low temperatures and in high magnetic fields. The high field magnet system at Durham is a 15 / 17 T superconducting magnet into which a *variable temperature insert* (VTI) is placed that allows temperatures from 1.6 K to 300 K to be reached. The VTI has a sealed sample space that contains either liquid or gaseous $^4$He under reduced pressure to control the temperature and an internal diameter of 12.65 mm in the magnet space. The specific heat measurements of superconducting materials are to be performed up to temperatures of 30 K.

### 5.4.1 External circuitry.

A schematic diagram of the external circuitry required to operate the system is shown in Fig. 6. All the electronic components of the system are computer controlled using the programming language ASYST. IEEE interfaces are used to connect the computer to each of the components except the VTI temperature controller that is connected using an RS232 interface. The superconducting magnet is controlled by an OXFORD IPS 120-10

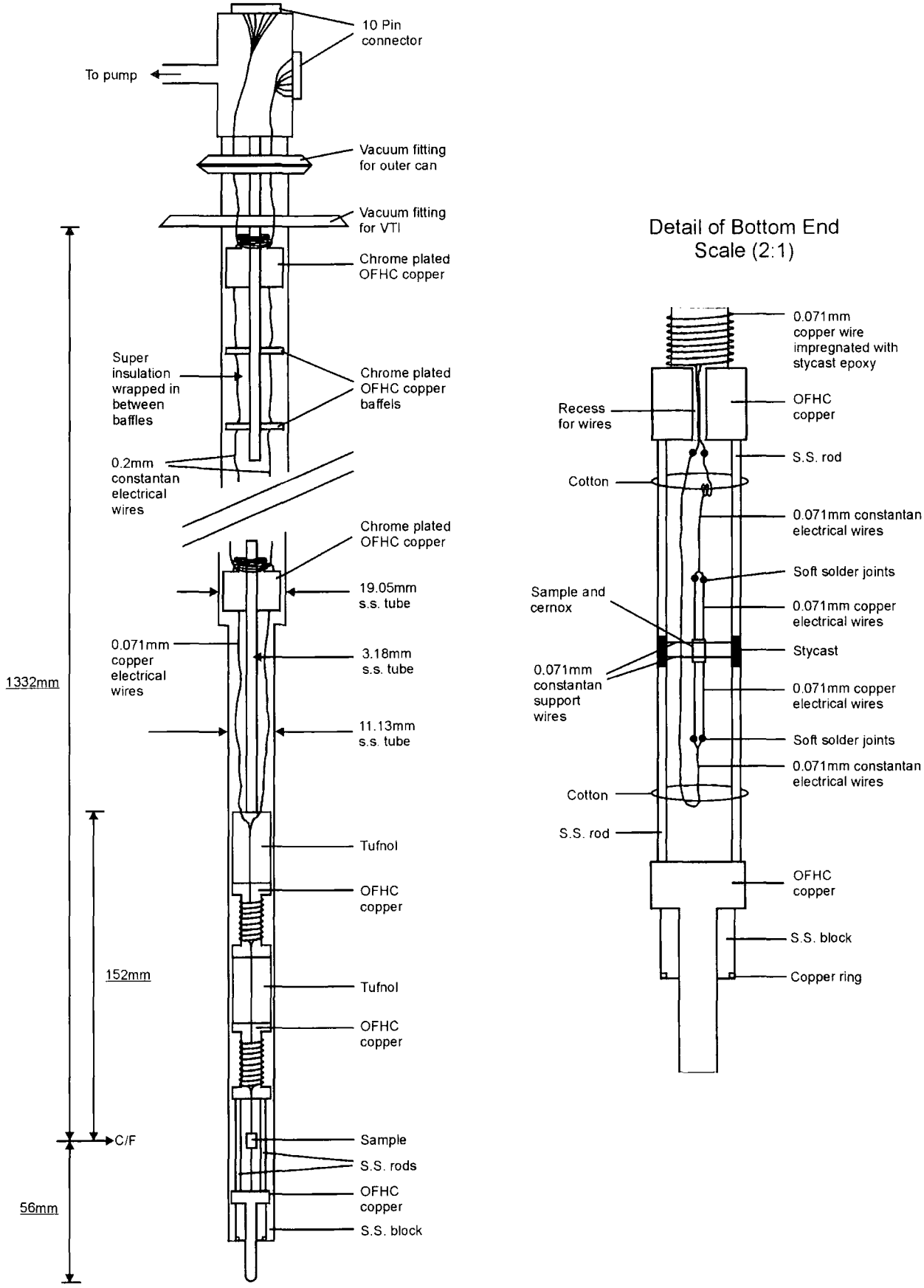


**Figure 7. Schematic diagram of the $c_p$ probe including detail of the bottom end.**

programmable power supply and the VTI temperature is controlled by an OXFORD ITC-502 temperature controller. The measurement simply consists of a Keithley 220 programmable current source to input the thermometer/heater current and a Keithley 2000 digital multimeter to read the voltage across the thermometer.

### 5.4.2 Probe design.

A schematic diagram of the specific heat probe is shown in Fig. 7. The lower part of the probe is encased by a thin walled stainless steel tube of outer diameter 11.13 mm, wall thickness 0.20 mm and length 322 mm. This is attached above the magnet space to a wider tube of outer diameter 19.05 mm, wall thickness 0.25 mm and length 1048 mm. The two tubes are hard soldered together producing a leak tight outer can that slides over the probe and is sealed to a vacuum fitting for the outer can at the top of the probe and a soft solder seal to the lower end. A single vacuum fitting for the VTI system is hard soldered on to the outside of this can and a valve at the top end of the probe can be connected to a vacuum pump and enables the internal pressure to be controlled. A third tube of outer diameter 3.18 mm is used as the central support for the probe and is hard soldered to the top section that contains the valve for the vacuum pump and electrical 10-pin connectors. To minimize convection and radiation leaks down the length of the probe, chrome plated *oxygen-free-high-conductivity* (OFHC) copper baffles are placed at regular intervals along the length of the central tube and super-insulation is wrapped in between them. Four chrome plated OFHC copper blocks are interspersed down the length of the central tube to act as heat sinks for the electrical wires. These electrical wires which are connected by soft solder joints at the top and bottom of the probe, provide a direct conduction path and are therefore the dominant source of heat leak down the probe. To minimize this heat leak thin (0.2 mm diameter) constantan wires are used rather than copper wires that have a much higher thermal conductivity. The wires are wrapped many times around each chrome plated OFHC copper heat sink to lower their temperature.

The bottom end of the probe consists of the measurement system (sample and thermometer/heater) the background and a thermal link between the two. The background of the system needs to be stable at the external temperature set in the VTI. Two OFHC copper blocks surround the measurement space and are joined together by two stainless steel rods, hard soldered at either end, to provide strength. Both rods are then lined with a thick copper wire (1.5 mm diameter) that is also soldered at either end to thermally connect

the two copper blocks. Both rod and wire are wrapped in kapton insulating tape to prevent heat leaks if they come in contact with the electrical wires. The upper copper block is joined by grub screws to successive tufnol blocks to reduce conduction and additional OFHC copper blocks to act as heat sinks for the electrical wires. The OFHC copper block at the bottom of the probe has a tail that sticks out of the end of the probe and is then directly immersed in the liquid or gaseous cryogen. The lower end is vacuum sealed by a soft solder joint between two thin copper rings that are hard soldered onto the end of the outer can and onto a stainless steel block that is also hard soldered on to the tail piece.

The constantan electrical wires from the upper part of the probe are joined to thin (0.071 mm diameter) copper wires in the region where the outer diameter of the can is reduced. To ensure that the wires are thermally sunk to the background they are wrapped many times around each of the two OFHC copper blocks directly above the measurement space and then impregnated with a stycast epoxy. All the wires in the probe are twisted in pairs to minimize electrical pickup.

The measurement system consists of a sample that is glued to two support wires on one side and then has the thermometer/heater chip glued to the opposite side. Thin constantan wires (0.071 mm diameter) of length 30 mm provide the electrical contact to the chip while maintaining high thermal resistance between the sample and background. These constantan wires are held in suspension by cotton wrapped around the stainless steel rods on either side. They connect the copper wires already epoxyed to the upper OFHC copper block to copper contacts that are joined by silver loaded epoxy to the chip surface. Two additional constantan wires (0.071 mm diameter) support the sample and are thermally sunk to the thick copper wires that line the stainless steel rods by stycast epoxy. The typical length of constantan wire between the edges of the sample and the background is about 2 mm, much smaller than the length of the thermal link provided by the electrical connections. Altering the length of the support wire between sample and background then determines the time constant of the measurement.

### 5.4.3 Temperature control.

The sample temperature is controlled by a double Cernox thermometer mounted on a single sapphire chip provided by Lake Shore Cryotronics. The chip has two semi-conducting resistors deposited on its surface, one used as a heater and one as a thermometer. Alternatively just one side of the chip can be used, acting as both

thermometer and heater. Cernox resistors have a large temperature dependent resistance (~ 900 Ω at 4.2 K) and sensitivity (~ 190 $\Omega K^{-1}$ at 4.2 K) at low temperatures making them ideal for low temperature measurement. A standard four terminal resistance measurement is used to measure the resistance and therefore temperature of the chip and the self-heating of the chip is used as the heater for the measurement. The resistance of these Cernox thermometers is relatively field-independent, typical measurements show a temperature error of less than 20 mK in magnetic fields up to 15 T and for temperatures up to 30 K [299].

### 5.4.4 Sample size and mounting.

The sample size depends on the heat capacity and thermal conductivity of the material to be measured. The largest size of sample that can fit in the available space is 6mm x 3mm x 3.5mm. For high accuracy measurements the heat capacity of the addenda should be a small fraction of the sample to be measured. Larger samples are therefore preferred but the time constant of the measurement is then also longer. A reasonable compromise is that the heat capacity of the sample should be at least twice that of the addenda.

To attach both the thermometer and the support wires to the sample General Electric (GE) varnish is used. This glue has excellent low temperature properties and cures at room temperature in about 3 hours. Unfortunately it has a specific heat capacity about 30 times larger than copper at low temperatures and so the amount of varnish used in each measurement must be consistent as it forms a significant part of the addenda.

## 5.5 Calculations of thermal properties of the probe.

When designing the specific heat probe, consideration has to be taken of the thermal properties of the materials to be used in construction. In sections where the heat leak or temperature stability is important then the relative thermal conductivity of the materials used has to be taken into account. Similarly when constructing the sample holder and surroundings of the measurement system, the heat capacity of the addenda should be a small fraction of the heat capacity of the sample.

| Material | Thermal Conductivity ($Wm^{-1}K^{-1}$) | | |
|---|---|---|---|
| | 4.2 K | 10 K | 30 K |
| Copper | 400 – 6000 | 900 – 10500 | 1020 – 3000 |
| Constantan | 0.92 | 3.3 | 12 |
| GE Varnish | 0.064 | 0.076 | 0.15 |
| Cotton/Nylon | 0.011 | 0.032 | 0.25 |
| Stainless Steel | 0.24 | 0.70 | 3.3 |
| Apiezon N grease | 0.095 | N/A | N/A |
| Sapphire | 65 – 130 | 500 – 1400 | 4000 – 10000 |

**Table 1. The thermal conductivity of various technological materials at 4.2 K, 10 K and 30 K from reference [300]. Where a range of values is indicated the material can come in a variety of forms each with a different thermal conductivity.**

| Material | Specific Heat Capacity ($mJK^{-1}g^{-1}$) | | | |
|---|---|---|---|---|
| | 4.2 K | 10 K | 30 K | 77 K |
| Copper (a) | 0.101 | 0.873 | 26.5 | 190 |
| $PbMo_6S_8$ (b) | 0.24 | 5.3 | 35 | 122 |
| Constantan (c) | 1.12 (Ho) / 0.52 | 1.69 | 21.6 | 175 |
| GE Varnish (d) | 3.17 | 24.4 | 160 | 500 |
| Apiezon N grease (e) | 2.4 | 24 | 176 | 541 |
| Cotton/Nylon (f) | 1.47 | N/A | N/A | N/A |
| Sapphire (g) | ~ 0.038 | 0.089 | 2.6 | 62.0 |

**Table 2. The specific heat capacity of various technological materials at 4.2 K, 10 K, 30 K and 77 K, from (a) [301] and [302] (77 K), (b) [183] and [43] (77 K), (c) [303] (4.2 K) and [304], (d) [305], (e) [306], (f) [307], (g) [308].**

Tables 1 and 2 provide an idea of the relative values of the thermal conductivity and specific heat of most of the materials used in the construction of the probe. Data for Tufnol was not available but it is known to be a poor thermal conductor and for $PbMo_6S_8$ a thermal conductivity similar to most ceramics is assumed of $< 1$ $WK^{-1}m^{-1}$ up to 30 K. From the

above data predictions can be made of some of the operating parameters that are necessary to run the probe successfully, allowing further optimisation of the probe design.

### 5.5.1 Internal time constants of the materials.

High accuracy specific heat data can be achieved using the relaxation method providing the measured temperature rise / decay is representative of the whole sample. If the sample is too large or has a very poor thermal conductivity then the temperature in the region of the thermometer will not be the same as that on the opposing side of the sample where the thermal link to the background is positioned. This kind of distribution in temperature can introduce large errors into the measurement especially in the region of phase transitions.

We consider a rectangular block of material with heat capacity $C^*(T)$, cross section $A^*$, thickness $L^*$, and thermal conductivity $\kappa^*(T)$. If the heat input is on one side of the sample then the characteristic time ($\tau^*$) for the thermal energy to reach the opposite side and the sample to reach thermal equilibrium is given from standard thermodynamic texts:

$$\tau^* = \frac{C^*(T)L^*}{\kappa^*(T)A^*} = \frac{c^*(T)L^{*2}\rho^*}{\kappa^*(T)} \qquad (5.25)$$

| Material | Density ($gm^{-3}$) | $\tau^*$ (internal time constant) (s) | | |
|---|---|---|---|---|
| | | 4.2 K | 10 K | 30 K |
| Copper | $9.0 \times 10^6$ | $1.4 - 20 \times 10^{-6}$ | $6.7 - 78 - \times 10^{-5}$ | $7.1 - 21 \times 10^{-4}$ |
| Constantan | $8.9 \times 10^6$ | 0.098 | 0.15 | 0.14 |
| $PbMo_6S_8$ | $6.1 \times 10^6$ | ~ 0.01 | ~ 0.30 | ~ 2.0 |
| Sapphire | $4.0 \times 10^6$ | $1.1 - 2.2 \times 10^{-5}$ | $2.3 - 6.4 \times 10^{-6}$ | $0.93 - 2.3 \times 10^{-5}$ |
| *System time constant* ($\tau^{sys}$) | - | ~ 6.0 | ~ 23 | ~ 36 |

**Table 3. Calculated internal time constants for copper, constantan, $PbMo_6S_8$ and sapphire from Eqn. (5.25). A length of 3 mm is used, a density as indicated in the table (values at room temperature [309]) and values of $c(T)$ and $\kappa(T)$ from tables 1 and 2. Also included are typical values of the system time constant ($\tau^{sys}$) from measurements on $PbMo_6S_8$.**

where $c^*(T)$ is the specific heat capacity of the material and $\rho^*$ is the density. The 'internal time constant' ($\tau^*$) of a material at temperature $T$ can therefore be calculated for a sample of given dimensions if the specific heat, thermal conductivity and density are known.

Accurate measurements are obtained when all of the constituent parts of the system reach thermal equilibrium on a much faster time scale than the rate of heat loss during the measurement ($\tau^{sys}$). This means that the sample, support wires and chip should all have values of $\tau^* << \tau^{sys}$. Typical values of $\tau^{sys}$ from measurements on $PbMo_6S_8$ are presented in table 3 and are much longer than the calculated values of $\tau^*$, for each part of the system, that are also quoted in the table. Furthermore, we can then define conditions for $\tau^{sys}$ to obtain good measurement accuracy, i.e. $\tau^{sys} >> 0.01$ s at 4.2 K, $\tau^{sys} >> 0.3$ s at 10 K and $\tau^{sys} >> 2$ s at 30 K.

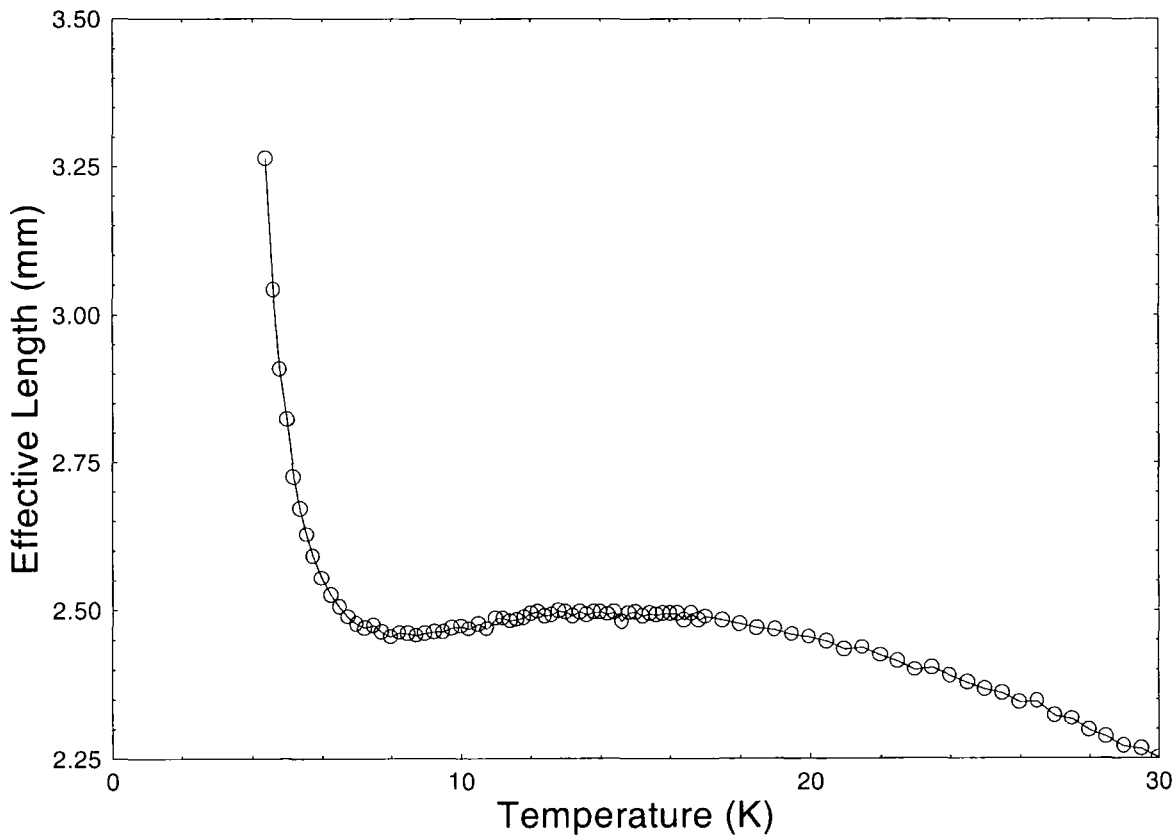


**Figure 8. Effective length calculated from Eqn. (5.26) as a function of temperature, from measurement of the heat capacity of a $PbMo_6S_8$ sample, using the relaxation method.**

### 5.5.2 Time constants of the support wires.

The two constantan support wires provide not only mechanical stability but also a means of controlling the thermal link to the background. With two wires lying across the sample we have four thermal links of identical cross section, thermal conductivity and virtually identical length. The electrical wires provide another four thermal links also of identical cross section and thermal conductivity to the support wires but of much greater length, ~ 30 mm compared to ~ 2 mm for the support wires. Using Eqn. (5.14) we can calculate the effective length of the thermal link from the sample to the background for an 'up' pulse.

$$L_{\text{eff}} = \kappa(T)A\left(\frac{\tau_{\text{up}}^{\text{sys}}(T)}{C_{\text{up}}(T)}\right)_{\text{exp}}\left[1-\frac{\partial T_{\text{B}}}{\partial T}\right]\left[1-I_2^2\frac{\partial R}{\partial T}\left(\frac{\tau(T)}{C(T)}\right)_{\text{exp}}\right]^{-1} \qquad (5.26)$$

The value of $I_2^2$ and the ratio $\tau_{\text{up}}^{\text{sys}}(T)/C_{\text{up}}(T)$ can be determined at each temperature $T$ by the results from the relaxation method, $\partial R / \partial T$ is calculated from the thermometer calibration, $\kappa(T)$ is taken from reference [300] and $A$ = 4 x ($\pi(0.035\text{x}10^{-3})^2$) m$^2$. The value of $\partial T_{\text{B}} / \partial T$ can not be calculated so we initially take it to be only a small correction and set $\partial T_{\text{B}} / \partial T \approx 0$.

Figure 8 shows the calculated values of $L_{\text{eff}}$ using Eqn. (5.26) and ignoring the (1- $\partial T_{\text{B}} / \partial T$) correction, where $\tau^{\text{sys}} / C$ is determined from measurement of the heat capacity of a $PbMo_6S_8$ sample, using the relaxation method. It can be seen from the graph that the calculated effective length is only marginally longer than the measured length of the support wires, these results confirm that the term $\partial T_{\text{B}} / \partial T$ constitutes only a small correction and so can be neglected. The reason for a larger calculated value could be due to the fact that there will also be some heat leak down the longer electrical wires. The average length of the thermal link will therefore be a weighted average of both thermal links. Since the calculated length is in reasonable agreement with a direct measurement we can conclude that the constantan wires do provide the main source of heat leak from the sample. Other methods of heat transfer such as gas conduction or radiation leaks are not significant and we can therefore directly control the heat leak by the type and size of wires used.

### 5.5.3 Negligible radiation effect.

When the sample is at a temperature higher than the background thermal energy will escape from the sample by conduction, convection and radiation. Heat leaks by convection

and radiation are very difficult to quantify and measure. Convection is minimised in the probe by evacuating the probe before cooling but heat transfer by radiation remains. For a sample in thermal equilibrium the heat leak due to radiation ($P_{rad}$) can be calculated from the Stefan-Boltzmann law and similarly the heat leak by conduction ($P_{cond}$) from the input power.

$$P_{rad} = e\sigma A\left(T^4 - T_B^4\right)$$
$$P_{cond} = I^2 R_H \qquad (5.27)$$

where $e$ is the emissivity ($0 \leq e \leq 1$) and $\sigma$ is Stefans constant ($\sigma = 5.67\text{x}10^{-8}$ $Wm^{-2}K^{-4}$). Typical values at 15 K are $I = 1$ mA, $R_H = 300\ \Omega$, $A = 8\text{x}10^{-6}$ $m^2$ and taking a maximum value for $e$ as 1 gives $P_{rad} = 2.3\text{x}10^{-8}$ W and $P_{cond} = 3.0\text{x}10^{-4}$ W. These results clearly show that any heat leak due to radiation is negligible compared to those by conduction.

## 5.6 Probe calibration.

Commissioning the probe requires the optimum working conditions of the probe to be established. The addenda contribution to the measured heat capacity must be measured as a

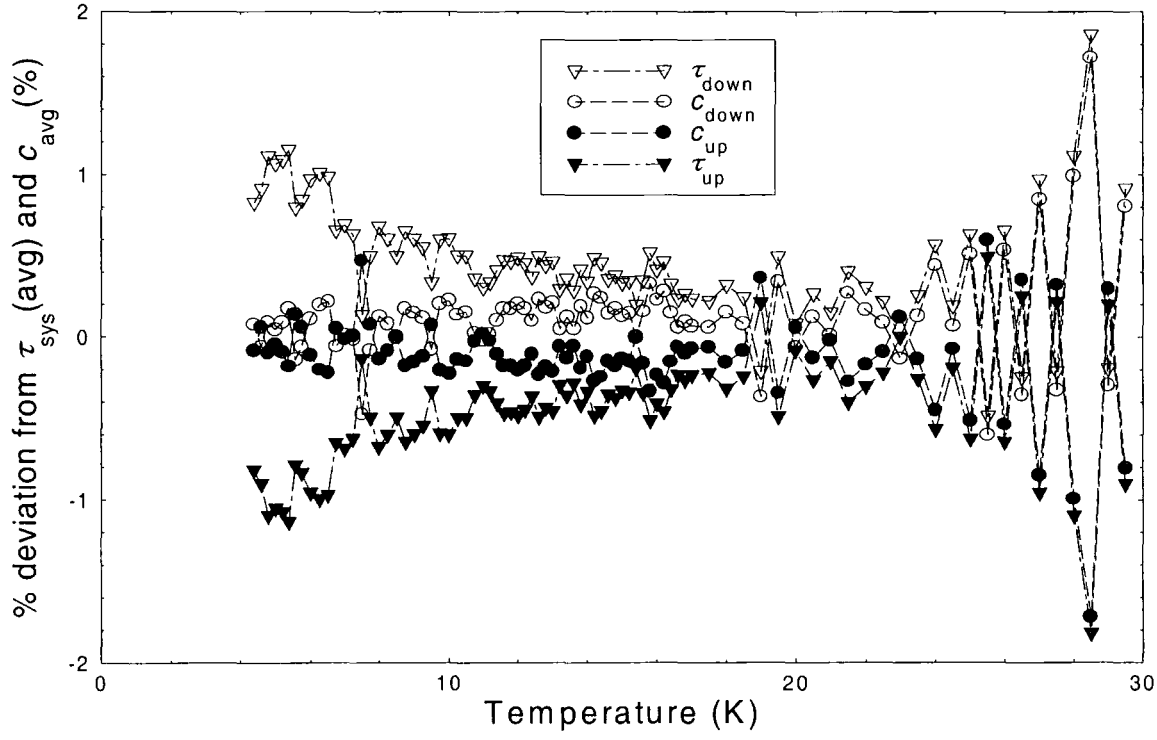


**Figure 9. Percentage difference from $\tau_{avg}^{sys}$ and $c_{avg}$, of the individual measurements $\tau_{up}$, $\tau_{down}$ and $c_{up}$, $c_{down}$ as a function of temperature, from the measurement of the heat capacity of a $PbMo_6S_8$ sample using the relaxation method.**

function of temperature and the accuracy of measurements on the probe determined.

### 5.6.1 Considerations for running relaxation method.

When operating the probe with the relaxation method, the size of the temperature step used to determine the heat capacity should be a small fraction of the actual temperature. Very small changes of temperature however, lead to greater inaccuracies in determining the value of $\Delta T$. A temperature step of about 100mK is used in the measurement, which up to 30 K is < 2 % of the actual temperature.

To reduce measurement errors, two increases and two decreases in temperature are monitored at each temperature and the characteristic time constant determined for each. Figure 9 shows the typical errors of using just up or down traces compared to an average value from a measurement on a sample of $PbMo_6S_8$. Measurement of either just up or just down traces introduces a systematic error in $c(T)$ of up to ± 0.5 %. Typical values of $\tau_{avg}^{sys}$ measured for a copper sample of mass 0.084 g, are 6.3 s at 4.2 K, 10.8 s at 10 K and 54.3 s at 30 K. The internal time constant of copper (section 5.5.4)

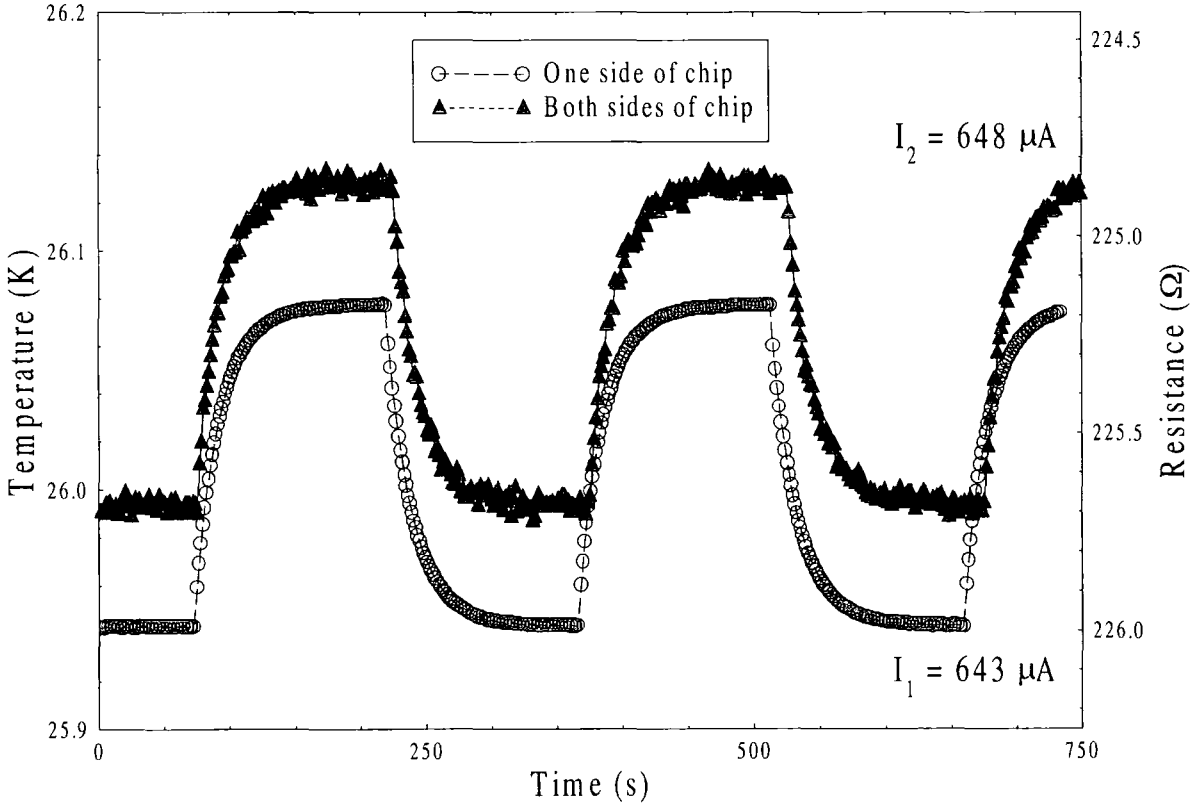


**Figure 10. Temperature of the addenda at 26 K as a function of time measured with one side of the chip and both sides of the chip.**

reaches a maximum value of $\tau^* = 2.1 \times 10^{-4}$ s at 30 K and is still much faster than these measured values of $\tau^{sys}$. This indicates that the sample reaches thermal equilibrium much faster than the heat leaks away and therefore the measurement procedure is accurate.

The thermometer and heater are traditionally separate components of the system and the double Cernox resistor can be used in this mode. When reading the thermometer however, low excitation currents ($\leq 10\mu A$) are required at the lowest temperatures to prevent self-heating of the thermometer and the sample temperature rising. For a fixed excitation current through the Cernox resistor the sensitivity decreases as the temperature is increased due to the reduction in $dR / dT$ at higher temperatures. To keep a large sensitivity the excitation current of the thermometer is therefore increased as we increase the measurement temperature. The self-heating of the thermometer can now be used as the system heater rather than using the second Cernox resistor on the chip as the system heater.

Figure 10 shows the difference in sensitivity of two traces measuring the addenda at 26 K using both sides of the chip compared to just one side. The difference in the measured heat capacity of the addenda when using just one resistor as both heater and thermometer, rather than separate heater and thermometer, is $\leq 1.0$ % throughout the range 5 to 24 K as measured using the relaxation technique. Above about 24 K the reduced sensitivity when using both sides of the chip produces much greater electrical noise and therefore less accurate data.

When running the relaxation method over a temperature range the total time of the trace is dependent on the number of points taken. Measurements on copper samples between 5 K and 30 K, at every 0.5 K, when taking four traces to determine each point would typically take over 12 hours. To reduce the running time for use in the magnet system the number of traces at each point was reduced from four to two. Analysis of the data on copper samples shows that the difference between the calculated average time constant of just the first two traces compared to all four traces is $\leq 0.6$ % throughout the range 5 to 30 K.

### 5.6.2 Gas Pressure.

Gas in the probe can play a vital role in determining the heat leak from the sample to the background. To prevent any thermal conduction through the gas the probe is pumped out at room temperature to a pressure of $10^{-1}$ mbar using a rotary pump and then pumped out with a diffusion pump to a pressure of $10^{-6}$ mbar. A pumping time of 1 hour on the diffusion

stack ensured that the gas had no significant effect on the measurement. The results in section (5.5.2) show that the system is operating in a regime where the main heat leak occurs down the constantan support wires.

### 5.6.3 Calculation of addenda.

To enable accurate specific heat measurements the system has to have a heat capacity (addenda) much smaller than the heat capacity of the sample to be measured. The heat capacity of the addenda has to be determined in the temperature region of interest so that it can be subtracted from future measurements, leaving just the heat capacity of the sample. Measurements of three copper samples of different masses and a direct measurement of the addenda (no sample) were made from 5 to 30 K in a dewar of liquid helium. For each of the four sets of data the results of $C$ as a function of $T$ were fitted above 10 K to a polynomial of the form $C = AT + BT^3 + CT^5 + DT^7$, where A, B, C and D are free parameters. Each resulting fit was used to determine the heat capacity of that sample at temperatures $T > 10$ K, for $T < 10$ K the raw data points provided sufficient accuracy.

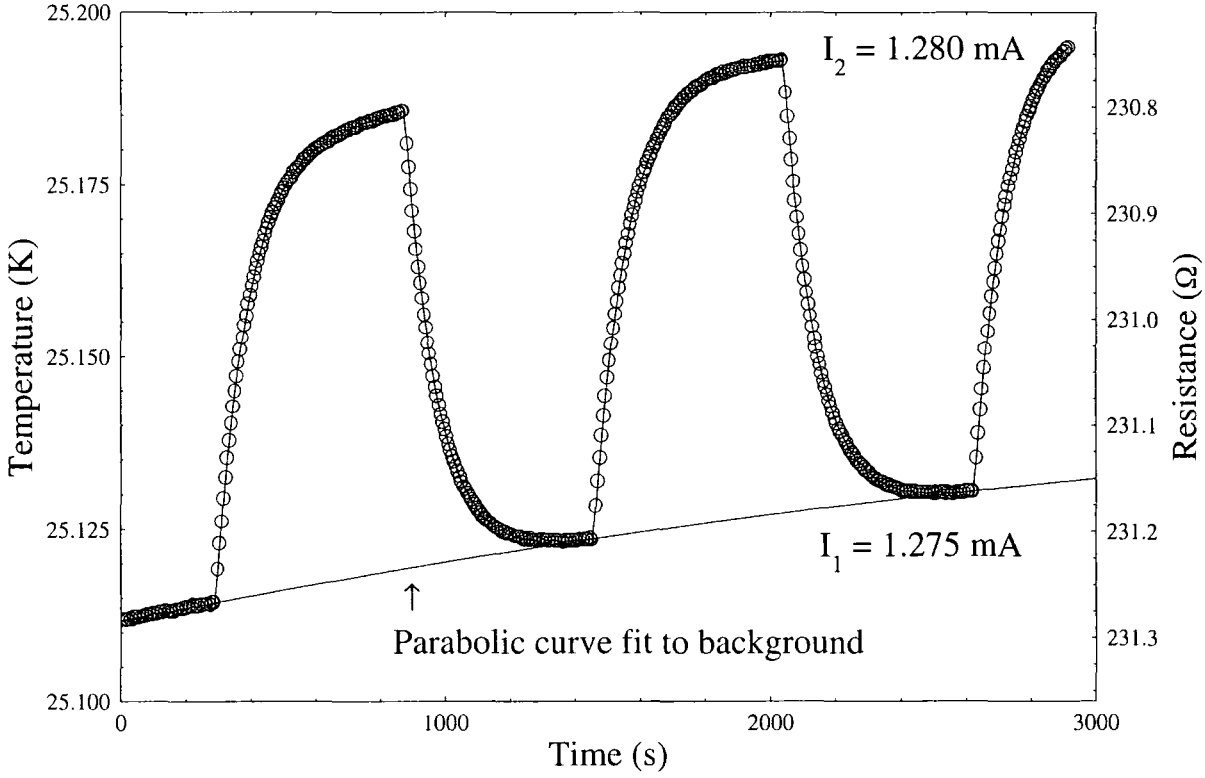


**Figure 11. Temperature of a copper sample, mass 0.272 g, as a function of time and a parabolic fit to the drifting background temperature.**

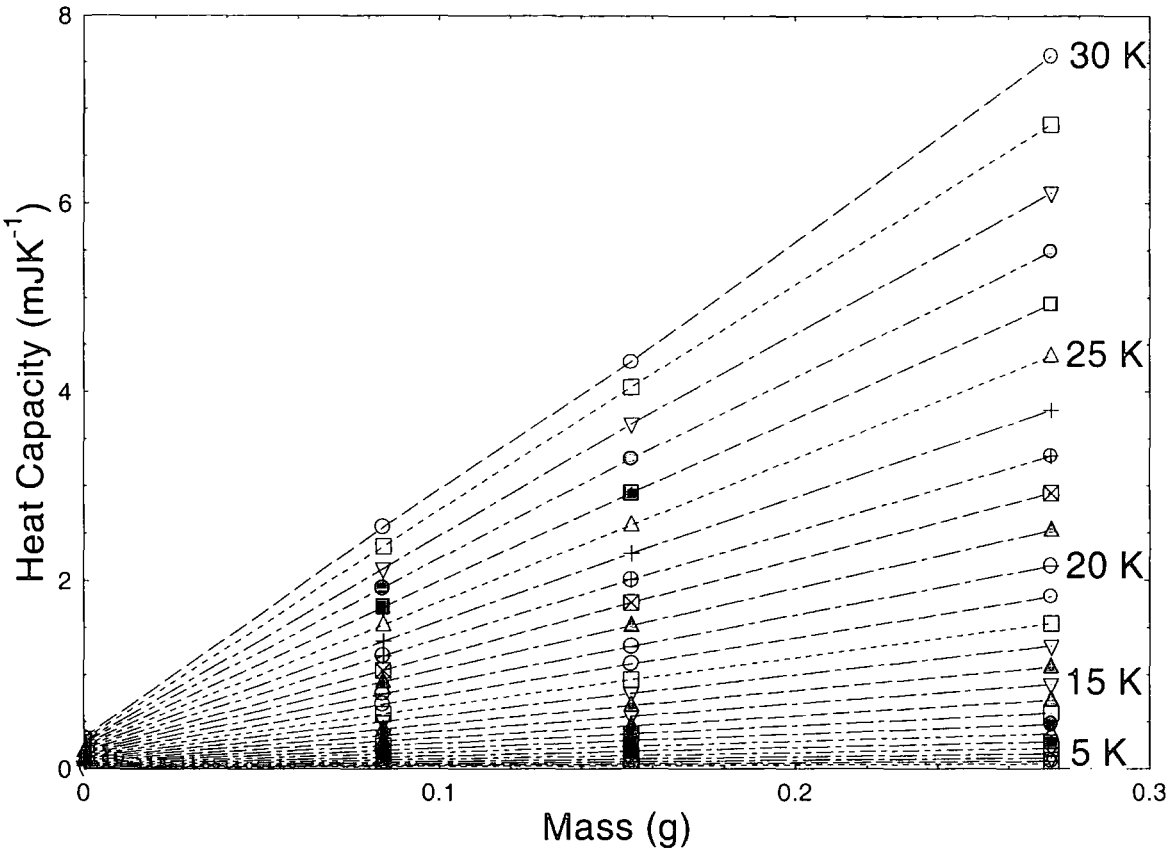


**Figure 12. Heat capacity for three copper samples and the addenda as a function of sample mass from 5 K to 30 K.**

At high temperatures (T > 15 K) for large samples, some of the measurements had a drifting sample temperature over the course of the measurement as shown in Fig. 9. Movement of the electrical wires against the surrounding struts and pressure variations in the dewar over the long measurement period are the most probable causes of these drifts. A parabolic fit to the base temperature as shown in Fig. 11, was used to correct for the temperature drift allowing exponential fits of the data.

Figure 12 shows the heat capacity of the addenda and copper samples at various temperatures plotted as a function of mass, where the addenda corresponds to a mass of zero, i.e. no copper sample. For a fixed temperature a straight line through the points has a gradient which is equal to the specific heat capacity at that temperature and an intercept that is the heat capacity of the addenda.

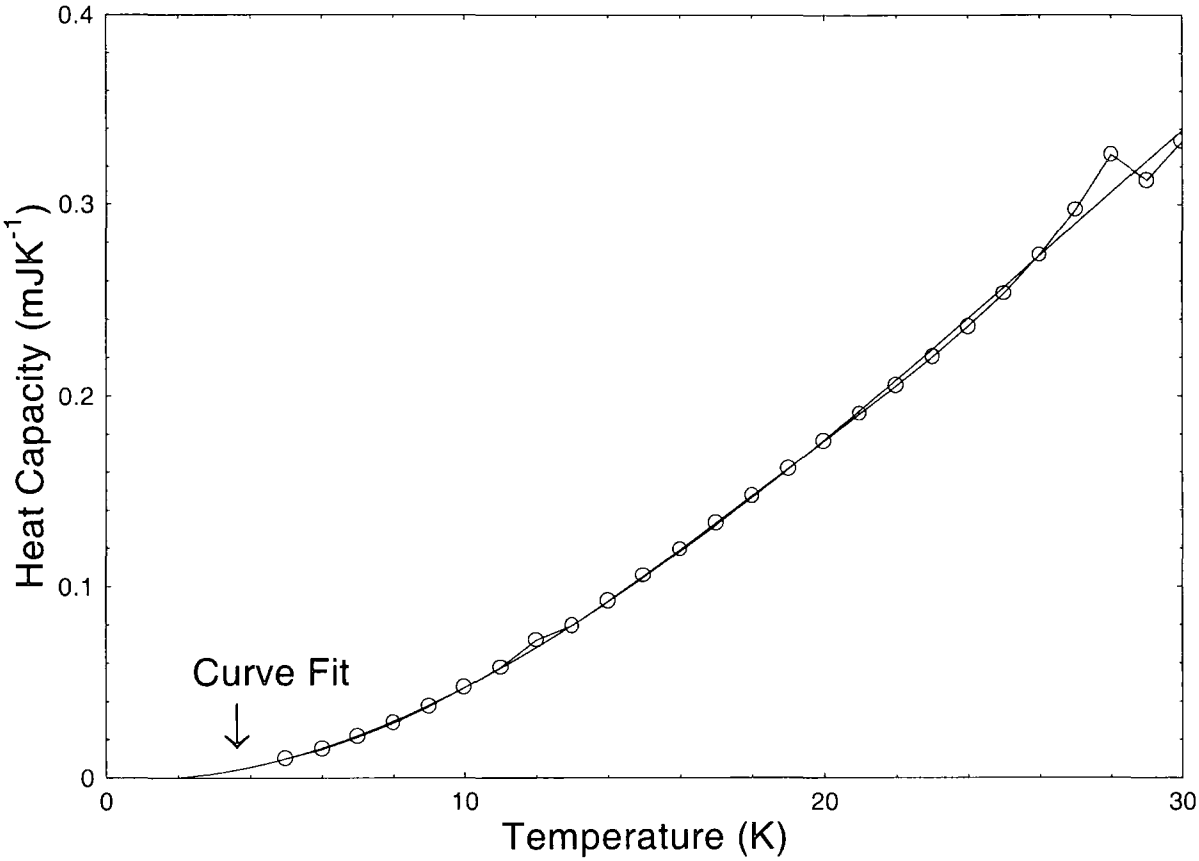


**Figure 13. Heat capacity of the addenda calculated from Fig. 12, as a function of temperature and a third order polynomial fit to the data.**

Figure 13 shows the calculated values of the addenda as a function of temperature from the data in Fig. 12. These calculated values of the addenda are used rather than the measured values since the error associated with a linear fit to four points is lower than the error due to a single measurement. In order to parameterise the data in Fig. 13, a least-squares curve fitting procedure was used to fit a smooth curve through the points.

| Order of polynomial | Coefficient |
|---|---|
| 0 | $-4.26274 \times 10^{-7}$ |
| 1 | $-9.65424 \times 10^{-7}$ |
| 2 | $+6.55382 \times 10^{-7}$ |
| 3 | $-8.19420 \times 10^{-9}$ |

**Table 3. The coefficients of the third order polynomial used to fit the addenda as a function of temperature according to the equation $C = \sum_i a_i T^i$ ($JK^{-1}$).**

The best fit to the data taking into account a low temperature (< 5 K) extrapolation towards $T$ = 0 K, was achieved with a third order polynomial as shown in Fig. 13. The maximum deviation of this polynomial from the measured values of the addenda is 5 % at 6 K and 12 K and 6.5 % at 28 K. Higher order polynomial fits gave no significant improvement. At temperatures below 5 K the extrapolation to values at 3 K produces an error estimated to be as high as 50 %. The actual error however in extrapolating to 3 K is of the order 1.5 $\mu JK^{-1}$ and so compromises typically about 10 % of the sample heat capacity for $PbMo_6S_8$ at these temperatures.

### 5.6.4 Calibration of the probe.

To determine the accuracy of measurements performed on this probe copper is used as a standard. The specific heat of copper has been measured by many authors and at low temperatures is given by the copper reference equation (CRE) determined by Osbourne et

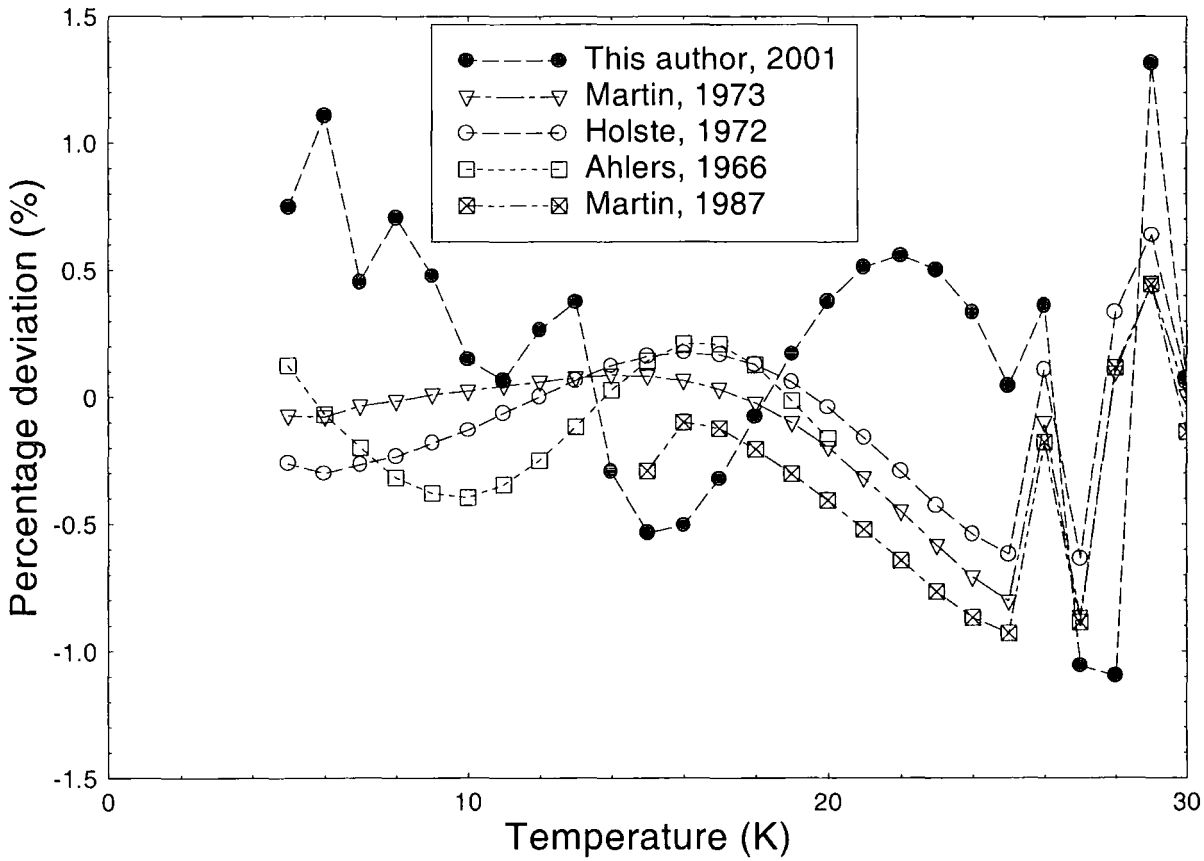


**Figure 14. Percentage deviation of the specific heat of copper measured by this author and others [310-313] from CRE as a function of temperature.**

al [301]. The measured specific heat of copper is determined from the gradient of the straight line fits to the data in Fig. 12.

Figure 14 shows the percentage deviation of the specific heat of copper measured by this author and by other authors [310-313] compared to the CRE. The data shows that we can measure the specific heat of copper from 9 to 26 K to an accuracy of better than 0.5 %, between 5 and 8 K to better than 1.1 % and between 27 and 30 K to better than 1.3 %. Using a Debye plot ($C$ / $T$ versus $T^2$) we can extract a value for the Sommerfeld constant as $\gamma = 0.67$ mJK$^{-2}$mole$^{-1}$ and for the Debye temperature $\theta_D = 341.5$ K. Values in the literature from measurements at very low temperatures give $\gamma \approx 0.69$ mJK$^{-2}$mole$^{-1}$ and $\theta_D \approx 344$ K [28].

## 5.7 Measurement procedure.

Operation of the specific heat probe employs two techniques, the relaxation method and the long range method which are run successively. The relaxation method takes many hours and provides accurate point by point data. The long range method takes a few minutes to run and gives a very sensitive readout of the heat capacity over a limited temperature range. Combining both techniques gives an accurate, sensitive measure of the heat capacity of a sample.

### 5.7.1 Sample mounting and probe preparation.

The sample is shaped to a rectangular block of typical size 4 mm long, 3 mm wide and 1.5 mm deep. Emery paper is used to smooth the surface of the sample and remove any oxidation layers, both top and bottom surfaces need to be smooth to provide a good interface between the sample, chip and support wires. The sample is secured in place by applying a thin layer of GE varnish to the underside of the thermometer chip and then holding it tight against the sample using cotton thread. The support wires are positioned flush on the top surface of the sample and a few drops of GE varnish applied. The assembly is left for three hours at room temperature for the GE varnish to dry after which the cotton is removed.

The GE varnish is prepared by diluting it in equal proportion with ethanol to make it less viscous. The mix of solvent and varnish is thoroughly shaken in a sealed glass jar for about twenty minutes and then a syringe is used to measure and apply the diluted varnish to the

surfaces. Once the GE varnish has dried the outer can is pulled over the probe and sealed at the top end using an o-ring and clamp and at the bottom and by a soft solder seal. The probe is then pumped out using a rotary and diffusion stack for 1 hour at room temperature. For measurements in a dewar the probe is slowly pre-cooled in liquid nitrogen to prevent thermal shock, for measurements in the VTI this is not necessary. Once the probe is in place the temperature of the VTI is set to 3 K and the probe left to completely cool down. This cooling process typically takes 3 hours in a dewar and 6 hours in the VTI due to the hard vacuum inside the probe. Running measurements before the probe has reached thermal equilibrium produces a background temperature that is unstable.

### 5.7.2 Relaxation method measurement procedure.

The Keithley programmable current supply is used to supply an excitation current through the thermometer that heats the chip and sets the initial temperature for that measurement. The current through the thermometer is then incremented and the resistance change of the thermometer monitored as the temperature of the sample increases. The excitation current is then changed back to its original value and the resistance change monitored once more to generate both an up and down trace for analysis. Once the final temperature change has been measured the excitation current is increased again to take the system to the next desired temperature where the process is repeated.

Measurements at about eight or ten temperatures over the entire temperature region to be measured are initially done manually. The calculated time constants from these measurements are used to input either quadratic or linear temperature dependencies for the measurement speed over appropriate temperature regions. The whole trace is then run automatically by the computer, waiting a length of ten time constants before starting a measurement and taking two hundred readings over seven time constants for each up and each down trace.

### 5.7.3 Long range technique measurement procedure.

The long range method is run after the relaxation method. The appropriate currents needed to hold the chip at each temperature are determined from the data on the relaxation method. The sample is held at a temperature several Kelvin above the region of interest and then the current through the chip is manually changed to a value consistent with holding the sample temperature at several Kelvin below the region of interest. The

computer is then activated, taking as many readings as are desired at a maximum rate of about 50 ms per reading. Typically one thousand readings are taken over a temperature drop of about six to eight Kelvin providing a very accurate reading of $dT / dt$. The short time span of this measurement (< 2 minutes) allows several traces to be taken generally at slightly different initial and final temperatures to allow errors to be checked.

### 5.7.4 Removing the probe.

Once all the data has been collected a volume of dry helium gas from a bladder is inserted into the probe and the probe allowed to thermally re-equilibrate. The probe can then be removed with both the inner and outer sections, which are sealed at top and bottom, warming up at a similar rate. If the probe is removed still under hard vacuum the outer can expands stretching the (still cold) inner section.

## 5.8 Conclusion.

A probe has been developed to measure the specific heat of low temperature superconductors from 3 K to 30 K and in magnetic fields up to 15 T. Two measurement techniques have been used to measure the specific heat, the relaxation method for good accuracy and the long range method for good sensitivity. Measurements have been taken on copper samples to calibrate the heat capacity of the addenda (chip and varnish). The results have been compared to the literature and show that the accuracy of the relaxation measurement with this system is better than 1.3 % in the temperature range 5 K to 30 K with an absolute error of 1.5 $\mu JK^{-1}$ at 3 K. A third order polynomial fit has been applied to the calculated addenda values and this is then used as a subtraction from the measured heat capacity of a sample.

The results taken by the long range method are transformed into heat capacity values using the data obtained from the relaxation method. The long range method produces a continuous reading of the heat capacity of the sample as a function of temperature, with a temperature resolution of about 10 mK. This technique therefore provides a significant improvement compared to the relaxation method in determining the temperature of phase transitions. The accuracy of the heat capacity values obtained by this method is about 20 % and at temperatures significantly above the background, uncertainties in the change in background temperature can produce errors in the recorded temperature.

# *Chapter 6. - Specific heat measurements on the series $(Pb_{1-x}Cu_{1.8x})Mo_6S_8$.*

## 6.1 Introduction.

Although $PbMo_6S_8$ has a superconducting transition temperature and upper critical field that make it an ideal candidate for high field applications, the critical current densities of this material are too low for industrial application. Improvements in material processing have led to a corresponding increase in the $J_c$ values that are close to the industry standard required [207] by improving the superconducting properties of the grain boundaries. Doping $PbMo_6S_8$ with small cations such as copper can lead to an improvement in the critical current density if these additional ions improve the carrier density at the grain boundaries. To investigate the effect of adding copper ions into the $PbMo_6S_8$ structure a series of $(Pb_{1-x}Cu_{1.8x})Mo_6S_8$ samples have therefore been fabricated with a range of values of $x$. A similar series of $Cu_xPbMo_6S_8$ has previously been fabricated by Sergent et al [191], where the copper ions were inserted as additional cations in the lattice rather than substituting for the lead ions as we have done here. The results of this series however were compromised by oxygen contamination during the fabrication process.

In this chapter specific heat measurements on samples of the series $(Pb_{1-x}Cu_{1.8x})Mo_6S_8$ are presented and compared to data from resistivity, susceptibility, magnetization and X-ray measurements taken by Dr. H J Niu [314, 315]. Due to the mixed composition of the starting material the fabrication process can produce samples that are not single phase. Specific heat measurements are ideally suited to studying the properties of mixed phase materials and can provide information about all the phases within the material. Analysis of the specific heat data is discussed therefore in terms of the phase composition of these samples and in comparison to results from other authors. Together with results from the resistivity and magnetisation measurements, the specific heat data is used to make estimates of various superconducting parameters using the BCS strong coupling theory and the GLAG theory.

Sections 6.2 and 6.3 detail the fabrication and experimental procedure respectively. The data is presented in section 6.4 and the analysis and implications of these results are discussed in section 6.5. The chapter is concluded in section 6.6.

## 6.2 Sample fabrication.

Six samples of the series $(Pb_{1-x}Cu_{1.8x})Mo_6S_8$ with $x$ = 0.00, 0.05, 0.10, 0.30, 0.50 and 1.00, were fabricated using a solid state reaction procedure. Elemental powders, Pb (99.999%), Cu (99.999%), S (99.998%) and Mo (99.95%) were used and the molybdenum powder was reduced under Ar (98%) + $H_2$ (2%) gas flow at 1000 °C for 4 hours to remove any oxygen. For each member of the series, 15 g of the starting powder was weighed out in the correct stoichiometric composition, cold pressed into pellets and then sealed inside a molybdenum crucible. Each sample was sintered in a tube furnace under an argon atmosphere using two heat treatments and a fixed temperature ramp rate of 60 °C / hr. In the first treatment the samples were held successively at 110 °C for 2 hrs, 130 °C for 4 hrs, 400 °C for 2 hrs, 450 °C for 4 hrs, 700 °C for 5 hrs and finally 750 °C for 5 hours before being cooled to room temperature. The samples were then removed, ground for 40 minutes, cold pressed and resealed in their molybdenum crucibles. The second sintering

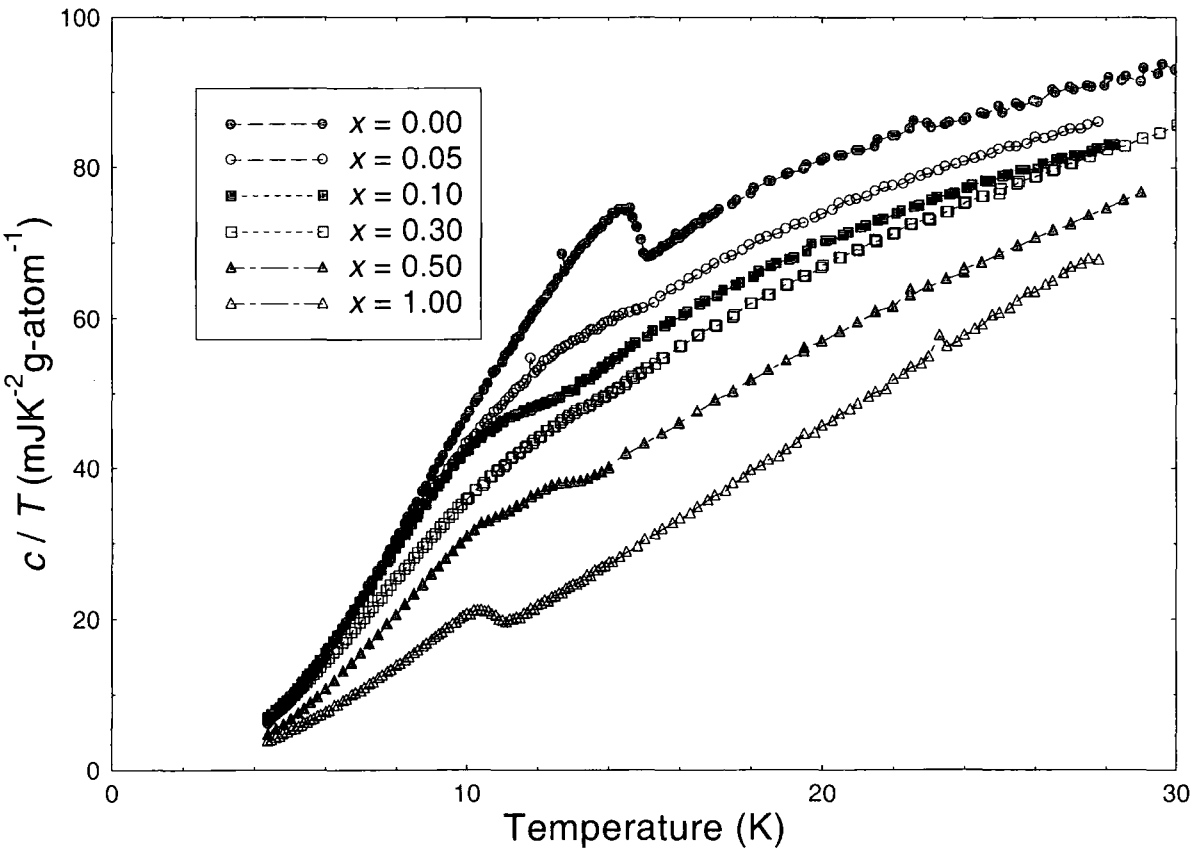


**Figure 1. $c$ / $T$ for $(Pb_{1-x}Cu_{1.8x})Mo_6S_8$ with $x$ = 0.00, 0.05, 0.10, 0.30, 0.50 and 1.00 as a function of temperature, measured by the relaxation method.**

held each sample at 750 °C for 4 hrs and then at 1000 °C for 40 hrs. Once cool the samples were ground into powder, wrapped in molybdenum foil and placed inside stainless steel tubes. The tubes were sealed at one end using tungsten inert gas and then the other end was sealed under vacuum, using a spot welder. Evacuating the tube prevented the formation of slag by spot welding in air. The tubes were then HIP'ed at 2000 bar and 800 °C for 8 hrs.

## 6.3 Experimental.

Specific heat measurements were taken using the relaxation method on each member of the series. Samples were prepared of mass 0.056 g ($x$ = 0.00), 0.048 g ($x$ = 0.05), 0.074 g ($x$ = 0.10), 0.049 g ($x$ = 0.30), 0.050 g ($x$ = 0.50) and 0.026 g ($x$ = 1.00). The relaxation method was run twice for each sample up to 30 K at intervals of 0.25 K for $T < T_c + 1.5$ K and at intervals of 0.5 K for $T > T_c + 1.5$ K. The first trace was started at 4.4 K and the second trace from 4.5 K so that the data from the second run would lie interspersed

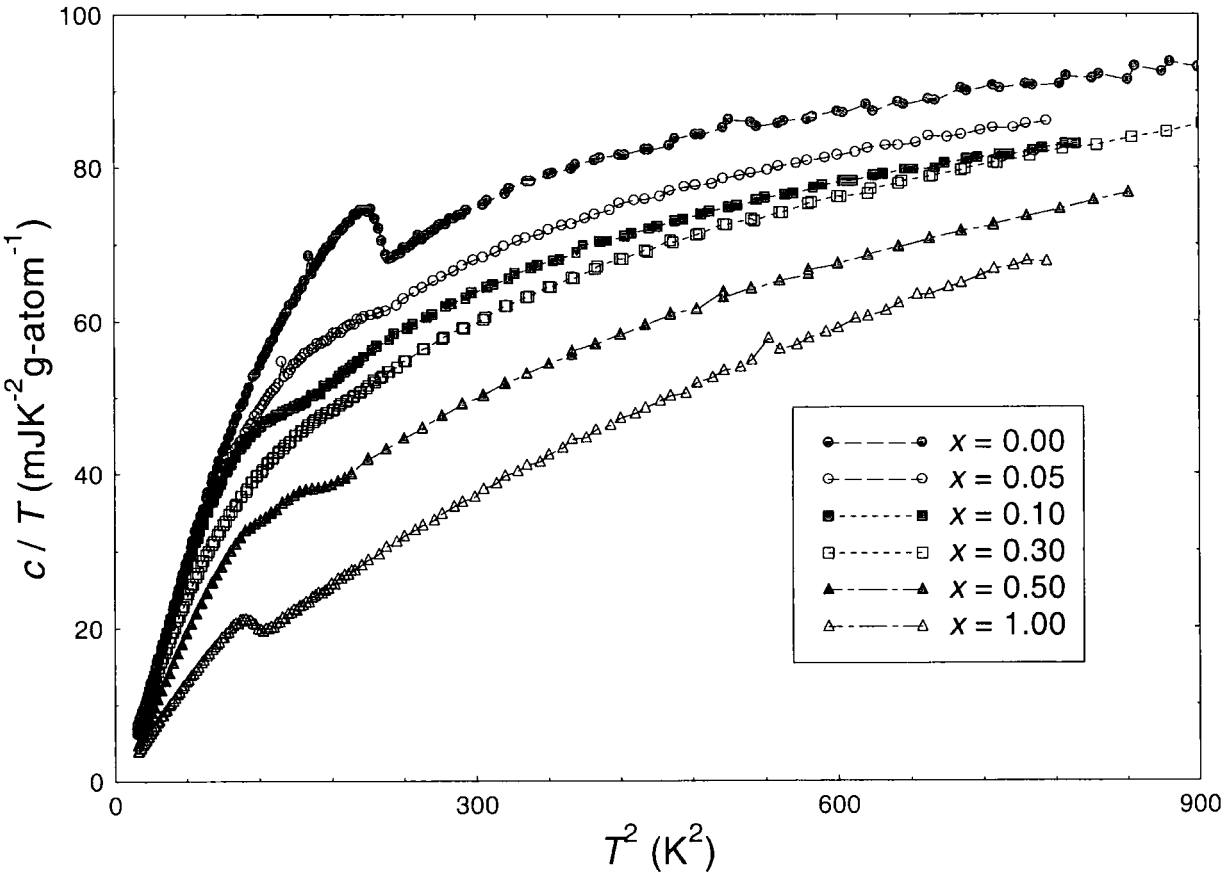


**Figure 2. Debye plot ($c$ / $T$ versus $T^2$) for $(Pb_{1-x}Cu_{1.8x})Mo_6S_8$ with $x$ = 0.00, 0.05, 0.10, 0.30, 0.50 and 1.00, measured by the relaxation method.**

between those of the first run.

Additional resistivity, susceptibility and X-ray diffraction measurements have been performed on each member of the series in zero applied magnetic field and further resistivity measurements have also been performed on the $x$ = 0.00, 0.30, 0.50 and 1.00 samples in magnetic fields up to 15 T [314]. Vibrating sample magnetometry (VSM) measurements have been carried out on all of the samples from 4.2 K to $T_c$ and in magnetic fields up to 12 T [315].

## 6.4 Results.

Figures 1 and 2 present the specific heat data obtained using the relaxation method. Figure 1 presents the data as $c$ / $T$ versus $T$ and Fig. 2 presents the results on a Debye plot. In each case the measured heat capacity results have the addenda subtracted from them using the polynomial expression in section 5.5.3 (table 3) and are then divided by the sample mass to give $c(T)$ in $JK^{-1}g^{-1}$. The results are converted into units of $JK^{-1}g\text{-}atom^{-1}$ by multiplying the value in $JK^{-1}g^{-1}$ by the molecular mass of the unit cell for each compound

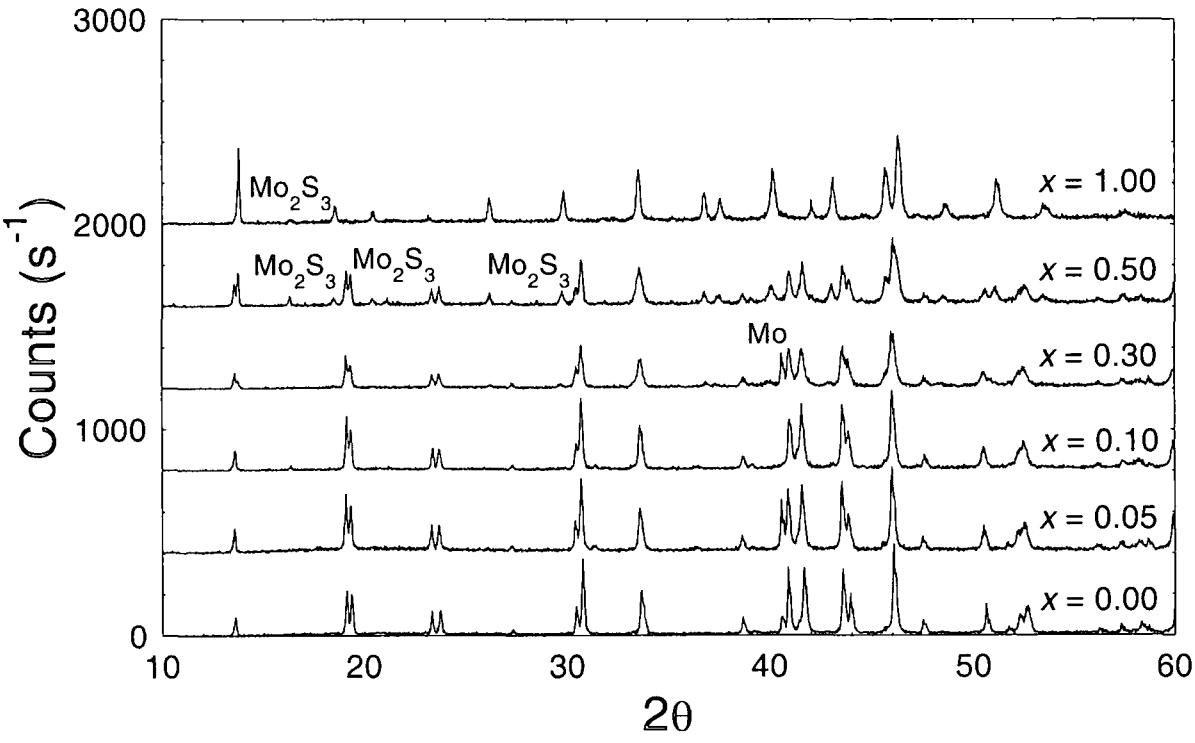


**Figure 3. X-ray diffraction patterns for $(Pb_{1-x}Cu_{1.8x})Mo_6S_8$ with $x$ = 0.00, 0.05, 0.10, 0.30, 0.50 and 1.00. Data taken from H J Niu [314, 315].**

and then dividing by the nominal number of atoms per unit cell.

The data in Fig. 1 show clear specific heat jumps for the samples $x$ = 0.00, 0.10, 0.50 and 1.00, whereas the samples $x$ = 0.05 and 0.30 have superconducting transitions that are less easily defined in the specific heat. The data from sample $x$ = 0.50 shows two specific heat jumps at temperatures 12.86 K and 10.65 K, indicating two phase transitions, the corresponding resistivity and susceptibility traces however do not exhibit this feature.

### 6.4.1 X-ray diffraction.

The X-ray diffraction results taken by Dr H J Niu are presented in Fig. 3. The patterns indicate that a small amount of $Mo_2S_3$ phase in the $x$ = 0.50 and 1.00 compounds and a small amount of pure molybdenum in the $x$ = 0.00, 0.05 and 0.30 compounds are the only secondary phases present. The two end compounds of the series, $PbMo_6S_8$ and $Cu_{1.8}Mo_6S_8$,

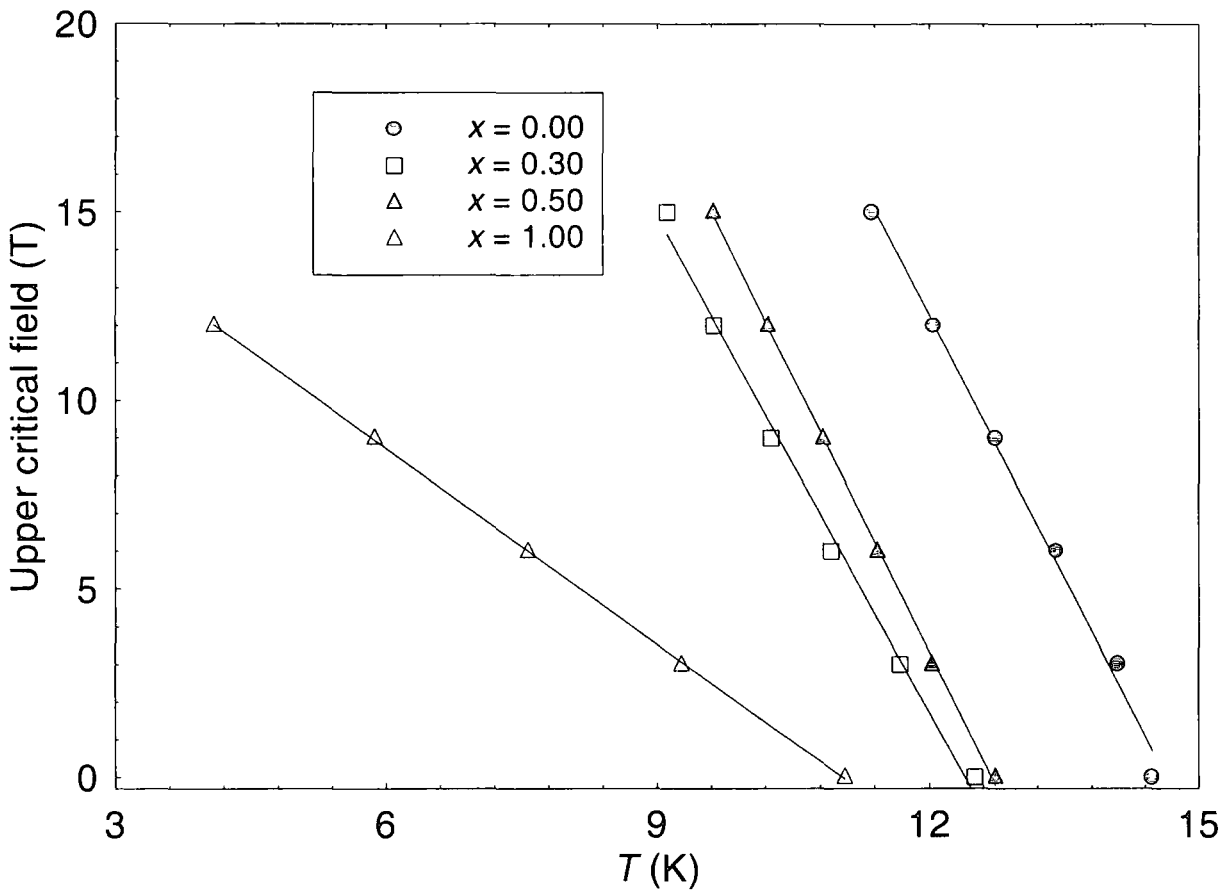


**Figure 4. Upper critical field as a function of temperature for $(Pb_{1-x}Cu_{1.8x})Mo_6S_8$ with $x$ = 0.00, 0.30, 0.50 and 1.00, determined from the midpoint of the resistivity transition. Data from H J Niu [314].**

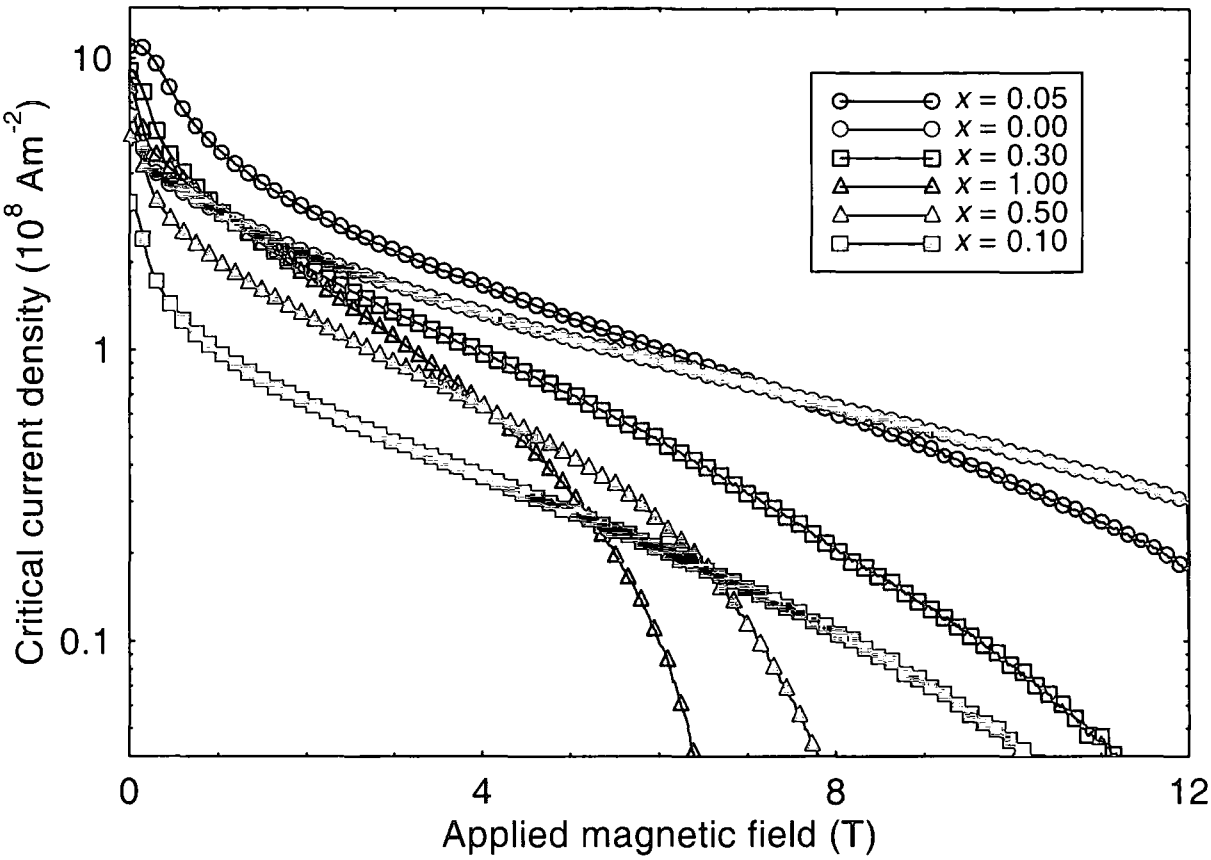


**Figure 5. Critical current density as a function of applied magnetic field for ($Pb_{1-x}Cu_{1.8x}$)$Mo_6S_8$ with $x$ = 0.00, 0.05, 0.10, 0.30, 0.50 and 1.00, determined from VSM measurements. Data from H J Niu [315].**

are predominantly single phase while the intermediate compounds all show $PbMo_6S_8$ peaks that are broadened. The $x$ = 0.30 and 0.50 samples show a mixture of broadened $PbMo_6S_8$ and broadened $Cu_{1.8}Mo_6S_8$ phases with the proportion of the $Cu_{1.8}Mo_6S_8$ phase increasing commensurately with increasing copper content.

### 6.4.2 Measurements in applied magnetic field.

Resistivity and VSM measurements taken in magnetic fields up to 15 T have been analysed by Dr. H J Niu and the results are presented in Fig.'s 4 and 5. The temperature dependence of the upper critical field $B_{c2}(T)$ presented in Fig. 4 has been determined from the midpoint of the resistivity transitions. Estimates of $B_{c2}(0)$ from the resistivity data can be made using WHH-Maki theory:

$$B_{c2}(0) = -0.693 T_c \left( \frac{dB_{c2}(T)}{dT} \right)_{T=T_c} \qquad (6.1)$$

Estimates for $B_{c2}(0)$ using Eqn. (6.1) are 47.3 T for $x$ = 0.00, 40.5 T for $x$ = 0.30, 43.4 T for $x$ = 0.50 and 13.4 T for $x$ = 1.00. The extrapolated values of $B_{c2}(0)$ for $PbMo_6S_8$ are lower than those of other authors that generally lie between 55 and 60 T [127, 183]. The estimated value for the $Cu_{1.8}Mo_6S_8$ sample however agrees well with pulse field data [139]. The analysis reveals that the slope $dB_{c2}(T)/dT$ of the mixed samples is similar to the $PbMo_6S_8$ sample, indicating that the reduction in $B_{c2}(0)$ compared to the undoped sample is due to the drop in the transition temperature.

Figure 5 shows the $J_c$ values determined from VSM measurements at 4.2 K in magnetic fields up to 12 T. The data suggests that the lowest doped sample $x$ = 0.05 has an improved critical current density at low fields compared to $PbMo_6S_8$.

## 6.5 Discussion.

| Copper Content | $T_{c(mid)}$ (K) | $T_{c(onset)}$ (K) | $\Delta T_c$ (K) | $c / T$ ($mJK^{-2}g\text{-}atom^{-1}$) | | $\Delta c / T_c$ ($mJK^{-2}g\text{-}atom^{-1}$) | $\rho_N$ ($\mu\Omega cm$) |
|---|---|---|---|---|---|---|---|
| | | | | At $T_{c(onset)}$ | at 15 .1 K | | |
| $x$ = 0.00 | 14.78 | **15.10** | 0.81 | 68.2 | 68.2 | 9.70 | 80 |
| $x$ = 0.05 | 14.11 | 14.81 | 2.00 | 61.1 | 61.7 | 2.68 | - |
| $x$ = 0.10 | 11.83 | 12.85 | 2.20 | 50.1 | 58.0 | 3.67 | - |
| $x$ = 0.30 | 13.23 | 13.90 | 1.40 | 49.7 | 53.5 | 1.45 | 144 |
| $x$ = 0.50 | 12.86<br>10.65 | 13.40<br>11.00 | 1.01<br>0.60 | 38.6<br>33.9 | 43.6 | 2.67<br>1.01 | 550 |
| $x$ = 1.00 | 10.67 | **11.05** | 0.95 | 19.7 | 30.8 | 4.57 | 82 |

**Table 1. $T_{c(mid)}$, $T_{c(onset)}$, $\Delta T_c$, $c / T$ at $T_{c(onset)}$ and 15.1 K, $\Delta c / T_c$ and $\rho_N$ for the series $(Pb_{1-x}Cu_{1.8x})Mo_6S_8$ with $x$ = 0.00, 0.05, 0.10, 0.30, 0.50 and 1.00.**

### 6.5.1 Structural phase analysis.

Analysis of the X-ray diffraction results [314] indicates that the $x$ = 0.00 and $x$ = 1.00 samples are single phase $PbMo_6S_8$ and $Cu_{1.8}Mo_6S_8$ respectively. The broadened $PbMo_6S_8$ peaks in the diffraction pattern of the $x$ = 0.05 and 0.10 samples indicate a distorted $PbMo_6S_8$ structure, suggesting that the copper ions have correctly substituted onto the lead

sites in the unit cell forming a $PbMo_6S_8(Cu)$ phase. The $x = 0.30$ and $x = 0.50$ samples exhibit a mixture of distorted $PbMo_6S_8$ structure and distorted $Cu_{1.8}Mo_6S_8$ structure suggesting that two phases are present, $PbMo_6S_8(Cu)$ and $Cu_{1.8}Mo_6S_8(Pb)$. The $Cu_{1.8}Mo_6S_8$ peaks occurring in the results of the $x = 0.50$ are larger than in the $x = 0.30$ sample and reveal a larger proportion of $Cu_{1.8}Mo_6S_8(Pb)$ phase in this sample. The two transitions visible in the specific heat data of the $x = 0.50$ sample are therefore assumed to be that of the $PbMo_6S_8(Cu)$ and $Cu_{1.8}Mo_6S_8(Pb)$ phase within the material with the $PbMo_6S_8(Cu)$ phase having the higher $T_c$.

The $x = 0.30$ sample has a broad transition in the specific heat data that we have interpreted as a single jump but could be an amalgamation of two phase transitions in the material. Given the small proportion of the $Cu_{1.8}Mo_6S_8(Pb)$ phase in this sample it is more likely however that the corresponding specific heat jump is too small to distinguish and the broad transition is that of the $PbMo_6S_8(Cu)$ phase.

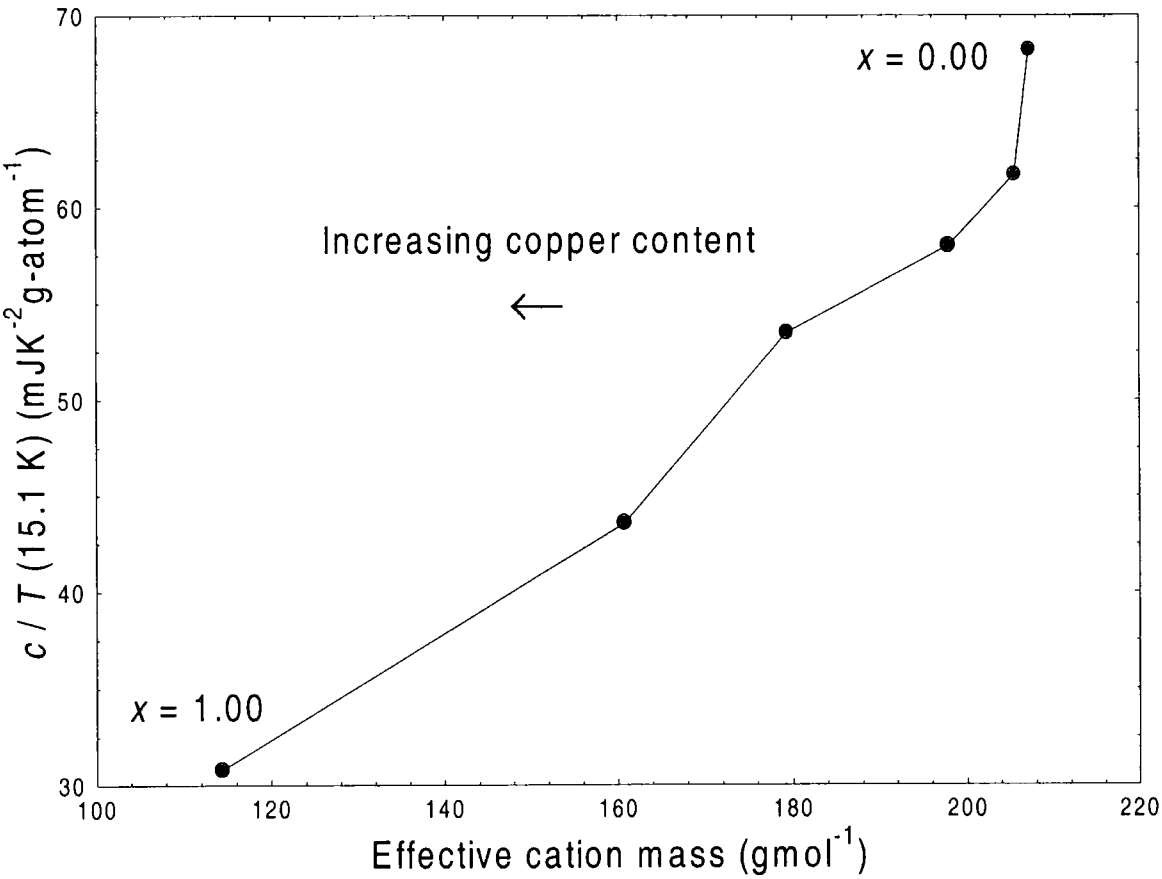


**Figure 6. $c$ / $T$ at 15.1 K as a function of the effective mass of the cation for the series $(Pb_{1-x}Cu_{1.8x})Mo_6S_8$ with $x = 0.00, 0.05, 0.10, 0.30, 0.50$ and 1.00.**

### 6.5.2 Normal state specific heat.

The values of $c$ / $T$ at the onset of the specific heat jump for the $x$ = 0.00 and $x$ = 1.00 samples are in agreement with data from other authors; 50 – 70 $mJK^{-2}g\text{-}atom^{-1}$ for $PbMo_6S_8$ [29, 68, 127, 183] and 15 $mJK^{-2}g\text{-}atom^{-1}$ for $Cu_{1.8}Mo_6S_8$ [316]. Estimates of the size of the electronic contribution to the specific heat ($\gamma$ ~ 8 $mJK^{-2}g\text{-}atom^{-1}$ for $PbMo_6S_8$ [68] and ~ 4 $mJK^{-2}g\text{-}atom^{-1}$ for $Cu_{1.8}Mo_6S_8$ [185]) are not large enough to account for the difference in $c$ / $T_c$ between the $PbMo_6S_8$ and $Cu_{1.8}Mo_6S_8$ compounds. The change in the normal state specific heat is therefore assumed to be due to a change in the phonon contribution ($c_L$). As the copper content is increased through the series the normal state specific heat systematically decreases, indicating a corresponding drop in $c_L$. The phonon spectra of $PbMo_6S_8$ and $Cu_2Mo_6S_8$ [43, 186, 317] have been determined from neutron scattering data and are dominated at low energies (< 10 meV) by a peak attributed to the metal ion in the lattice. This peak occurs at a higher energy (~ 8 meV) in the $Cu_2Mo_6S_8$ compound than in the $PbMo_6S_8$ compound (~ 5 meV) due to the lighter mass of the cation (207.2 $gmol^{-1}$ for Pb, 63.55 $gmol^{-1}$ for Cu) and thus at low temperatures more phonons will be excited in the $PbMo_6S_8$ structure. Figure 6 shows the value of $c$ / $T$ measured at 15.1 K as a function of the effective mass of the cation, where the temperature 15.1 K is used so that all of the samples are in the normal state. The data in Fig. 6 shows that the normal state specific heat drops as the effective cation mass is reduced and is consistent with the neutron scattering data. We can therefore conclude that the normal state specific heat drops systematically with increasing copper content due to a reduction in the effective mass of the cation and a corresponding drop in the phonon density of states.

Common procedure for analysis of the lattice contribution requires the normal state data to be characterised using a Debye plot of $c$ / $T$ versus $T^2$. Figure 2 shows that the simple approximation used in this procedure, of $c_L = AT^3$, is not applicable above $T_c$ and higher order terms are needed. The full functional form of the Debye model is given by:

$$c_L = 9R\left(\frac{T}{\theta_D}\right)^3 \int_0^{\theta_D/T} \frac{x^4 e^x}{\left(e^x - 1\right)^2} dx \qquad (6.2)$$

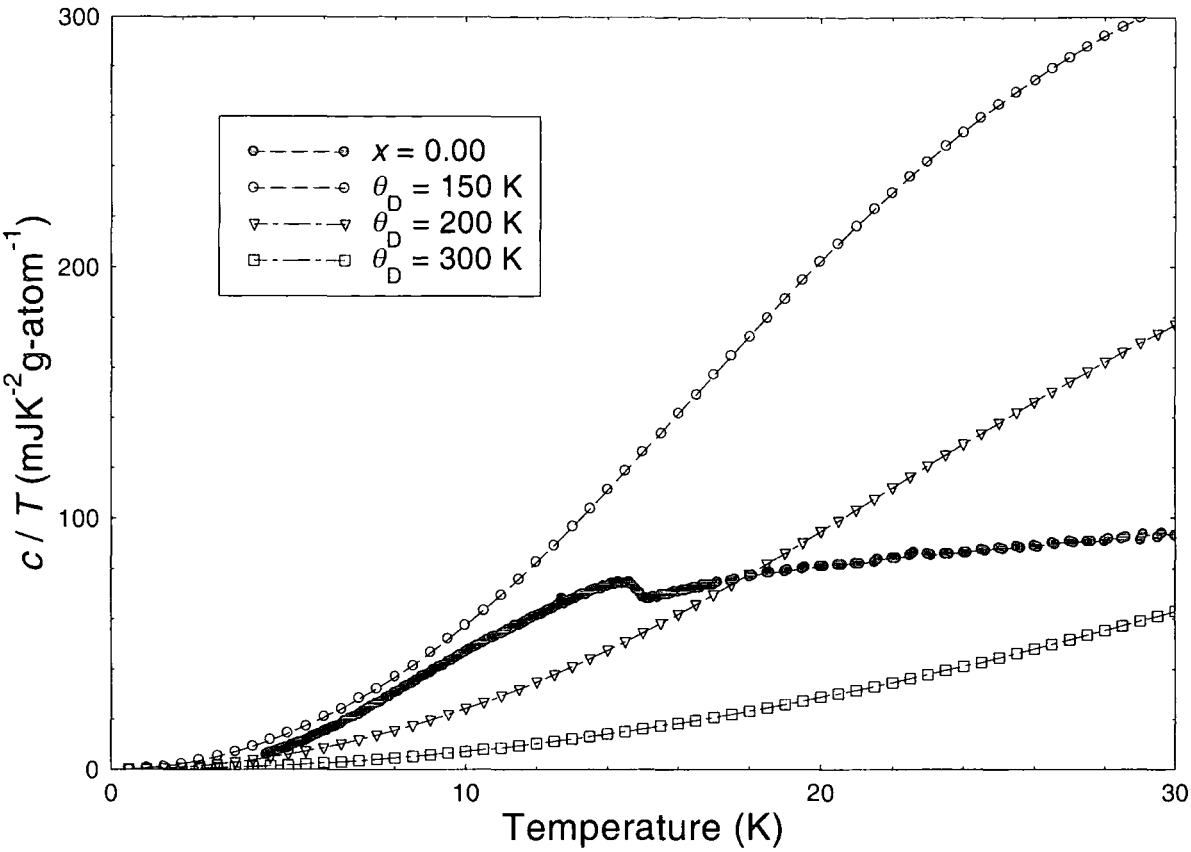


**Figure 7. $c$ / $T$ as a function of temperature for sample $x$ = 0.00 and calculated from Eqn. (6.2) for Debye temperatures of 150 K, 200 K and 300 K.**

Calculations of $c_L$ using this full functional form are presented in Fig. 7 with the data for the $x$ = 0.00 sample. It is clear from Fig 7. that a single value of $\theta_D$ is not sufficient to represent the normal state data. More complicated analysis can be done using several values of $\theta_D$ as a simple approximation to the phonon spectrum [68, 318]. These methods rely on specific heat data at very low temperatures to characterise an initial value of $\theta_D$, either in the superconducting state where the electronic contribution vanishes exponentially or from doped samples with a similar phonon density of states where the $T_c$ is suppressed. Estimates of $\gamma$ and $\theta_D$ and the corresponding subtraction of the lattice contribution can therefore not be achieved without either superconducting data at very low temperatures or normal state data (in large magnetic fields).

### 6.5.3 Specific heat jump.

Due to the width of the superconducting transitions, extrapolation of the data above and

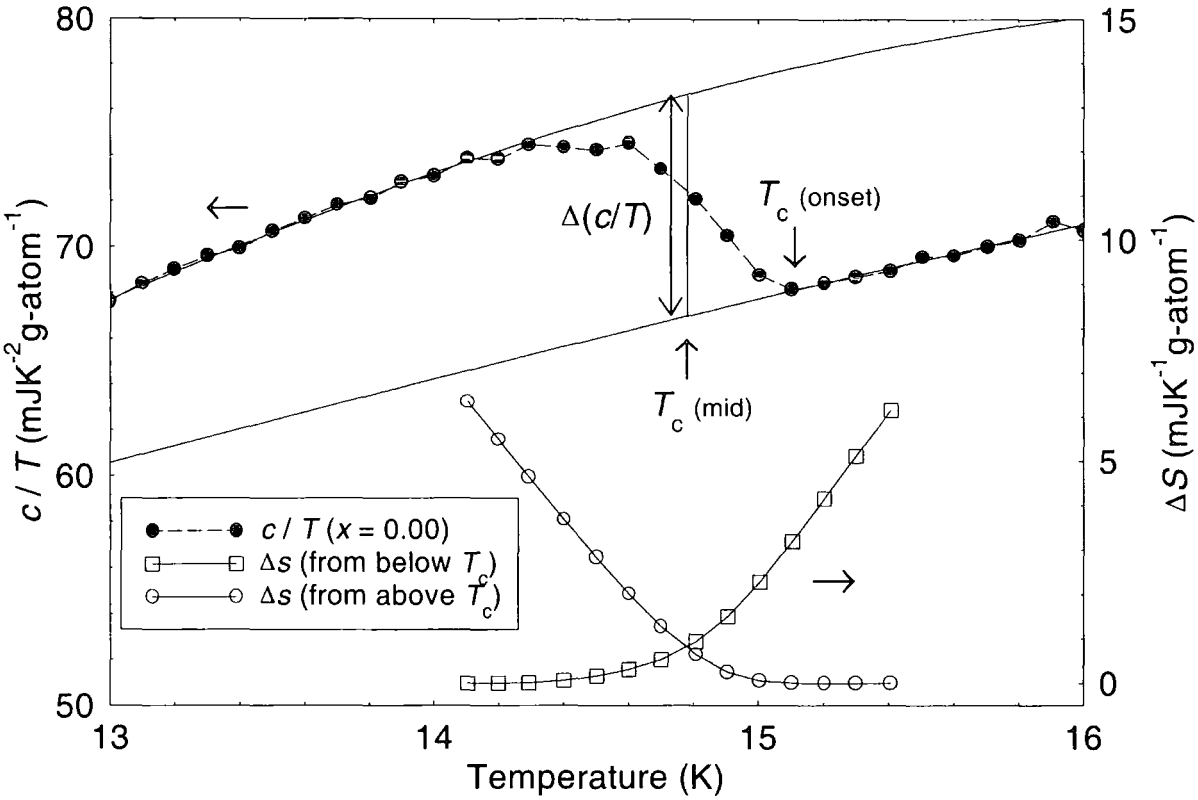


**Figure 8. $c$ / $T$ and $\Delta S$ as a function of temperature for $x$ = 0.00, showing extrapolations (solid lines) to data above and below the specific heat jump, allowing $T_{c(mid)}$, $T_{c(onset)}$, $\Delta T_c$ and $\Delta c/T$ to be determined.**

below the jump region is used for each sample to determine the transition temperature and size of the specific heat jump ($\Delta c/T_c$).

Figure 8 shows the analysis for the $x$ = 0.00 sample. The data above and below the jump region are fitted to separate polynomials of the form $c / T = a + bT^2 + cT^4 + dT^6$ where a, b, c and d are constants. The fitted curves are then extrapolated into the jump region and the difference between the measured data and the extrapolated curves is calculated. To define the temperature of the midpoint of the specific heat jump ($T_{c(mid)}$) an idealised transition is calculated that has the same entropy change, from normal to superconducting states, as the measured jump. Integrating the difference between the data and both of the extrapolated curves gives the entropy change ($S = \int (c(T) / T)\, dT$), as shown at the bottom of Fig. 8, and allows the temperature at which the integrated values are equal to be defined as $T_{c(mid)}$. Once $T_{c(mid)}$ is defined, the size of the jump in the specific heat ($\Delta c/T_c$) of the idealised transition is determined from the extrapolated curves at $T_{c(mid)}$. The onset of the

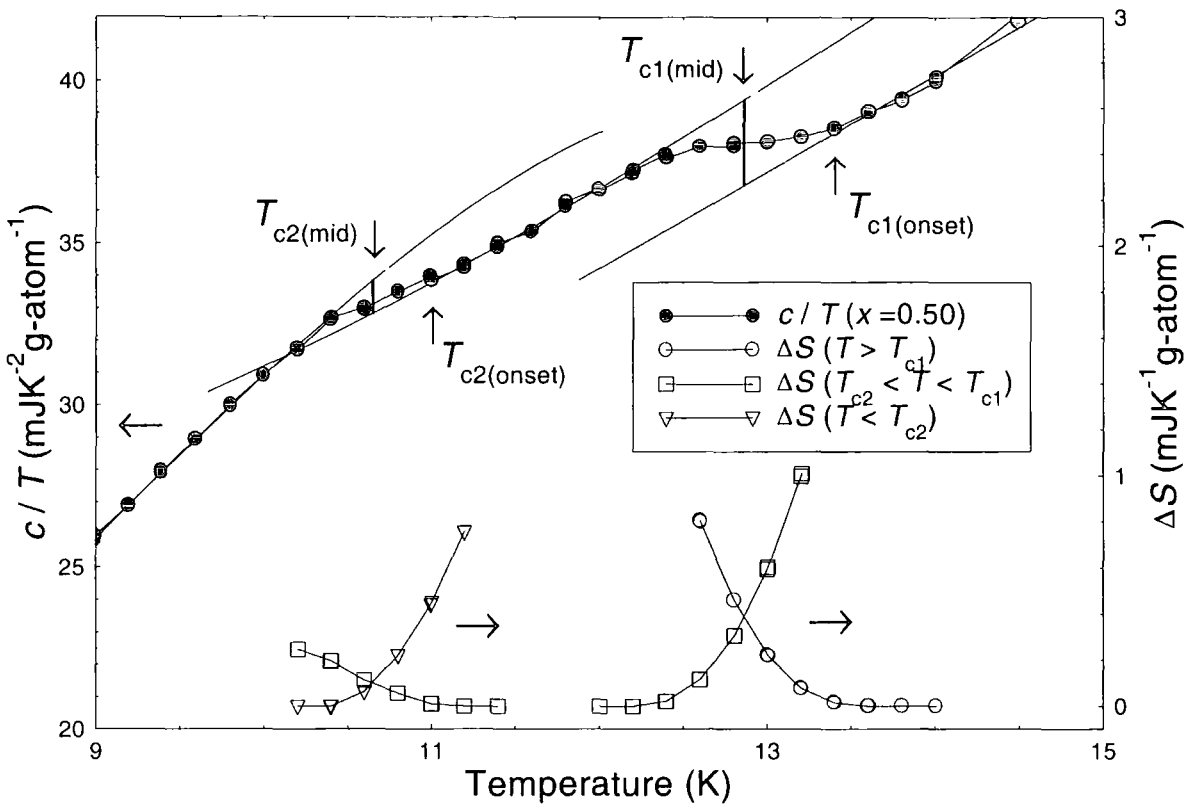


**Figure 9. $c$ / $T$ and $\Delta S$ as a function of temperature for $x$ = 0.50 at both transitions ($T_{c1}$ and $T_{c2}$) showing extrapolations (solid lines) to data above and below each jump.**

superconducting transition ($T_{c(onset)}$) can be defined as the temperature at which the data deviates from the extrapolated curve above $T_c$ by more than 1 %. The temperature of the completion of the jump can be similarly defined and the superconducting transition width $\Delta T_c$ can then be determined. Figure 9 shows the data for the sample $x$ = 0.50, analysis is done at both specific heat anomalies (defined $T_{c1}$ and $T_{c2}$) giving two values of $T_{c(mid)}$, $T_{c(onset)}$, $\Delta T_c$ and $\Delta c/T_c$.

The finite width of the measured specific heat jump is a characteristic of materials that contain a distribution of superconducting parameters due to defects, impurities or strain fields [110]. The sharpest specific heat transitions are obtained for the $x$ = 0.00 and $x$ = 1.00 samples indicating that these are the most homogeneous samples. The widths of the specific heat transition in these samples of $\Delta T_c$ < 1 K is in good agreement with specific heat data from other authors [127, 316]. The low doped compounds ($x$ = 0.05 and 0.10) have much broader transitions indicating a range of compositions within the two samples. Substitution of the copper atoms onto the lead sites inevitably leads to a variation in stoichiometry within the material and is the most likely explanation for the larger transition

widths since these samples are still single phase. The $x = 0.30$ compound has a transition width that is smaller than the low doped compounds although the severely reduced jump height makes determination of the onset and completion of the jump extremely difficult. The $x = 0.50$ compound has two transitions both of which have a similar width to the parent compounds. The presence of two phases within this sample could promote a smaller distribution of superconducting parameters of each of the respective phases.

The size of the specific heat jumps presented in table 1 show that the end compounds ($PbMo_6S_8$ and $Cu_{1.8}Mo_6S_8$) have the largest values of $\Delta c/T_c$, with the jump size for the $PbMo_6S_8$ compound being almost twice as large as that of the $Cu_{1.8}Mo_6S_8$ sample. The intermediate compounds have broader superconducting transitions that render the determination of $\Delta c/T_c$ accurate to only about a factor of two, whereas for the $PbMo_6S_8$ and $Cu_{1.8}Mo_6S_8$ compounds the corresponding accuracy is around 10 %. There is no evidence of a systematic variation in $\Delta c/T_c$ with copper content, $T_c$ or $\Delta T_c$. The size of the specific heat jump for the $x = 0.00$ sample, at 9.7 $mJK^{-2}g\text{-}atom^{-1}$ is similar to data from Alekseevskii et al of 10.7 $mJK^{-2}g\text{-}atom^{-1}$ [68] and from Cors et al of 9.8 $mJK^{-2}g\text{-}atom^{-1}$ [127]. Data from Fradin et al [29] and Meulen et al [183] give values of 14.3 $mJK^{-2}g\text{-}atom^{-1}$ and 13.6 $mJK^{-2}g\text{-}atom^{-1}$ respectively that are significantly higher but there is no correlation evident between the jump height and the transition temperature for these samples. The differences in the values of $\Delta c/T_c$ and $T_c$ for samples of $PbMo_6S_8$ with the same nominal composition suggest that sample fabrication plays an important role in determining both superconducting ($T_c$, $\Delta c/T_c$) and normal state properties ($\gamma$).

Comparison of $\Delta c/T_c$ for $Cu_{1.8}Mo_6S_8$ can be made with the data of Flukiger et al [316] for a sample of nominal composition $Cu_{2.4}Mo_6S_8$. The specific heat data exhibits two specific heat jumps at around $T$ = 10.9 K and 6.3 K and are identified as the superconducting transitions of the phases $Cu_{1.8}Mo_6S_8$ and $Cu_{3.2}Mo_6S_8$ respectively. Estimating the fraction of each phase in the sample gives an estimate of the size of the specific heat jump for a sample of single phase $Cu_{1.8}Mo_6S_8$ of 4.4 $mJK^{-2}g\text{-}atom^{-1}$ and 1.9 $mJK^{-2}g\text{-}atom^{-1}$ for a sample of single phase $Cu_{3.2}Mo_6S_8$. The value of 4.57 $mJK^{-2}g\text{-}atom^{-1}$ determined from the data presented here is therefore in good agreement with this estimate.

## 6.5.4 Determination of the Sommerfeld constant ($\gamma$).

| | $\omega_{ln}$ (K) | $T_c$ (K) | $\gamma$ (mJK$^{-2}$ g-atom$^{-1}$) | $\Delta c / T_c$ (mJK$^{-2}$ g-atom$^{-1}$) | $\Delta c / \gamma T_c$ | $c / T_c$ (mJK$^{-2}$ g-atom$^{-1}$) |
|---|---|---|---|---|---|---|
| $PbMo_6S_8$ (a) | $\infty$ (w) | **13.7** | **8.0** | **10.7** | 1.33 | **53** |
| $PbMo_6S_8$ (b) | 181 | **13.3** | **7.0** | **14.3** | 2.05 | **59** |
| $PbMo_6S_8$ (c) | - | **14.5** | - | **9.8** | - | **72** |
| $PbMo_6S_8$ (d) | 185 | **14.3** | **6.5** | **13.6** | 2.09 | **62** |
| $PbMo_6S_8$ (e) | $\infty$ (w)<br>183 (s) | **14.8** | 6.78 (w)<br>4.62 (s) | **9.7** | 1.43 (w)<br>2.10 (s) | **68** |
| $Cu_{1.8}Mo_6S_8$ (f) | - | **10.7** | **4.0** | - | - | **11** |
| $Cu_{1.8}Mo_6S_8$ (g) | - | **10.8** | - | 4.4 | - | **15** |
| $Cu_{1.8}Mo_6S_8$ (e) | $\infty$ (w)<br>163 (s) | **10.7** | 3.20 (w)<br>2.34 (s) | **4.57** | 1.43 (w)<br>1.95 (s) | **19** |

**Table 2. $\gamma$, $\Delta c / T_c$, $\Delta c / \gamma T_c$ and $c / T_c$ for $PbMo_6S_8$ taken from references (a) Alekseevskii [68] (b) Fradin [29] (c) Cors [127] (d) Meulen [183] (e) this author (f) Alekseevskii [185] and (g) [316], values in bold type are either quoted in the reference or determined from the data presented in that reference. The values of $\omega_{ln}$ are determined using the modified BCS relation (Eqn. 6.3) and the values of $\Delta c / \gamma T_c$ in the table. The estimates of $\gamma$ for the $PbMo_6S_8$ sample from this author are made using values of $\Delta c / \gamma T_c$ = 1.43 in the weak coupling regime (w) and 2.10 in the strong coupling regime (s), these values correspond to a value of $\omega_{ln} = \infty$ for the weak coupling limit and $\omega_{ln}$ = 183 K in the strong coupling regime. Similarly estimates for $\gamma$ and $\Delta c / \gamma T_c$ for the $Cu_{1.8}Mo_6S_8$ sample from this author are made using $\omega_{ln} = \infty$ in the weak coupling limit and a value of $\omega_{ln}$ = 163 K determined from tunnelling data of Poppe et al [319, 320] in the strong coupling regime.**

The modified BCS relation [321] for the ratio of the superconducting to normal state electronic contribution to the specific heat is given by:

$$\frac{\Delta c}{\gamma T_c} = 1.43\left[1 + 53\left(\frac{T_c}{\omega_{ln}}\right)^2 \ln\left(\frac{\omega_{ln}}{3T_c}\right)\right] \qquad (6.3)$$

The ratio $\Delta c / \gamma T_c$ is equal to 1.43 in the weak coupling limit but has an additional correction factor that accounts for strong coupling and is characterised by the ratio $T_c / \omega_{ln}$, where $\omega_{ln}$ is a weighted average phonon frequency. Table 2 shows the range of values of various superconducting parameters that have been determined from specific heat data on $PbMo_6S_8$ and $Cu_{1.8}Mo_6S_8$. Also included in table 2 are values of $\omega_{ln}$ calculated for those samples where the ratio $\Delta c / \gamma T_c$ can be determined. The results of Fradin et al and Meulen et al give a value for $PbMo_6S_8$ of the ratio $\Delta c / \gamma T_c \sim 2.0$, suggesting $PbMo_6S_8$ to be a strong coupling material in agreement with measurements on the size of the energy gap [319, 320, 322].

Since the normal state specific heat is dominated by the phonon contribution (section 6.5.1) and the values of $c / T_c$ between the $PbMo_6S_8$ sample measured here and those from other authors are similar, we can conclude that the density of states and therefore the average weighted phonon frequency will also be similar. Under these assumptions the data of Cors et al and Fradin et al in table 1 for $PbMo_6S_8$ provide an estimate for the strong coupling ratio of $\Delta c / \gamma T_c$ in Eqn. (6.3). Taking the weak and strong coupling regimes to have values of this ratio as 1.43 and 2.1 respectively and using the measured value of $\Delta c / T_c$ we can estimate the value of $\gamma$ for our $PbMo_6S_8$ sample to lie between 6.78 $mJK^{-2}g\text{-}atom^{-1}$ (weak coupling) and 4.62 $mJK^{-2}g\text{-}atom^{-1}$ (strong coupling). Both of these estimates of $\gamma$ lie significantly lower than the corresponding values in table 1 determined for equivalent samples with the same ratio of $\Delta c / \gamma T_c$. Since these estimates are lower regardless of the coupling strength we suggest that the size of the specific heat jump is principally determined through $\gamma$ by the electronic density of states at the Fermi level.

Estimates for the value of $\gamma$ for $Cu_{1.8}Mo_6S_8$ cannot be made in the same manner, since there are no values available in the literature of both $\gamma$ and $\Delta c / T_c$ for the same sample. Tunnelling data however allows the BCS ratio $2\Delta(0) / k_B T_c$ to be determined and compared to the modified BCS relation (Eqn. 6.4) for strong coupling superconductors [323]:

$$\frac{2\Delta(0)}{k_B T_c} = 3.52\left[1 + 12.5\left(\frac{T_c}{\omega_{ln}}\right)^2 \ln\left(\frac{\omega_{ln}}{2T_c}\right)\right] \qquad (6.4)$$

A value of $2\Delta(0) / k_B T_c = 3.9$ has been determined for a $Cu_{1.8}Mo_6S_8$ sample with $T_c$ = 10.6 K [319, 320] that gives a value of the ratio $T_c / \omega_{ln} = 0.065$ from Eqn. (6.4) and a corresponding value for $\Delta c / \gamma T_c = 1.95$ using Eqn. (6.3). If this value is taken as an estimate for the strong coupling ratio in Eqn. (6.3) $\gamma$ can be estimated to lie between 3.20 $mJK^{-2}g\text{-}atom^{-1}$ (weak coupling) and 2.34 $mJK^{-2}g\text{-}atom^{-1}$ (strong coupling). Similar to the $PbMo_6S_8$ sample the estimated value of $\gamma$ lies significantly lower than the data available (table 1). Since the normal state heat capacity of the $Cu_{1.8}Mo_6S_8$ samples is in agreement with the data of Flukiger et al [316] the average phonon frequency and therefore the ratios $T_c / \omega_{ln}$ and $\Delta c / \gamma T_c$ will also be similar. The conclusion then follows as before that the value of $\gamma$ for the materials presented here are lower than those of Alekseevskii [185] due to a reduction in the density of states. Furthermore, since the estimated values of $\gamma$ for the $Cu_{1.8}Mo_6S_8$ sample are about

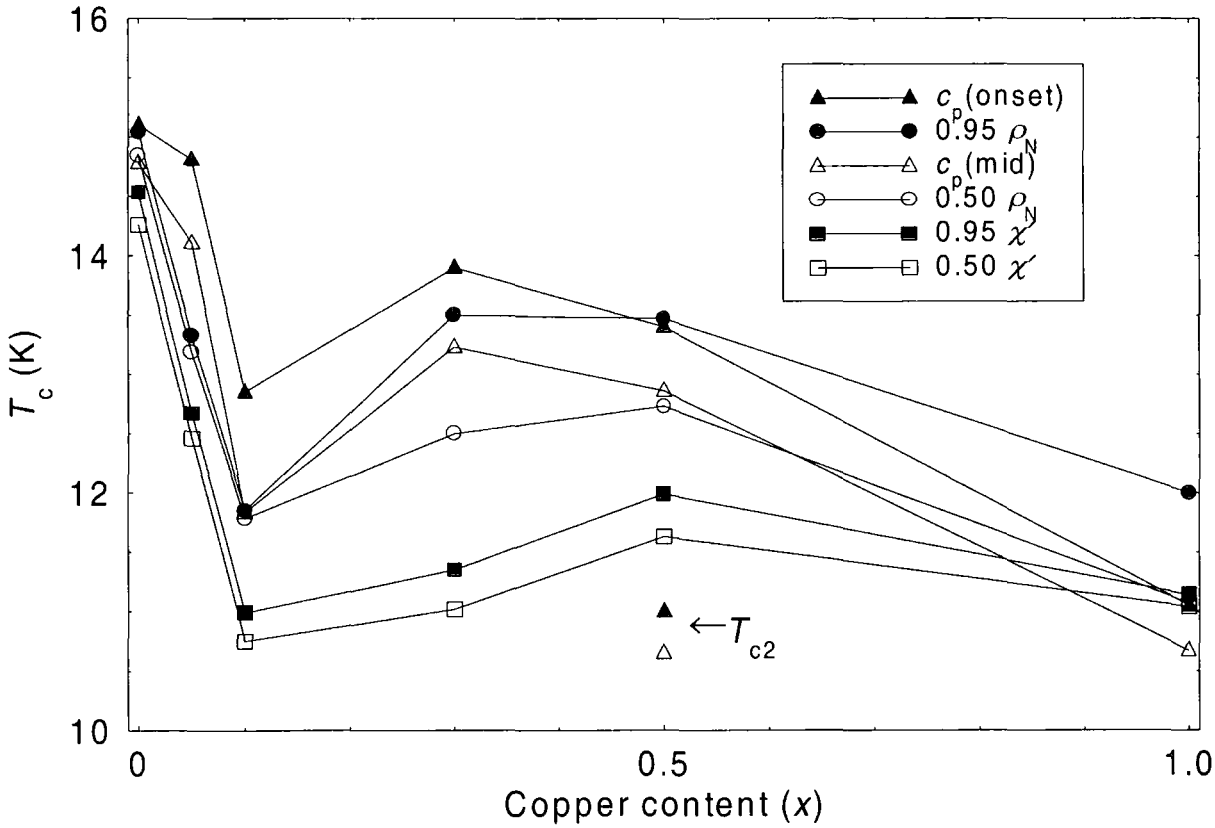


**Figure 10. $T_{c(onset)}$ and $T_{c(mid)}$ determined from specific heat ($c_p$), resistivity (0.95 and 0.50 $\rho_N$) and susceptibility (0.95 and 0.50 $\chi'$) as a function of copper content ($x$) in the series $(Pb_{1-x}Cu_{1.8x})Mo_6S_8$. Secondary transitions in the specific heat of the $x$ = 0.50 sample are labelled $T_{c2}$.**

half that of the $PbMo_6S_8$ sample, we conclude that the density of states is lower in $Cu_{1.8}Mo_6S_8$ by about a factor two and this is the primary reason for the smaller specific heat jump of this sample.

### 6.5.5 Transition temperature ($T_c$).

The transition temperatures of the $Cu_{1.8}Mo_6S_8$ and $PbMo_6S_8$ compounds determined from the specific heat data are among the highest values reported for these compounds [127, 316]. The resistivity and susceptibility data on these samples can also be analysed to give an onset and midpoint of the superconducting transition, defined as 0.95 and 0.50 of the normal state resistivity or susceptibility. Figure 10 presents the onset and midpoints of the superconducting transition of each member of the series as determined by specific heat, resistivity and susceptibility measurements. The results show general agreement between all three techniques for the two end compounds $PbMo_6S_8$ and $Cu_{1.8}Mo_6S_8$, however discrepancies between the techniques are apparent for the intermediate compounds. The susceptibility measurement gives the lowest values of $T_{c(onset)}$ and $T_{c(mid)}$ for all of the samples except the $Cu_{1.8}Mo_6S_8$ compound. The resistivity and specific heat measurements give similar values of $T_{c(onset)}$ and $T_{c(mid)}$ and are both between 1 - 2 K higher than the susceptibility results for the intermediate compounds. Differences between the three techniques are expected due to the nature of the measurements. Detecting the superconducting transition by a susceptibility measurement requires a much larger proportion of the grain boundaries to be superconducting than a resistivity measurement and so generally produces a lower $T_c$. The specific heat is a bulk measurement however that does not rely on grain boundaries and is therefore able to measure the superconducting properties of all parts of the sample.

As the copper content is increased all three measurement techniques show a drop in both $T_{c(onset)}$ and $T_{c(mid)}$ from the highest value for $x = 0.00$ to the lowest value for $x = 1.00$ and a transition temperature for the $x = 0.10$ sample that is lower than the other intermediate samples. Apart from the $x = 0.10$ sample, the specific heat results show a general decrease

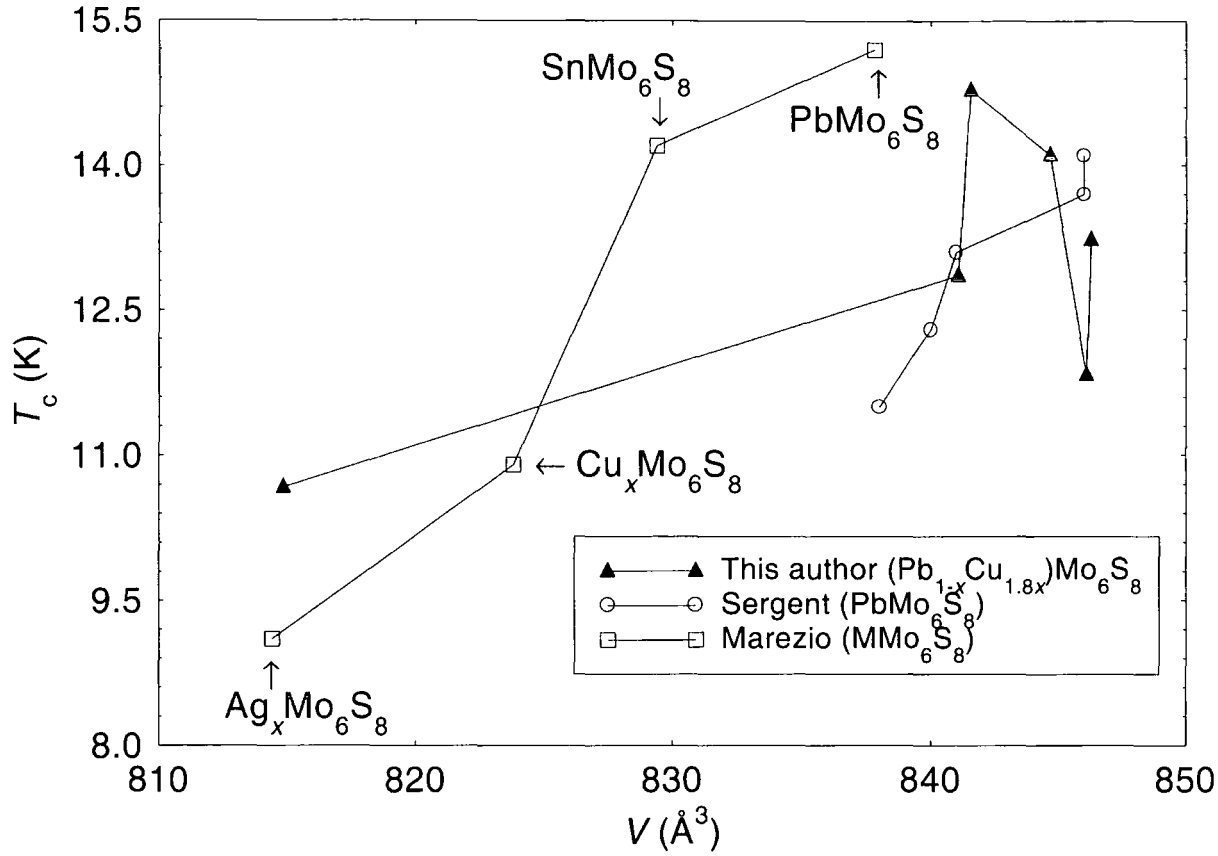


**Figure 11. $T_{c(onset)}$ and $T_{c(mid)}$ from specific heat measurements as a function of unit cell volume for the $(Pb_{1-x}Cu_{1.8x})Mo_6S_8$ series, compared with results from Sergent [191] and Marezio [190].**

in $T_c$ with increasing copper content whereas the other techniques do not. The resistivity onset values give similar values for the $x$ = 0.05, 0.30 and 0.50 samples and the susceptibility and resistivity midpoint give $T_{c(onset)}$ and $T_{c(mid)}$ values for the $x$ = 0.50 sample higher than the $x$ = 0.30 sample. The transition of the $Cu_{1.8}Mo_6S_8$(Pb) phase detected in the specific heat of the $x$ = 0.50 sample has $T_{c(onset)}$ and $T_{c(mid)}$ values equal to that of the $x$ = 1.00 sample, within the measurement error.

Most of the Chevrel phases have superconducting properties that are sensitive to stoichiometry and the nature of the metal cation [172]. Substituting or inserting different cations into the unit cell alters the superconducting properties of the host material by changing the lattice dimensions and the charge transfer from the metal ion. Both of these effects can alter the superconducting density of states at the Fermi level and therefore the superconducting properties. Calculations from susceptibility and specific heat measurements indicate that the density of states of $PbMo_6S_8$ at the Fermi level is about

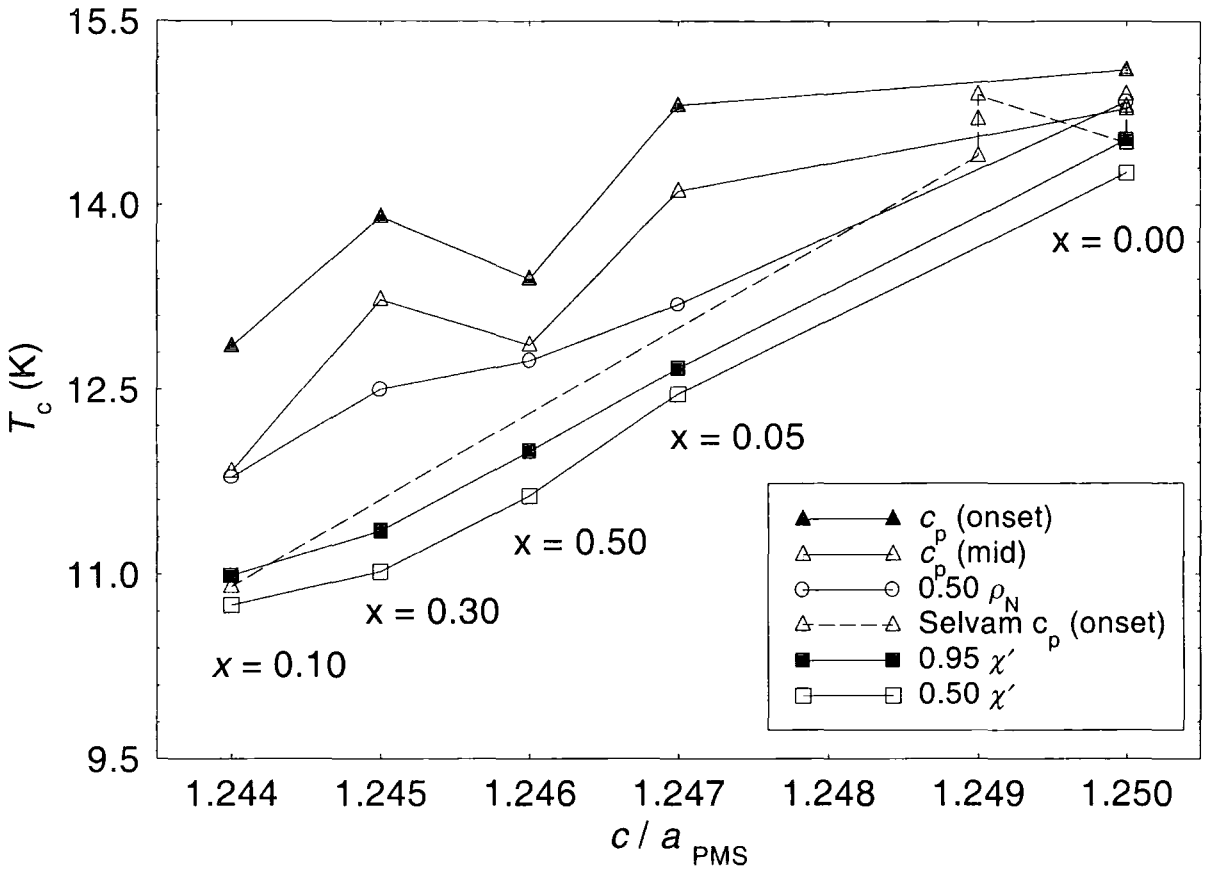


**Figure 12. $T_{c(onset)}$ and $T_{c(mid)}$ from specific heat, resistivity and susceptibility measurements for the $(Pb_{1-x}Cu_{1.8x})Mo_6S_8$ series as a function of $c$ / $a$ ratio for the $PbMo_6S_8$ phase and compared to results for $PbMo_6S_8$ by Selvam [162].**

twice as large as that of $Cu_{1.8}Mo_6S_8$ [172]. Substituting copper ions for lead ions in the unit cell systematically reduces the charge transfer from the metal ions to the $Mo_6S_8$ clusters. The corresponding variation in $T_c$ is not systematic however suggesting that the change in lattice dimensions also has an influence on the density of states at the Fermi level.

Variations in $T_c$ of $PbMo_6S_8$ with different fabrication routes have been correlated with the ratio of $c$ / $a$ (the hexagonal lattice parameters) and with the volume of the unit cell, parameters both determined from X-ray data [162, 191]. The values of $T_{c(mid)}$ determined from the specific heat measurements are presented in Fig. 11 as a function of the unit cell volume along with data from Sergent et al [191] on samples of $PbMo_6S_8$ fabricated by different routes and data from Marezio et al [190] on different Chevrel phases. The values of $T_{c(onset)}$ and $T_{c(mid)}$ determined from all three measurements are plotted in Fig. 12 as a function of $c$ / $a$ ratio for the $PbMo_6S_8$ phase along with data from Selvam [162] on

different samples of $PbMo_6S_8$. The upper transition in the specific heat data for the $x$ = 0.50 sample is assumed to be the $PbMo_6S_8$(Cu) phase and plotted accordingly.

The results in Fig. 11 show no correlation between the $T_c$ and unit cell volume for the doped samples although the values of the unit cell volume for both $PbMo_6S_8$ and $Cu_{1.8}Mo_6S_8$ samples are in good agreement with the data of Marezio and Sergent. The data in Fig. 12 however show a definite correlation between the $T_c$ and $c$ / $a$ ratio of the $PbMo_6S_8$(Cu) phase and are also in good agreement with the data on $PbMo_6S_8$ from Selvam. The increase in the $c$ / $a$ ratio corresponds to the lattice becoming more cubic. There is less overlap between the superconducting $Mo_6S_8$ clusters in $PbMo_6S_8$ compared to $Cu_{1.8}Mo_6S_8$ and therefore a higher density of states at the Fermi level. The low $T_c$ of the $x$ = 0.10 sample can therefore be explained from Fig. 12 due to its distorted lattice and low density of states. The data from the $Cu_{1.8}Mo_6S_8$ phases in both the $x$ = 0.50 and $x$ = 1.00 samples do not agree with this hypothesis however, having equal values of $T_c$ despite a change in the density of states ($c$ / $a$ = 1.065 for $x$ = 0.50 and $c$ / $a$ = 1.068 for $x$ = 1.00).

Standard BCS theory gives $T_c$ as a function of the electronic density of states at the Fermi level ($N(E_F)$), a pairing potential ($V$) and an average Debye frequency $\langle\omega_D\rangle$ [10]:

$$T_c = 1.14\langle\omega_D\rangle\exp[-1/N(E_F)V] \tag{6.5}$$

If we take $\langle\omega_D\rangle$ = 200 K [29] then we can calculate a value for $N(E_F)V$ from the value of $T_c$ for our $PbMo_6S_8$ sample. Since $N(E_F) \propto \gamma_v / (1+\lambda)$ [110] where $\lambda$ is the electron-phonon coupling constant and $\gamma_v$ is the unit-volume Sommerfeld constant ($JK^{-2}m^{-3}$), we can then determine the change in $N(E_F)V$ from a change in $\gamma$. Using the value of $\gamma$ in the weak coupling regime from table 2 the $T_c$ of $Cu_{1.8}Mo_6S_8$ is then calculated as 1.09 K.

Allen and Dynes [189] have determined a modified equation for $T_c$ that takes into account strong coupling corrections:

$$T_c = f_1 f_2 \frac{\omega_{ln}}{1.20}\exp\left[\frac{-1.04(1+\lambda)}{\lambda-\mu^*-0.62\lambda\mu^*}\right] \tag{6.6}$$

Frequently used approximations for the correction factors $f_1$ and $f_2$ and the coloumb potential $\mu^*$ are $f_1 = f_2 \approx 1$, unless $\lambda >> 1$, and $\mu^*$ = 0.1[83]. The electron-phonon coupling constant can be written as [188]:

$$\lambda = \frac{N(E_F)\langle I^2\rangle}{M\langle\omega^2\rangle} = \frac{A\gamma_v\langle I^2\rangle}{M\langle\omega^2\rangle(1+\lambda)} \tag{6.7}$$

where A is a constant, $\langle I^2 \rangle$ is an average of the electron-phonon interactions over the Fermi surface and $M$ is the molar mass. Assuming that $\langle I^2 \rangle$ remains constant and that we can replace $\langle \omega^2 \rangle$ by $\omega_{ln}^2$ [83], we can use the data so far obtained for $PbMo_6S_8$ in the strong coupling regime to calculate a value of $\lambda$ and determine the constant $A\langle I^2 \rangle$. Using the appropriate values for $Cu_{1.8}Mo_6S_8$ of $\omega_{ln}$, $M$ and $\gamma$ in the strong coupling regime, the transition temperature of $Cu_{1.8}Mo_6S_8$ is then calculated as 10.0 K. Repeating this calculation keeping $\omega_{ln}$ and $M$ constant but changing $\gamma$ gives a value for $T_c$ of $Cu_{1.8}Mo_6S_8$ as 5.5 K. Similarly if $\gamma$ and $M$ are kept constant but $\omega_{ln}$ is allowed to change, $T_c$ for $Cu_{1.8}Mo_6S_8$ is calculated as 16.0 K and if $\omega_{ln}$ and $\gamma$ are kept constant but $M$ is changed, $T_c$ for $Cu_{1.8}Mo_6S_8$ is calculated as 15.9 K.

The conclusion from these calculations is that the reduction in $\gamma$ dominates the corresponding drop in $T_c$ from $PbMo_6S_8$ to $Cu_{1.8}Mo_6S_8$. The correlation of $T_c$ with the $c / a$ ratio for the doped samples, as seen in Fig. 12, is then consistent with this dependence since $\gamma$ is proportional to the density of states at the Fermi level which in turn is affected by the lattice parameters. Within the weak coupling BCS theory the calculated change in $\gamma$ produces an estimate for the $T_c$ of $Cu_{1.8}Mo_6S_8$ that is an order of magnitude to low. Within the strong coupling theory however the change in $\gamma$ also produces a drop in the strength of the electron-phonon coupling ($\lambda$) and the calculated $T_c$ is then only a factor of two lower than the observed value. The reduction in the effective mass of the cation and the phonon frequency from $PbMo_6S_8$ to $Cu_{1.8}Mo_6S_8$ both produce an increase in the electron-phonon coupling constant and a corresponding smaller increase in $T_c$ as expected for a material with stronger electron-phonon coupling. Taken together the changes in $\gamma$, $\omega_{ln}$ and $M$ are all required within the strong-coupling theory to explain the observed change in $T_c$.

### 6.5.6 Determination of kappa.

Using the estimated values of $\gamma$ for both $PbMo_6S_8$ and $Cu_{1.8}Mo_6S_8$ samples, estimates of other superconducting parameters can be made using both modified BCS theory and GLAG theory [110]. The thermodynamic critical field at $T = 0$ K can be estimated in both the weak and strong coupling regimes from the ratio $\gamma T_c^2 / \mu_0 H_c^2(0)$ and the modified BCS relation [321]:

$$\frac{\gamma_v T_c^2}{\mu_0 H_c^2(0)} = 1.68\left[1 - 12.2\left(\frac{T_c}{\omega_{ln}}\right)^2 \ln\left(\frac{\omega_{ln}}{3T_c}\right)\right] \tag{6.9}$$

In the strong coupling regime the ratio of $T_c$ / $\omega_{ln}$ can be determined from the ratio $\Delta c$ / $\gamma T_c$ (Eqn. 6.3) for $PbMo_6S_8$ and the ratio $2\Delta(0)$ / $k_B T_c$ (Eqn. 6.4) for $Cu_{1.8}Mo_6S_8$, as in section 6.5.4. In the weak coupling limit $\mu_0 H_c(0)$ can be determined by setting $T_c$ / $\omega_{ln}$ equal to zero. Using values of $B_{c2}(0)$ and $dB_{c2}$ / $dT$ determined from the resistivity data, estimates of $\kappa_1(0)$ and $\kappa_2(T)$ can also be made using the previously determined values of $\mu_0 H_c(0)$ and $\Delta c$ / $T_c$ and GLAG theory:

$$\kappa_1(T) = \frac{B_{c2}(T)}{\sqrt{2}B_c(T)} \tag{6.10}$$

$$\left.\frac{\Delta c}{T_c}\right|_B = \frac{\left(\frac{dB_{c2}}{dT}\right)^2}{1.16\mu_0\left(2\kappa_2^2(T) - 1\right)} \tag{6.11}$$

| | $\mu_0 H_c(0)$ (T) ($\gamma_v$, $T_c$, $\omega_{ln}$) | | $B_{c2}(0)$ (T) ($0.5\rho_N$) | $dB_{c2}$ / dT ($TK^{-1}$) ($0.5\rho_N$) | $\rho_N$ ($\mu\Omega$cm) |
|---|---|---|---|---|---|
| | Weak | Strong | | | |
| $PbMo_6S_8$ | 0.31 | 0.27 | 47.28 | -4.66 | 80 |
| $Cu_{1.8}Mo_6S_8$ | 0.16 | 0.15 | 13.39 | -1.73 | 82 |

**Table 3. Superconducting parameters calculated for both $PbMo_6S_8$ and $Cu_{1.8}Mo_6S_8$. The values of $\mu_0 H_c(0)$ are calculated in both strong and weak coupling regimes from Eqn. (6.9) and data in table 2, $\rho_N$ is determined from the resistivity data and $B_{c2}(0)$ and $dB_{c2}$ / dT are determined from the midpoints of the resistive transitions [314].**

| | $\kappa_1(0)$ ($\mu_0 H_c(0)$, $B_{c2}(0)$) | | $\kappa_2(T_c)$ ($\Delta c$ / $T_c$, $dB_{c2}/dT$) | $\kappa_2(T_c)$ (VSM) |
|---|---|---|---|---|
| | Weak | Strong | | |
| $PbMo_6S_8$ | 107 | 122 | 93 | 139 |
| $Cu_{1.8}Mo_6S_8$ | 58 | 65 | 48 | 68 |

**Table 4. Values of $\kappa_1(0)$ and $\kappa_2(T_c)$ calculated from various experimental data for both $PbMo_6S_8$ and $Cu_{1.8}Mo_6S_8$ where $\kappa_1(0)$ is determined in both strong and weak coupling regimes. $\kappa_1(0)$ and $\kappa_2(T_c)$ are calculated from Eqn.'s (6.10) and (6.11) respectively using data from table 3 and values of $\Delta c$ / $T_c$ from table 2. Values of $\kappa_2(T_c)$ determined from magnetic (VSM) measurements are also included [315].**

The results of the above calculations are presented in table 3 and table 4. The values of the thermodynamic critical field for $PbMo_6S_8$ are similar to values on previous samples [324] and also with the results from VSM data on these samples that gives $\mu_0 H_c(0) = 0.24$ T for $PbMo_6S_8$ and 0.11 T for $Cu_{1.8}Mo_6S_8$ [315]. An increase in both $\gamma$ and $T_c$ is therefore sufficient to explain the increase in $\mu_0 H_c(0)$ from $Cu_{1.8}Mo_6S_8$ to $PbMo_6S_8$.

The estimates of kappa from the specific heat results and the data in tables 2 and 3 are in good agreement with the value of kappa determined from VSM measurements. The consistency of these values for kappa given the relatively large errors associated with the determination of $\gamma$ and the various assumptions made is taken as reasonable justification for the method of determining $\gamma$. We have already determined that the reduction in $\gamma$ for $Cu_{1.8}Mo_6S_8$ compared to $PbMo_6S_8$ is responsible for both the drop in the size of the specific heat jump (section 6.5.4) and the drop in $\mu_0 H_c(0)$, however these changes would lead to a corresponding increase in kappa. The observed reductions in $B_{c2}(0)$ and $dB_{c2}(T) / dT$ would on their own produce values of kappa for $Cu_{1.8}Mo_6S_8$ that are much lower than those determined here and so changes in both $\gamma$ and the upper critical field are necessary to explain this reduction in kappa.

The Ginzburg-Landau parameter $\kappa_{GL}$ is also given by the equation:

$$\kappa_{GL} = \kappa^c + \kappa^d = \frac{342.34 T_c}{(S/S_F)^2 \gamma^{5/2}} \left( \frac{m^*}{m_e} \right)^4 + 2.37 \times 10^6 \rho_N \gamma^{1/2} \qquad (6.12)$$

where $\rho_N$ is the normal state resistivity, $m^* / m$ is the ratio of effective conduction mass to the electron mass and $S / S_F$ is the ratio of the actual to the free electron Fermi surface areas. Estimates of $m^* / m$ taken from reference [180] on thin film data are 9.6 and 8 for $PbMo_6S_8$ and $Cu_{1.8}Mo_6S_8$ respectively. The ratio of $S / S_F$ typically lies between 0.3 and 0.6 and is taken here as 0.4 for both $PbMo_6S_8$ and $Cu_{1.8}Mo_6S_8$ as in reference [203] page 75. Using the values of $\gamma$, $T_c$ and $\rho_N$ in tables 2 and 3, $\kappa_{GL}$ is then estimated as 77 and 117 for $PbMo_6S_8$ and 90 and 151 for $Cu_{1.8}Mo_6S_8$ in the weak and strong coupling regimes respectively. The dirty limit contribution to $\kappa_{GL}$ is larger for $PbMo_6S_8$ than for $Cu_{1.8}Mo_6S_8$ due to the increase in $\gamma$, however $\kappa^d$ only constitutes about one third of the total ($\kappa_{GL}$) and so these materials must lie somewhere between the dirty and clean limits. The corresponding values of $\kappa^c$ are unreliable due to uncertainties in ($m^* / m$) and ($S / S_F$) and since $\kappa^c$ is the larger of the two contributions to $\kappa_{GL}$, the estimates of $\kappa_{GL}$ are also uncertain.

## 6.6 Conclusion.

A series of high quality $(Pb_{1-x}Cu_{1.8x})Mo_6S_8$ samples have been fabricated with superconducting transition temperatures for the $PbMo_6S_8$ and $Cu_{1.8}Mo_6S_8$ samples among the highest ever reported. Specific heat measurements have been performed in zero field on all these samples and compared to complementary resistivity, susceptibility, magnetisation and X-ray diffraction measurements. At low levels of copper doping ($x \leq 0.10$) the X-ray diffraction patterns show that these samples are single phase $PbMo_6S_8$ with a solid solution of copper. Higher doping levels produce a mixture of $PbMo_6S_8$ and $Cu_{1.8}Mo_6S_8$ phases confirmed by the X-ray diffraction patterns and a double specific heat transition for the $x = 0.50$ sample.

In-field resistivity data has been used to estimate the upper critical field for all of the samples and shows only a slight reduction in $B_{c2}(0)$ with increasing copper content even for the samples with the highest copper content. The estimated values of $B_{c2}(0)$ are significantly higher than the upper critical field of $Nb_3Sn$ for all of the samples except the $Cu_{1.8}Mo_6S_8$ sample which is about three times smaller than that of $PbMo_6S_8$. Values of the critical current density calculated from VSM measurements show that at very low levels of copper doping ($x = 0.05$) the critical current density at low fields is higher than for

$PbMo_6S_8$. This indicates that improvement in the grain boundary properties of $PbMo_6S_8$ may be possible by doping with small cations.

The specific heat measurements have shown a systematic drop in the normal state specific heat as the copper content is increased through the series. This change in the specific heat is correlated with a reduction in the mass of the cation that leads to an increase in the characteristic phonon frequency of the cation and a lower phonon density of states at low temperatures. Substitution of lead ions for copper therefore leads to a systematic reduction in the lattice contribution to the specific heat at these temperatures.

Estimates of $\gamma$ have been made for both $PbMo_6S_8$ and $Cu_{1.8}Mo_6S_8$ from BCS theory in the weak coupling regime and modified BCS theory and complementary data from other authors in the strong coupling regime. These estimates reveal that the value of $\gamma$ for $PbMo_6S_8$ is about twice as large as that for $Cu_{1.8}Mo_6S_8$ and indicate that the relative size of the specific heat jumps for the two compounds is determined by the relative size of $\gamma$.

As copper is substituted onto the lead ion sites the $T_c$ of these samples drops in between that of the two end compounds ($PbMo_6S_8$ and $Cu_{1.8}Mo_6S_8$), this change can be correlated to a change in the lattice parameters and hence a corresponding change in the density of states and $\gamma$. Weak coupling BCS theory is not sufficient however to explain the observed difference in $T_c$ of the two end compounds based solely on a change in $\gamma$. Using strong coupling BCS theory we can explain the observed change in $T_c$ from $PbMo_6S_8$ to $Cu_{1.8}Mo_6S_8$ using estimated values of $\omega_{ln}$, $M$ and $\gamma$ in the strong coupling regime for both of these two compounds. The reduction in $\gamma$ with increasing copper content produces a reduction in the transition temperature that is partly offset by the effect of corresponding reductions in $\omega_{ln}$ and $M$.

Using the measured values of $T_c$ and $\Delta c / T_c$, the estimated values of $\gamma$ and $\omega_{ln}$ and values of $\rho_N$ and $B_{c2}(0)$ from resistivity measurements, values of $\mu_0 H_c(0)$, $\kappa_1(0)$ and $\kappa_2(T_c)$ have all been determined. All of these calculated values are in good agreement with values of $\mu_0 H_c(0)$ and $\kappa_2(T_c)$ determined from VSM measurements and previous data on $PbMo_6S_8$ samples. The values of $\mu_0 H_c(0)$, $\kappa_1(0)$ and $\kappa_2(T_c)$ are about twice as large for $PbMo_6S_8$ as for $Cu_{1.8}Mo_6S_8$ and these differences can be accounted for within the strong coupling BCS theory and GLAG theory. The changes in $\gamma$ are sufficient to account for the differences in $\mu_0 H_c(0)$ however changes in the upper critical field are also required to explain the values

of kappa determined for $Cu_{1.8}Mo_6S_8$. Estimates of $\kappa_{GL}$ based on values of ($m^*$ / $m$) and ($S$ / $S_F$) from the literature are unreliable due to uncertainties in these two factors.

The excellent agreement between parameters derived from specific heat data and separate estimates from magnetisation measurements provides justification for the method of estimating $\gamma$ and indicates the compatibility between the results of both BCS and GLAG theories. The need to use a modified BCS theory to explain the variation in $T_c$ demonstrates that these compounds have a strong electron-phonon coupling mechanism. Finally through the strong coupling BCS theory and the GLAG theory we have shown that the drop in both the normal state specific heat ($c$ / $T$) and the superconducting properties $T_c$, $\Delta c$ / $\gamma T_c$ and $\mu_0 H_c(0)$ can all be related to the change in the normal state properties $\gamma$, $\omega_{ln}$ and $M$ when replacing lead with copper.

# *Chapter 7 - Specific heat measurements on Chevrel phase superconductors doped with magnetic ions.*

## 7.1 Introduction.

Of the vast range of Chevrel phase compounds that have been fabricated $SnMo_6S_8$ and $PbMo_6S_8$ have the highest values of $T_c$ and $B_{c2}(0)$. These two compounds have therefore been extensively investigated in terms of their industrial potential and also to improve the understanding of this class of materials and of superconducting materials in general. Recent improvements in the fabrication of HIP'ed $(Pb,Sn)Mo_6S_8$ wires have produced values of $J_c$ that are close to those required by industry for commercial applications [207]. Other methods of improving $J_c$ have also been investigated and in particular the effect of doping with small cations such as copper to improve the carrier density at the grain boundaries or with magnetic ions to increase the number of flux pinning sites.

Other research on Chevrel phase materials has concentrated on the properties of those compounds containing magnetic ions. Compounds of the form $MMo_6S_8$ and $MMo_6Se_8$ where M is a rare-earth ion have been fabricated and the majority have values of $T_c$ below 5 K for the sulphide series and below 9 K for the selenide series [150]. Many of these compounds also display a magnetically ordered phase that is generally antiferromagnetic and has an ordering temperature below 1.1 K. The coexistence of superconducting and antiferromagnetic states has been confirmed for most of the $MMo_6S_8$ phases at low temperatures [155, 284] and has led to many investigations into the nature of the ordered states in these materials and the effect of magnetic ordering on their superconducting properties. Pseudoternary systems have also been fabricated by substituting or inserting magnetic ions into the unit cell of non-magnetic Chevrel phases [149, 191, 200]. These 'dilute' magnetic systems display many of the traits of the parent compound, such as high values of $B_{c2}(0)$ and $T_c$, as well as effects due to the magnetic ions, such as the compensation effect whereby the upper critical field is improved compared to the parent compound [200].

To investigate the effect of substituting magnetic ions into the $SnMo_6S_8$ and $PbMo_6S_8$ structures members of the series $(Sn_{1-x}Eu_x)Mo_6S_8$ and members of the series $(Pb_{1-x}M_x)Mo_6S_8$ where M = Eu and Gd have been fabricated. The magnetic ions Eu and Gd have been chosen because they both have the similar large values of the Bohr magneton

and so the effects of the magnetic ions can be easily seen. The europium ions are generally in the +2 state whereas the gadolinium ions are in the +3 state and so effects due to the different valence states can also be studied.

In this chapter specific heat measurements on these samples taken by the author are presented along with data from resistivity, susceptibility, magnetisation, X-ray, EDX and TEM measurements taken by Dr. I J Daniel, Dr. D N Zheng, Dr. H J Niu, Dr. M Goringe and N A Morley [325-327]. Phase transitions within the material arising from structural, magnetic or superconducting ordering and the properties of mixed phase materials can all be detected using specific heat measurements. This is therefore an ideal method for studying the nature of these materials and investigating the effect of doping on the normal state, superconducting and magnetic properties. Analysis of the specific heat data is separated into superconducting and magnetic parts. The mean field model is used to discuss the effect of the magnetic ions and to model the magnetic contribution to the specific heat using the calculations detailed in chapter 4. Both the magnetic and superconducting contributions are then discussed in terms of the phase composition of these samples and in comparison to results from other authors. Together with results from the other measurements on these samples the specific heat data is used to make estimates of various superconducting parameters using the BCS strong coupling theory and the GLAG theory.

Sections 7.2 and 7.3 detail the fabrication and experimental procedure respectively. The specific heat data is presented in section 7.4 along with a summary of the additional data taken on these samples. The analysis of the magnetic and superconducting contributions to the specific heat is detailed in section 7.5 and the implications of these results are discussed in section 7.6. The chapter is concluded in section 7.7.

## 7.2 Sample fabrication.

Samples of nominal composition $(Sn_{1-x}Eu_x)Mo_6S_8$ with $x$ = 0.00, 0.35 and 0.50, $(Pb_{0.75}Eu_{0.25})Mo_6S_8$ and $(Pb_{1-x}Gd_x)Mo_6S_8$ with $x$ = 0.00, 0.04, 0.10 and 0.30, were fabricated using solid state reaction procedures. Elemental high-purity powders were used in each case and the molybdenum powder for the $(Pb_{0.75}Eu_{0.25})Mo_6S_8$ sample was reduced under Ar (98%) + $H_2$ (2%) gas flow at 900 °C for 4 hours to remove any oxygen. For each member 15 g of the starting powder was weighed out in the correct stoichiometric

composition and then sintered in a tube furnace under an argon atmosphere using one of three different heat treatments.

The samples of composition $(Sn_{1-x}Eu_x)Mo_6S_8$ were formed by initially reacting EuS and $MoS_2$ separately in evacuated sealed quartz tubes at 420 °C for 10 hrs, 450 °C for 15 hrs and 650 °C for 8 hrs for EuS and 450 °C for 8 hrs and 650 °C for 10 hrs for $MoS_2$, all with a ramp rate of 33 °C / hr. These precursors were then ground together for 40 mins, cold pressed into pellets, sealed in molybdenum crucibles and then reacted at 1150 °C for 45 hrs. Each sample was then removed once more, ground for 40 mins and reacted at 1450 °C for 7 hrs for the $x = 0.0$ sample, 1450 °C for 8 hrs for the $x = 0.50$ sample and at 1350 °C for 0.5 hrs and 1450 °C for 7.5 hrs for the $x = 0.35$ sample. The samples were finally ground, cold pressed, wrapped in molybdenum foil and sealed under vacuum in a stainless steel tube. The tubes were reacted in a HIP at 2000 bar and 800 °C for 2.75 hrs and a further 5.75 hrs at 800 °C while the pressure ramped linearly down to 1 bar.

The $(Pb_{0.75}Eu_{0.25})Mo_6S_8$ sample was sealed in a molybdenum crucible and then sintered at 80 °C for 3 hrs, 420 °C for 8 hrs and 650 °C for 10 hrs, all with a ramp rate of 33 °C / hr, then ramped at a rate of 100 °C / hr to 1000 °C and held for 10 hrs. The powder was then ground for 40 mins and reacted at 1100 °C for 24 hrs and then again at 1150 °C for 24 hrs with intermediate grinding. As for the other samples the powder was then removed, ground, cold pressed, wrapped in molybdenum foil and sealed under vacuum in a stainless steel tube. The sample was then reacted in a HIP at 2000 bar and 800 °C for 8 hrs.

Finally the samples of composition $(Pb_{1-x}Gd_x)Mo_6S_8$ were reacted at 450 °C in a evacuated sealed quartz tube for 4 hrs followed by a temperature ramp at 33 °C / hr to 650 °C and then held for another 8 hrs. The samples were then ground for 1 hour, cold pressed into pellets, sealed in molybdenum crucibles and then reacted again at 1150 °C for 44 hrs and once more at 1500 °C for 6 hrs with intermediate grinding. These samples were finally ground, cold pressed, wrapped in molybdenum foil and sealed under vacuum in a stainless steel tube before being reacted in a HIP at 2000 bar and 900 °C for 6 hrs.

## 7.3 Experimental.

Specific heat measurements were taken using the relaxation method on each of the eight samples. Samples were prepared of mass 52 mg ($SnMo_6S_8$), 47 mg ($(Sn_{0.65}Eu_{0.35})Mo_6S_8$) 46 mg ($(Sn_{0.50}Eu_{0.50})Mo_6S_8$), 43 mg ($(Pb_{0.75}Eu_{0.25})Mo_6S_8$), 57 mg ($PbMo_6S_8$), 45 mg ($(Pb_{0.96}Gd_{0.04})Mo_6S_8$), 16 mg ($(Pb_{0.90}Gd_{0.10})Mo_6S_8$) and 59 mg ($(Pb_{0.70}Gd_{0.30})Mo_6S_8$),. The relaxation method was run for each sample at intervals of 0.25 K for T < ~ 7 K, at intervals of 0.5 K from 7 K up to $T_c$ – 3 K, at intervals of 0.25 K from $T_c$ – 3 K up to $T_c$ + 1.5 K and then at intervals of 1 K from $T_c$ + 1.5 K up to 30 K. Specific heat data was also taken using the long range method for the $(Pb_{0.90}Gd_{0.10})Mo_6S_8$ and $(Pb_{0.70}Gd_{0.30})Mo_6S_8$ samples, both of which exhibited large features in the specific heat at temperatures below 5.5 K. All of these measurements were completed in the high field magnet system at Durham at fields of 0, 3, 6, 9, 12, and 15 T.

X-ray diffraction measurements were carried out on all of the samples and transmission electron microscopy (TEM) and energy dispersive X-ray spectroscopy (EDX) were performed on all of the samples except the $(Pb_{0.75}Eu_{0.25})Mo_6S_8$ sample [326]. Resistivity measurements were performed in zero applied field for all of the samples except the $(Pb_{0.04}Gd_{0.96})Mo_6S_8$ sample and further resistivity measurements were carried out in applied fields up to 15 T for the three samples in the $(Sn_{1-x}Eu_x)Mo_6S_8$ series, the $(Pb_{0.75}Eu_{0.75})Mo_6S_8$ sample and $(Pb_{0.70}Gd_{0.30})Mo_6S_8$ sample [325-327]. Additional vibrating sample magnetometry measurements were performed on all but the $(Pb_{0.75}Eu_{0.25})Mo_6S_8$ and $(Pb_{0.96}Gd_{0.04})Mo_6S_8$ samples at 4.2 K up to applied fields of 15 T and susceptibility measurements were performed on the $(Sn_{1-x}Eu_x)Mo_6S_8$ samples and the $(Pb_{0.75}Eu_{0.25})Mo_6S_8$ sample [325, 327].

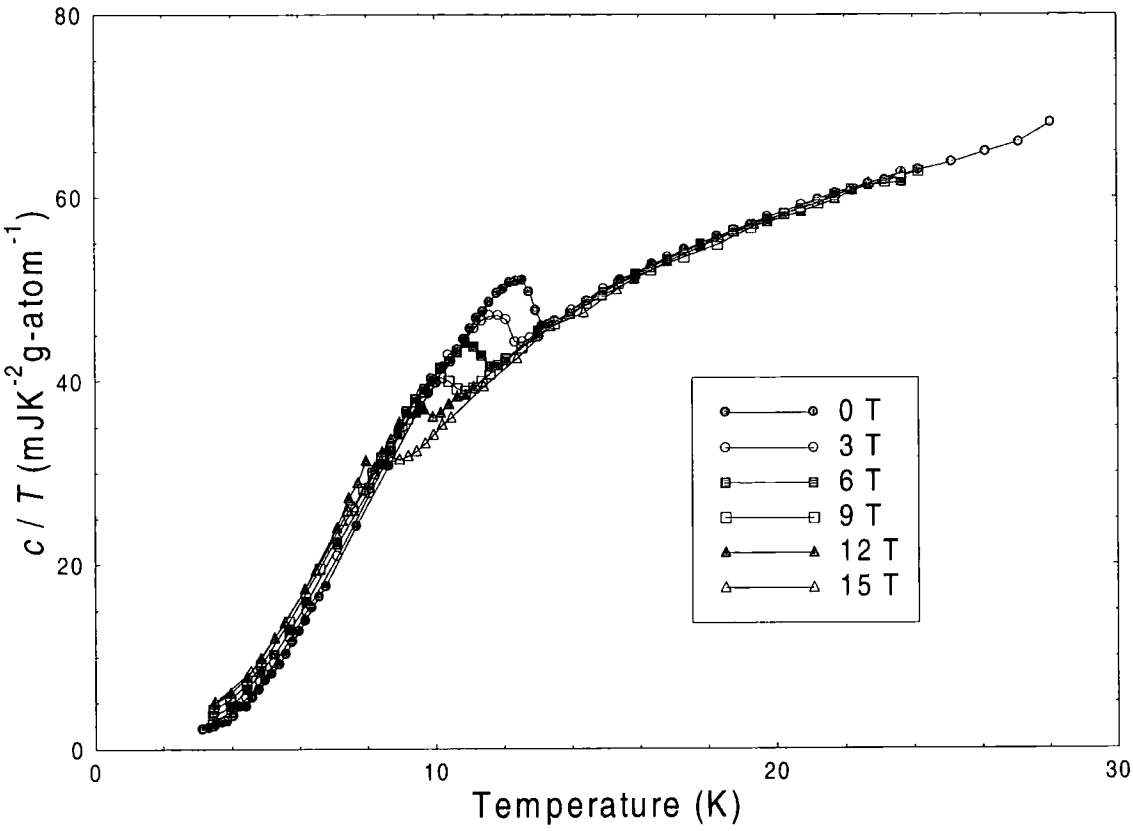


**Figure 1.** *c / T* **as a function of temperature and applied field for $SnMo_6S_8$.**

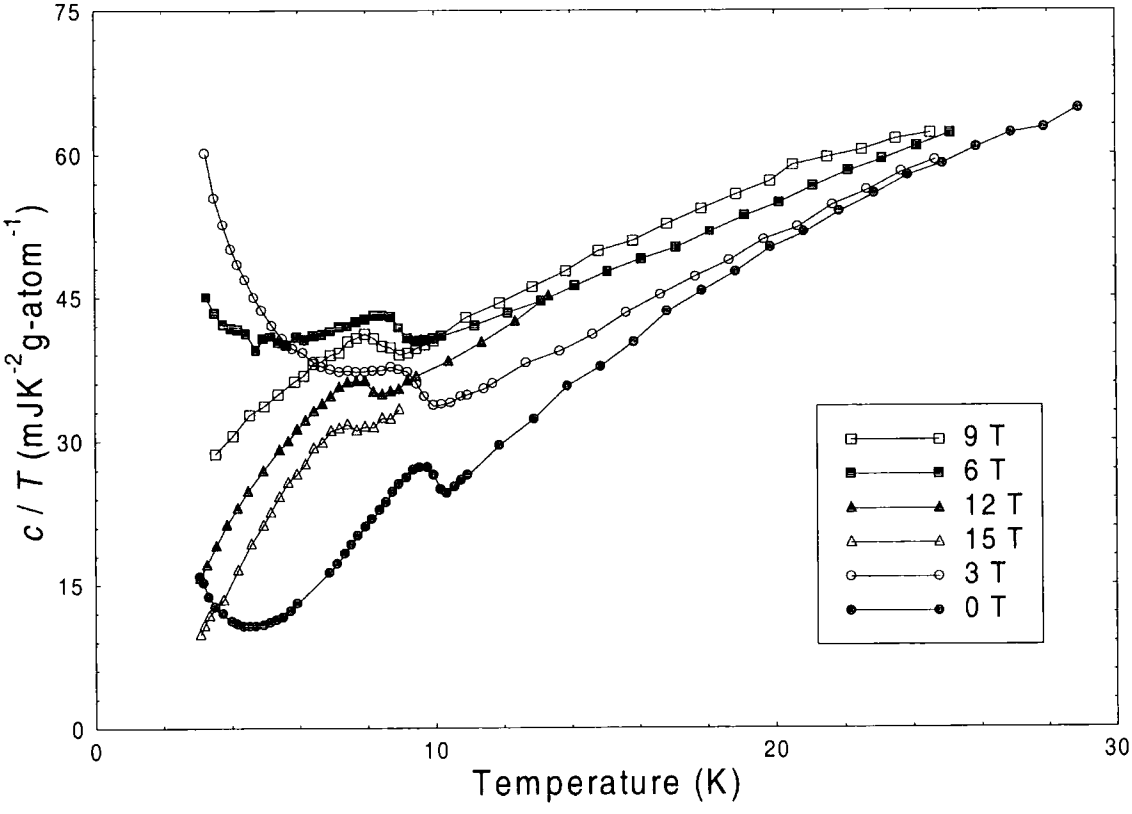


**Figure 2.** *c / T* **as a function of temperature and applied field for $(Sn_{0.65}Eu_{0.35})Mo_6S_8$.**

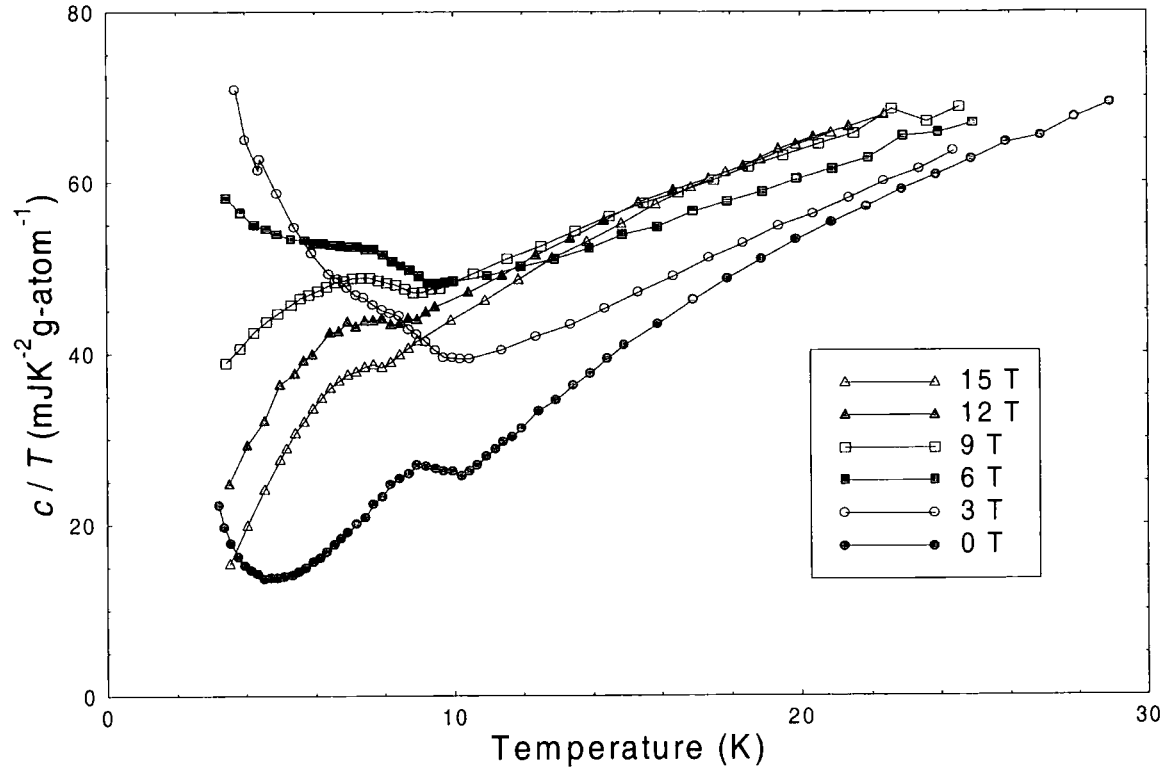


**Figure 3.** *c / T* **as a function of temperature and applied field for** $(Sn_{0.50}Eu_{0.50})Mo_6S_8$.

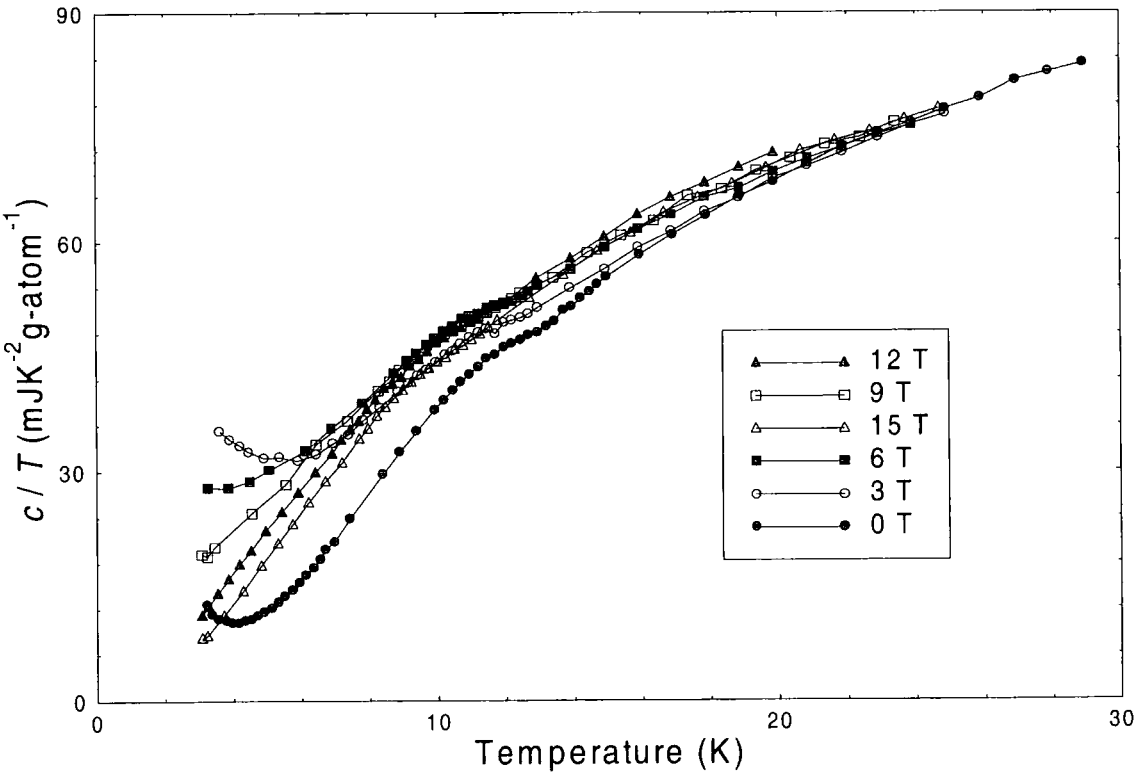


**Figure 4.** *c / T* **as a function of temperature and applied field for** $(Pb_{0.75}Eu_{0.25})Mo_6S_8$.

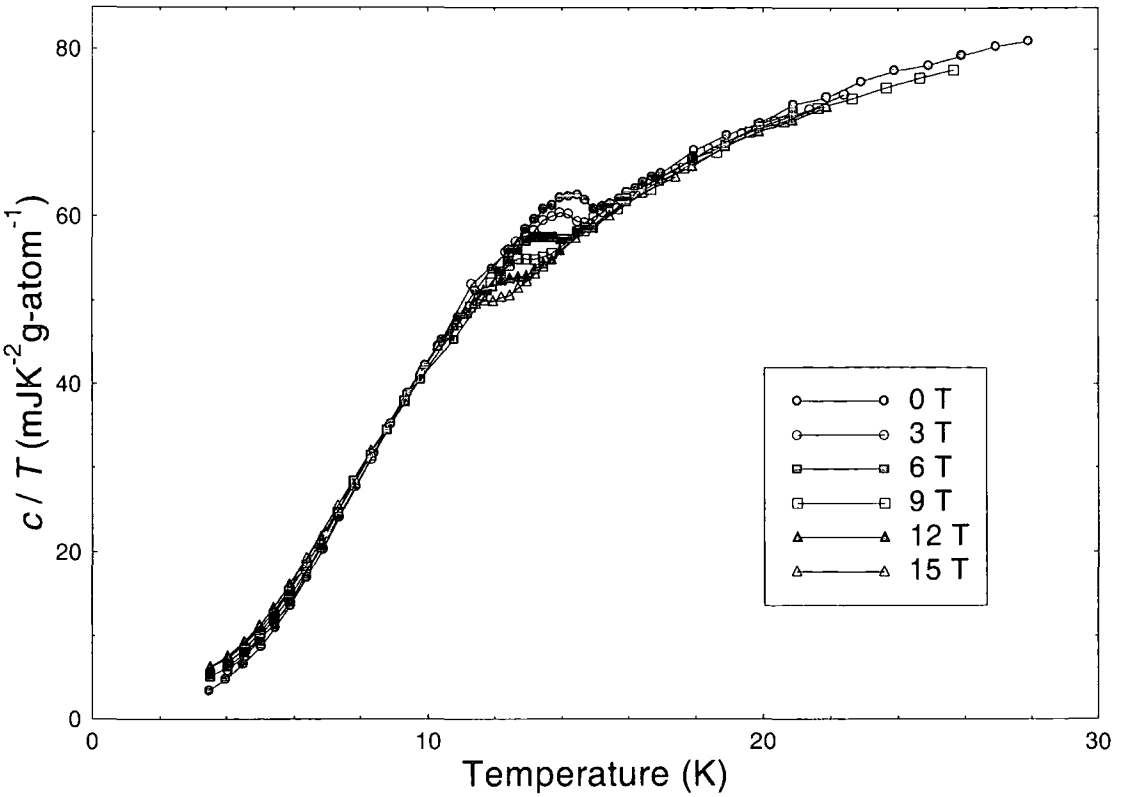


**Figure 5.** *c / T* **as a function of temperature and applied field for $PbMo_6S_8$.**

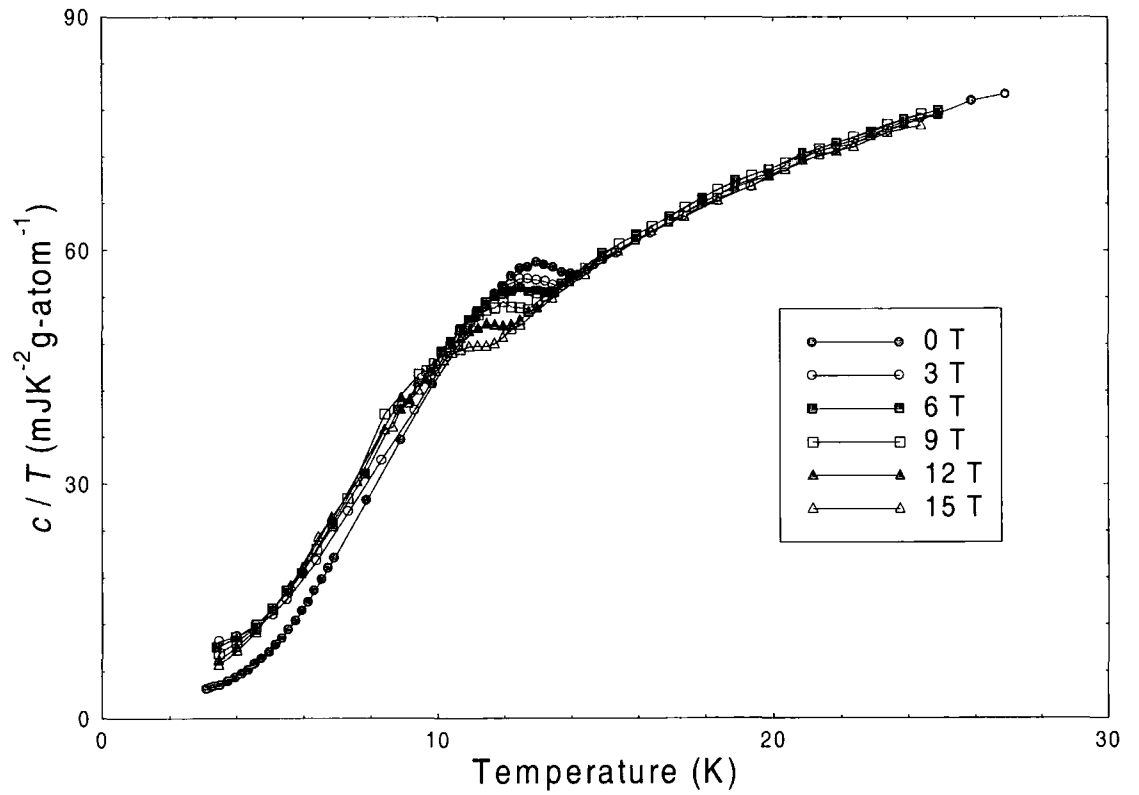


**Figure 6.** *c / T* **as a function of temperature and applied field for $(Pb_{0.96}Gd_{0.04})Mo_6S_8$.**

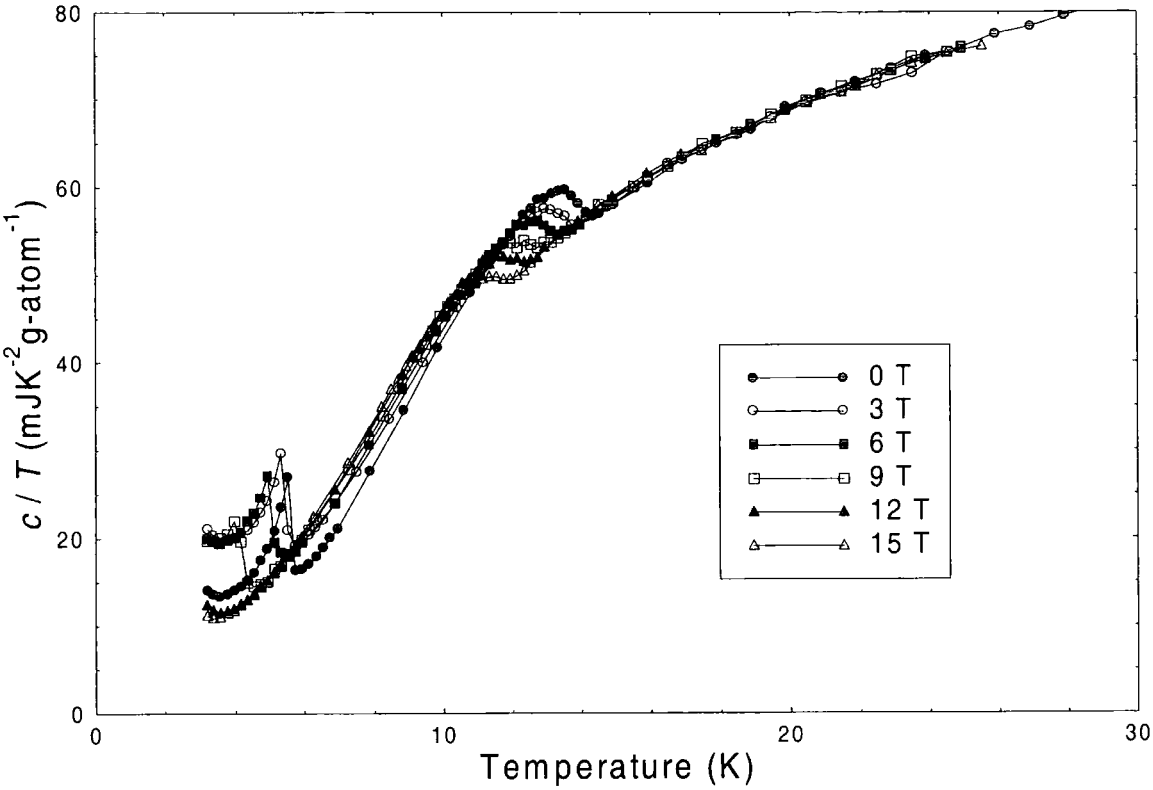


**Figure 7.** *c / T* **as a function of temperature and applied field for $(Pb_{0.90}Gd_{0.10})Mo_6S_8$.**

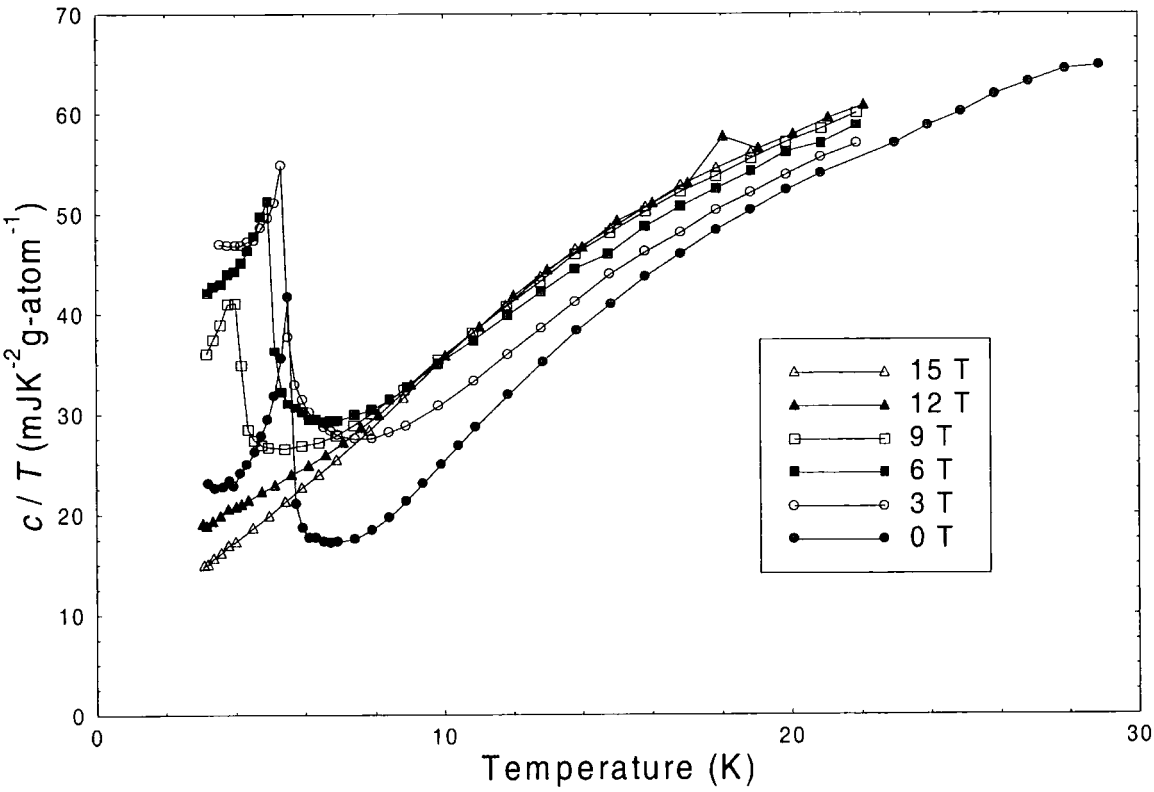


**Figure 8.** *c / T* **as a function of temperature and applied field for $(Pb_{0.70}Gd_{0.30})Mo_6S_8$.**

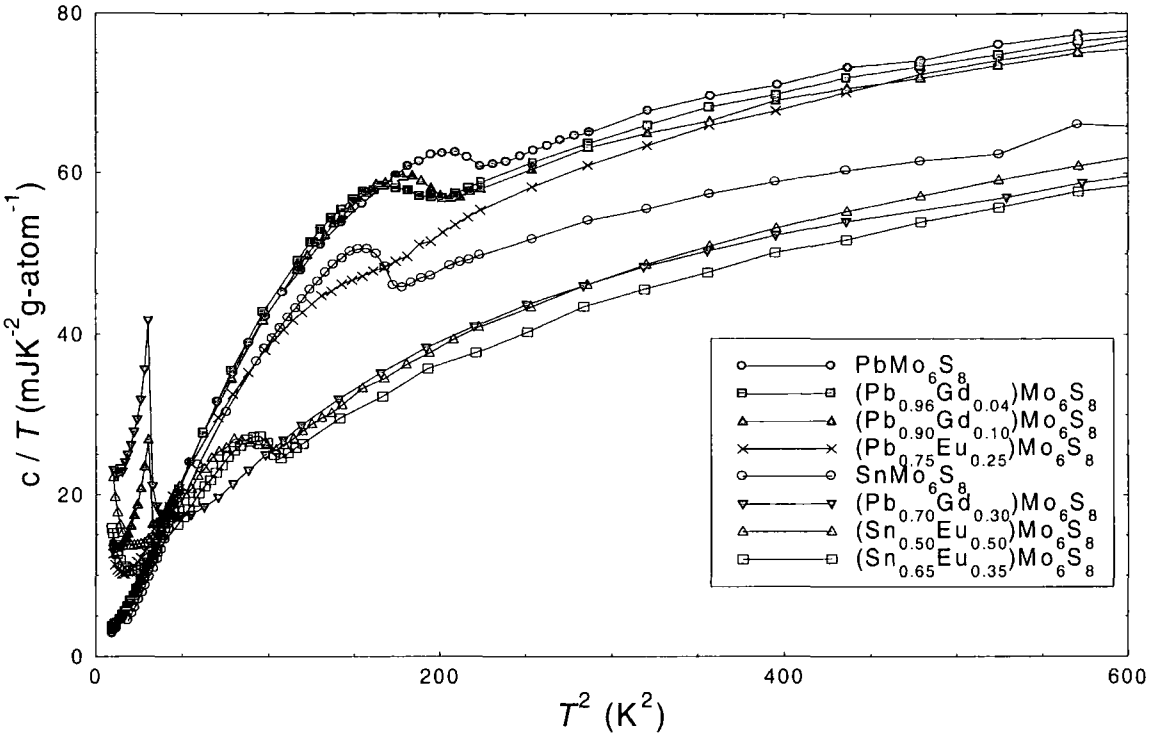


**Figure 9.** $c$ / $T$ **as a function of** $T^2$ **in zero applied field for** $(Sn_{1-x}Eu_x)Mo_6S_8$ **with** $x$ **= 0.0, 0.35 and 0.50,** $(Pb_{0.75}Eu_{0.25})Mo_6S_8$ **and** $(Pb_{1-x}Gd_x)Mo_6S_8$ **with** $x$ **= 0.0, 0.04, 0.10 and** $(Pb_{0.70}Gd_{0.30})Mo_6S_8$.

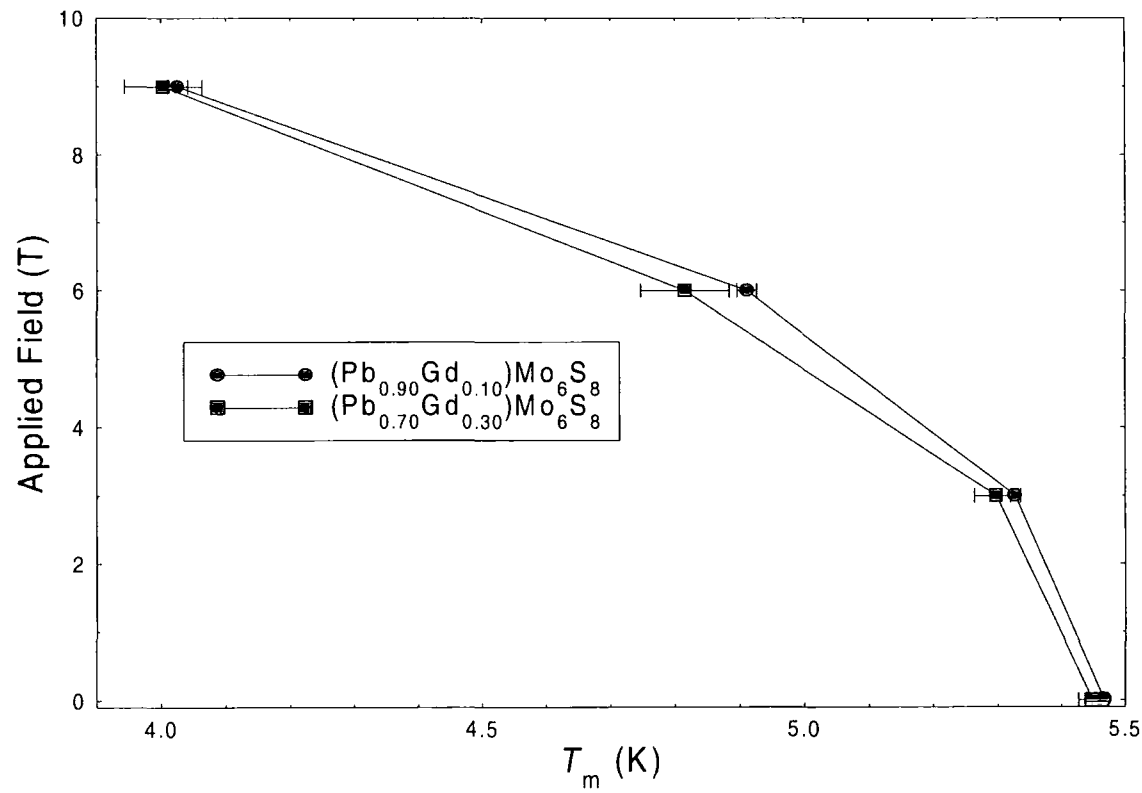


**Figure 10. Applied field as a function of magnetic ordering temperature for** $(Pb_{0.90}Gd_{0.10})Mo_6S_8$ **and** $(Pb_{0.70}Gd_{0.30})Mo_6S_8$.

## 7.4 Results.

Figures 1 to 8 present the specific heat data obtained using the relaxation method as $c / T$ versus $T$ for all of the eight samples in applied magnetic fields from 0 to 15 T. Figure 9 presents the specific heat of all of the eight samples in zero applied field on a Debye plot ($c / T$ versus $T^2$). In each case the measured heat capacity results have the addenda subtracted from them using the polynomial expression in section 5.5.3 (table 3) and are then divided by the sample mass to give $c(T)$ in $JK^{-1}g^{-1}$. The results are converted into units of $JK^{-1}g$-atom$^{-1}$ by multiplying the value in $JK^{-1}g^{-1}$ by the molecular mass of the unit cell for each compound and then dividing by the nominal number of atoms per unit cell (e.g. for $PbMo_6S_8$, 1 $mJK^{-1}g^{-1}$ = 1.0393 $JK^{-1}mole^{-1}$ = (1.0393 / 15) $JK^{-1}g$-atom$^{-1}$).

Figure 10 shows the temperature of the sharp peak in the specific heat of the $(Pb_{0.90}Gd_{0.10})Mo_6S_8$ and $(Pb_{0.70}Gd_{0.30})Mo_6S_8$ samples determined from the long range pulse. The noise on the long range pulse data for the $(Pb_{0.70}Gd_{0.30})Mo_6S_8$ sample was approximately 20 times greater than that for the $(Pb_{0.90}Gd_{0.10})Mo_6S_8$ sample and consequently the accuracy of the values of $T_m(B)$ determined for the $(Pb_{0.70}Gd_{0.30})Mo_6S_8$ sample is a factor four lower than for the $(Pb_{0.90}Gd_{0.10})Mo_6S_8$ sample. Within the error of the measurement we can therefore take the values of $T_m(B)$ for both samples to be the same and so in zero field $T_m$ = 5.467 ± 0.012 K.

Although 75 % of the specific heat data was fine, some minor corrections were required on the following sets: The data taken on the $SnMo_6S_8$ sample was compared to two subsequent, separate measurements in zero field on the same sample and found to be incorrect in both temperature and the magnitude of the specific heat. A short between the two current carrying leads of the thermometer / heater was taken to be responsible and so a percentage correction to the current through the thermometer / heater was included. The original data was then re-analysed and found to be in agreement in zero field with the results from the subsequent measurements; The data taken on the $(Sn_{0.65}Eu_{0.35})Mo_6S_8$ sample in both 12 T and 15 T applied fields was affected by large temperature drifts that made analysis of this data extremely inaccurate above 9 K and 13 K respectively; The normal state specific heat of the 3 T, 12 T and 15 T traces for the $(Pb_{0.96}Gd_{0.04})Mo_6S_8$ sample were all offset by a constant amount from the normal state specific heat of the 0 T, 6 T and 9 T traces and the time constant ($\tau^{sys}$) in going from the 9 T trace to the subsequent 3 T trace was approximately doubled. This was attributed to one of the support wires

having become detached from the sample (confirmed upon opening the probe) after the 9 T trace and so a 5 % reduction in the addenda was used to account for this.

The specific heat results show a clear jump in the specific heat capacity of each sample in zero applied field, in the region between 9 K and 15 K, except for the $(Pb_{0.70}Gd_{0.30})Mo_6S_8$ sample where no such transition is visible. In addition the $(Pb_{0.90}Gd_{0.10})Mo_6S_8$ and $(Pb_{0.70}Gd_{0.30})Mo_6S_8$ samples show a sharp peak in the specific heat at about 5.5 K in zero applied field. All of the jumps in the specific heat occur at successively lower temperatures as the applied field is increased and for the low temperature jumps in the $(Pb_{0.90}Gd_{0.10})Mo_6S_8$ and $(Pb_{0.70}Gd_{0.30})Mo_6S_8$ samples the position of the peak is lowered to a temperature below the base temperature of the measurement (~ 3K) in fields above 9 T.

In the samples with large levels of doping ($(Sn_{0.65}Eu_{0.35})Mo_6S_8$, $(Sn_{0.50}Eu_{0.50})Mo_6S_8$, $(Pb_{0.75}Eu_{0.75})Mo_6S_8$ and $(Pb_{0.70}Gd_{0.30})Mo_6S_8$), the normal state specific heat has a field dependent contribution. The superposition of this field dependent contribution and the

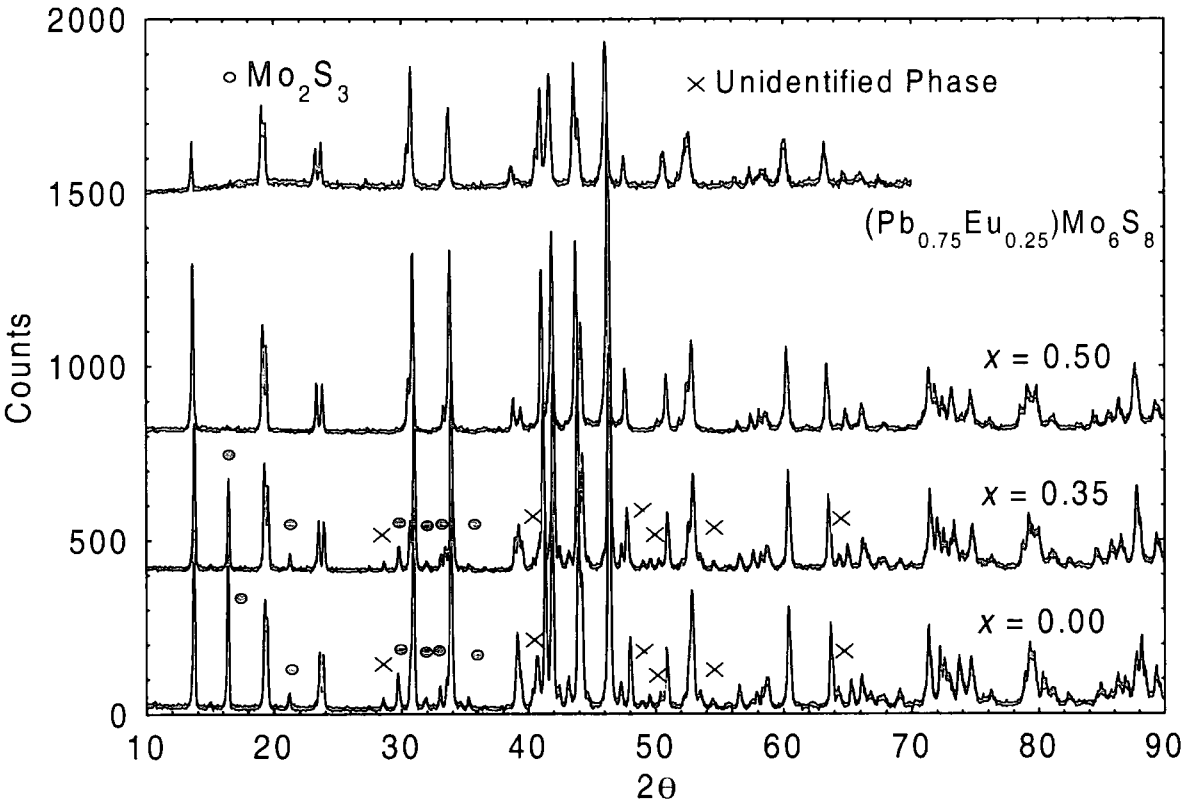


**Figure 11. X-ray diffraction patterns for $(Sn_{1-x}Eu_x)Mo_6S_8$ with $x$ = 0.00, 0.35 and 0.50 and for $(Pb_{0.75}Eu_{0.25})Mo_6S_8$. Data taken by H J Niu on a single set of samples.**

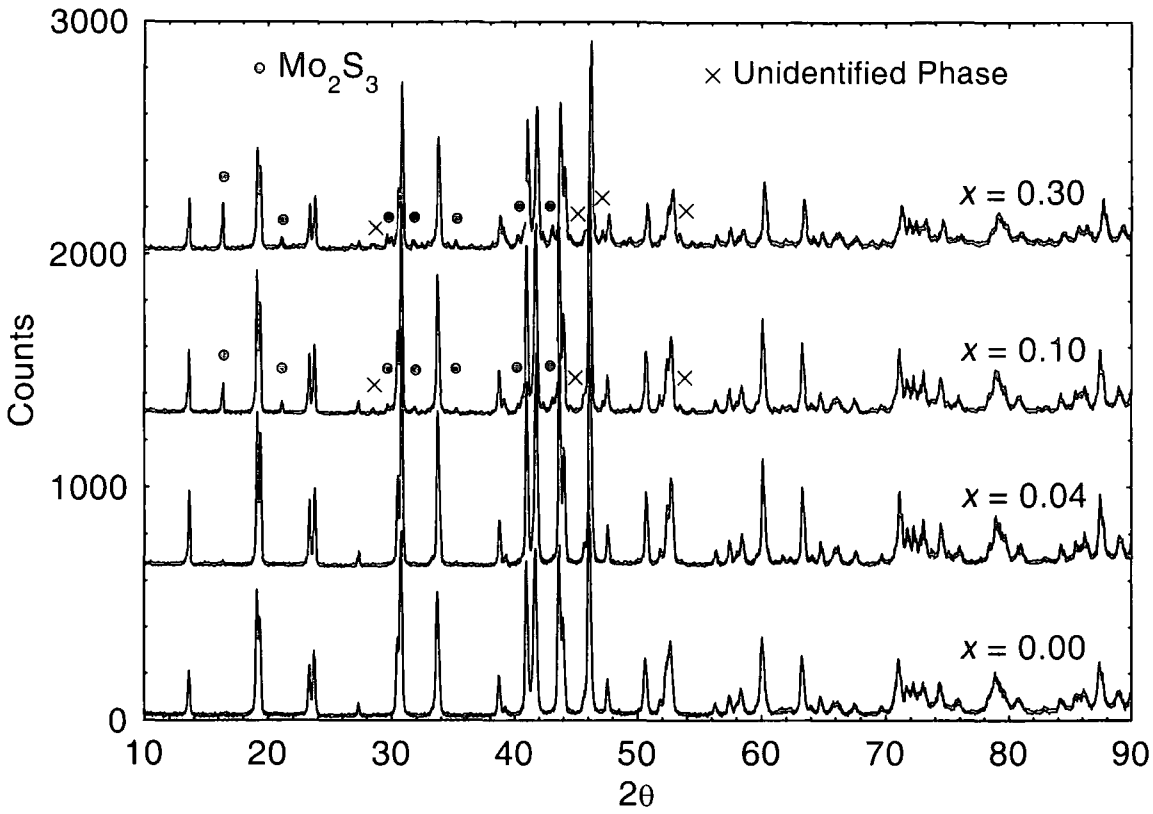


**Figure 12. X-ray diffraction patterns for $(Pb_{1-x}Gd_x)Mo_6S_8$ with $x$ = 0.00, 0.04, 0.10 and 0.30. Data taken by H J Niu on a single set of samples.**

superconducting contribution makes analysis of the specific heat jump extremely difficult. Subtraction of this magnetic background is necessary therefore for accurate analysis.

Comparison of the magnitude of the normal state specific heat ($c_n$) in zero applied field (Fig. 9) shows that there is considerable variation between the samples. The change in $c_n$ of the samples in the $(Sn_{1-x}Eu_x)Mo_6S_8$ series is non systematic with the values of $c_n$ at 15 K of the $x$ = 0.35 and 0.50 samples being respectively 23 % and 18 % lower than that of the $x$ = 0.00 sample. In the $(Pb_{1-x}Gd_x)Mo_6S_8$ series however there is a systematic reduction in the value of $c_n$ as the level of doping is increased, the reduction is only about 5 % up to the $x$ = 0.10 sample whereas $c_n$ of the $x$ = 0.30 sample is about 30 % lower. The normal state specific heat of the $(Pb_{0.75}Eu_{0.25})Mo_6S_8$ sample lies in between that of the $(Pb_{0.90}Gd_{0.10})Mo_6S_8$ sample and the $SnMo_6S_8$ sample.

### 7.4.1 X-ray diffraction.

Figures 11 and 12 show the X-ray diffraction results taken by Dr H J Niu. The data shows the $SnMo_6S_8$ and $(Sn_{0.65}Eu_{0.35})Mo_6S_8$ samples have a small amount of $Mo_2S_3$

**Figure 13. EDX micrograph of $(Sn_{0.65}Eu_{0.35})Mo_6S_8$ sample. The darker regions are secondary phase $Mo_2S_3$. Data taken by M Goringe.**

**Figure 14. EDX micrograph of $(Sn_{0.50}Eu_{0.50})Mo_6S_8$ sample. The darker region is secondary phase $Mo_2S_3$. Data taken by M Goringe.**

present, traces of Mo and traces of an unidentified phase that is probably EuS whereas the $(Sn_{0.50}Eu_{0.50})Mo_6S_8$ and $(Pb_{0.75}Eu_{0.25})Mo_6S_8$ samples are single phase. The data also shows that the $PbMo_6S_8$ and $(Pb_{0.96}Gd_{0.04})Mo_6S_8$ samples are single phase whereas the $(Pb_{0.90}Gd_{0.10})Mo_6S_8$ and $(Pb_{0.70}Gd_{0.30})Mo_6S_8$ samples have small amounts of $Mo_2S_3$ present and traces of an unidentified phase that is probably $Gd_2S_3$.

The lattice parameters have been determined for each sample and the unit cell volume calculated. For the $(Sn_{1-x}Eu_x)Mo_6S_8$ series the samples have unit cell volumes of 832.9 $Å^3$, 832.9 $Å^3$ and 833.8 $Å^3$, for $x$ = 0.00, 0.35 and 0.50 respectively, the $(Pb_{0.75}Eu_{0.25})Mo_6S_8$ sample has a unit cell volume of 833.5 $Å^3$ and the $(Pb_{1-x}Gd_x)Mo_6S_8$ series have unit cell volumes of 841.9 $Å^3$, 839.8 $Å^3$, 839.8 $Å^3$ and 833.4 $Å^3$, for $x$ = 0.00, 0.04, 0.10 and 0.30 respectively.

### 7.4.2 TEM and EDX measurements.

The TEM measurements on the $(Sn_{1-x}Eu_x)Mo_6S_8$ and $(Pb_{1-x}Gd_x)Mo_6S_8$ series show that the samples are all greater than 90 % dense and that the grain boundaries are clean. Figures 13 and 14 show the results from the EDX measurements on the $(Sn_{0.65}Eu_{0.35})Mo_6S_8$ and

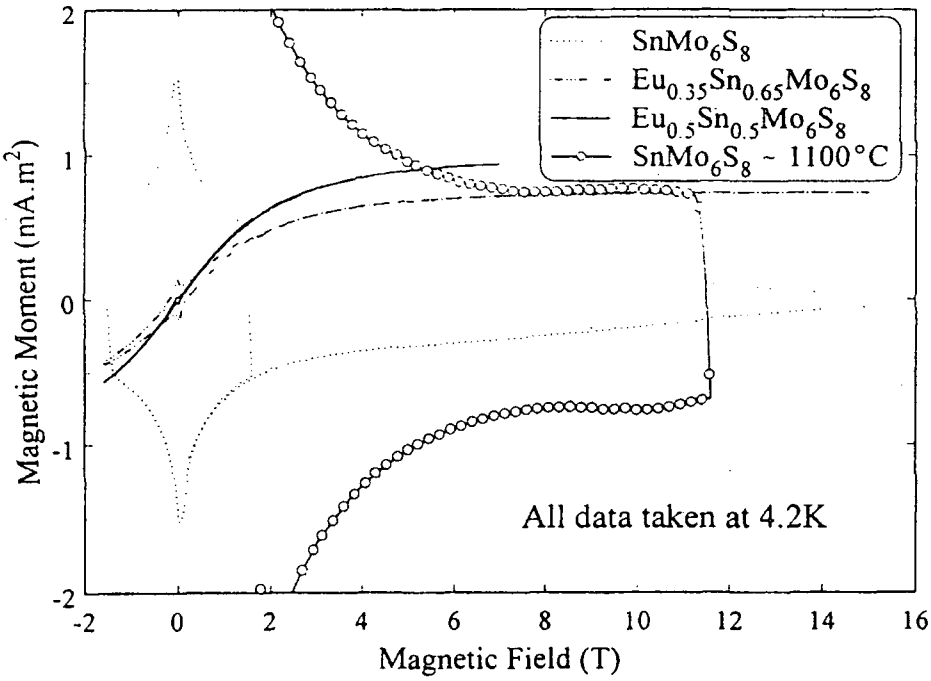


**Figure 15. Magnetisation as a function of applied field for the $(Sn_{0.65}Eu_{0.35})Mo_6S_8$ and $(Sn_{0.50}Eu_{0.50})Mo_6S_8$ samples. Data taken using a VSM by I J Daniel [325].**

$(Sn_{0.50}Eu_{0.50})Mo_6S_8$ samples respectively. The EDX measurements show mostly a uniform phase (light grey in Fig.'s 13 and 14) with a very small amount of secondary phase (darker colour in Fig.'s 13 and 14) in the $(Sn_{0.50}Eu_{0.50})Mo_6S_8$ sample and a larger amount in the $(Sn_{0.65}Eu_{0.35})Mo_6S_8$ sample. The magnetic ions in each case are distributed uniformly throughout the majority phase but the compositional analysis shows no europium or tin in the dark secondary phase suggesting $Mo_2S_3$ present. For the samples in the series $(Pb_{1-x}Gd_x)Mo_6S_8$ analysis of the EDX measurements on individual grains indicates that the vast majority of the grains have a gadolinium content at approximately the level of doping.

### 7.4.3 Resistivity, susceptibility and magnetization measurements.

The resistivity and susceptibility results on the samples in the series $(Sn_{1-x}Eu_x)Mo_6S_8$ both show sharp transitions for the undoped sample ($\Delta T_c \approx 0.5$ K) and transitions for the $(Sn_{0.65}Eu_{0.35})Mo_6S_8$ and $(Sn_{0.50}Eu_{0.50})Mo_6S_8$ samples that are broadened, $\Delta T_c \approx 1.0$ K and 2.0 K respectively. Both resistivity and lossless susceptibility data for the $(Sn_{0.50}Eu_{0.50})Mo_6S_8$ sample show two distinct gradients during the superconducting transition indicative of two distinct superconducting transitions, the higher temperature transition associated with the grains and the lower with degraded properties of the grain boundaries. The resistivity and susceptibility data taken on the $(Pb_{0.75}Eu_{0.25})Mo_6S_8$ show a broadened superconducting transition of width about $\Delta T_c \approx 0.5$ K. The resistivity data form the $(Pb_{0.70}Gd_{0.30})Mo_6S_8$ sample also show a broadened ($\Delta T_c \approx 1.5$ K) superconducting transition at about 9.0 K (onset) that is not visible in the specific heat.

Figure 15 shows the VSM measurements taken on the $(Sn_{0.65}Eu_{0.35})Mo_6S_8$ and $(Sn_{0.50}Eu_{0.50})Mo_6S_8$ samples. The data for these two samples, the $(Pb_{0.90}Gd_{0.10})Mo_6S_8$ and $(Pb_{0.70}Gd_{0.30})Mo_6S_8$ samples all show a superposition of a paramagnetic background and a superconducting hysteresis. The $J_c$ values calculated from the VSM data show a systematic reduction with increased doping from $3.4 \times 10^8$ $Am^{-2}$ (4.2 K, 0 T) for $SnMo_6S_8$ to $6.8 \times 10^6$ $Am^{-2}$ for the $(Sn_{0.50}Eu_{0.50})Mo_6S_8$ sample and similarly from $1.8 \times 10^8$ $Am^{-2}$ (4.2 K, 6 T) for the $PbMo_6S_8$ sample to $6 \times 10^7$ $Am^{-2}$ for the $(Pb_{0.90}Gd_{0.10})Mo_6S_8$ sample.

## 7.5 Analysis.

Analysis is carried out on the specific heat data to determine the magnetic contribution to the total specific heat, this can then be subtracted to allow the superconducting and normal state specific heat to be analysed.

### 7.5.1 Analysis of magnetic contribution.

| Sample | $n_{cell}$ ($c_m^{sat}$) | $n_{cell}$ (stoichiometry) | $T_M^{AF}$ (K) |
|---|---|---|---|
| $(Sn_{0.65}Eu_{0.35})Mo_6S_8$ | 0.37 | 0.35 | 0.35 |
| $(Sn_{0.50}Eu_{0.50})Mo_6S_8$ | 0.50 | 0.50 | 0.35 |
| $(Pb_{0.75}Eu_{0.25})Mo_6S_8$ | - | 0.25 | - |
| $(Pb_{0.70}Gd_{0.30})Mo_6S_8$ / $Gd_2S_3$ | 0.24 | 0.30 | 0.82 / 5.467 |

**Table 1. Values of $n_{cell}$ determined from the approximate expression (Eqn. 7.1) with $J$ = 3.5 and the value of $c_m^{sat}$. The values of $n_v$ determined from the composition are also presented. The values of $T_M^{AF}$ determined from the fitting of the calculated data for the $(Sn_{0.65}Eu_{0.35})Mo_6S_8$ and $(Sn_{0.50}Eu_{0.50})Mo_6S_8$ samples and from the data for the sample of nominal composition $(Pb_{0.70}Gd_{0.30})Mo_6S_8$ are included.**

In order to characterise the total magnetic contribution to the specific heat ($c_m$) in terms of the mean field model, five free parameters need to be determined; $S$, $J$, $L$ (quantum numbers), $n_v$ (number of magnetic ions per unit volume) and $T_m$ (zero field ordering temperature). In chapter four however an approximate expression was derived for the saturation value of $c_{m(peak)}$ (i.e. $c_m^{sat}$) above $T_m$ (c.f. Fig.'s 15 – 18, Chapter 4) in terms of just the parameters $J$ and $n_{cell}$ (number of magnetic ions per unit cell). When analysing the experimental data if a region above $T_M$ can be identified where the maximum value of the magnetic contribution to the specific heat is constant then we can make use of this approximate expression.

Of the eight samples measured here only the strongly doped samples, $(Sn_{0.65}Eu_{0.35})Mo_6S_8$, $(Sn_{0.50}Eu_{0.50})Mo_6S_8$, $(Pb_{0.25}Eu_{0.75})Mo_6S_8$ and $(Pb_{0.70}Gd_{0.30})Mo_6S_8$, show a magnetic contribution to the specific heat for temperatures above $T_m$ (Fig.'s 1 - 8). The

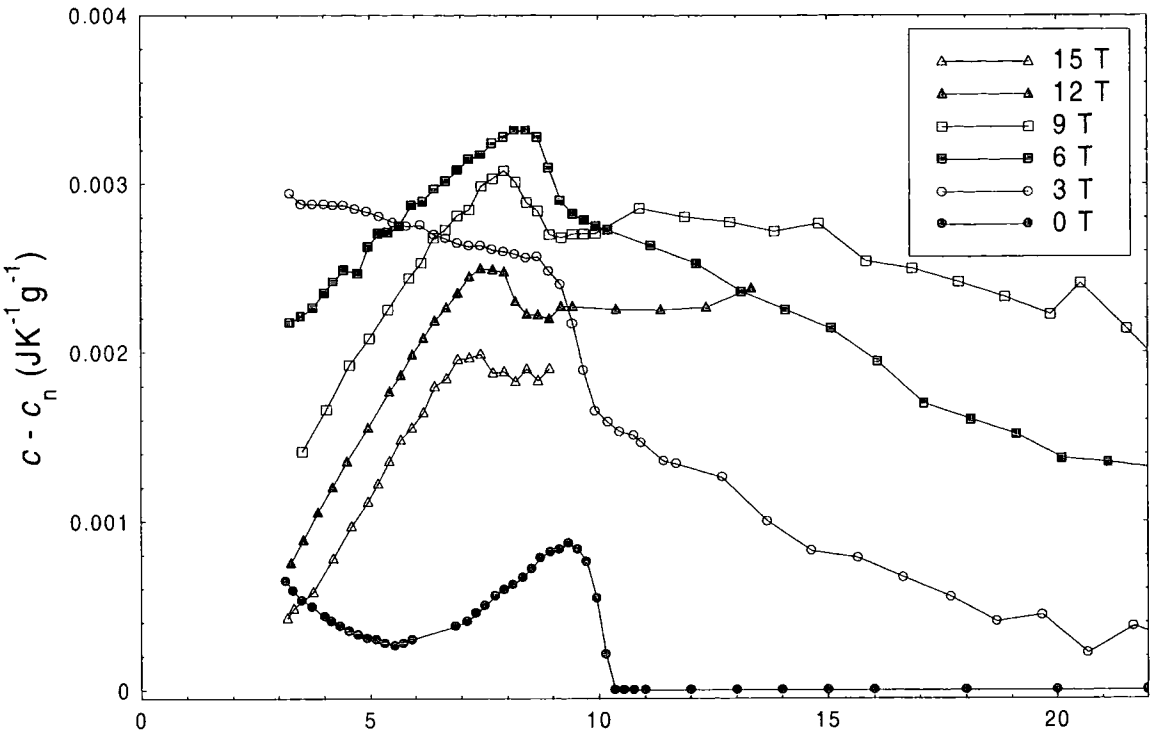


**Figure 16.** $c$ - $c_n$ as a function of temperature and applied field for $(Sn_{0.65}Eu_{0.35})Mo_6S_8$.

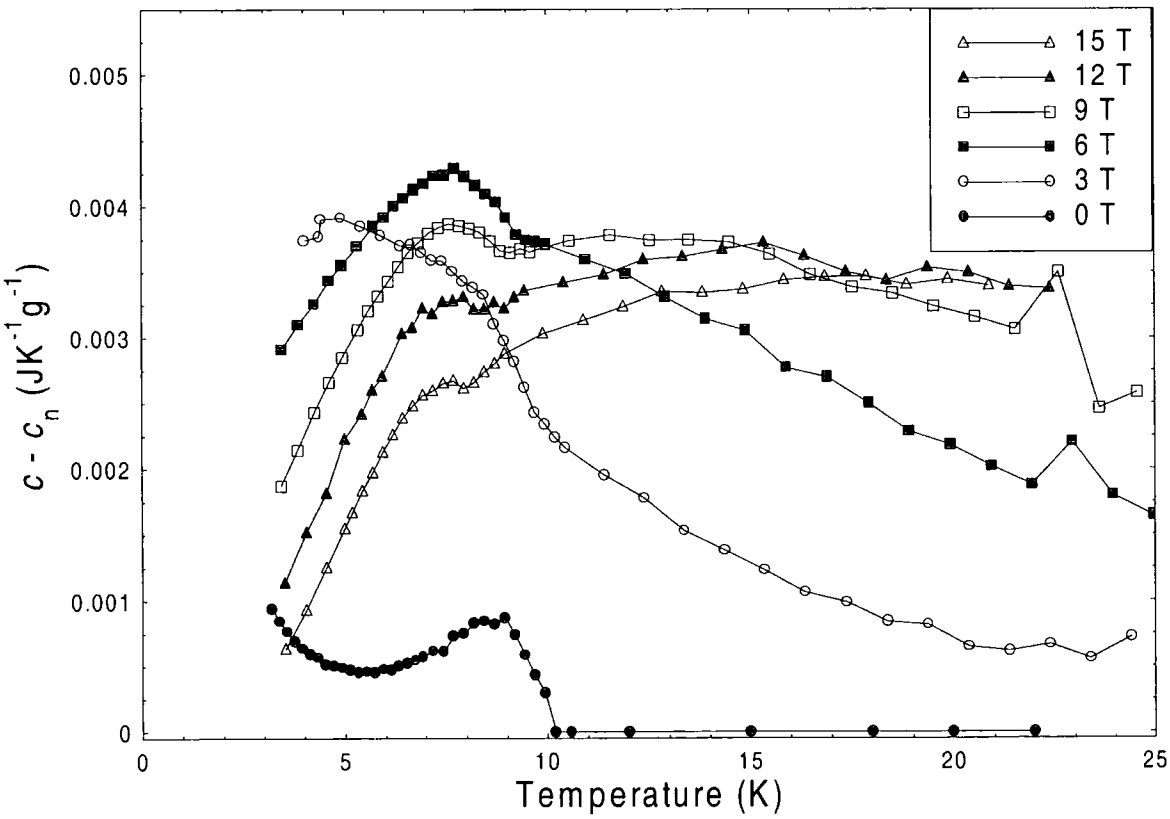


**Figure 17.** $c$ - $c_n$ as a function of temperature and applied field for $(Sn_{0.50}Eu_{0.50})Mo_6S_8$.

$(Pb_{0.96}Gd_{0.04})Mo_6S_8$ sample shows no evidence of magnetic ordering or a paramagnetic contribution and although the $(Pb_{0.90}Gd_{0.10})Mo_6S_8$ sample does have a peak associated with magnetic ordering, the magnitude of $c_m$ for $T > T_m$ is not large enough to analyse. The three samples doped with europium all show a magnetic contribution to the specific heat in-field and an upturn in the zero field specific heat at temperatures below about 5 K. The magnetic ordering temperature in these samples however is below the base temperature of these measurements (~ 3 K). The nature of the magnetic ordering in the phases $EuMo_6S_8$ and $GdMo_6S_8$ is known to be antiferromagnetic [150]. Since the low temperature peak in $c$ associated with magnetic ordering of the $(Pb_{0.90}Gd_{0.10})Mo_6S_8$ and $(Pb_{0.70}Gd_{0.30})Mo_6S_8$ samples is suppressed with increasing applied field and the upturn in $c$ of the europium doped samples is also suppressed in high fields, we therefore assume that these doped compounds are also antiferromagnetic.

For each of these four samples that display a magnetic contribution for $T > T_m^{AF}$ the zero field specific heat is subtracted from the in-field data. The zero field specific heat however also has to be determined for $T < T_c$ since the superconducting contribution of the europium doped samples and the presence of an upturn at low temperatures in the zero field data of all four samples cannot be modelled. The normal state specific heat ($c_n$) of each sample has therefore been extrapolated by eye from Fig.'s 2, 3, 4 and 8, down to the lowest temperatures, subtracted from the in-field traces and replotted.

For the europium doped samples there is no peak due to magnetic ordering visible in any of the specific heat data and so we conclude that $T_m^{AF} < 3$ K for these compounds. Figures 16 and 17 show the magnetic and superconducting contributions to the specific heat for the $(Sn_{0.65}Eu_{0.35})Mo_6S_8$ and $(Sn_{0.50}Eu_{0.50})Mo_6S_8$ samples respectively, with corresponding $T_{c(onset)}$ values from the specific heat in zero field of 10.25 K and 10.08 K. Above these $T_{c(onset)}$ values therefore the contributions to the specific heat in Fig.'s 16 and 17 are entirely magnetic in origin. The data in Fig. 16 for the $(Sn_{0.65}Eu_{0.35})Mo_6S_8$ sample shows a maximum value of $c_m$ at about 12 K for the 9 T trace, the 12 T and 15 T data were compromised at temperatures above ~ 8 K by large temperature drifts and so analysis of these traces is less accurate. The data in Fig. 17 for the $(Sn_{0.50}Eu_{0.50})Mo_6S_8$ sample show a much clearer peak in $c_m$ for the 9 T and 12 T traces between 10 K and 15 K, the 15 T data however reaches a peak value of about 8 % lower than the 9 T and 12 T.

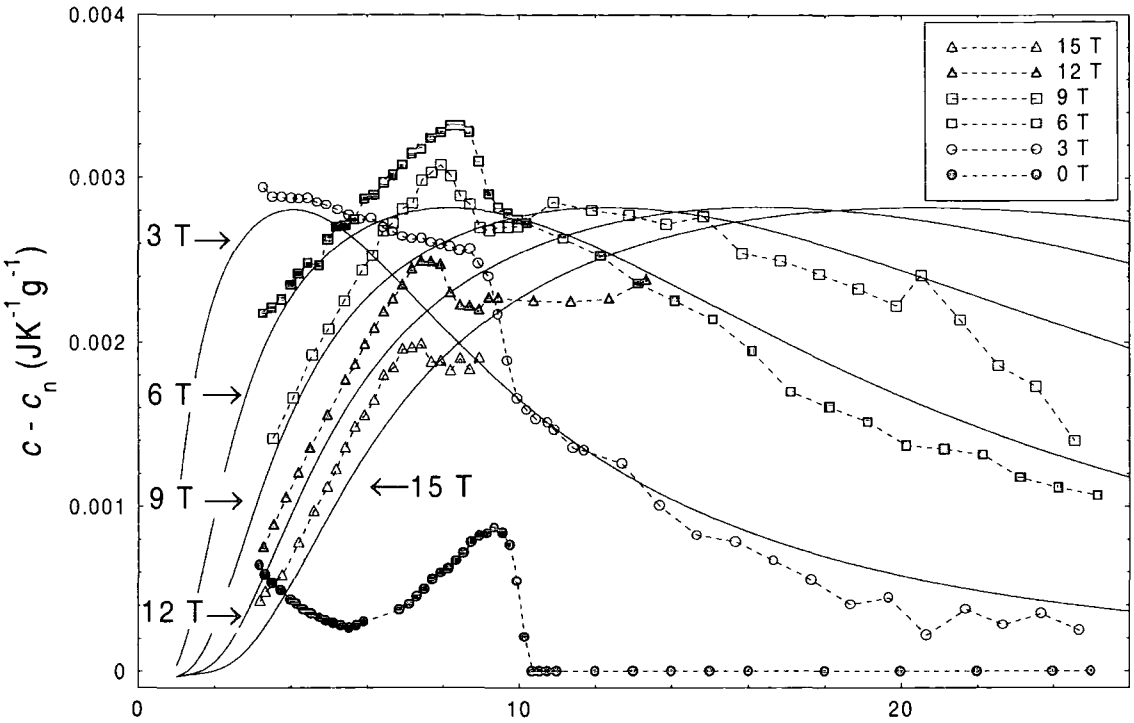


**Figure 18. Experimental data (symbols) of $c_m$ as a function of temperature and applied field for $(Sn_{0.65}Eu_{0.35})Mo_6S_8$ and calculated values (lines), with $J = S = 3.5$, $L = 0$, $g_J = 2.0$, $T_m^{AF} = 0.35$ K, $n_v = 1.30 \times 10^{27}$ m$^{-3}$.**

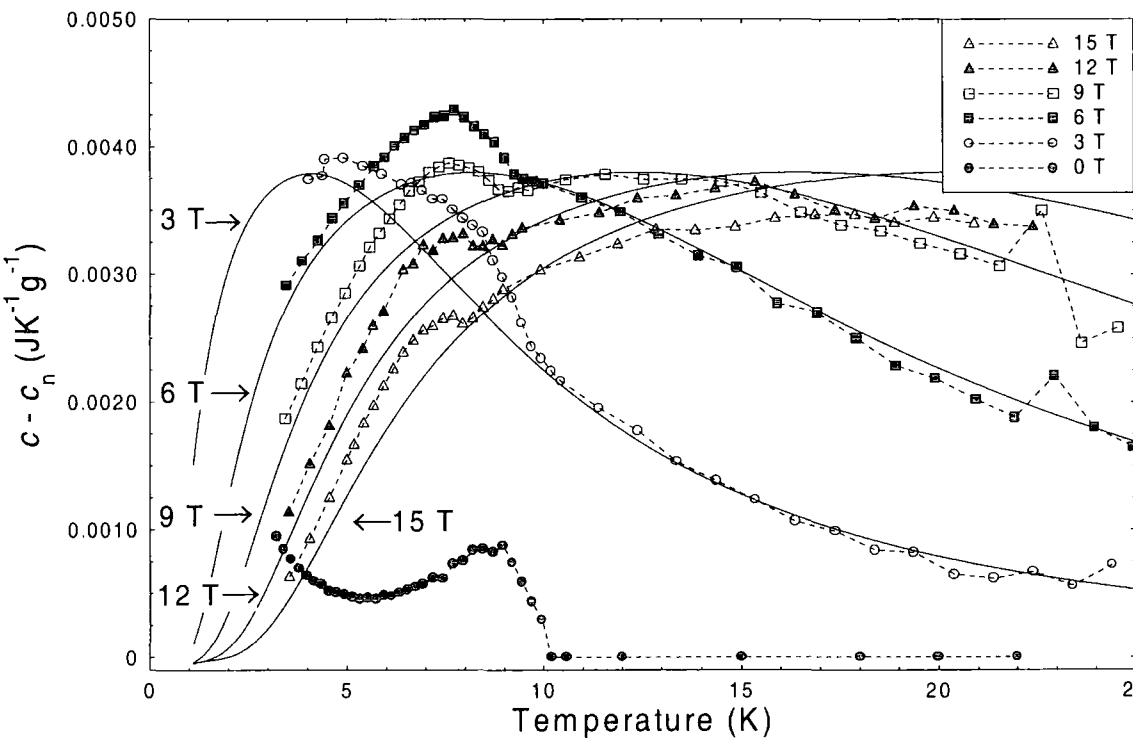


**Figure 19. Experimental data (symbols) of $c_m$ as a function of temperature and applied field for $(Sn_{0.50}Eu_{0.50})Mo_6S_8$ and calculated values (lines), with $J = S = 3.5$, $L = 0$, $g_J = 2.0$, $T_m^{AF} = 0.35$ K, $n_v = 1.75 \times 10^{27}$ m$^{-3}$.**

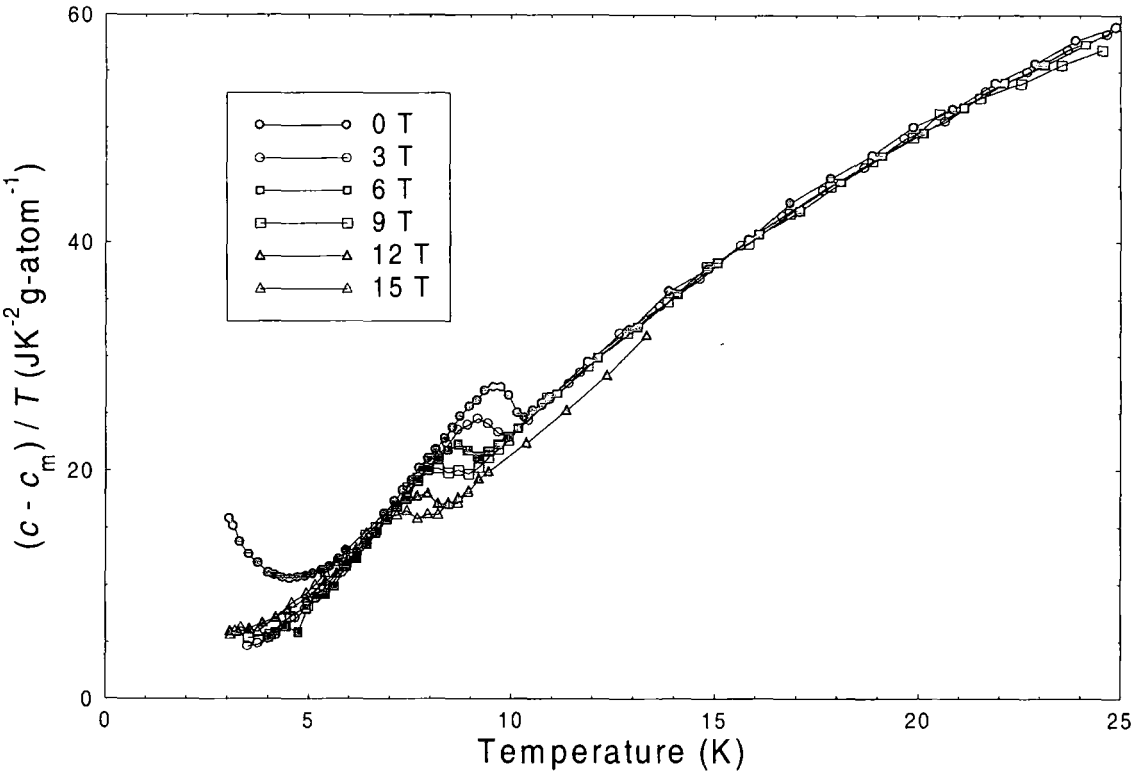


**Figure 20.** $c - c_m$ as a function of temperature and applied field for $(Sn_{0.65}Eu_{0.35})Mo_6S_8$.

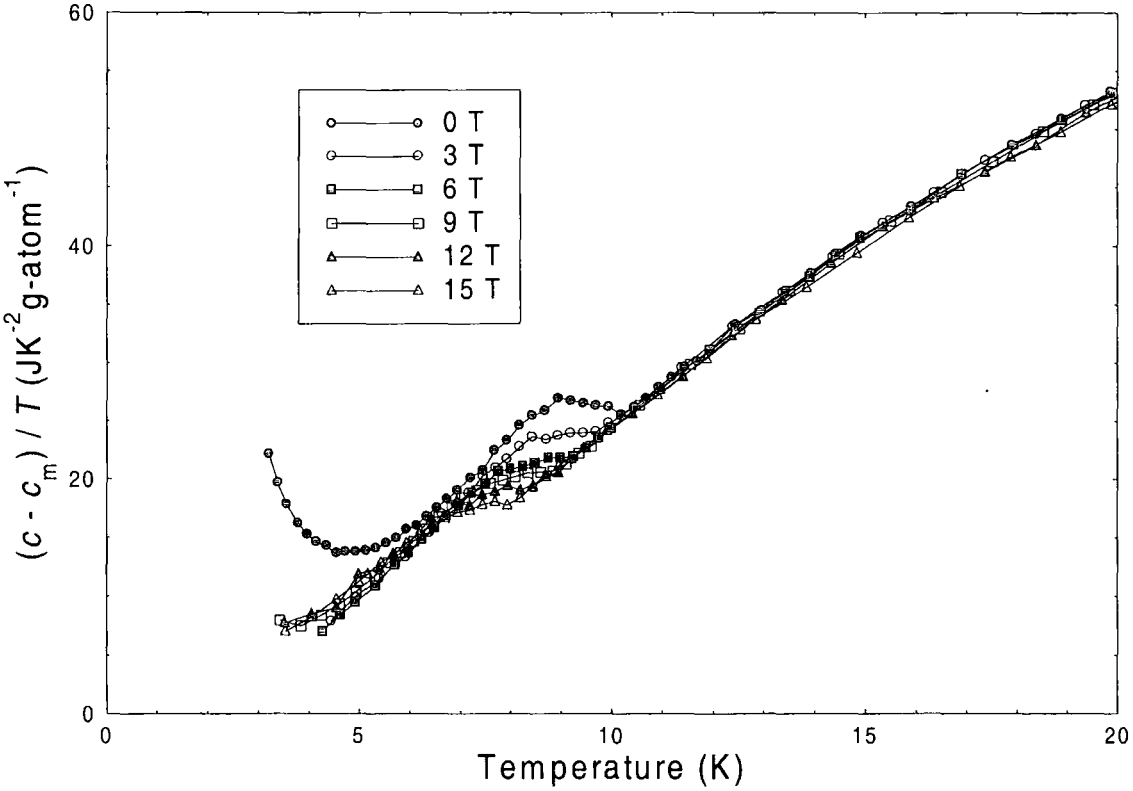


**Figure 21.** $c - c_m$ as a function of temperature and applied field for $(Sn_{0.50}Eu_{0.50})Mo_6S_8$.

In order to analyse the magnetic contribution of the $(Sn_{0.65}Eu_{0.35})Mo_6S_8$ and $(Sn_{0.50}Eu_{0.50})Mo_6S_8$ samples we assume that $J$ = 3.5 (the free ion value) for both samples. Estimates for the number of magnetic ions per unit cell can then be made using:

$$c_m^{sat} = AR n_{cell}\left(\frac{J}{J+1}\right) \tag{7.1}$$

where $A$ = 1.1245. Values of $n_{cell}$ are estimated from the specific heat data as 0.37 and 0.50 for the $x$ = 0.35 and $x$ = 0.50 samples respectively. These estimates are in excellent agreement with the stoichiometric values. Using these estimates of $n_{cell}$ and taking $J = S$ = 3.5 and $L$ = 0 the magnetic contribution to the specific heat was calculated for both samples for a range of values of $T_m^{AF}$ between 0 K and 3 K. An estimate for the actual value of $T_m^{AF}$ for each sample was then determined by the best agreement between calculated and experimental data.

Figures 18 and 19 show the results for the $(Sn_{0.65}Eu_{0.35})Mo_6S_8$ and $(Sn_{0.50}Eu_{0.50})Mo_6S_8$ samples, where the value of $T_m^{AF}$ that gave the closest match to the experimental data was $T_m^{AF}$ = 0.35 K in both cases. Changing $T_m^{AF}$ by 0.25 K however produces a change in the magnitude of $c_m$ of less than 5 % for $T > T_c$, hence the accuracy of the values of $T_m^{AF}$ determined from this fitting are about ± 0.5 K. The values of $n_v$ used for the $x$ = 0.35 and $x$ = 0.50 samples were respectively 3 % higher and 3 % lower than the theoretical values. These values of $n_v$ were used to achieve the best match between calculation and data for the magnitude of $c_m^{sat}$, since changing the value of $T_M^{AF}$ by < 0.5 K has little effect on the calculated value of $c_{m(peak)}$ but a much larger effect on the high temperature data beyond $c_{m(peak)}$.

The calculations and experimental data are in very good agreement for both of these samples in fields up to 9 T. For the $(Sn_{0.65}Eu_{0.35})Mo_6S_8$ sample the calculated values lie generally within 15 % of the experimental data and for the $(Sn_{0.50}Eu_{0.50})Mo_6S_8$ sample the calculated values lie generally within 5 % of the experimental data. The 12 T and 15 T data however do not agree as well, for the $(Sn_{0.65}Eu_{0.35})Mo_6S_8$ sample the 12 T and 15 T experimental data is compromised and for the $(Sn_{0.50}Eu_{0.50})Mo_6S_8$ sample the experimental data is up to 10 % lower than the calculated data for $T$ > 15 K.

The calculated values of $c_m$ as a function of temperature and applied field can then be subtracted from the total specific heat capacity to leave just the normal state and superconducting contributions to the specific heat. Figures 20 and 21 show the results of this subtraction for the $(Sn_{0.65}Eu_{0.35})Mo_6S_8$ and $(Sn_{0.50}Eu_{0.50})Mo_6S_8$ samples. Apart from

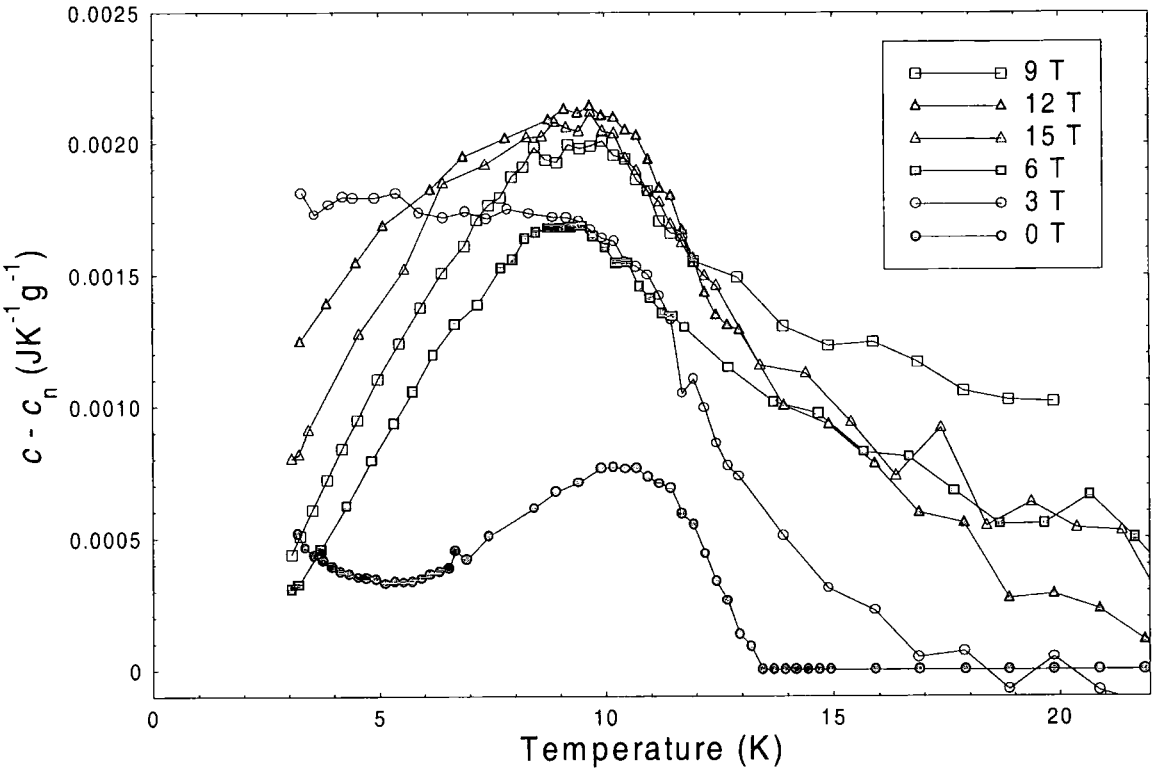


**Figure 22.** $c$ - $c_n$ as a function of temperature and applied field for $(Pb_{0.75}Eu_{0.25})Mo_6S_8$.

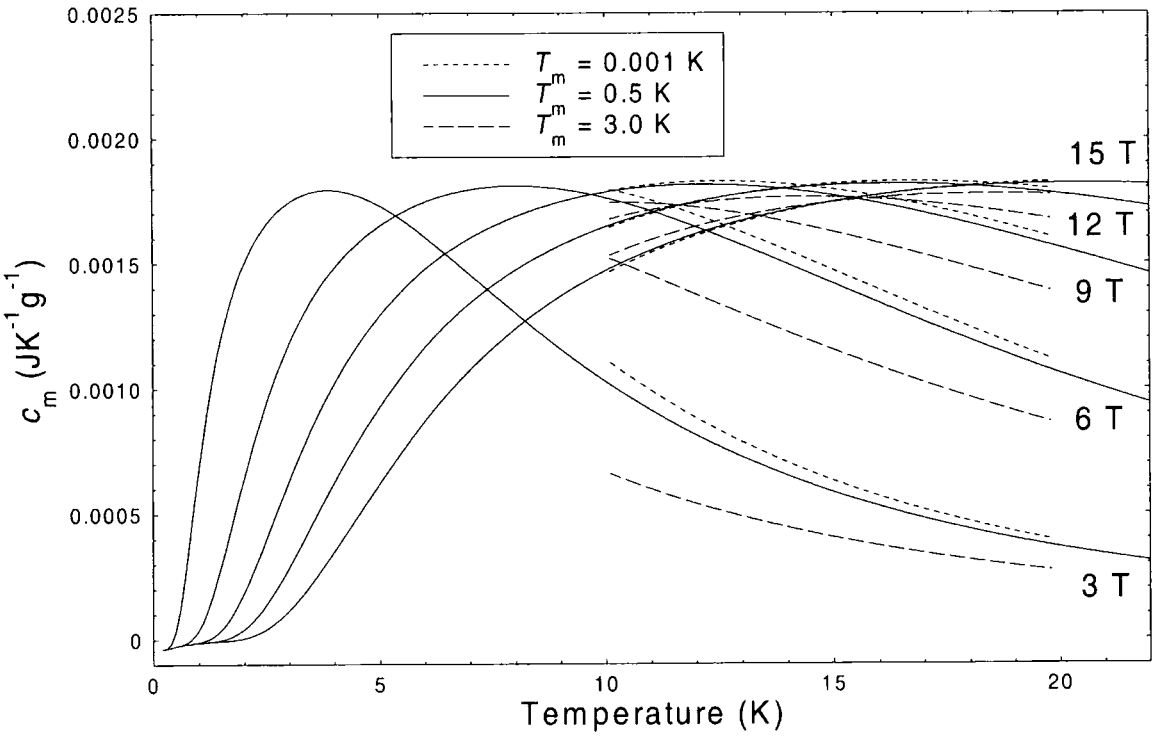


**Figure 23.** $c_m$ as a function of temperature and applied field for $(Pb_{0.75}Eu_{0.25})Mo_6S_8$, calculated as in chapter 4 with $J = S = 3.5$, $L = 0$, $g_J = 2.0$, $T_m^{AF} = 0.35$ K and $n_v = 9.0 \times 10^{26}$ m$^{-3}$.

the low temperature upturn in the zero field data that cannot be accounted for without adding fluctuations into the mean field model, the resulting specific heat curves are now characteristic of a non-magnetic superconductor similar to the data for $SnMo_6S_8$ and $PbMo_6S_8$ (Fig.'s 1 and 5).

The data in Fig. 22 for the $(Pb_{0.75}Eu_{0.25})Mo_6S_8$ sample shows no maximum value in $c_m$ for $T > T_c$ since all of the field traces are still increasing in magnitude as they approach the superconducting transition temperature. Therefore in order to analyse the magnetic contribution of the $(Pb_{0.75}Eu_{0.25})Mo_6S_8$ sample we assume that $n_v$ = 9.0 x $10^{26}$ $m^{-3}$, the calculated value from the lattice parameters and we also assume an arbitrary ordering temperature of $T_m^{AF}$ ~ 1K. Using these values and $J = S = 3.5$ and $L = 0$ the free ion values, the magnetic contribution to the specific heat was calculated for this sample for a range of values of $T_m^{AF}$ between 0 K and 3 K. Figure 23 shows the results for the $(Pb_{0.75}Eu_{0.25})Mo_6S_8$ sample for values of $T_m^{AF}$ = 0.001 K, 0.50 K and 3.0 K. Changing the value of $T_m^{AF}$ from 0.001 K to 3.0 K produces a change in the magnitude of $c_m$ of up to about 40 %. The temperature dependence above $T_c$ does not agree however with the experimental data for any values of $T_m^{AF}$ in this range. The experimental data drops to zero

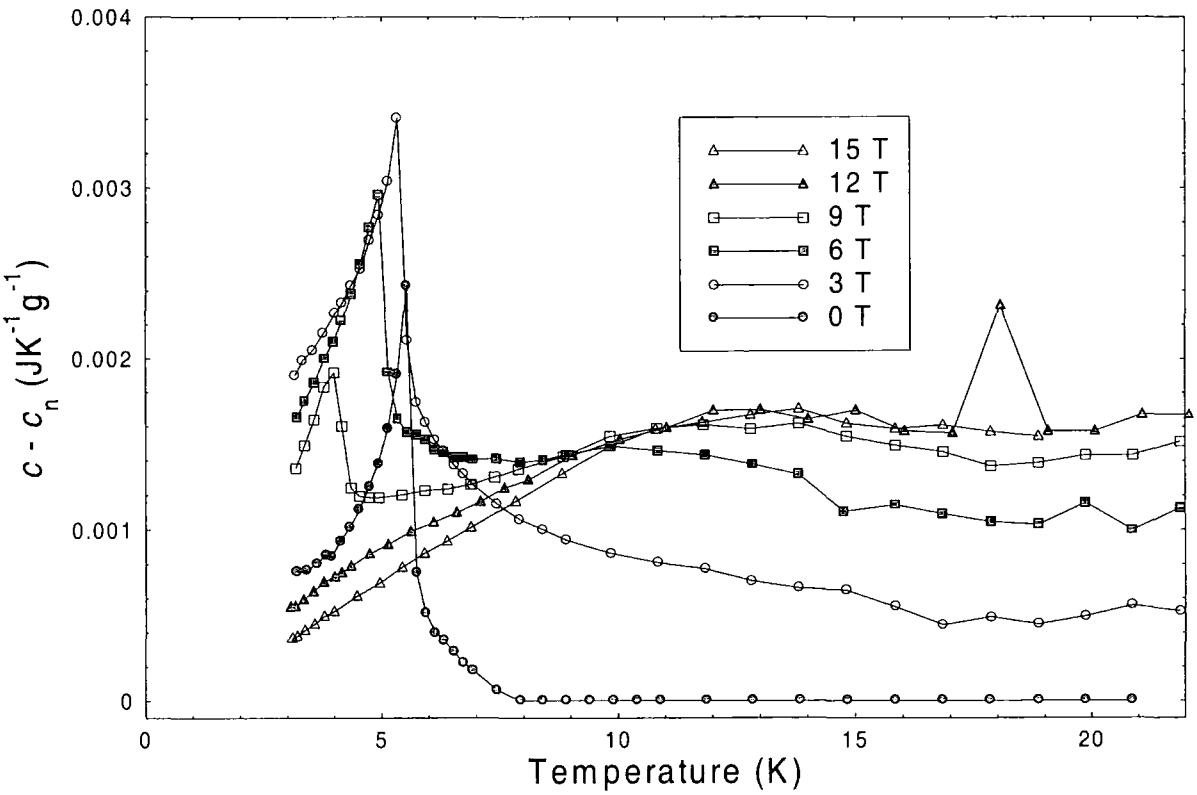


**Figure 24.** $c$ - $c_n$ **as a function of temperature and applied field for** $(Pb_{0.70}Gd_{0.30})Mo_6S_8$.

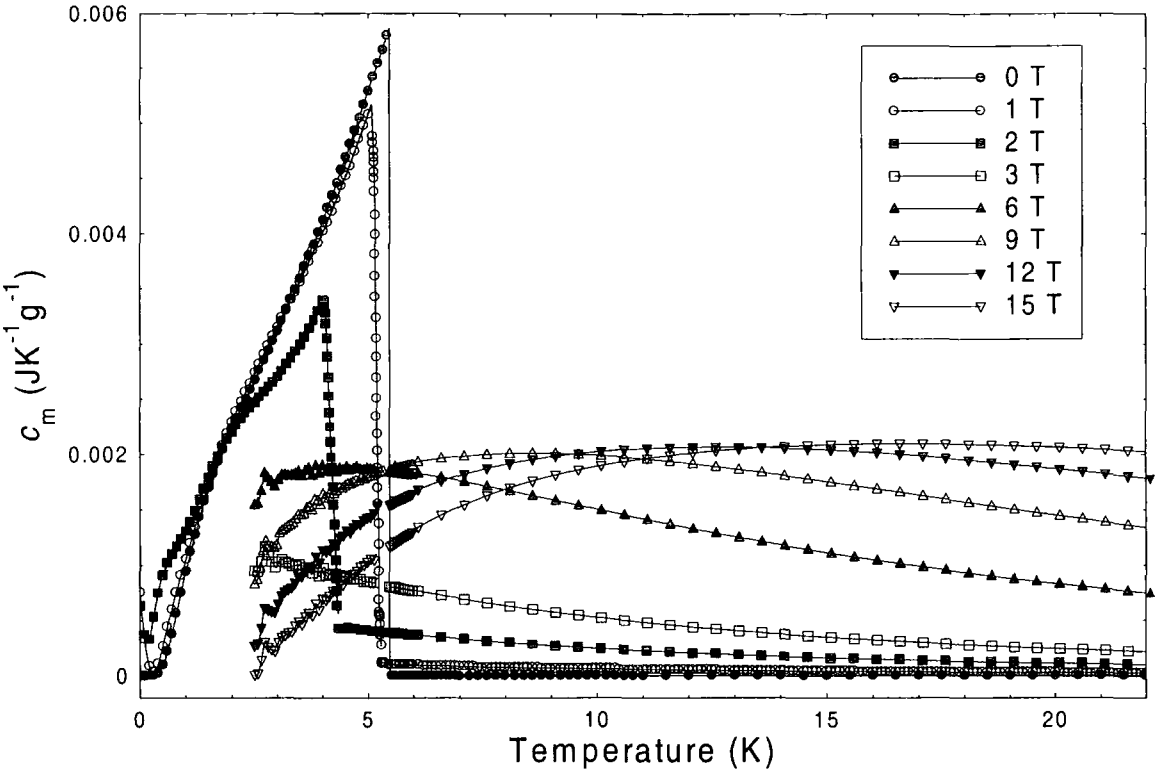


**Figure 25. $c_m$ as a function of temperature and applied field for $(Pb_{0.70}Gd_{0.30})Mo_6S_8$ calculated as in chapter 4, with $J = S = 3.5$, $L = 0$, $g_J = 2.0$, $T_m^{AF} = 5.467$ K and $n_v = 1.08 \times 10^{27}$ m$^{-3}$.**

at much lower temperatures than the calculated data and the experimental 12 T and 15 T data do not have a peak above $T_c$ unlike the calculated curves. Since we cannot reproduce the temperature dependence of $c_m$ above $T_c$ and the presence of superconducting transitions in the specific heat prevent any more detailed analysis, we conclude that for this sample we are unable to model the magnetic contribution to the specific heat.

The value of $T_m^{AF}$ for the $(Pb_{0.70}Gd_{0.30})Mo_6S_8$ samples has been determined as 5.467 ± 0.012 K from the long range pulse technique (section 7.4.1). The data in Fig. 24 shows the magnetic and superconducting contributions to the specific heat for the $(Pb_{0.70}Gd_{0.30})Mo_6S_8$ sample. Since we know from the resistivity data that $T_{c(onset)}$ is about 9.0 K in zero field the contribution to the specific heat above this temperature is entirely magnetic in origin. The data shows a maximum value for the 12 T and 15 T traces in a temperature region between about 12 K and 15 K. If we take this value of $c_m$ to be the saturation value ($c_m^{sat}$) and assume that $J = 3.5$, the free ion value, then we can use Eqn. (7.1) to determine an estimate of $n_{cell} = 0.24$ for the doping level in this sample. This value of $n_{cell}$ is 20 % smaller than the value determined from the composition.

Using the theoretical value of $n_v$ = 1.08 x $10^{27}$ $m^{-3}$, with $T_m^{AF}$ = 5.467 K and using the free ion parameters $J = S = 3.5$ and $L = 0$, we can calculate the magnetisation and therefore the magnetic contribution to the specific heat capacity as detailed in chapter 4. Figure 25 shows the results of those calculations. For $T \leq T_m$ the calculations of $c_m$ are significantly different from the data in Fig. 24. The peak in the zero field calculation is larger than any of those in an applied field, has a maximum value of 0.00587 $JK^{-1}g^{-1}$, and falls to half of the peak value at approximately $0.5T_m^{AF}$. The experimental zero field result however has a maximum value of 0.00243 $JK^{-1}g^{-1}$, is smaller than the peaks in applied fields of 3 T and 6 T and falls rapidly to half of the peak value at approximately $0.85T_m^{AF}$. Furthermore in the calculations a field of approximately 2.7 T is sufficient to drive $T_m(B)$ below $T$ = 0 K (the calculations of $c_m$ for fields > 2 T are very noisy at low temperatures and have been omitted for clarity), whereas the experimental results reveal a peak in $c_m$ at temperatures above 3 K for fields as large as 9 T. For $T > T_m$ the value of $c_{m(peak)}$ (above $T_m$) determined from these rigorous calculations is approximately 20 % larger than the experimental data. Recalculating the data for $0.80n_v$ or alternatively for $J = S = 3.5 / 2$ is sufficient to match the value of $c_{m(peak)}$ from the calculations with the value of $c_{m(peak)}$ from the experimental

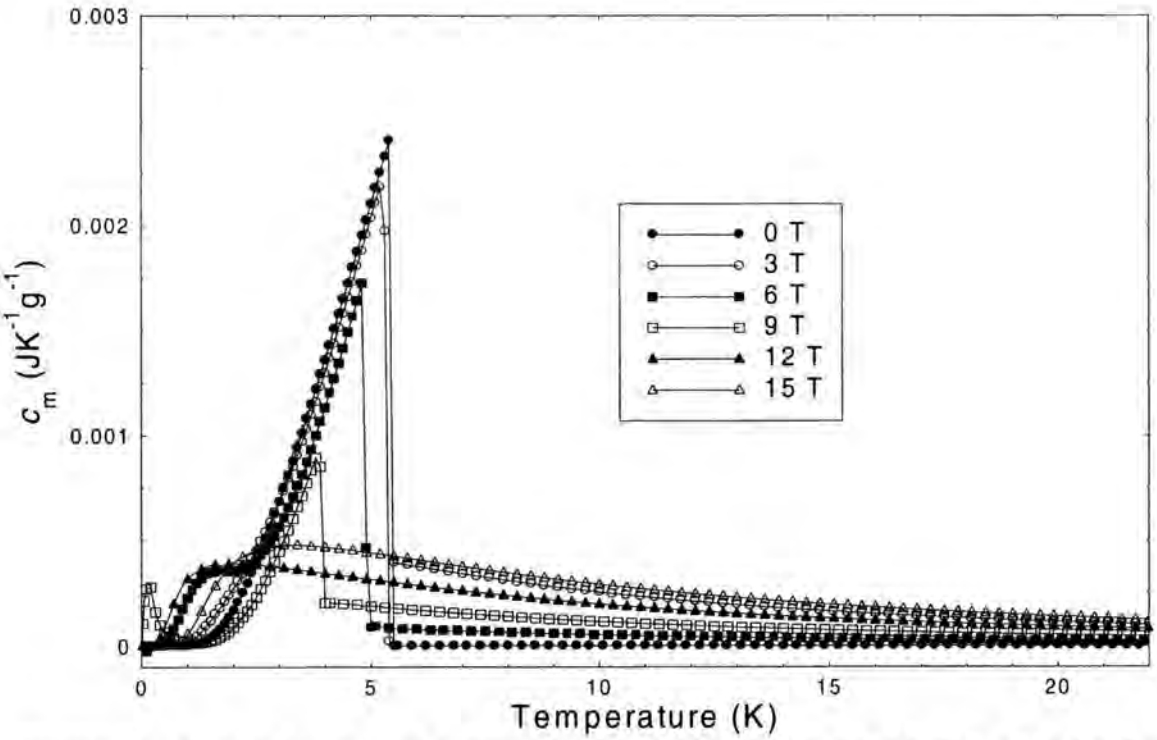


**Figure 26. $c_m$ as a function of temperature and applied field for $Gd_2S_3$ with $J = S = 0.32$, $L = 0$, $g_J = 2.0$, $T_M^{AF}$ = 5.467 K and $n_v$ = 0.9598 x $10^{27}$ $m^{-3}$.**

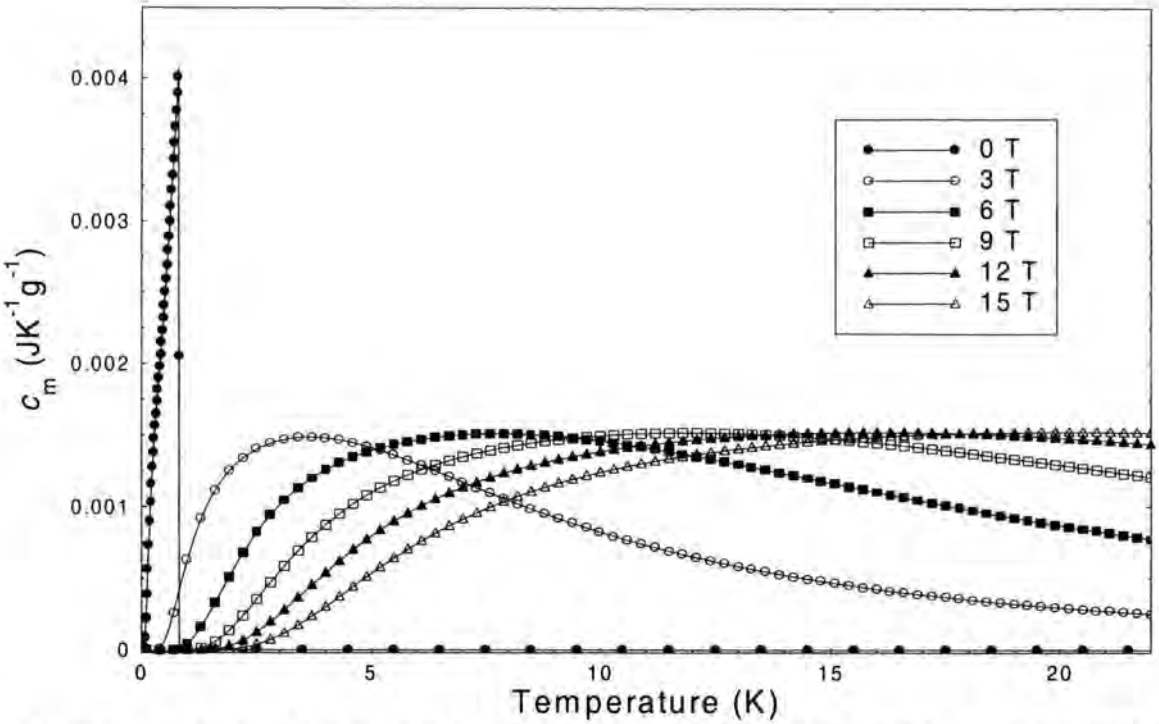


**Figure 27.** $c_m$ **as a function of temperature and applied field for** $(Pb_{0.75}Gd_{0.25})Mo_6S_8$ **with** $J = S = 3.5$, $L = 0$, $g_J = 2.0$, $T_M^{AF} = 0.82$ **K and** $n_v = 0.756 \times 10^{27}$ **m**$^{-3}$.

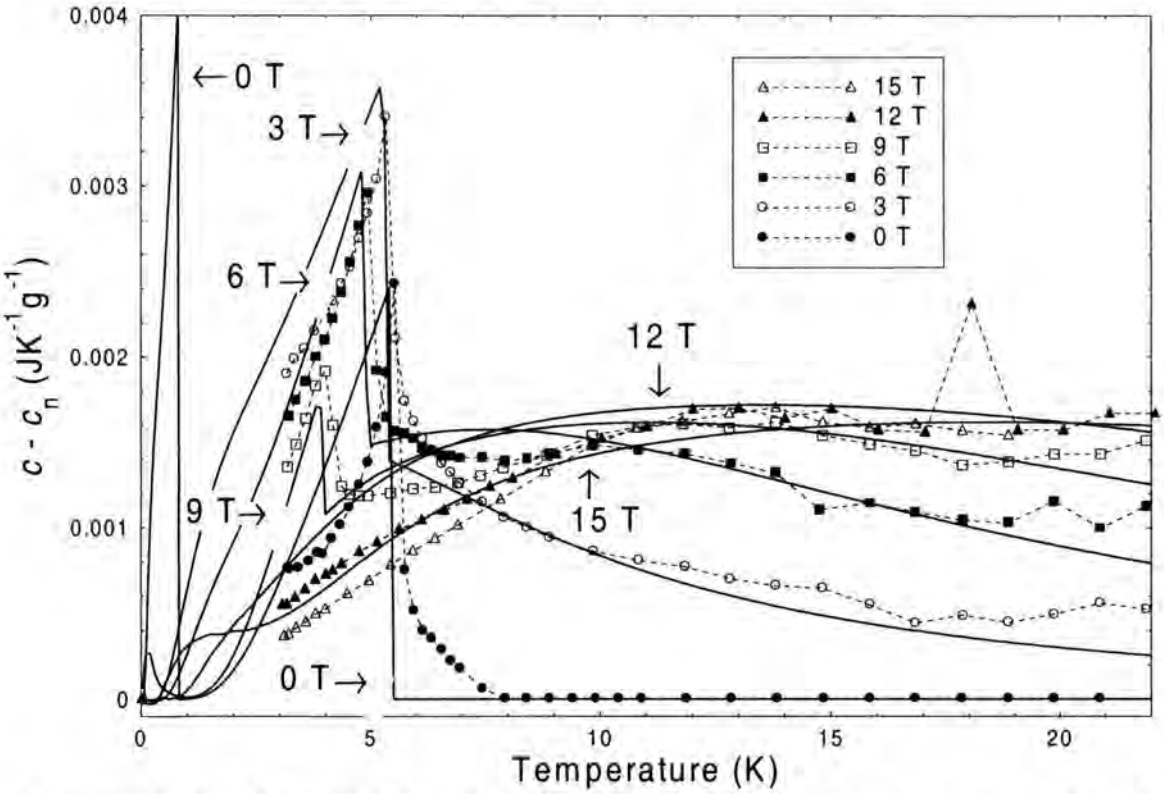


**Figure 28. Total calculated** $c_m$ **(solid lines) as a function of temperature and applied field from** $(Pb_{0.75}Gd_{0.25})Mo_6S_8$ **and** $Gd_2S_3$ **phases (Fig.'s 26 and 27) and experimental data (symbols) for sample of nominal composition** $(Pb_{0.70}Gd_{0.30})Mo_6S_8$.

data. The data for 3 T and 6 T however which in Fig. 25 are lower than the experimental data become even lower still if the criteria $0.80n_v$ or $J = S = 3.5 / 2$ are used.

Specific heat measurements on $GdMo_6S_8$ show a sharp peak associated with magnetic ordering at about 0.82 K in zero field [182] and smaller peaks associated with impurity phases between 3 K and 5 K. On diluting a magnetic system one might expect the ordering temperature to be reduced however there is no evidence for a significant increase in the ordering temperature on changing $GdMo_6S_8$ to $(Pb_{0.70}Gd_{0.30})Mo_6S_8$. These results suggest therefore that the peak at ~ 5.5 K in the $(Pb_{0.70}Gd_{0.30})Mo_6S_8$ and $(Pb_{0.90}Gd_{0.10})Mo_6S_8$ samples is due to an impurity phase that is probably $Gd_2S_3$. These two samples are probably therefore a mixture of $Gd_2S_3$ phase ordering at ~ 5.5 K and $(Pb_{1-x}Gd_x)Mo_6S_8$ phase that orders at $T \leq 0.82$ K.

The temperature dependence of the peak in the specific heat with applied field is determined in the rigorous calculation by the values of $J$ and $g_J$ only. Using the measured temperature dependence of the specific heat peak (Fig. 10) determined from the long-range pulse measurements a value of $J = S = 0.32$ is calculated. Once the values of $J$ and $g_J$ have been determined the height of the zero field peak is determined only by $n_v$.. The peak in Fig. 24 at ~ 5.5 K is due to the secondary phase ($Gd_2S_3$) only in zero field and is therefore used to determine a value of $n_v = 0.9598 \times 10^{27}$ m$^{-3}$ for this phase. Taking $T_M^{AF} = 5.467$ K and the values of $J$ and $n_v$ as above, the contribution to $c_m$ from this secondary phase is then calculated. To determine the equivalent contribution from the majority $(Pb_{1-x}Gd_x)Mo_6S_8$ phase we assume that $T_M^{AF} = 0.82$ K for this phase and that $J = S = 3.5$ and $L = 0$ the free ion values. The value of $n_v$ for this phase is then determined by the best fit of the summation of the contributions to $c_m$ from both phases to the experimental data. The values of $n_v$ determined for both phases indicate that the $Gd_2S_3$ phase comprises by mass about 6 % of the material and the composition of majority phase is therefore $(Pb_{0.75}Gd_{0.25})Mo_6S_8$. Figures 26, 27 and 28 show respectively the calculated contributions to $c_m$ from the $Gd_2S_3$ phase, the $(Pb_{0.75}Gd_{0.25})Mo_6S_8$ phase and the total magnetic specific heat from both phases in comparison with the experimental results.

The total calculated magnetic contribution to the specific heat capacity in Fig. 28 is in excellent agreement with the experimental data. The temperature and magnitude of the sharp peaks in $c_m$, in particular the magnitude of the 3 T and 6 T peak being larger than the zero field peak, and the general temperature dependence of $c_m$ are in good agreement with the experimental data for all fields. The calculations below the ordering temperature are in

surprisingly good agreement with the data considering the simple model used and presented in Fig.'s 27 and 28 is the additional peak we expect in zero field at ~ 0.82 K due to the $(Pb_{0.75}Gd_{0.25})Mo_6S_8$ phase. The main discrepancies between the data and calculations occur in the region of the ordering temperature where temperature fluctuations and more complex exchange interactions need to be considered. The results of the modelling of $c_m$ for all four samples are summarised in table 1.

The data in Fig. 3 for the $(Pb_{0.90}Gd_{0.10})Mo_6S_8$ sample shows similar characteristics to the $(Pb_{0.70}Gd_{0.30})Mo_6S_8$ sample in the low temperature region. The presence of specific heat peaks at the same temperatures as those in the specific heat of the $(Pb_{0.70}Gd_{0.30})Mo_6S_8$ sample indicate that there is some secondary phase $Gd_2S_3$ also present in this sample. Using the height of the zero field peak we can estimate the fraction of $Gd_2S_3$ in this sample to be about 0.6 % by mass.

### 7.5.2 Analysis of superconducting contribution.

| Sample | $T_{c(onset)}$ (K) | $T_{c(mid)}$ (K) | $\Delta T_c$ (K) | $\Delta c / T_c$ ($mJK^{-2}g\text{-}atom^{-1}$) | $c / T$ ($mJK^{-2}g\text{-}atom^{-1}$) | | $\rho_N$ ($\mu\Omega cm$) |
|---|---|---|---|---|---|---|---|
| | | | | | At $T_{c(onset)}$ | At 15.1 K | |
| $SnMo_6S_8$ | 13.26 | 12.8 | 1.2 | 9.48 | 45.9 | 50.1 | 177 |
| $(Sn_{0.65}Eu_{0.35})Mo_6S_8$ | 10.25 | 9.92 | 1.0 | 6.48 | 24.5 | 38.5 | 610 |
| $(Sn_{0.50}Eu_{0.50})Mo_6S_8$ | 10.08 | 9.55 | 1.25 | 6.04 | 25.6 | 41.3 | 3400 |
| $(Pb_{0.75}Eu_{0.25})Mo_6S_8$ | 13.33 | 12.56 | 1.75 | 4.26 | 49.4 | 55.8 | 900 |
| $PbMo_6S_8$ | 15.08 | 14.53 | 1.25 | 5.76 | 60.7 | 60.9 | 160 |
| $(Pb_{0.96}Gd_{0.04})Mo_6S_8$ | 14.07 | 13.23 | 2.0 | 7.38 | 56.8 | 59.3 | - |
| $(Pb_{0.90}Gd_{0.10})Mo_6S_8$ | 14.46 | 13.69 | 1.6 | 8.5 | 56.8 | 58.4 | 420 |
| $(Pb_{0.70}Gd_{0.30})Mo_6S_8$ | 9.2 | 8.0 | 1.8 | - | 22.4 | 41.7 | 670 |

**Table 2. $T_{c(onset)}$, $T_{c(mid)}$, $\Delta T_c$, $\Delta c / T_c$, $c / T$ at $T_{c(onset)}$, $c / T$ at 15.1 K and $\rho_N$ for all samples. The values of $\rho_N$ and the values of $T_{c(onset)}$, $T_{c(mid)}$ and $\Delta T_c$ for the $(Pb_{0.70}Gd_{0.30})Mo_6S_8$ sample are taken from the resistivity data taken by D N Zheng, I J Daniel and N A Morley, all other parameters are taken from the specific heat data.**

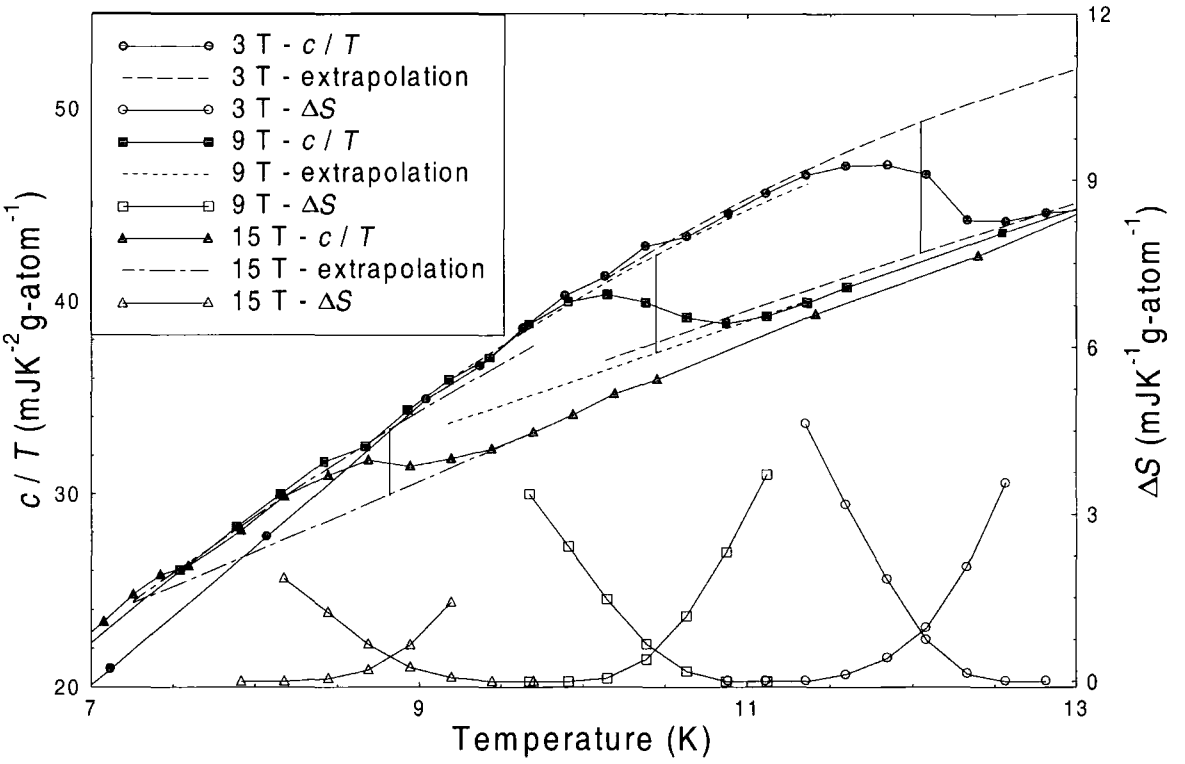


**Figure 29.** $c / T$ **as a function of temperature for** $SnMo_6S_8$ **in applied fields 3T, 9T and 15 T with extrapolated lines (**$c_{fitting}$**) from above and below the specific heat transition. Also shown is the calculated entropy change from** $c_{data}$ **-** $c_{fitting}$ **from above and below the specific heat transition for each field.**

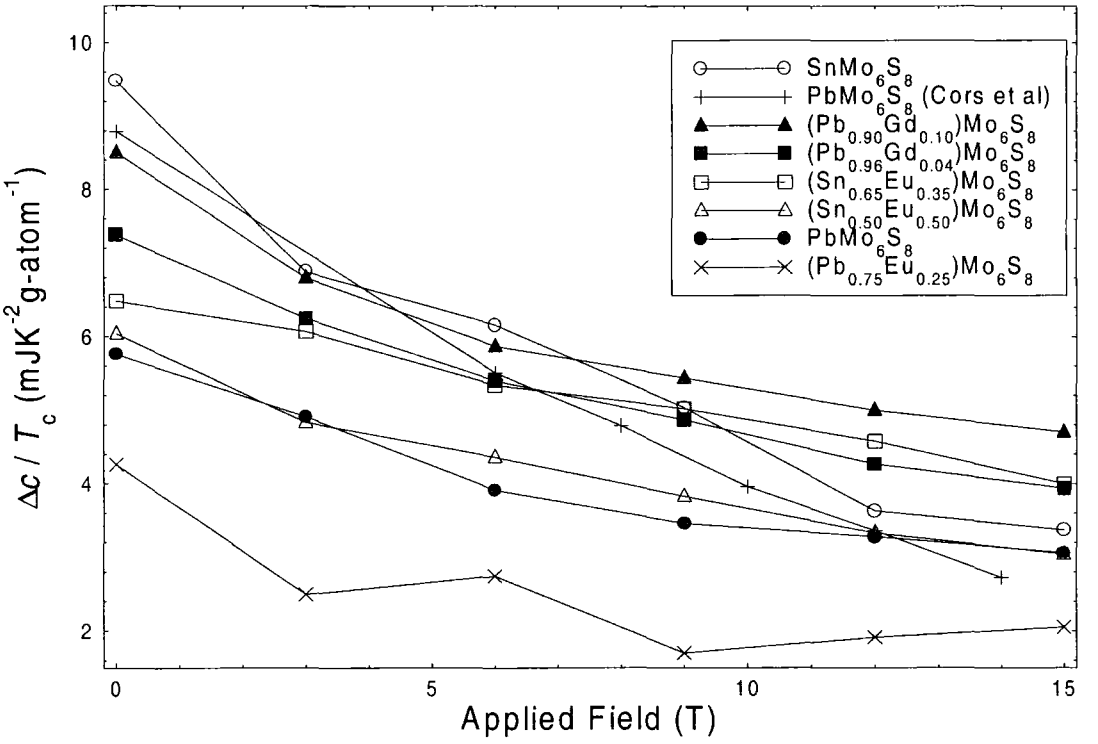


**Figure 30.** $\Delta c / T_c$ **as a function of applied field for all eight samples.**

The specific heat jumps of these samples are not infinitely sharp due to temperature fluctuations and inhomogeneities in the sample. For the purposes of analysis an idealised specific heat jump is therefore calculated for each sample, at each applied magnetic field such that the entropy change from superconducting to normal state is the same for the idealised transition as for the actual data. The process of fitting and extrapolating the data either side of the jump region and using these extrapolations to calculate an idealised transition is described in detail in section 6.5.3. The resulting transition occurs at a temperature that defines the mid-point of the specific heat transition ($T_{c(mid)}$) and allows a value of the size of the specific heat jump ($\Delta c$ / $T_c$) to be determined at $T_{c(mid)}$. The fitted curves above and below the transition allow values of the onset and width of the superconducting transition, $T_{c(onset)}$ and $\Delta T_c$, to be determined by defining the temperatures at which the measured data deviates from the extrapolated curves by more than 1 %.

For the undoped $SnMo_6S_8$ and $PbMo_6S_8$ samples and the lightly doped $(Pb_{0.96}Gd_{0.04})Mo_6S_8$ and $(Pb_{0.90}Gd_{0.10})Mo_6S_8$ samples there is no visible magnetic contribution to be taken into account in the region of $T_c$ and so the analysis of the specific heat jump is performed on the raw data (Fig.'s 1, 5, 6 and 7). For the $(Sn_{0.65}Eu_{0.35})Mo_6S_8$ and $(Sn_{0.50}Eu_{0.50})Mo_6S_8$ samples the magnetic contribution has been subtracted, as described in the previous section, and so the analysis of the specific heat jump is performed on the remaining data ($c$ - $c_m$) presented in Fig.'s 20 and 21. Accurate analysis of the specific heat jump in the raw data at 3 T (Fig.'s 2 and 3) is not possible for these two samples, after the subtraction however analysis can be performed to an accuracy of better then 20 %.

The magnetic contribution of the $(Pb_{0.75}Eu_{0.25})Mo_6S_8$ sample could not be subtracted and the analysis of the specific heat jump is carried out on the raw data. The size of the magnetic contribution in the region of $T_c$ is much bigger for the $(Sn_{0.65}Eu_{0.35})Mo_6S_8$ and $(Sn_{0.50}Eu_{0.50})Mo_6S_8$ samples than for the $(Pb_{0.75}Eu_{0.25})Mo_6S_8$ sample and so the analysis of the specific heat jump is not significantly affected by the magnetic background of this sample. The $(Pb_{0.70}Gd_{0.30})Mo_6S_8$ sample has no visible superconducting specific heat jump and so analysis of the superconducting transition is carried out using the corresponding resistivity data.

Figure 29 shows as a typical example the analysis of the specific heat jump for the $SnMo_6S_8$ sample in fields of 3 T, 9 T and 15 T and Fig. 30 presents the values of $\Delta c$ / $T_c$ for

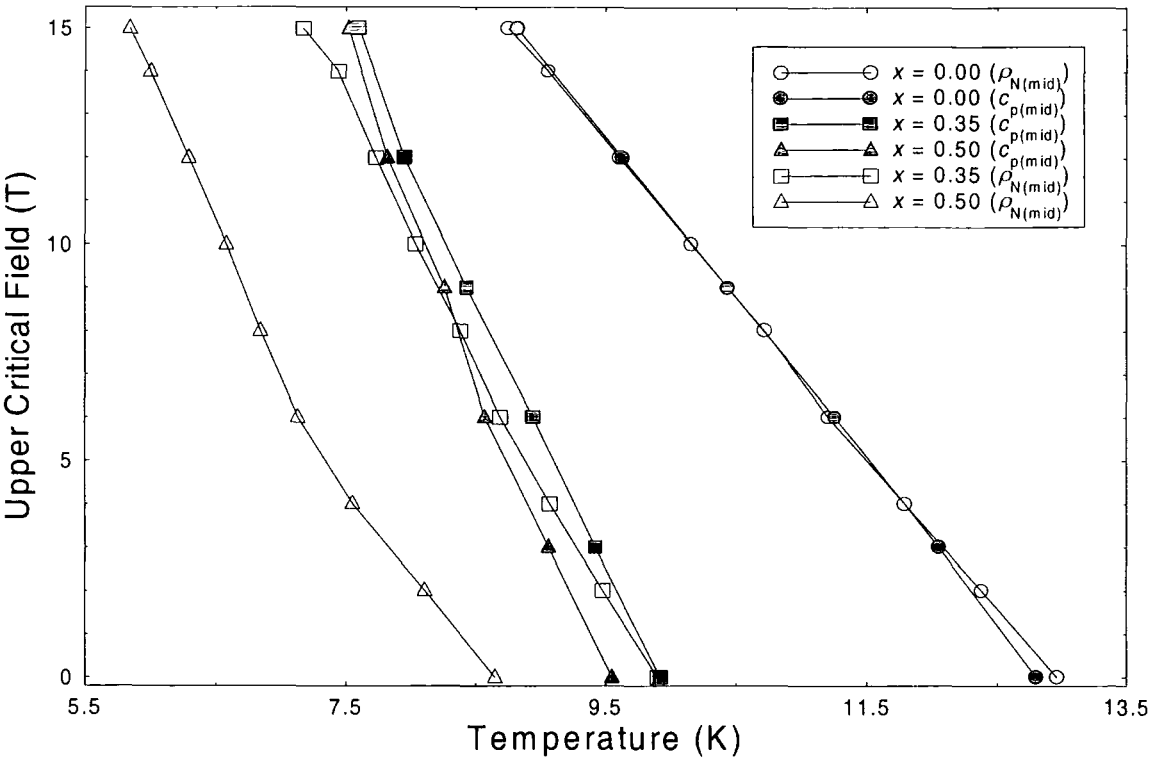


**Figure 31. Upper critical field as a function of temperature for $(Sn_{1-x}Eu_x)Mo_6S_8$ samples compounds with the corresponding data analysis from resistivity measurements (I J Daniel) [325].**

all of the samples and for each applied field. The accuracy of the resulting values of $\Delta c / T_c$ is about 10 % in zero field, whereas for larger applied fields where the specific heat jump is much smaller then the accuracy of the estimated values of $\Delta c / T_c$ is reduced to about a factor 2. The accuracy of the values of $T_{c(onset)}$ and $T_{c(mid)}$ determined from this analysis ranges from 2 % for the sharpest specific heat transitions to about 5 % for the broader transitions.

The results of the specific heat analysis from all of the samples in zero applied field are summarised in table 2. The results of a similar analysis from the resistivity of the $(Pb_{0.70}Gd_{0.30})Mo_6S_8$ sample which does not have a visible superconducting specific heat jump and the values of the normal state resistivity for all of the samples are also included. The data in table 2 shows that by doping with rare-earth ions the transition temperature is suppressed, the normal state specific heat is reduced and the normal state resistivity is increased. These changes are not completely systematic but generally become larger as the doping level is increased. In the $(Sn_{1-x}Eu_x)Mo_6S_8$ series $\Delta c / T_c$ drops systematically with increasing doping and the $(Pb_{0.75}Eu_{0.25})Mo_6S_8$ sample has a value of $\Delta c / T_c$ in zero field

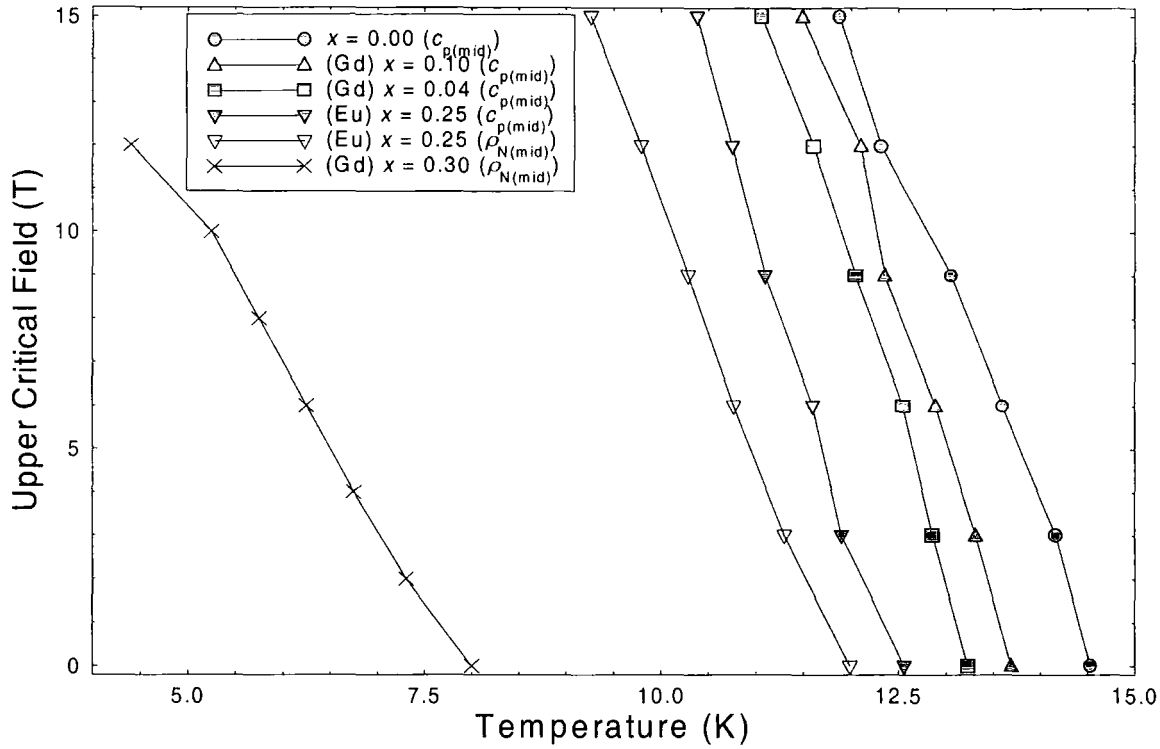


**Figure 32. Upper critical field as a function of temperature for $(Pb_{1-x}M_x)Mo_6S_8$ samples, where M = Gd or Eu, from the specific heat analysis and the corresponding data from resistivity measurements for the $(Pb_{0.70}Gd_{0.30})Mo_6S_8$ (D N Zheng [326]) and $(Pb_{0.75}Eu_{0.25})Mo_6S_8$ samples (N A Morley [327]).**

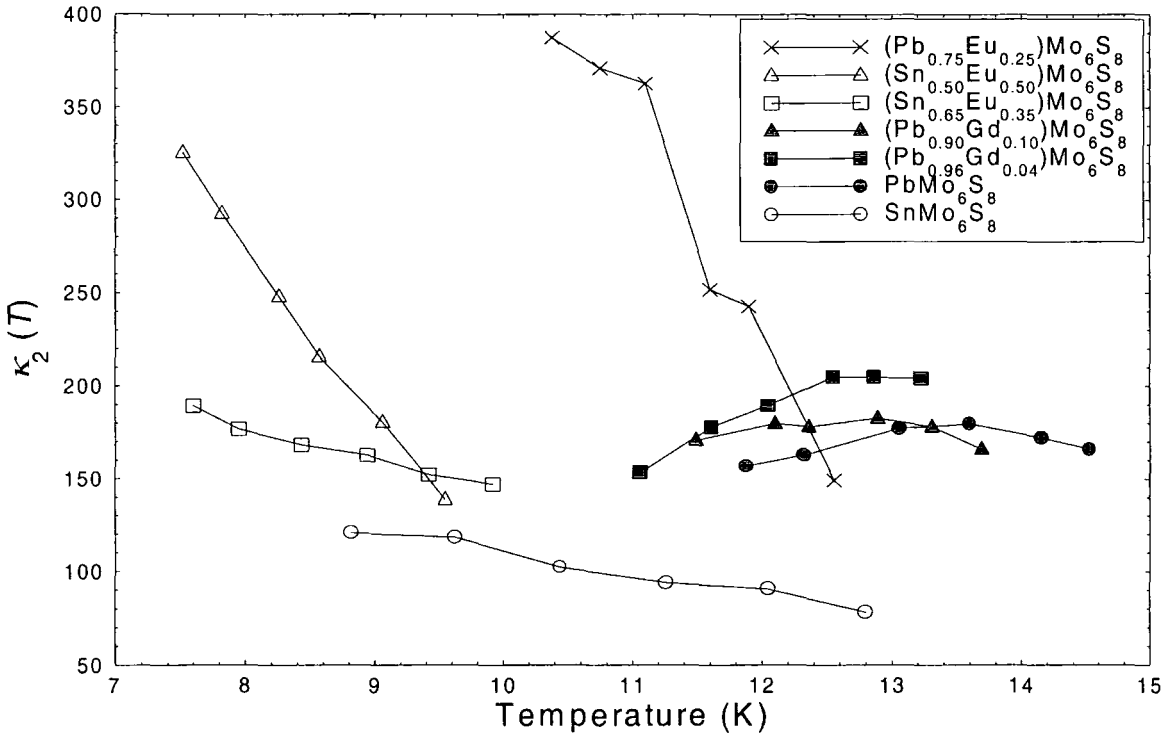


**Figure 33. $\kappa_2$ as a function of temperature for all eight samples (from $\Delta c$ / $T_c$ and $dB_{c2}$ / $dT$).**

| Sample | $dB_{c2}/dT$ ($T_c$) ($TK^{-1}$) | | $B_{c2}(0)$ (T) | | $\kappa_2(T_c)$ |
|---|---|---|---|---|---|
| | $c_{p(mid)}$ | $\rho_{N(mid)}$ | $c_{p(mid)}$ | $\rho_{N(mid)}$ | ($\Delta c / T_c$, $(dB_{c2}/dT)_{Tc}$) |
| $SnMo_6S_8$ | -3.9 | -3.5 | 34.7 | 31.4 | 78 |
| $(Sn_{0.65}Eu_{0.35})Mo_6S_8$ | - 6.1 | -4.7 | 41.6 | 32.2 | 147 |
| $(Sn_{0.50}Eu_{0.50})Mo_6S_8$ | - 5.5 | -3.8 | 36.5 | 22.6 | 139 |
| $(Pb_{0.75}Eu_{0.25})Mo_6S_8$ | - 5.0 | -4.4 | 43.3 | 36.6 | 149 |
| $PbMo_6S_8$ | - 6.4 | - | 64.4 | - | 166 |
| $(Pb_{0.96}Gd_{0.04})Mo_6S_8$ | - 8.9 | - | 81.6 | - | 204 |
| $(Pb_{0.90}Gd_{0.10})Mo_6S_8$ | - 7.8 | - | 73.8 | - | 166 |
| $(Pb_{0.70}Gd_{0.30})Mo_6S_8$ | - | -2.9 | - | 16.3 | - |

**Table 3. $dB_{c2}/dT$ ($T_c$), $B_{c2}(0)$ and $\kappa_2(T_c)$ calculated for all of the samples. Values of $dB_{c2}/dT$ ($T_c$) and $B_{c2}(0)$ are determined from both the mid-point of the specific heat transition and the mid-point of the resistivity transition. The values of $\kappa_2(T_c)$ are determined from $\Delta c / T_c$ in zero field and $dB_{c2}/dT$ ($T_c$) from the specific heat analysis.**

lower than all of the other samples except the $(Pb_{0.70}Gd_{0.30})Mo_6S_8$ sample. In the $(Pb_{1-x}Gd_x)Mo_6S_8$ series the size of the zero field specific heat jump increases with doping level up to $x = 0.10$ and then drops back to below the resolution of the measurements when $x = 0.30$.

Figures 31 and 32 show the temperature dependence of $B_{c2}(T)$ as determined from the mid-point of the specific heat jump for the tin and lead compounds respectively, data from the resistivity measurements are also included where appropriate. Due to the very large values of $B_{c2}(0)$ for these compounds only the values of $B_{c2}(T)$ and $dB_{c2}/dT$ for $T > \sim 0.7T_c$ can be determined and therefore rigorous analysis of the data using WHH-Maki theory cannot be performed. The data in Fig.'s 31 and 32 is fitted instead to a second order polynomial and the value of $dB_{c2}(T)/dT$ calculated at each applied field value. Using the value of $dB_{c2}(T)/dT$ as $T \rightarrow T_c$ and WHH-Maki theory a simple estimate of $B_{c2}(0)$ for each sample can be made:

$$B_{c2}(0) = -0.693 T_c \left( \frac{dB_{c2}(T)}{dT} \right)_{T=T_c} \tag{7.2}$$

The values of $dB_{c2}(T) / dT$ and $\Delta c / T_c$ at each field can also be used to determine the temperature dependence of $\kappa_2$ for each sample:

$$\left.\frac{\Delta c}{T_c}\right|_B = \frac{\left(\frac{dB_{c2}}{dT}\right)^2}{1.16\mu_0\left(2\kappa_2^2(T)-1\right)} \tag{7.3}$$

Figure 33 shows the values of $\kappa_2$ determined from Eqn. (7.3). The accuracy of these values is determined not only by the accuracy of the specific heat analysis ($\Delta c / T_c$) but also by the fitting of the $B_{c2}(T)$ as a function of $T$ data. A simple parabolic fitting was applied to the data in Fig.'s 31 and 32. The small number of points on each curve and the errors of up to 5 % in the values of $T_{c(mid)}$ leads to a similar error in the values of $dB_{c2}(T) / dT$ and errors in the estimates of $B_{c2}(0)$ of up to 20 %.

Table 3 summarises for each sample, the values of $dB_{c2}(T) / dT$ as $T \rightarrow T_c$ and $B_{c2}(0)$ from both specific heat and resistivity measurements. The values of $\kappa_2$ at $T_c$ determined using the values of $dB_{c2}(T_c) / dT$ and $\Delta c / T_c$ from the specific heat analysis are also included. The data shows that the estimates of $B_{c2}(0)$ and $\kappa_2(T_c)$ are larger for the doped samples in both the $(Sn_{1-x}Eu_x)Mo_6S_8$ and $(Pb_{1-x}Gd_x)Mo_6S_8$ series than for the parent compounds. The estimates of $B_{c2}(0)$ and of $\kappa_2(T_c)$ for the $(Pb_{0.75}Eu_{0.25})Mo_6S_8$ sample are both lower than the $PbMo_6S_8$ sample, similarly the $(Pb_{0.70}Gd_{0.30})Mo_6S_8$ sample has a much lower value of $B_{c2}(0)$ than the other samples and a value of $\kappa_2(T_c)$ that cannot be estimated from Eqn. (7.3) since $\Delta c / T_c$ is undetectable. The samples with the lowest level of doping in each series also have the maximum values of both $B_{c2}(0)$ and $\kappa_2(T_c)$. Similar estimates of $dB_{c2}(T_c) / dT$ and $B_{c2}(0)$ from the mid-point of the resistive transitions, for all the europium doped samples, follow the same trends as the results from the specific heat data. Figure 33 shows a positive temperature dependence of $\kappa_2$ with decreasing temperature for all of the $(Sn_{1-x}Eu_x)Mo_6S_8$ samples and the $(Pb_{0.75}Eu_{0.25})Mo_6S_8$ sample. The corresponding data for the $(Pb_{1-x}Gd_x)Mo_6S_8$ samples is inconclusive however with both negative and positive curvature.

## 7.6 Discussion.

### 7.6.1 Structural phase analysis.

The results from the X-ray measurements show that all of the fabricated samples are predominantly single phase with the largest amounts of secondary phase material occurring

in the $SnMo_6S_8$, $(Sn_{0.65}Eu_{0.35})Mo_6S_8$, $(Pb_{0.90}Gd_{0.10})Mo_6S_8$ and $(Pb_{0.70}Gd_{0.30})Mo_6S_8$ samples. As the doping level is increased through both of the series $(Sn_{1-x}Eu_x)Mo_6S_8$ and $(Pb_{1-x}Gd_x)Mo_6S_8$ the peaks in the XRD pattern corresponding to the Chevrel phase broaden indicating a change in the lattice parameters of the unit cell, this is confirmed by analysis of the XRD patterns that shows in the $(Pb_{1-x}Gd_x)Mo_6S_8$ series the unit cell volume decreases as the doping level is increased. The specific heat analysis shows a single superconducting jump for all of the samples except $(Pb_{0.70}Gd_{0.30})Mo_6S_8$ and no evidence for the magnetic transition of EuS at about 16.5 K [16] in the specific heat of any of the europium doped samples. The estimates of the fraction of $Gd_2S_3$ in the $(Pb_{0.70}Gd_{0.30})Mo_6S_8$ and $(Pb_{0.90}Gd_{0.10})Mo_6S_8$ samples from the specific heat analysis reveals that this secondary phase comprises at most 6 % of the mass of the samples. These results along with the uniform distribution of the magnetic ions observed in the EDX measurements, all indicate that the majority of the magnetic ions have been correctly substituted onto the metal lattice sites to form the corresponding $SnMo_6S_8$(Eu) and $PbMo_6S_8$(Gd) phases.

### 7.6.2 Normal state specific heat.

The data in Fig. 9 shows that the simple Debye approximation of $c_n = \gamma T + AT^3$ is not applicable to the normal state specific heat of these samples. Characterisation of the lattice contribution to the specific heat of these samples cannot therefore be carried out using a single Debye temperature, even if the full functional form of the Debye model is used (section 6.5.2).

The magnitude of $c$ / $T$ at the onset of the specific heat jump for both the $SnMo_6S_8$ and $PbMo_6S_8$ samples is in good agreement with data from other authors; 35 – 47 $mJK^{-2}g\text{-}atom^{-1}$ for $SnMo_6S_8$ [29, 328] and 50 – 70 $mJK^{-2}g\text{-}atom^{-1}$ for $PbMo_6S_8$ [29, 68, 127, 183]. Although the difference in the value of $c$ / $T$ at 15 K between the Sn and Pb compounds is relatively small (10 $mJK^{-2}g\text{-}atom^{-1}$), estimates of the electronic contribution to the specific heat ($\gamma \sim 5.5$ $mJK^{-2}g\text{-}atom^{-1}$ for $SnMo_6S_8$ [68] and ~ 8 $mJK^{-2}g\text{-}atom^{-1}$ for $PbMo_6S_8$ [328]) are not large enough to account for this difference. The change in the magnitude of the normal state specific heat is therefore assumed to be due to the phonon contribution ($c_L$). The phonon spectra of both $SnMo_6S_8$

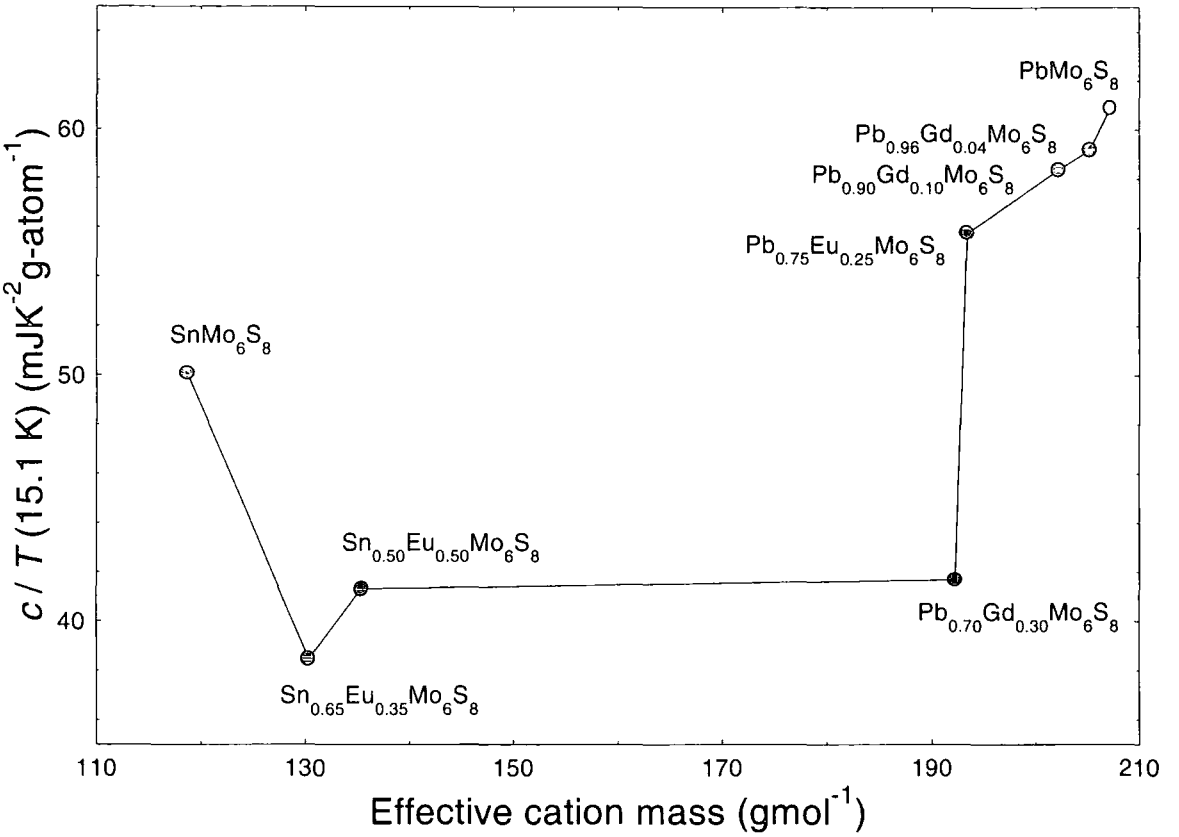


**Figure 34.** *c / T* **at 15.1 K as a function of effective cation mass for all of the samples in zero applied field.**

and $PbMo_6S_8$ have been determined from neutron scattering data [186, 317] and are dominated at low energies (< 10 meV) by a peak attributed to an Einstein mode of the metal ion in the lattice. This peak occurs at about 5 meV for both compounds, however the magnitude of the peak is smaller for the $SnMo_6S_8$ compound than for the $PbMo_6S_8$ compound and so at low temperatures $c_L$ will be smaller for $SnMo_6S_8$ than for $PbMo_6S_8$.

As the magnetic ions are substituted onto the lead or tin lattice sites the normal state specific heat is reduced. In the $(Sn_{1-x}Eu_x)Mo_6S_8$ series the $(Sn_{0.65}Eu_{0.35})Mo_6S_8$ sample has a lower normal state specific heat than the $(Sn_{0.50}Eu_{0.50})Mo_6S_8$ sample, whereas in the $(Pb_{1-x}M_x)Mo_6S_8$ samples (where M = Gd or Eu) there is a systematic reduction as $x$ is increased. Figure 34 shows the value of $c / T$ at 15.1 K for each sample in zero applied field as a function of effective cation mass, where the temperature 15.1 K is used so that all the samples are in the normal state. Apart from the $SnMo_6S_8$ and $(Pb_{0.70}Gd_{0.30})Mo_6S_8$ samples that are respectively higher and lower than expected a clear linear trend can be seen between the value of $c / T$ and the effective cation mass of the samples. Neutron diffraction measurements on $Cu_2Mo_6S_8$ show that the low energy peak associated with the Einstein

mode of the metal ion is at a higher energy (~ 8 meV) than in $PbMo_6S_8$. We have therefore proposed (section 6.5.2) that the systematic reduction in the normal state specific heat of the series $(Pb_{1-x}Cu_{1.8x})Mo_6S_8$ as more copper is added, is due to the increase in the average energy of this Einstein peak. Although no similar neutron diffraction studies have been carried out on either $EuMo_6S_8$ or $GdMo_6S_8$ the general correlation observed in Fig. 34 supports the hypothesis that a larger cation mass has a corresponding lower energy Einstein mode and therefore a larger heat capacity at low temperatures.

### 7.6.3 Specific heat jump.

The size of the specific heat jump in zero field for the $SnMo_6S_8$ sample is in good agreement with data from other authors that are typically 7 – 10 $mJK^{-2}g\text{-}atom^{-1}$ [29, 328] and also has relatively small transition width, indicative of a good quality, homogeneous sample. The size of the specific heat jump in zero field for the $PbMo_6S_8$ sample (5.76 $mJK^{-2}g\text{-}atom^{-1}$) is approximately 50 % smaller than samples from other authors that are typically 9 - 14 $mJK^{-2}g\text{-}atom^{-1}$ [29, 127] and also the $PbMo_6S_8$ sample fabricated here in Durham as part of the series $(Pb_{1-x}Cu_{1.8x})Mo_6S_8$ (chapter 6). The $T_c$ of this sample is as high as the best samples in the literature and the transition width of 1.25 K also indicates a good quality, homogeneous sample.

For the $(Sn_{1-x}Eu_x)Mo_6S_8$ series the width of the zero field transition remains approximately constant throughout the series indicating there is little variation in the homogeneity of the samples with doping, a surprising result considering the large doping levels involved. The doped samples $(Pb_{1-x}M_x)Mo_6S_8$ where M = Gd or Eu however, all have broader zero field transitions than the $PbMo_6S_8$ sample which indicates a range of compositions within the sample. Substitution of the rare-earth ions leads to a variation in stoichiometry within the material and is the most probable reason for the larger transition widths in the doped samples since the XRD measurements indicate that the samples are still predominantly single phase.

In the $(Sn_{1-x}Eu_x)Mo_6S_8$ series the value of $\Delta c / T_c$ decreases with increasing doping level. Since the introduction of rare-earth ions leads to competition between the magnetic and superconducting ordering we would expect a smaller number of Cooper pairs to be present in the doped samples and therefore a smaller specific heat jump. For the $(Pb_{1-x}M_x)Mo_6S_8$

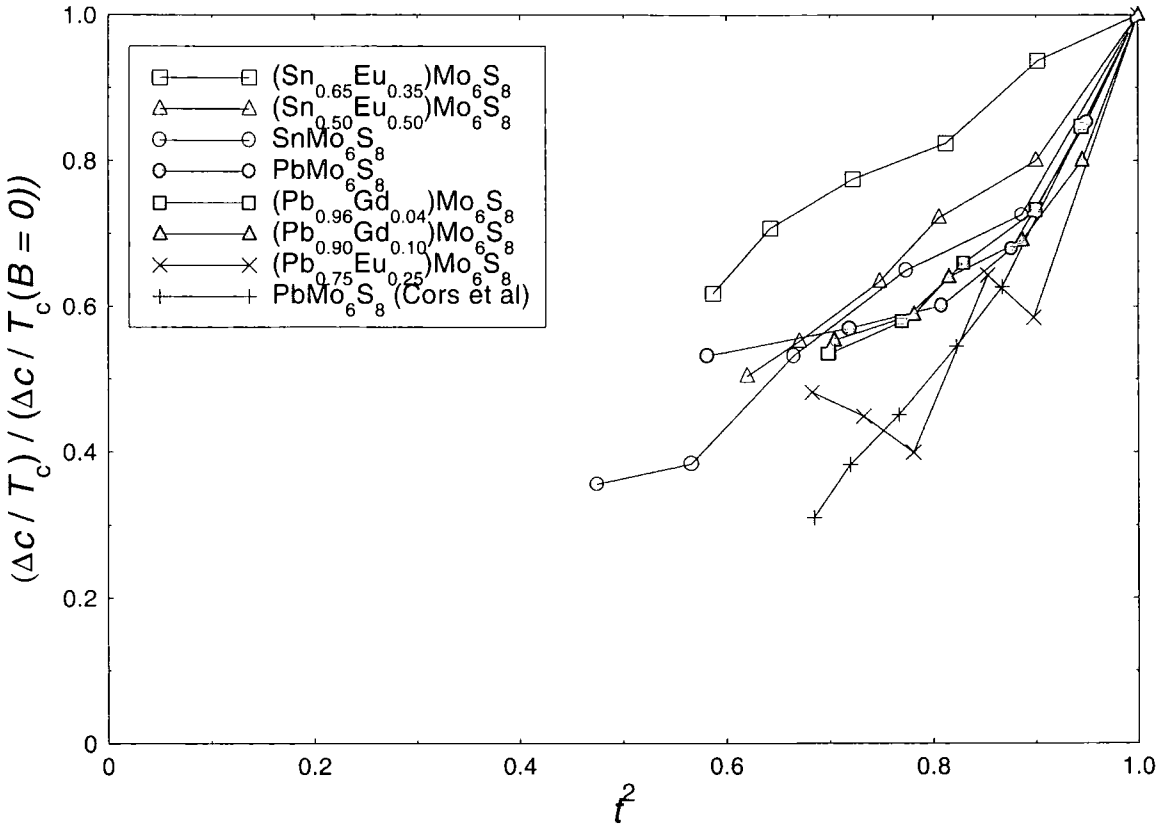


**Figure 35. $(\Delta c / T_c) / (\Delta c / T_c(B = 0))$ as a function of $t^2$ for all eight samples. Also included is data on $PbMo_6S_8$ from Cors et al [127].**

samples (where M = Gd or Eu) however $\Delta c / T_c$ increases initially as the doping level is increased to a level of $x = 0.10$ and then drops considerably for the $(Pb_{0.75}Eu_{0.25})Mo_6S_8$ sample and is undetectable for the $(Pb_{0.70}Gd_{0.30})Mo_6S_8$ sample. This non-typical behaviour is compromised however by the $PbMo_6S_8$ sample, which as we have previously mentioned has a much smaller jump height than comparable $PbMo_6S_8$ samples. Compared to a more typical value for $PbMo_6S_8$ of 10 $mJK^{-2}g\text{-}atom^{-1}$, the doped samples do have a lower jump height than the undoped sample (although not systematically) as expected due to the competition between magnetic and superconducting ordering.

The temperature dependence of $\Delta c / T_c$ has been modelled by both Maki [124] and Vijfeijken [126]. A plot of the reduced jump height (i.e. the ratio $(\Delta c / T_c) / (\Delta c / T_c(B = 0))$) as a function of the reduced critical temperature squared (i.e. $(T_c / T_c(B = 0))$) should follow a straight line through the origin according to Vijfeijken with gradient $1 / [1 - (1 / 2\kappa^2) \ln\kappa]$ and according to Maki a non-linear dependence which lies above that predicted by Vijfeijken. Figure 35 presents the data for all eight samples plotted in this manner and for comparison the data from Cors et al on a $PbMo_6S_8$ sample [127]. The figure shows that

virtually all the data lies below the straight line (0,0) to (1,1) and so no comparison can be made with the models of either Maki or Vijfeijken. In particular we can note that in Vijfeijken's model if the data lies below the line (0,0) to (1,1) then this implies that the factor $1 / [1 - (1 / 2\kappa^2) \ln\kappa] < 1$ and this then implies the non-physical result for these samples of $\kappa < 1$. Values of $\kappa$ have been measured for $PbMo_6S_8$ that are typically ~ 100 [161, 324] in clear contradiction with the temperature dependence implied by Vijfeijken's model and the model of Maki.

### 7.6.4 Determination of Sommerfeld constant.

| | $\omega_{ln}$ (K) | $T_c$ (K) | $\gamma$ (mJK$^{-2}$ g-atom$^{-1}$) | $\Delta c / T_c$ (mJK$^{-2}$ g-atom$^{-1}$) | $\Delta c / \gamma T_c$ | $c / T_c$ (mJK$^{-2}$ g-atom$^{-1}$) |
|---|---|---|---|---|---|---|
| $SnMo_6S_8$ (a) | ∞ (w) | **11.4** | **5.6** | **6.93** | 1.24 | **35** |
| $SnMo_6S_8$ (b) | 186 | **12.2** | **5.3** | **10.3** | 1.96 | **47** |
| $SnMo_6S_8$ (c) | ∞ (w)<br>194.6 (s) | **12.80** | 6.63 (w)<br>4.84 (s) | **9.48** | 1.43 (w)<br>1.96 (s) | **45.9** |
| $PbMo_6S_8$ (d) | ∞ (w) | **13.7** | **8.0** | **10.7** | 1.33 | **53** |
| $PbMo_6S_8$ (e) | 185 | **14.3** | **6.5** | **13.6** | 2.09 | **62** |
| $PbMo_6S_8$ (c) | ∞ (w)<br>198.0 (s) | **14.53** | 4.03 (w)<br>2.81 (s) | **5.76** | 1.43 (w)<br>2.09 (s) | **60.7** |

**Table 4. $\gamma$, $\Delta c / T_c$, $\Delta c / \gamma T_c$ and $c / T_c$ for $SnMo_6S_8$ and $PbMo_6S_8$ taken from references (a) Alekseevskii [328] (b) Fradin [29] (c) this author (d) Alekseevskii [68] and (e) Meulen [183]. Values in bold type are either quoted in the reference or determined from the data presented in that reference. The values of $\omega_{ln}$ are determined using the modified BCS relation (Eqn. 7.4) and the values of $\Delta c / \gamma T_c$ in the table. The estimates of $\gamma$ for the $PbMo_6S_8$ and $SnMo_6S_8$ samples from this author are made using values of $\Delta c / \gamma T_c = 1.43$ in the weak coupling regime (w) and 1.96 and 2.09 in the strong coupling regime (s) for $SnMo_6S_8$ and $PbMo_6S_8$ respectively. These values of the ratio $\Delta c / \gamma T_c$ correspond to a value of $\omega_{ln} = \infty$ for the weak coupling limit and $\omega_{ln} = 195$ K for $SnMo_6S_8$ and 198 K for $PbMo_6S_8$ in the strong coupling regime.**

Since the normal state specific heat of these samples does not fit a simple Debye relation ($c_n = \gamma T + AT^3$) we cannot determine a value for the Sommerfeld constant ($\gamma$) from this method. Estimates for the value of $\gamma$ can be made however by comparing the specific heat data taken here by that of other authors who have determined values of $\gamma$ (section 6.5.4).

The modified BCS relation [321] for the ratio of the superconducting to normal state electronic contribution to the specific heat is given by:

$$\frac{\Delta c}{\gamma T_c} = 1.43\left[1+53\left(\frac{T_c}{\omega_{ln}}\right)^2 \ln\left(\frac{\omega_{ln}}{3T_c}\right)\right] \qquad (7.4)$$

The ratio $\Delta c$ / $\gamma T_c$ is equal to 1.43 in the weak coupling limit but has an additional correction factor that accounts for strong coupling and is characterised by the ratio $T_c$ / $\omega_{ln}$, where $\omega_{ln}$ is a weighted average phonon frequency. Table 4 shows the results from analysis by other authors, values of the ratio $\Delta c$ / $\gamma T_c$ range between 1.24 and 1.96 for $SnMo_6S_8$ [29, 328] and between 1.33 and 2.09 for $PbMo_6S_8$ [68, 183]. These data show that different fabrication methods can produce samples of the same material that have properties characteristic of either a strong or weak coupling superconductor.

The magnitude of $c_n$ for both the $SnMo_6S_8$ and $PbMo_6S_8$ samples measured here are similar to those of Alekseevskii et al, Fradin et al and Meulen et al (section 7.6.2). Since the normal state specific heat is dominated by the phonon contribution, we can conclude that the density of states and therefore the weighted average phonon frequency of these samples must also be similar to the samples of Alekseevskii, Fradin and Meulen. We can then take the values of the ratio $\Delta c$ / $\gamma T_c$ as 1.43 and 1.96 for $SnMo_6S_8$ and 1.43 and 2.09 for $PbMo_6S_8$ in the weak and strong coupling regimes respectively. Using the measured values of $\Delta c$ / $T_c$ we estimate the value of $\gamma$ for our $SnMo_6S_8$ sample to lie between 6.63 $mJK^{-2}g\text{-}atom^{-1}$ (weak coupling) and 4.84 $mJK^{-2}g\text{-}atom^{-1}$ (strong coupling) and for our $PbMo_6S_8$ sample to lie between 4.03 $mJK^{-2}g\text{-}atom^{-1}$ (weak coupling) and 2.76 $mJK^{-2}g\text{-}atom^{-1}$ (strong coupling). These results are summarised in table 4.

The estimated values of $\gamma$ in the weak and strong coupling regimes for the $SnMo_6S_8$ sample lie respectively above and below the results of Alekseevskii et al and Fradin et al. It is therefore not possible to draw any conclusions about either the strength of the electron-phonon coupling or the density of states for this sample. The estimated values of $\gamma$ for the $PbMo_6S_8$ sample however, are about half of the corresponding value in the literature in the

same coupling regime. Since these estimates are ~ 50 % lower independent of strength of the coupling, we suggest that the size of the specific heat jump for this sample which is also about 50 % lower than comparable samples, is determined principally by $\gamma$ through the density of states at the Fermi level.

For the doped samples there is no comparable data in the literature and therefore estimates of $\gamma$ cannot be made. We can note however that for the $(Pb_{1-x}Gd_x)Mo_6S_8$ series the $(Pb_{0.96}Gd_{0.04})Mo_6S_8$ and $(Pb_{0.90}Gd_{0.10})Mo_6S_8$ samples have similar values of the normal state specific heat and therefore similar values of $\omega_{ln}$ to the $PbMo_6S_8$ sample. This indicates that in both strong and weak coupling regimes an increase in $\gamma$ for these samples compared to the $PbMo_6S_8$ sample, is sufficient to explain the observed increase in $\Delta c$ / $T_c$ with doping. Substitution of $Gd^{3+}$ ions for $Pb^{2+}$ ions increases the number of valence electrons at the $Mo_6S_8$ clusters and can therefore change the density of states at the Fermi level. At low levels of doping ($x \leq 0.10$) we therefore propose that $\gamma$ is increased due to an increase in the charge transfer from the cation to the $Mo_6S_8$ clusters (since $N(E_F) \propto \gamma$) and that this in turn accounts for the increase in $\Delta c$ / $T_c$ with doping. At higher levels of doping competition between the superconducting and magnetic ordering reduces the density of states and therefore $\gamma$ to such a degree that $\Delta c$ / $\gamma T_c$ is below the experimental resolution.

### 7.6.5 Transition temperature.

The transition temperatures in zero applied field of all of the samples fabricated here are in reasonable agreement with equivalent samples fabricated by other authors. $SnMo_6S_8$ samples in the literature typically have transition temperatures around 14 K and samples of $PbMo_6S_8$ typically have a $T_c$ between 14 K and 15 K, compared to 12.8 K and 14.5 K for our $SnMo_6S_8$ and $PbMo_6S_8$ samples respectively.

Fischer et al have fabricated members of the series $(Sn_{1-x}Eu_x)Mo_6S_8$ and $(Pb_{1-x}Eu_x)Mo_6S_8$ [200] and Sergent et al have fabricated several members of the series $(Pb_{1-x}Eu_x)Mo_6S_8$ and $(Pb_{1-x}Gd_x)Mo_6S_8$ [191] that can all be compared to the equivalent samples here. The transition temperatures of the parent compounds in these series are about 10 K and 12 K for the $SnMo_6S_8$ and $PbMo_6S_8$ compounds respectively in the series fabricated by Fischer et al and 11.5 K for the $PbMo_6S_8$ compounds in the two series of Sergent et al. The $(Sn_{1-x}Eu_x)Mo_6S_8$ series of Fischer et al has a transition temperature that remains constant at ~ 10 K for doping levels up to $x$ = 0.50 and in the $(Pb_{1-x}Eu_x)Mo_6S_8$ series of Fischer et al the

$(Pb_{0.70}Eu_{0.30})Mo_6S_8$ sample has a $T_c$ of 13.6 K that is higher than the parent compound. As rare-earth ions are substituted into the samples of Sergent et al the transition temperature remains constant at ~ 11.5 K up a doping level of $x = 0.1$ and then drops to about 10.5 K for $(Pb_{0.75}Eu_{0.25})Mo_6S_8$ and 5.0 K for $(Pb_{0.70}Gd_{0.30})Mo_6S_8$. Unlike these series the doped samples that we have fabricated all have a $T_c$ lower than the parent compound even at very low doping levels e.g. for $(Pb_{0.96}Gd_{0.04})Mo_6S_8$ the $T_c$ is 1.3 K lower than the $PbMo_6S_8$ sample.

The low transition temperature of the parent compounds in the series of Sergent et al and Fischer et al and the different effect of doping on $T_c$ compared to the samples measured here is probably due to the fabrication procedure. The samples of Sergent et al and Fischer et al were all reacted in quartz tubing at a maximum reaction temperature of 1050 °C. Reactions at high temperatures in quartz tubing have been shown however to introduce oxygen into the Chevrel phase and reduce the transition temperature of $PbMo_6S_8$ as low as

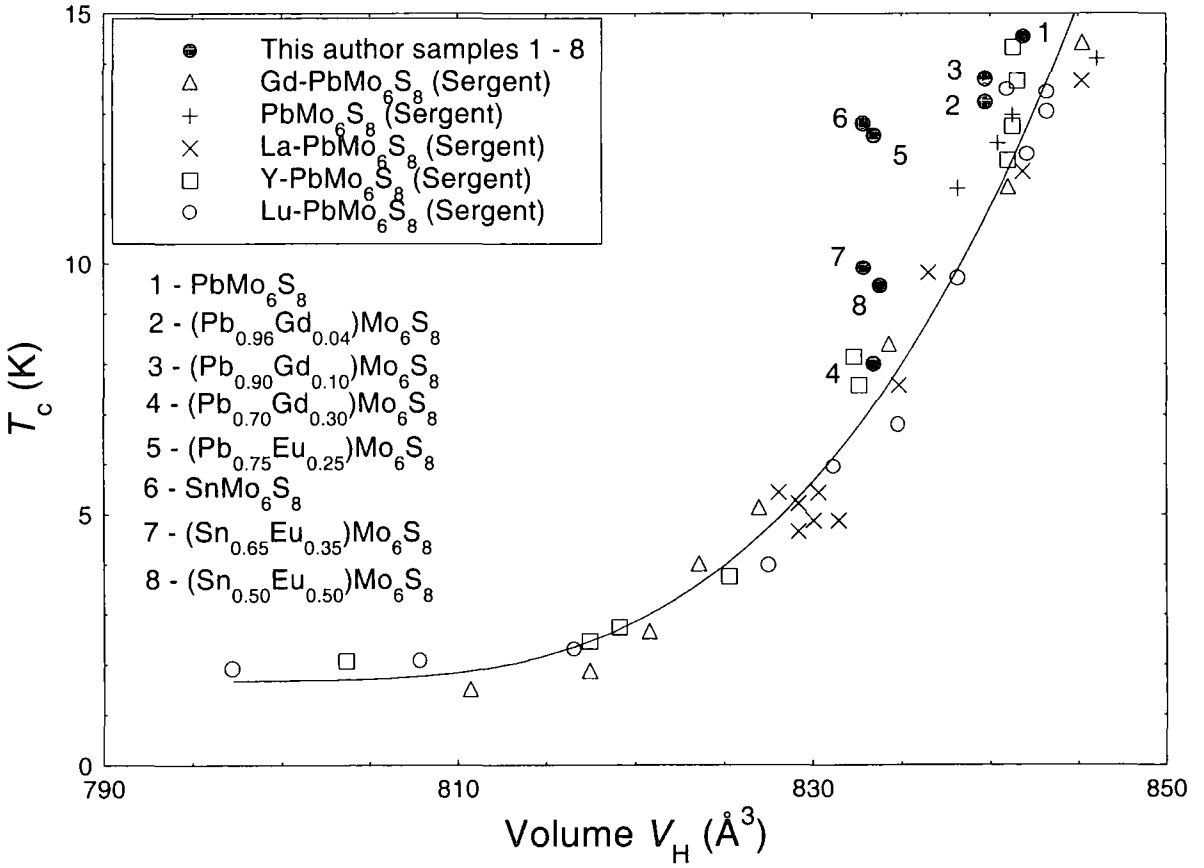


**Figure 36. $T_c$ as a function of the volume of the unit cell for the sample fabricated here and various Chevrel phases fabricated by Sergent et al [191].**

11.6 K [162]. Furthermore, a maximum reaction temperature of 1000 °C has been shown to be insufficient to fully substitute the rare-earth ions into the unit cell rather than as a secondary phase [160, 329], which in the case of $Gd_2S_3$ can act as an oxygen getter and improve the superconducting properties. The samples we have fabricated were reacted under argon, in a molybdenum crucible and at a maximum temperature of either 1450 °C or 1500 °C. We therefore propose that the difference in the values of $T_c$ between members of our series and those discussed above are due to the fabrication process and that the effects of oxygen contamination in our samples are negligible.

The superconducting properties of the Chevrel phases are sensitive to changes in both stoichiometry and the nature of the metal cation [172]. Substituting different cations into the unit cell alters the superconducting properties of the host material by changing the lattice dimensions and the charge transfer from the metal ion. Both of these effects can alter the superconducting density of states at the Fermi level and therefore the superconducting properties. The substitution of $Eu^{2+}$ ions however in place of either $Sn^{2+}$ ions or $Pb^{2+}$ ions of the same valence does have an effect on $T_c$ and the systematic increase in the number of $Gd^{3+}$ ions substituted onto the $Pb^{2+}$ ion sites is not followed by a systematic decrease in $T_c$. Both of these anomalies indicate that charge transfer effects are not sufficient to explain the change in $T_c$ with doping and that changes in the lattice dimensions could also have an influence on the density of states at the Fermi level. Another important effect of substituting with rare-earth ions is the competition between the antiferromagnetic exchange interaction of the rare-earth ions and the superconducting ordering among the conduction electrons. This competition can also act to reduce $T_c$ and produces transition temperatures for the $REMo_6S_8$ phases of < 2 K, however we would expect the reduction of $T_c$ due to this effect alone to be commensurate with the level of doping in a similar way to charge transfer effects.

Variations in $T_c$ of many Chevrel phases have been correlated with the ratio of $c$ / $a$ (the hexagonal lattice parameters) and the volume of the hexagonal unit cell ($V_H$), both parameters determined from X-ray data [162, 191]. Measurements on many members of the series $(Pb_{1-x}M_x)Mo_6S_8$ where M is a rare-earth element show a universal correlation between $T_c$ and the volume of the unit cell when M is a trivalent ion but not when M is a divalent ion [191]. Figure 36 shows those results and the corresponding values of $T_{c(mid)}$ determined from the specific heat measurements and $V_H$ for the eight samples measured here. The data in Fig. 36 shows that when tin ions are replaced by divalent europium ions

the volume of the unit cell remains constant but when lead ions are replaced by trivalent gadolinium ions there is a correlation between $V_H$ and $T_c$ in good agreement with the data of Sergent et al. Furthermore there is no evidence among our samples of correlation between $T_c$ and the $c$ / $a$ ratio.

These results suggest that the reduction in $T_c$ with doping is due to a combination of changes in the density of states at the Fermi level, due to changes in the lattice parameters and the charge transfer, and competition between the magnetic and superconducting ordering in these compounds. For the samples doped with gadolinium the change in $T_c$ can be correlated to the change in the volume of the unit cell and is almost certainly also affected by the increase in charge transfer to the $Mo_6S_8$ clusters and the increase in competition between the magnetic and superconducting ordering. The samples doped with europium ions have a reduction in $T_c$ that will be due in part to the magnetic-superconducting competition but is not correlated with either charge transfer effects, which are small since $Eu^{2+}$ and $Sn^{2+}$ have the same valence, or changes in the lattice parameters.

### 7.6.6 Upper critical field.

The estimated values of $B_{c2}(0)$ from the specific heat analysis $PbMo_6S_8$ and $SnMo_6S_8$ are in reasonable agreement with data from other authors [127, 139, 183, 200]. The $B_{c2}(0)$ values for all of the samples however (table 3, section 7.5.2) have a large error associated with the simple parabolic fitting used and the small number of points available. Nevertheless the values clearly show an increase in $B_{c2}(0)$ with doping for $(Sn_{1-x}Eu_x)Mo_6S_8$, even at high levels of doping ($x = 0.50$), and an increase in $B_{c2}(0)$ for low levels of doping ($x \leq 0.10$) in $(Pb_{1-x}Gd_x)Mo_6S_8$.

GLAG theory describes the relation between the dirty contribution to the upper critical field and the normal state resistivity:

$$B_{c2}^{d}(0) = 3.06\times10^{3}\,\rho_N\gamma_v T_c \qquad (7.5)$$

The values of the normal state resistivity for these compounds are presented in table 2 and apart from the $(Pb_{0.75}Eu_{0.25})Mo_6S_8$ sample that has the largest value of $\rho_N$, they show a systematic increase with doping level. Using the values of $\rho_N$ and $T_c$ from table 2 and the values of $\gamma_v$ estimated in section (7.6.4) we can calculate the value of $B_{c2}{}^{d}(0)$ from Eqn. (7.5) as 30.2 T and 37.3 T for $SnMo_6S_8$ and 17.4 T and 25.5 T for $PbMo_6S_8$ in the strong and weak coupling regimes respectively.

For the $SnMo_6S_8$ sample the calculated values of $B_{c2}{}^{d}(0)$ in both strong and weak coupling regimes are in reasonable agreement with the value of $B_{c2}(0)$ estimated from the specific heat analysis. Given the errors inherent in the specific heat analysis of $B_{c2}(0)$, we cannot determine from these simple calculations to which coupling regime the $SnMo_6S_8$ sample belongs. To produce the estimated values of $B_{c2}(0)$ using Eqn. (7.5) for the $(Sn_{0.65}Eu_{0.35})Mo_6S_8$ and $(Sn_{0.50}Eu_{0.50})Mo_6S_8$ samples and the values of $\rho_N$ and $T_c$ from table 2, values of $\gamma_v \approx 2.8$ $mJK^{-2}g\text{-}atom^{-1}$ and 0.5 $mJK^{-2}g\text{-}atom^{-1}$ respectively would be needed. These values are smaller than $\gamma_v$ for the $SnMo_6S_8$ sample by a factor 2 and 11 for the $x$ = 0.35 and 0.50 samples respectively. Such a large decrease in $\gamma_v$ is possible for the $(Sn_{0.65}Eu_{0.35})Mo_6S_8$ sample but very unlikely for $(Sn_{0.50}Eu_{0.50})Mo_6S_8$ sample since $\Delta c$ / $T_c$ for these samples are within 8 % of each other and between 60 – 70 % of the undoped sample.

For the $PbMo_6S_8$ sample, the calculated value of $B_{c2}{}^{d}(0)$ in either the strong or weak coupling regime comprises only about 30 % of the value of $B_{c2}(0)$ estimated from the specific heat analysis. For the $(Pb_{1-x}Gd_x)Mo_6S_8$ series the value of $\gamma_v$ increases with doping level (section 7.6.4) up to $x$ = 0.10 and is then severely reduced at higher levels ($x$ = 0.30). However given the factor 2.6 increase in $\rho_N$ for the $(Pb_{0.90}Gd_{0.10})Mo_6S_8$ sample compared to the $PbMo_6S_8$ sample, the value of $\gamma_v$ would need to be smaller for the $(Pb_{0.90}Gd_{0.10})Mo_6S_8$ sample to explain the increase of ~ 10 T in the value of $B_{c2}(0)$ from Eqn. (7.5) alone.

This analysis shows that considering these Chevrel phase materials as dirty superconductors is insufficient to explain the observed changes in the upper critical field. Contributions to $B_{c2}(0)$ in the clean limit are clearly required for the $(Pb_{1-x}M_x)Mo_6S_8$ samples to explain the large (60+ T) values of $B_{c2}(0)$ estimated from the specific heat analysis. Increases in $B_{c2}(0)$ compared to the parent compound by doping with rare-earth ions have also been seen previously by Fischer et al [200] in the series $(Sn_{1-x}Eu_x)Mo_6S_8$. In this series $B_{c2}(0)$ was measured by pulse field data and showed an increase of as much as 45 % for the $x$ = 0.50 sample. Samples of $(Pb_{0.70}Eu_{0.30})Mo_6S_8$ and $(Pb_{1.00}Gd_{0.20})Mo_6S_8$ fabricated and measured by Fischer et al [149, 200] also showed similar rises in $B_{c2}(0)$ compared to the pure $PbMo_6S_8$ samples.

The introduction of the magnetic ions can lead to magnetic field induced superconductivity, or the compensation effect, whereby the exchange field produced by the magnetic ions compensates for the polarisation of the electron spins due to the external field [266]. If the orbital critical field of the material is greater than the paramagnetic limit superconductivity can be induced at fields larger than the normal upper critical field in the absence of the magnetic ions. A characteristic of this effect is a positive rather than negative curvature in $B_{c2}(T)$ as a function of $T$ for high levels of doping [144, 200], this is due to the competition between the exchange field that increases with increased doping and the external field.

The specific heat and resistivity data obtained for the $(Sn_{0.65}Eu_{0.35})Mo_6S_8$, $(Sn_{0.50}Eu_{0.50})Mo_6S_8$ and $(Pb_{0.75}Eu_{0.25})Mo_6S_8$ samples and the resistivity data obtained for the $(Pb_{0.70}Gd_{0.30})Mo_6S_8$ sample all show some evidence for positive curvature in the slope of $B_{c2}(T)$ as a function of $T$ (Fig.'s 31 and 32). We therefore conclude that the compensation effect has some effect, along with the normal state resistivity, in determining the upper critical field of these materials [200]. Furthermore given this change in curvature in the initial slope of $B_{c2}(T)$ as a function of $T$, the estimated values of $B_{c2}(0)$ for the $(Sn_{0.65}Eu_{0.35})Mo_6S_8$, $(Sn_{0.50}Eu_{0.50})Mo_6S_8$ and $(Pb_{0.75}Eu_{0.25})Mo_6S_8$ samples become extremely unreliable due to the lack of data for $T < 0.7T_c$. Comparison however with the data of Fischer et al [200], where pulse field data enabled measurements down to $0.1T_c$, suggests that the actual value of $B_{c2}(0)$ for samples exhibiting this type of behaviour are higher than that estimated by the initial slope ($dB_{c2} / dT$). Lastly we note that there is no evidence of any change in the curvature of $B_{c2}(T)$ as a function of $T$ for the samples with low levels of doping ($(Pb_{0.96}Gd_{0.04})Mo_6S_8$ and $(Pb_{0.90}Gd_{0.10})Mo_6S_8$) in agreement with Fischer et al. The estimated values of $B_{c2}(0)$ for these samples are therefore more reliable.

### 7.6.7 Thermodynamic critical field and kappa.

The estimated values of $\gamma_v$ allow the value of the thermodynamic critical field at $T = 0$ K for both $PbMo_6S_8$ and $SnMo_6S_8$ samples to be calculated in both the strong and weak coupling regimes using the modified BCS relation [321]:

$$\frac{\gamma_v T_c^2}{\mu_0 H_c^2(0)} = 1.68\left[1 - 12.2\left(\frac{T_c}{\omega_{ln}}\right)^2 \ln\left(\frac{\omega_{ln}}{3T_c}\right)\right] \tag{7.6}$$

In the strong coupling regime the ratio of $T_c$ / $\omega_{ln}$ can be determined from the ratio $\Delta c$ / $\gamma T_c$ (Eqn. 7.4) and in the weak coupling limit $\mu_0 H_c(0)$ can be determined by setting $T_c$ / $\omega_{ln}$ equal to zero. GLAG theory allows us to then estimate the value of $\kappa_1(0)$ using the values of $B_{c2}(0)$ and $\mu_0 H_c(0)$ [110]:

$$\kappa_1(T) = \frac{B_{c2}(T)}{\sqrt{2}B_c(T)} \tag{7.7}$$

| | $\mu_0 H_c(0)$ (T) ($\gamma_v$, $T_c$, $\omega_{ln}$) | | $\kappa_1(0)$ ($\mu_0 H_c(0)$, $B_{c2}(0)$) | | $\kappa_2(T_c)$ ($\Delta c$ / $T_c$, ($dB_{c2}/dT)_{Tc}$) |
|---|---|---|---|---|---|
| | Weak | Strong | Weak | Strong | |
| $SnMo_6S_8$ | 0.26 | 0.24 | 94 | 102 | 78 |
| $PbMo_6S_8$ | 0.24 | 0.21 | 190 | 217 | 166 |

**Table 5. Values of $\mu_0 H_c(0)$, $\kappa_1(0)$ and $\kappa_2(T_c)$ calculated from various experimental data for both $SnMo_6S_8$ and $PbMo_6S_8$. $\mu_0 H_c(0)$ is calculated from Eqn. (7.6) using values of $\omega_{ln}$, $\gamma_v$ and $T_c$ from table 4. $\kappa_1(0)$ is calculated from Eqn. (7.7) using the values of $\mu_0 H_c(0)$ and the estimates of $B_{c2}(0)$ in table 3 from the specific heat analysis. The values of $\kappa_2(T_c)$ were calculated in section (7.5.2) from the values of $\Delta c$ / $T_c$ in zero field and $dB_{c2}$ / $dT$ ($T_c$) from the specific heat analysis.**

Table 5 presents the values of $\mu_0 H_c(0)$ and $\kappa_1(0)$ calculated for both $SnMo_6S_8$ and $PbMo_6S_8$ in the strong and weak coupling regimes respectively. Also presented for comparison are the values of $\kappa_2(T_c)$ calculated in section (7.5.2) from the values of $\Delta c$ / $T_c$ in zero field and $dB_{c2}$ / $dT$ ($T_c$) determined from the specific heat analysis. The values of $\mu_0 H_c(0)$ determined for the $PbMo_6S_8$ sample are between 4 % and 15 % lower than the results of Zheng et al for a $PbMo_6S_8$ sample measured using a VSM [324], and 23 % lower than the estimated values for the $PbMo_6S_8$ sample fabricated as part of the series $(Pb_{1-x}Cu_{1.8x})Mo_6S_8$ (chapter 6). Although this agreement is reasonable considering the estimates of $\gamma_v$ and $\omega_{ln}$ involved an increase in the values of $\mu_0 H_c(0)$ by 23 % is sufficient to make the estimates of $\kappa_1(0)$ equal to those of $\kappa_2(T_c)$.

Estimates of the value of $\kappa$, $\kappa_1(T_c)$ and $\kappa_2(T_c)$ from other authors range from 90 to 130 for samples of $PbMo_6S_8$, similar estimates for $SnMo_6S_8$ are not available however. We

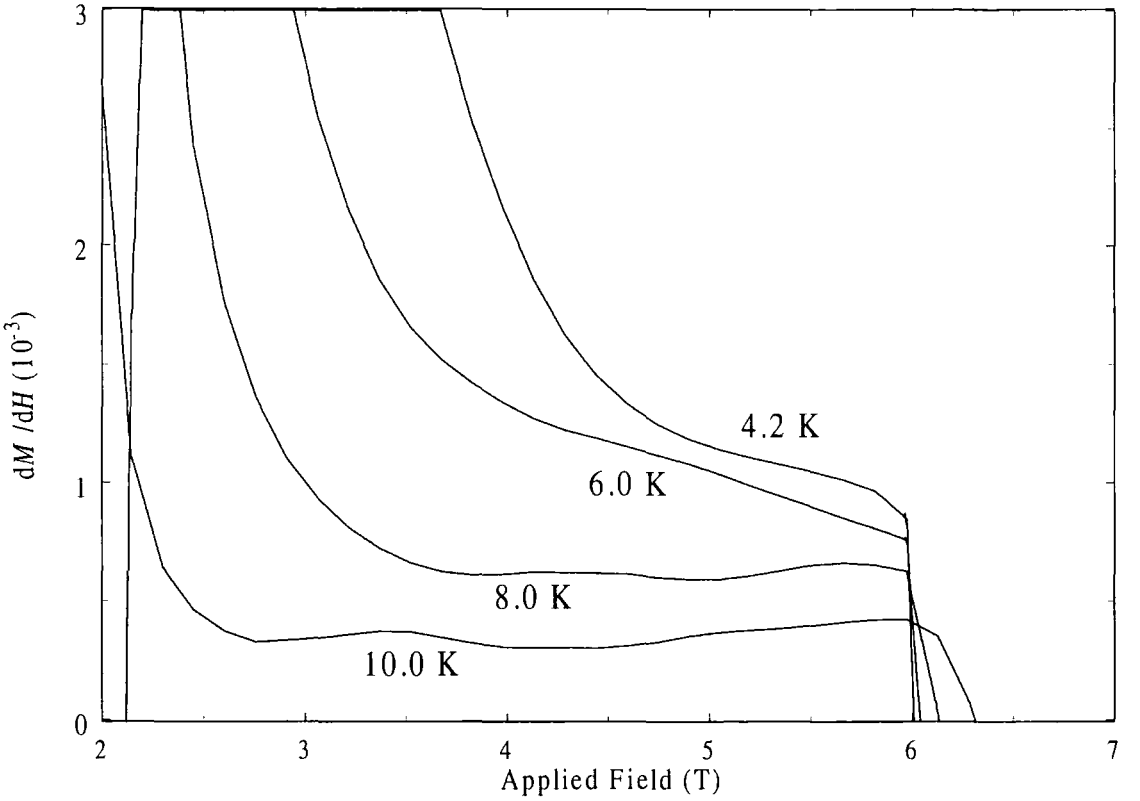


**Figure 37. d*M* / d*H* as a function of applied magnetic field at low temperatures for $Pb_{1.1}Mo_6S_9$, measured using a VSM. Data taken by I J Daniel [325].**

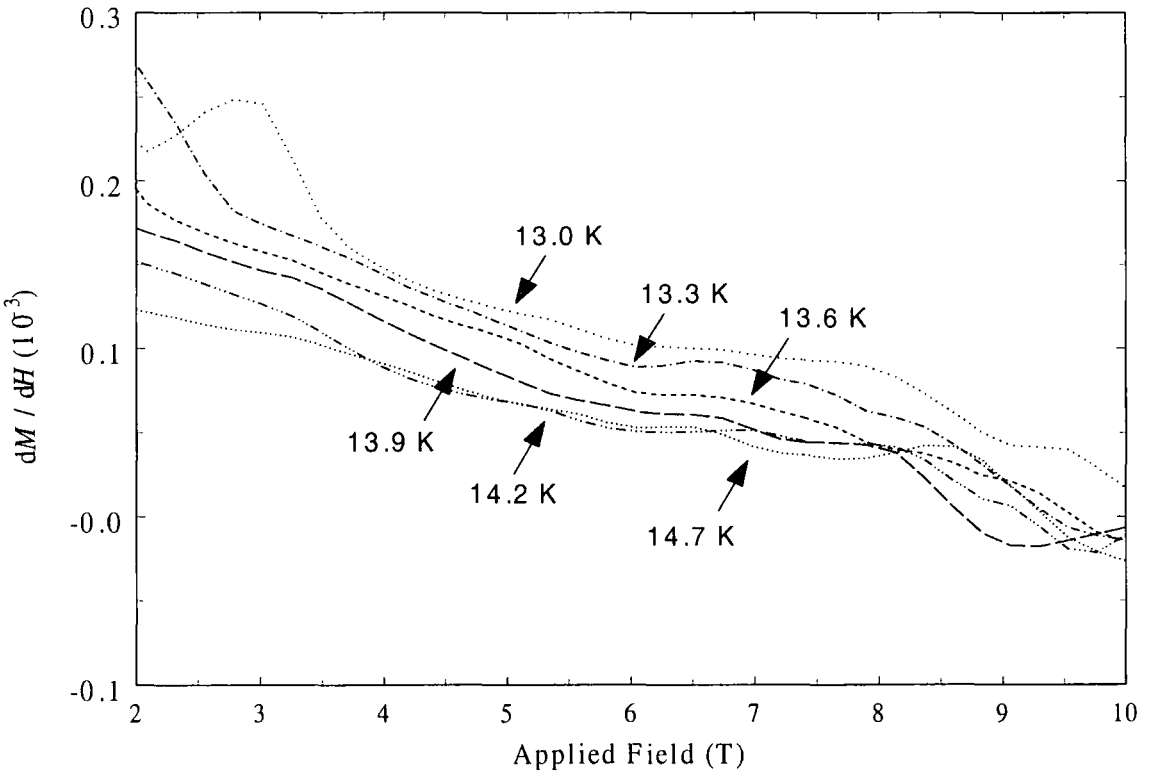


**Figure 38. d*M* / d*H* as a function of applied field at high temperatures for $Pb_{1.1}Mo_6S_9$, measured using a VSM. Data taken by I J Daniel [325].**

previously proposed (section 7.6.4) that the density of states at the Fermi level for this $PbMo_6S_8$ sample was lower than for comparable samples and this produced the estimated values of $\gamma_v$ that are about half of those from other authors. From Eqn.'s (7.4) and (7.6) a factor two increase in $\gamma_v$ would also produce values of $\Delta c / T_c$ and $\mu_0 H_c(0)$ that are larger by factors of 2 and $\sqrt{2}$ respectively. The effect on the estimated values of $\kappa_1(0)$ and $\kappa_2(T_c)$ would be to reduce both values to about 120, which is in agreement with the estimates from other authors. We therefore propose that the large values of $\kappa_1(0)$ and $\kappa_2(T_c)$ estimated here for the $PbMo_6S_8$ sample, are determined principally by the density of states at the Fermi level.

For the doped samples the presence of the magnetic ions increases the electron scattering and so decreases the coherence length ($\xi$). This acts to increase $B_{c2}(0)$ and so we would therefore expect both $\kappa_1(T_c)$ and $\kappa = \lambda / \xi$ (where $\lambda$ is the penetration depth) to be larger for the doped samples. At $T_c$ the generalised GLAG theory [103] gives $\kappa = \kappa_1 = \kappa_2$, the estimated values of $\kappa_2(T_c)$ for the $(Sn_{1-x}Eu_x)Mo_6S_8$ series (table 3) are therefore in reasonable agreement with this predicted increase of $\kappa_1(T_c)$ and $\kappa$. For the $(Pb_{1-x}M_x)Mo_6S_8$ samples however there is no overall agreement on the effect of doping on the value of $\kappa_2(T_c)$. This uncertainty is in part due to the large errors in determining the values of $dB_{c2} / dT$ from the specific heat analysis but also due to the unusually large value of $\kappa_2(T_c)$ for this $PbMo_6S_8$ sample. It is worth noting that a more typical value of $\kappa_2(T_c) \sim 100$ for the $PbMo_6S_8$ sample would then produce similar conclusions for the effect of magnetic doping on $\kappa_2(T_c)$ as in the $(Sn_{1-x}Eu_x)Mo_6S_8$ series.

The temperature dependence of $\kappa_2(T_c)$ for the $(Sn_{1-x}Eu_x)Mo_6S_8$ samples and for the $(Pb_{0.75}Eu_{0.25})Mo_6S_8$ sample is positive as $T$ is reduced (Fig. 33), in good agreement with data on $PbMo_6S_8$ by Decroux et al [161]. The generalised GLAG theory also predicts a positive temperature dependence as $T$ is reduced for both $\kappa_1(T)$ and $\kappa_2(T)$ in the limit of strong spin-orbit scattering [110]. The predicted values of $\kappa_1(0)$ and $\kappa_2(0)$ from this theory however are $\sim 1.2\kappa(T_c)$ which for the data in Fig. 33 and that of Decroux et al corresponds to a temperature of more than $0.8T_c$. So although the general temperature dependence is in agreement with theory the magnitude of the changes in $\kappa_2(T)$ of the experimental data are much larger than predicted. Further comparison with theory cannot be completed due to the lack of estimates of $\kappa_2(T)$ for $T < 0.7T_c$.

Magnetisation data taken using a VSM on a sample of nominal composition $Pb_{1.1}Mo_6S_9$ has been taken by a colleague [325]. The author has analysed the data by averaging the results from the up and down field sweeps, subtracting the normal state background taken at 15.1 K and then taking the derivative. The resulting data of d$M$ / d$H$ as a function of applied field at low and high temperatures has been smoothed using a 21 point window and is presented in Fig.'s 37 and 38 respectively. The value of d$M$ /d$H$ is inversely related to the value of $\kappa_2(T)$ in the extended GLAG theory by [103]:

$$\left(\frac{dM}{dH}\right) = -\frac{1}{\beta_A\left(2\kappa_2^2(T)-1\right)} \tag{7.8}$$

The data in Fig.'s 38 and 39 clearly show a region at each temperature where the value of d$M$ / d$H$ is approximately constant. These values of d$M$ / d$H$ become larger as the temperature is reduced indicating that the value of $\kappa_2(T)$ becomes smaller as the temperature is reduced. These results are in clear contradiction with the results of the specific heat analysis for the compound $PbMo_6S_8$ (Fig. 33), which do not show a monotonic decrease with temperature. No explanation is proposed for this anomalous result.

### 7.6.8 Coexistence of superconducting and magnetic ordering.

The specific heat results for the $(Sn_{0.65}Eu_{0.35})Mo_6S_8$ and $(Sn_{0.50}Eu_{0.50})Mo_6S_8$ samples show a field dependent background for temperatures above and below $T_c$ (Fig.'s 7 and 8) and no evidence of a peak in the specific heat data at 16.5 K due to secondary phase EuS. The magnetisation measurements performed at 4.2 K on these samples (Fig. 15) show a superposition of a paramagnetic background and superconducting hysteresis. Additionally the resistivity, susceptibility and specific heat measurements for these samples all indicate that the bulk of the samples are superconducting at 4.2 K and that the onset of the zero field transitions are reduced by doping with magnetic ions. X-ray and EDX measurements also indicate that the samples are predominantly single phase with a uniform distribution of magnetic ions. These results all indicate that magnetic ordering coexists with superconducting ordering in the bulk of the material and is not just a property of secondary phase material within the sample (e.g. EuS) or limited to the grain boundaries. For the $(Pb_{0.75}Eu_{0.25})Mo_6S_8$ sample we do not have magnetisation or EDX data available, however the resistivity, susceptibility, specific heat and X-ray measurements all indicate a similar state of coexistence to the $(Sn_{0.65}Eu_{0.35})Mo_6S_8$ and $(Sn_{0.50}Eu_{0.50})Mo_6S_8$ samples.

In the series $(Pb_{1-x}Gd_x)Mo_6S_8$ only the specific heat data for the $x = 0.30$ sample (Fig. 4) shows a field dependent background for temperatures above and below $T_c$. The magnetisation measurements performed on both the $(Pb_{0.90}Gd_{0.10})Mo_6S_8$ and $(Pb_{0.70}Gd_{0.30})Mo_6S_8$ samples at 4.2 K show a superposition of a paramagnetic background and superconducting hysteresis. The presence of secondary phase $Gd_2S_3$ in both of these samples as determined by the specific heat analysis could however be responsible for this paramagnetic behaviour in the magnetisation results. The field dependent background in the specific heat data for the $(Pb_{0.70}Gd_{0.30})Mo_6S_8$ sample is to large however to be determined only by secondary phase $Gd_2S_3$ in the proportions indicated by the analysis. The resistivity measurement on this sample indicates that the bulk of the material is superconducting at 7.0 K and that the onset of the zero field transition is reduced compared to that of the $PbMo_6S_8$ sample by doping with magnetic ions. X-ray and EDX measurements indicate that the sample is mainly $(Pb_{1-x}Gd_x)Mo_6S_8$ phase with a uniform distribution of magnetic ions. These results all indicate that magnetic ordering coexists

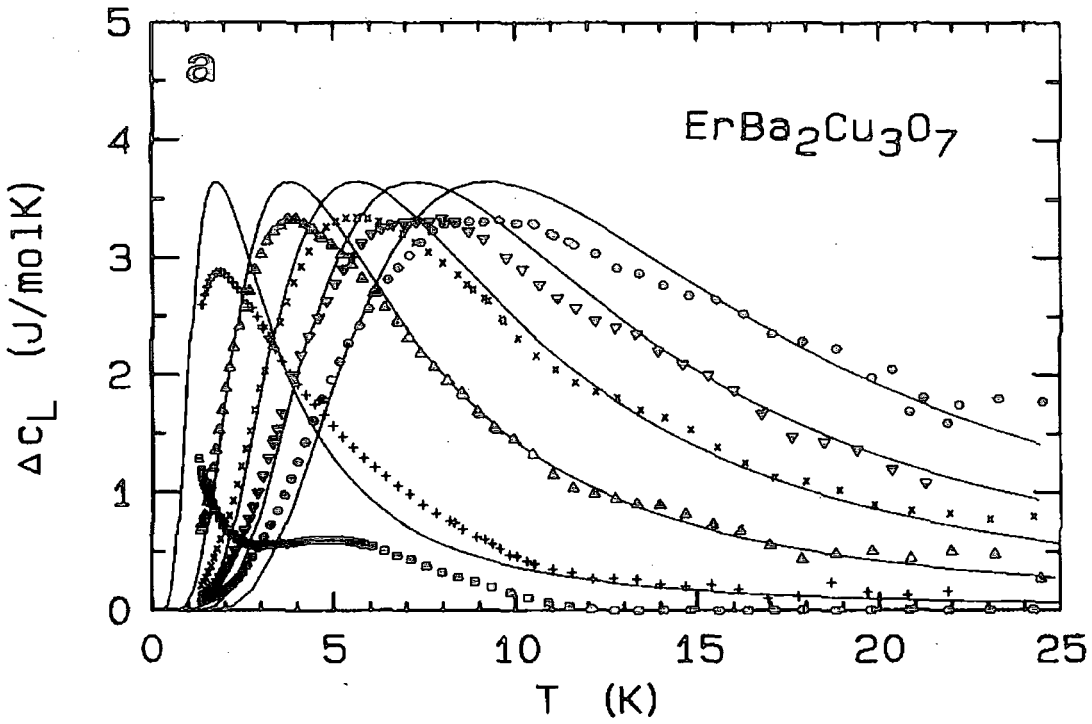


**Figure 39.** $c - (\gamma T + \beta T^3)$ **as a function of temperature and applied field (0 T, 1 T, 2 T, 3 T, 4 T and 5 T) for** $ErBa_2Cu_3O_7$**, experimental data is presented as symbols and fits to the data using an anisotropic Schottky function by the solid lines [330].**

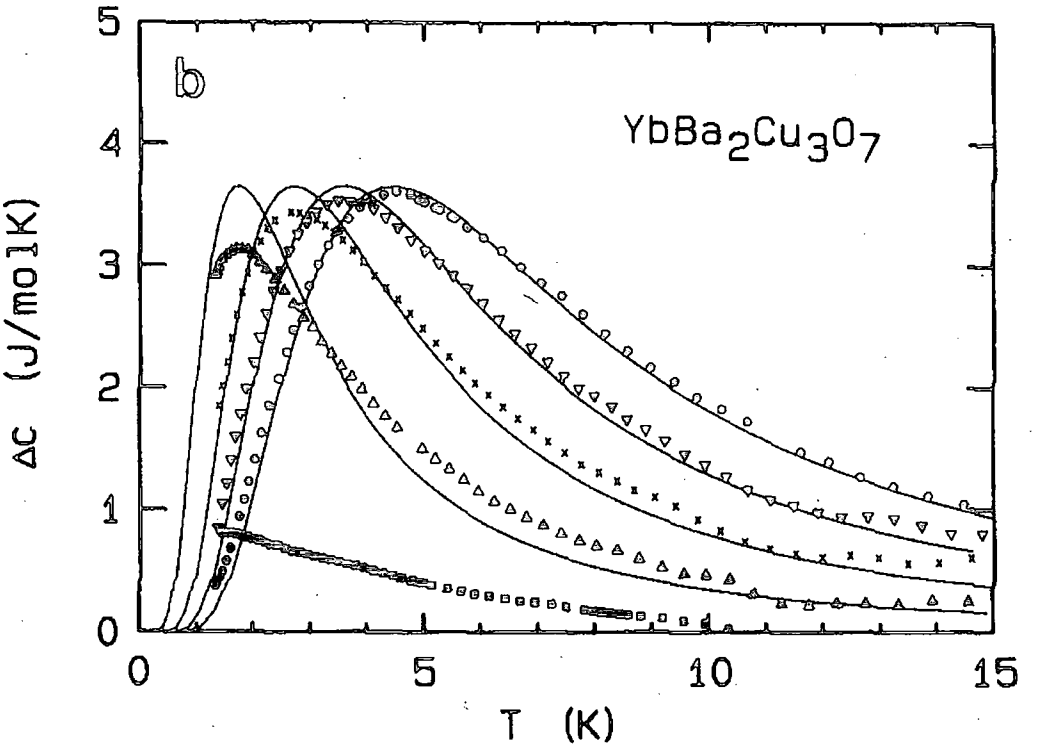


**Figure 40.** $c - (\gamma T + \beta T^3)$ **as a function of temperature and applied field (0 T, 1 T, 2 T, 3 T, 4 T and 5 T) for** $YbBa_2Cu_3O_7$**, experimental data is presented as symbols and fits to the data using an anisotropic Schottky function by the solid lines [330].**

with superconducting ordering in the bulk of this material and that although the observed specific heat below 5.5 K is dominated by $Gd_2S_3$, the magnetic contribution at higher temperatures is predominantly due to the $(Pb_{1-x}Gd_x)Mo_6S_8$ phase. The lack of any significant field dependence above $T_c$ in the specific heat data of the $(Pb_{0.96}Gd_{0.04})Mo_6S_8$ and $(Pb_{0.90}Gd_{0.10})Mo_6S_8$ samples means that we cannot determine whether there is any magnetic ordering in these samples due to the $(Pb_{1-x}Gd_x)Mo_6S_8$ phase.

For those samples ($(Sn_{0.65}Eu_{0.35})Mo_6S_8$, $(Sn_{0.50}Eu_{0.50})Mo_6S_8$ and $(Pb_{0.70}Gd_{0.30})Mo_6S_8$) with large levels of doping the magnetic properties are well characterised by the mean field model. The agreement between the experimental results and the calculations of $c_m$ are excellent. The optimum values of the free parameters used in the fitting are very close to both the free ion values for that magnetic ion for $J$ and $g_J$, the values of $T_M^{AF}$ for the equivalent $REMo_6S_8$ compound and the $n_v$ values determined from the lattice parameters. Due to the large M-M interatomic distances within the Chevrel phase structure the exchange interaction between the magnetic ions is relatively weak, this leads to a system of essentially isolated magnetic ions in an almost isotropic structure. These conditions are the

essential requirements for a system to behave like the mean field model, in fact one of the best known examples of a model mean field ferromagnet is $HoRh_4B_4$ because of a similar crystal structure [219].

The discrepancies between the experimental and calculated data are probably due to many effects that are not included in the mean field model such as thermal fluctuations, short range ordering and spin waves below the ordering temperature. Crystal field effects can also alter the energy level splitting especially in the region of defects or secondary phases and can alter the values of $J$ and $g_J$ in that region.

Similar magnetic contributions to the specific heat have been observed in the high temperature superconductors $ErBa_2Cu_3O_7$ and $YbBa_2Cu_3O_7$ as shown in Fig.'s 39 and 40. This data shows a series of well defined peaks in both compounds that are spaced relatively linearly with applied field with the value of $c_{m(peak)}$ increasing in magnitude as the applied field is increased. The calculations performed in chapter 4 indicate that an increase in the value of $c_{m(peak)}$ with applied field is a characteristic of a material that orders antiferromagnetically. Neutron scattering data [330] taken on these compounds confirm that the material orders antiferromagnetically at low temperatures.

| Material | $c_m^{sat}$ ($JK^{-1}mole^{-1}$) | $J$ ($c_m^{sat}$) | $\partial(\mu_0 H_{ext}) / \partial T_{peak}$ ($TK^{-1}$) | $g_J(J+1)$ ($\partial(\mu_0 H_{ext}) / \partial T_{peak}$) |
|---|---|---|---|---|
| $GdBa_2Cu_4O_8$ (a) | 5.0 | 1.2 | 0.6 | 10.9 |
| $ErBa_2Cu_3O_7$ (b) | 3.5 | 0.6 | 0.6 | 10.9 |
| $YbBa_2Cu_3O_7$ (b) | 3.5 | 0.6 | 1.0 | 6.5 |
| $DyBa_2Cu_3O_7$ (b) | 2.5 | 0.4 | 0.4 | 16.4 |
| Gd – free ion | - | 3.5 (theory) | - | 9 (theory) |
| Er – free ion | - | 7.5 (theory) | - | 10.2 (theory) |
| Yb – free ion | - | 3.5 (theory) | - | 5.1 (theory) |
| Dy – free ion | - | 7.5 (theory) | - | 11.3 (theory) |

**Table 6. Values of $c_m^{sat}$ and $\partial(\mu_0 H_{ext}) / \partial T_{peak}$ determined from the specific heat data of (a) Ho et al [303] and (b) Meulen et al [330] and the values of $J$ and $g_J(J+1)$ estimated from these results using Eqn.'s (7.9) and (7.10). Also included are the theoretical values of $J$ and $g_J(J+1)$ for the free ions.**

The data in Fig.'s 39 and 40 and similar specific heat data on other high temperature superconductors can be used to determine the values of $J$ and $g_J(J + 1)$ for the magnetic ions using the two approximate expressions derived in chapter 4:

$$c_m^{sat} = A\frac{n_{cell}RJ}{(J+1)} \tag{7.9}$$

$$\frac{\partial(\mu_0 H_{ext})}{\partial T_{peak}} = \frac{A^*}{g_J(J+1)} \tag{7.10}$$

where A = 1.1245, $A^*$ = 6.540, R = 8.314 $JK^{-1}mole^{-1}$ and $n_{cell}$ is the number of magnetic ions per unit cell. The results are presented in table 6 and show a reasonable agreement between the theoretical values of $g_J(J + 1)$ for a free ion and the values determined from Eqn. (7.10). The values of $J$ however that are determined from Eqn. (7.9) do not agree with the free ion values for these magnetic ions. The anisotropic nature of these superconductors produces large crystal field effects that can change the energy level splitting of the magnetic ions. We therefore suggest that the magnetic ions in these materials have a triplet spin state for the Gd system and a doublet spin state for the Er, Yb and Dy systems, rather than the full multiplet. Furthermore since the values of $g_J(J + 1)$ are close to the free ion values we suggest that the spacing between these doublet and triplet energy levels is similar to that of the free ion system, whereas the other levels are at much higher energies because of the crystalline electric field.

The lowest energy levels for both the $ErBa_2Cu_3O_7$ and $YbBa_2Cu_3O_7$ systems are known to be doublets [330] in agreement with the above hypothesis. Figures 39 and 40 show fits to the experimental data by Meulen et al using an anisotropic Schottky function with additional higher energy doublets, giving values of $g_JJ$ = 3.2 and 1.6 for $ErBa_2Cu_3O_7$ and $YbBa_2Cu_3O_7$ respectively. The fitted curves however do not show any change in the value of $c_{m(peak)}$ with applied field and overestimate the value of $c_m^{sat}$. Using the values of $J$ and $g_J(J + 1)$ in table 6 that we have determined from our analysis, values of $g_J$ are calculated as 6.8 for Er and 4.1 for Yb. We can then calculate values of $g_JJ$ = 4.1 and 2.5 for $ErBa_2Cu_3O_7$ and $YbBa_2Cu_3O_7$ respectively in reasonable agreement with the estimated values of Meulen et al and a factor two smaller than the free ion values ($g_JJ$ = 9.0 for Er and 4.0 for Yb). Under these proposals therefore the mean field model can also describe the magnetic contribution to the specific heat of these materials, with values of $J$ and $g_J$ for the magnetic ions altered from their free ion values by anisotropy.

## 7.7 Conclusions.

A series of Chevrel phase samples have been fabricated of the form $(M_{1-x}M`_x)Mo_6S_8$ where M = Pb and Sn, and M` = Gd and Eu. Specific heat measurements have been performed on these samples from 3 K to 30 K and in magnetic fields up to 15 T. Additional resistivity, susceptibility, magnetisation, X-ray diffraction, EDX and TEM measurements have also been performed to enable characterisation of the materials and to determine their magnetic and superconducting properties. All of the samples were fabricated at ~ 1500 °C to ensure correct substitution of the magnetic ions into the unit cell. The results of the X-ray diffraction, EDX and specific heat measurements indicate that the materials are predominantly single phase with small amounts of $Mo_2S_3$, Mo and $Gd_2S_3$ present in some of the samples.

By substituting with magnetic ions into the unit cell a system of essentially isolated magnetic ions is created within a superconducting structure. The resulting compounds have a combination of the superconducting properties of the parent compound and the magnetic properties of the equivalent $REMo_6S_8$. The samples with large doping levels show evidence in the specific heat and the magnetisation of the coexistence of magnetic ordering and superconducting ordering within the material. The superconducting properties of these samples determined by resistivity, susceptibility and specific heat are all modified compared to the parent compound indicating that the magnetic ordering is a property of the bulk of the material and not just limited to impurity phases or grain boundaries.

The magnetic ordering in these heavily doped samples is characteristic of a system that can be described by the mean field formalism. The particular crystal structure of these Chevrel phase materials leads to a relatively weak exchange interaction between the magnetic ions that is virtually isotropic and so very close to an ideal mean field system. The magnetic contribution to the specific heat has been modelled using mean field theory as detailed in chapter 4 and the agreement between the calculations and the experimental data is excellent. The values of the free parameters used in these calculations are the free ion values of $J$, $g_J$, the ordering temperatures characteristic of the equivalent $REMo_6S_8$ material and values of $n_v$ that are close to those determined from the lattice parameters. The discrepancies between the experimental and calculated data are mostly in the region of the ordering temperature and for temperatures below this. Effects due to temperature

fluctuations, crystalline fields and spin waves that are not taken into account by this model are the most probable explanation for these differences [20].

For the $(Sn_{0.65}Eu_{0.35})Mo_6S_8$ and $(Sn_{0.50}Eu_{0.50})Mo_6S_8$ samples the magnetic contribution to the specific heat ($c_m$) impedes the analysis of the superconducting jumps. The excellent agreement between the calculated values of $c_m$ and the experimental data allows the magnetic contribution to be subtracted and a much better analysis of the superconducting transition to be performed. Accurate analysis of the specific heat jump for these two samples in an applied field of 3 T was not possible using the raw data, after subtracting the magnetic contribution however the analysis was accurate to better than 20 %.

For the $(Pb_{0.70}Gd_{0.30})Mo_6S_8$ sample the magnetic contribution to the specific heat is most accurately modelled by adding together the contribution of a $(Pb_{0.75}Gd_{0.25})Mo_6S_8$ phase and an impurity phase $Gd_2S_3$. The field dependence of the temperature of the specific heat peak due to the antiferromagnetic phase transition of the $Gd_2S_3$ phase is used to determine a value of $J = 0.32$ for this phase. The height of the zero field peak is then used to determine that $Gd_2S_3$ comprises approximately 6 % of this sample by mass. The specific heat of the $(Pb_{0.90}Gd_{0.10})Mo_6S_8$ sample shows a similar set of peaks, although the magnetic contribution above $T_M^{AF}$ is too small to model analysis of these peaks indicates that $Gd_2S_3$ comprises ~ 0.6 % of the sample by mass.

Comparison has also been made with similar data on the high temperature superconductors $GdBa_2Cu_4O_8$ and $REBa_2Cu_3O_7$, where RE = Er, Yb and Dy, using the approximate expressions for the saturation value of $c_{m(peak)}$ and the change in the temperature of $c_{m(peak)}$ with applied field. Using the values of $J$ and $g_J(J + 1)$ determined from these expressions we find that these systems have a ground state that is altered by anisotropy and can be represented by either a doublet or triplet ground state with a similar energy spacing to the free ion case.

The specific heat measurements on the Chevrel phase compounds show a drop in the normal state specific heat as magnetic ions are substituted into the lattice. This change in the specific heat can be correlated for almost all of the samples with a change in the effective mass of the cation. By changing the effective cation mass the characteristic phonon frequency is also changed. At these low temperatures the normal state specific heat is therefore determined by the level of doping in the material.

Estimates of $\gamma$ have been made for both the $SnMo_6S_8$ and $PbMo_6S_8$ compounds from BCS theory in the strong and weak coupling regimes and complementary data from other

authors. These estimates reveal that the value of $\gamma$ for the $SnMo_6S_8$ sample is comparable to those from other authors but the corresponding value for $PbMo_6S_8$ is about half of those from other authors in both strong and weak coupling regimes. The low value of $\gamma$ for this sample is therefore due to a value of the density of states at the Fermi level that is lower than comparable samples. This value of $\gamma$ is the principle reason for the small specific heat jump for this sample that is also about half the size of data on $PbMo_6S_8$ from other authors. At low levels of doping ($x \leq 0.10$) in the $(Pb_{1-x}Gd_x)Mo_6S_8$ system we estimate the value of $\gamma$ increases with increased doping level and produces a systematic increase in the size of the specific heat jump. An increase in the charge transfer to the $Mo_6S_8$ clusters, as more $Gd^{3+}$ ions are introduced, is the most likely reason for this increase in $\gamma$. We suggest that at higher levels of doping the competition between the superconducting ordering and magnetic ordering becomes the dominant factor reducing $\gamma$ and therefore the size of the specific heat jump to a level below the experimental resolution.

The temperature dependence of the size of the specific heat jump has been compared to the models of Maki and Vijfeijken. None of the samples have a temperature dependence that allows comparison with either of these theories.

The values of $T_c$ are lower for all of the doped samples than for the parent compounds. This degradation in $T_c$ with doping is not systematic but can be correlated to the unit cell volume and therefore a change in the density of states at the Fermi level for the $(Pb_{1-x}Gd_x)Mo_6S_8$ series, which is partly due to an increase in the charge transfer to the $Mo_6S_8$ clusters. All of the doped samples however are subject to competition between the magnetic and superconducting ordering in the material. This competition reduces the number of Cooper pairs and so reduces the transition temperature and is probably the major factor in the reduction of $T_c$ for the heavily doped samples.

The estimated values of the upper critical field for the $(Sn_{1-x}Eu_x)Mo_6S_8$ samples are larger than for the $SnMo_6S_8$ sample and similarly for $x \leq 0.10$ the estimated values of $B_{c2}(0)$ for the $(Pb_{1-x}Gd_x)Mo_6S_8$ samples are larger than the $PbMo_6S_8$ sample. This increase in $B_{c2}(0)$ with the addition of magnetic ions is a result of the compensation effect and an increase in $\rho_N$ within the doped samples. An upward curvature in the plot of $B_{c2}(T)$ as a function of $T_c$ that is characteristic of this effect is seen for high levels of doping but not for lower levels in agreement with the work of Fischer [144, 200]. Analysis of these results

show that both clean and dirty contributions are required within the extended GLAG theory to explain the observed trends in $B_{c2}(0)$ and the estimated trends in $\gamma$.

The values of $J_c$ for the doped samples are systematically reduced compared to the parent compounds. This reduction is probably a result of a reduction in carrier density due to competition between magnetic and superconducting ordering for the highly doped samples and degradation in the grain boundary properties with doping. The very broad resistivity and susceptibility transitions for the $(Sn_{0.65}Eu_{0.35})Mo_6S_8$ and $(Sn_{0.50}Eu_{0.50})Mo_6S_8$ samples indicate that the connectivity and intragrain critical current properties are reduced.

Using the measured values of $T_c$, $\Delta c$ / $T_c$ and $\rho_N$ and the estimated values of $\gamma$, $\omega_{ln}$ and $B_{c2}(0)$ values of $\mu_0 H_c(0)$ and $\kappa_1(0)$ have been estimated for $SnMo_6S_8$ and $PbMo_6S_8$ and the temperature dependence of $\kappa_2(T)$ for all of the samples. The estimated values of $\mu_0 H_c(0)$ for $PbMo_6S_8$ are smaller than estimates from other authors and similarly the estimated values of $\kappa_1(0)$ and $\kappa_2(T_c)$ are both significantly higher than estimates from other authors. These discrepancies are primarily due to the low value of $\gamma$ for this sample compared to these other results, taking a value of $\gamma$ that is more typical of the literature the calculated values of $\kappa_1(0)$ and $\kappa_2(T_c)$ are then both in good agreement with the literature.

Introducing magnetic ions into the material systematically increases the values of $\kappa_2(T_c)$ for the $(Sn_{1-x}Eu_x)Mo_6S_8$ series due to an increase in the electron scattering and therefore a corresponding reduction in the coherence length. A similar trend is not observed for the $(Pb_{1-x}Gd_x)Mo_6S_8$ series, however if a more typical value for $\kappa_2(T_c)$ for the $PbMo_6S_8$ is taken then the data do show an increase in $\kappa_2(T_c)$ with doping. The values of $\kappa_2(T)$ increase as $T$ is reduced for all of the $(Sn_{1-x}Eu_x)Mo_6S_8$ samples and the $(Pb_{0.75}Eu_{0.25})Mo_6S_8$ sample in agreement with the modified GLAG theory. The very large increase that is observed for all of these samples for a relatively small reduction in temperature cannot however be accounted for by the theoretical temperature dependencies of $\kappa_2(T)$. The change in $\kappa_2(T)$ for the $(Pb_{1-x}Gd_x)Mo_6S_8$ samples as $T$ is reduced is variable and no significant trends can be determined for these samples. Estimates of $\kappa_2(T)$ however from VSM measurements on a sample of nominal composition $Pb_{1.1}Mo_6S_9$ clearly show that $\kappa_2(T)$ should decrease as the temperature is reduced. This contradiction between the results of magnetisation and specific heat data on very similar samples is to be the subject of future work.

In conclusion, $T_c$ and $J_c$ of the Chevrel phase compounds $SnMo_6S_8$ and $PbMo_6S_8$ are degraded by substituting with magnetic ions. The upper critical field however is increased

for some doping levels, possibly due to the compensation effect and an increase in the normal state resistivity. Most of these changes can be explained within modified BCS theory and GLAG theory due to changes in the normal state parameters $\rho_N$, $\gamma$, $M$ and $\omega_{ln}$. The magnetic properties of the heavily doped samples are characteristic of a nearly ideal mean field system and show the coexistence of magnetic and superconducting ordering in the bulk of the sample. The magnetic contribution to the specific heat has been modelled using the calculations from the mean field theory and excellent agreement has been found. Data on high temperature superconductors has also been shown to be consistent with a mean field model description if anisotropic effects are taken into account.

# Chapter 8 - Future Work

Future work in this area will need to concentrate on two aspects. Firstly the effect of substituting small cations and magnetic ions on the superconducting properties of $PbMo_6S_8$ and $SnMo_6S_8$ will need to be extended to cover a wider range of magnetic and non-magnetic ions. The results in chapters 6 and 7 suggest that there is a range of doping levels in which the critical temperature of the parent compound are only degraded by a small amount and in some cases (e.g. $B_{c2}(0)$) are actually improved. Specifically, if data can be collated on the entire series of $(Pb_{1-x}RE_x)Mo_6S_8$ and $(Sn_{1-x}RE_x)Mo_6S_8$ (RE = rare-earth ion) then the effect of substituting magnetic ions into these compounds can be systematically analysed and the phase diagram of the magnetic and superconducting properties of these materials deduced. Taking data down to much lower temperatures (< 1 K) would also be a great advantage, this would enable the magnetic transitions of these materials to be measured, a much more in depth analysis performed and provide a better insight into the coexistence of magnetic and superconducting ordering.

Secondly the calculations of the magnetic contribution to the specific heat in chapter 4 need to be extended to include effects such as temperature fluctuations and anisotropy. The excellent agreement in chapter 7 between the experimental data and the calculated values using the mean field model is due to the crystal structure of these materials. The zero field data taken on these samples however shows that fluctuations are required to explain the data even in these 'ideal' mean field systems, similarly the comparison with high temperature superconductors in chapter 7 shows that complexities have to be introduced when dealing with other crystal structures.

In terms of the materials and measurement procedures outlined in this thesis, several improvements are suggested for future study. Firstly the fabrication of these Chevrel phase materials needs to be improved to ensure that the measured $J_c$ values are an indication of the intrinsic properties of these materials and not just grain boundary limited values. The results in chapter 7 indicate that some of the samples with large amounts of magnetic doping have grain boundary properties that are severely degraded, this severely limits therefore any study of the effect of doping with magnetic ions on $J_c$.

Secondly the design of the specific heat probe in chapter 5 could be improved to ensure that in high magnetic fields the support wires stay firmly fixed to the sample and to enable

easier access for mounting and de-mounting the sample. The probe has been designed and commissioned here in Durham and gives data accurate to about 1 % using the relaxation technique and a resolution of about 10 mK using the long range pulse. Further characterisation of the probe however, should be carried out to improve the accuracy of the data taken using the long-range pulse. If the accuracy of this technique could be consistently improved then this quick and easy method for measuring the specific heat would become a far superior measurement to the relaxation method.

# References:


[1] H. K. Onnes, *Proceedings of the Royal Academy*, vol. 11, pp. 168 - 185, 1908.

[2] H. K. Onnes, *Communications from the Physical Laboratory of the University of Leiden*, vol. 124c, pp. 21 - 25, 1911.

[3] C. P. Poole, H. A. Farach, and R. J. Creswick, *Superconductivity*: Academic Press, 1995.

[4] J. G. Bednorz and K. A. Muller, *Zeitschrift Fur Physik D*, vol. 64, pp. 189 - 193, 1986.

[5] M. K. Wu, J. R. Ashburn, C. J. Torng, P. H. Hor, R. L. Meng, L. Gao, Z. J. Huang, Y. Q. Wang, and C. W. Chu, *Physical Review Letters*, vol. 58, pp. 908 - 910, 1987.

[6] A. Schilling, M. Cantoni, J. D. Guo, and H. R. Ott, *Nature*, vol. 363, pp. 56 - 58, 1993.

[7] C. W. Chu, L. Gao, F. Chen, Z. J. Huang, R. L. Meng, and Y. Y. Xue, *Nature*, vol. 365, pp. 323 - 325, 1993.

[8] A. J. Rutgers, *Physica*, vol. 1, pp. 1055 - 1058, 1934.

[9] F. London and H. London, *Proceedings of the Royal Society of London*, vol. A149, pp. 71 - 89, 1935.

[10] J. Bardeen, L. N. Cooper, and J. R. Schrieffer, *Physical Review*, vol. 108, pp. 1175 - 1204, 1957.

[11] L. N. Cooper, *Physical Review*, vol. 104, pp. 1189 - 1190, 1956.

[12] V. L. Ginzburg and L. D. Landau, *Zhurnal Eksperimentalnoj i Teoreticheskoj Fisiki*, vol. 20, pp. 1064 - 1082, 1950.

[13] A. A. Abrikosov, *Journal of Experimental and Theoretical Physics*, vol. 5, pp. 1174 - 1182, 1957.

[14] W. H. Kleiner, L. M. Roth, and S. H. Autler, *Physical Review*, vol. 133, pp. A1226 - A1227, 1964.

[15] L. P. Gor'kov, *Soviet Physics JETP*, vol. 36, pp. 1364 - 1367, 1959.

[16] N. W. Ashcroft and N. D. Mermin, "Solid State Physics," , 1981, pp. 643 - 724.

[17] E. Ising, *Z. Physics*, vol. 31, pp. 253 - 258, 1925.

[18] L. Onsager, *Physical Review*, vol. 65, pp. 117 - 149, 1944.

[19] F. Bloch, *Z. Physics*, vol. 74, pp. 295 - 335, 1932.

[20] A. P. Miller, "Theory of specific heat of solids," in *Specific heat of solids*, C. Y. Ho, Ed., 1988, pp. 28 - 34.

[21] R. F. Wielinga, "Critical behaviour in magnetic crystals," in *Progress in low temperature physics. Vol. VI*, C. J. Gorter, Ed. Amsterdam, 1971, pp. 333 - 373.

[22] E. C. Stoner, *Magnetism of matter*. London: Methuer and Co. Ltd., 1934.

[23] P. L. Dulong and A. T. Petit, *Annales de Chimie et de Physique*, vol. 10, pp. 395 - 413, 1819.

[24] A. Einstein, *Annal de Physik*, vol. 22, pp. 180 - 190, 1907.

[25] N. W. Ashcroft and N. D. Mermin, "Solid state physics," , 1981, pp. 421 - 509.

[26] P. Debye, *Annales der Physik Leipz*, vol. 39, pp. 789 - 839, 1912.

[27] F. Heiniger, E. Bucher, and J. Muller, *Physik Kondense Materie*, vol. 5, pp. 243 - 284, 1966.

[28] N. E. Phillips, *Critical reviews in solid state sciences*, vol. 2, pp. 467 - 553, 1971.

[29] F. Y. Fradin, G. S. Knapp, S. D. Bader, G. Cinader, and C. W. Kimball, "Electron and phonon properties of A15 compounds and Chevrel phases," in *Superconductivity in d- and f- band metals*, D. H. Douglass, Ed., 1976, pp. 297 - 312.

[30] P. M. Marcus and A. J. Kennedy, *Physical Review*, vol. 114, pp. 459 - 467, 1959.

[31] A. B. Bhatia and G. K. Horton, *Physical Review*, vol. 98, pp. 1715 - 1721, 1955.

[32] G. K. Horton and H. Schiff, *Canadian Journal of Physics*, vol. 36, pp. 1127 - 1130, 1958.

[33] J. A. Rayne, *Physical Review*, vol. 108, pp. 649 - 651, 1957.

[34] P. A. Finn, G. M. McManus, and J. A. Rayne, *Journal of Physics and Chemistry of Solids*, vol. 15, pp. 189 - 195, 1960.

[35] R. Brout and W. Visscher, *Physical Review Letters*, vol. 9, pp. 54 - 56, 1962.

[36] P. G. Dawber and R. J. Elliott, *Proceedings of the Royal Society of London*, vol. A273, pp. 222 - 236, 1963.

[37] Y. Kagan and Y. A. Iosilevskii, *Soviet Physics JETP*, vol. 15, pp. 182 - 189, 1962.

[38] Y. Kagan and Y. Iosilevskii, *Soviet Physics JETP*, vol. 18, pp. 562 - 564, 1964.

[39] W. M. Hartmann, H. V. Culbert, and R. P. Huebener, *Physical Review B*, vol. 1, pp. 1486 - 1493, 1970.

[40] H. Culbert and R. P. Huebener, *Physics Letters*, vol. 24A, pp. 530 - 531, 1967.

[41] J. A. Cape, G. W. Lehman, W. V. Johnston, and R. E. DeWames, *Physical Review Letters*, vol. 16, pp. 892 - 895, 1966.

[42] G. K. Panova and B. N. Samoilov, *Soviet Physics JETP*, vol. 22, pp. 320 - 322, 1966.

[43] S. D. Bader, G. S. Knapp, S. K. Sinha, P. Schweiss, and B. Renker, *Physical Review Letters*, vol. 37, pp. 344 - 348, 1976.

[44] A. Sommerfeld, *Zeitschrift Fur Physik*, vol. 47, pp. 1 - 32, 1927.

[45] E. C. Stoner, *Proceedings of the Royal Society of London*, vol. A154, pp. 656 - 678, 1936.

[46] N. F. Mott, *Advances in Physics*, vol. 13, pp. 325 - 422, 1964.

[47] D. Weaire, *Proceedings of the Physical Society*, vol. 92, pp. 956 - 961, 1967.

[48] O. K. Andersen and A. R. Mackintosh, *Solid State Communications*, vol. 6, pp. 285 - 290, 1968.

[49] F. M. Mueller, A. J. Freeman, J. O. Dimmock, and A. M. Furdyna, *Physical Review B*, vol. 1, pp. 4617 - 4635, 1970.

[50] N. W. Ashcroft and J. W. Wilkins, *Physics Letters*, vol. 14, pp. 285 - 287, 1965.

[51] P. B. Allen and M. L. Cohen, *Physical Review*, vol. 187, pp. 525 - 538, 1969.

[52] S. S. Shinozaki and A. Arrott, *Physical Review*, vol. 152, pp. 611 - 622, 1966.

[53] W. L. McMillan and J. M. Rowell, *Physical Review Letters*, vol. 14, pp. 108 - 112, 1965.

[54] B. Bleaney and R. W. Hill, *Proceedings of the Physical Society*, vol. 78, pp. 313 - 315, 1961.

[55] W. H. Keesom and J. A. Kok, *Physica*, vol. 1, pp. 743 - 748, 1932.

[56] W. H. Keesom and J. A. Kok, *Physica*, vol. 1, pp. 175 - 181, 1934.

[57] W. H. Keesom and J. A. Kok, *Physica*, vol. 1, pp. 503 - 512, 1934.

[58] W. H. Keesom and J. A. Kok, *Physica*, vol. 1, pp. 595 - 608, 1934.

[59] W. H. Keesom and P. H. v. Laer, *Physica*, vol. 5, pp. 193 - 201, 1938.

[60] F. J. Morin and J. P. Maita, *Physical Review*, vol. 129, pp. 1115 - 1120, 1963.

[61] N. E. Phillips, M. H. Lambert, and W. R. Gardener, *Review of Modern Physics*, vol. 36, pp. 131 - 133, 1964.

[62] H. R. O'Neal and N. E. Phillips, *Physical Review*, vol. 137, pp. A748 - A759, 1965.

[63] C. A. Bryant and P. H. Keesom, *Physical Review*, vol. 123, pp. 491 - 499, 1961.

[64] B. J. C. v. d. Hoeven and P. H. Keesom, *Physical Review*, vol. 135, pp. A631 - A637, 1964.

[65] B. J. C. v. d. Hoeven and P. H. Keesom, *Physical Review*, vol. 134, pp. A1320 - A1321, 1964.

[66] C. J. Gorter and H. Casimir, *Physica*, vol. 1, pp. 306 - 320, 1934.

[67] W. S. Corak, B. B. Goodman, and C. B. Satterthwaite, *Physical Review*, vol. 96, pp. 1442 - 1444, 1954.

[68] N. E. Alekseevskii, G. Wolf, C. Hohlfeld, and N. M. Dobrovolskii, *Journal of Low Temperature Physics*, vol. 40, pp. 479 - 493, 1980.

[69] N. V. Zavaritskii, *Soviet Physics JETP*, vol. 7, pp. 773 - 779, 1958.

[70] B. J. C. v. d. Hoeven and P. H. Keesom, *Physical Review*, vol. 137, pp. A103 - A107, 1965.

[71] G. Seidel and P. H. Keesom, *Physical Review*, vol. 112, pp. 1083 - 1088, 1958.

[72] N. E. Phillips, *Physical Review*, vol. 134, pp. A385 - A391, 1964.

[73] R. Radebaugh and P. H. Keesom, *Physical Review*, vol. 149, pp. 209-216, 1966.

[74] D. C. Rorer, D. G. Onn, and H. Meyer, *Physical Review*, vol. 138, pp. A1661 - A1668, 1965.

[75] J. F. d. Silva, N. W. J. v. Duykeren, and Z. Dokoupil, *Physica*, vol. 32, pp. 1253 - 1273, 1966.

[76] D. K. Finnemore, D. E. Mapother, and R. W. Shaw, *Physical Review*, vol. 118, pp. 127 - 129, 1960.

[77] D. L. Decker, D. E. Mapother, and R. W. Shaw, *Physical Review*, vol. 112, pp. 1888 - 1898, 1958.

[78] J. E. Neighbor, J. F. Cochran, and C. A. Shiffman, *Physical Review*, vol. 155, pp. 384 - 387, 1967.

[79] D. K. Finnemore, T. F. Stromberg, and C. A. Swenson, *Physical Review*, vol. 149, pp. 231-243, 1966.

[80] P. W. Anderson, *Journal of Physics and Chemistry of Solids*, vol. 11, pp. 26 - 30, 1959.

[81] D. Markowitz and L. P. Kadanoff, *Physical Review*, vol. 131, pp. 563 - 575, 1963.

[82] J. R. Clem, *Annals of Physics*, vol. 40, pp. 268 - 295, 1966.

[83] M. Furuyama, N. Kobayashi, and Y. Muto, *Physical Review B*, vol. 40, pp. 4344-4354, 1989.

[84] J. D. N. Cheeke and E. Ducla-Soares, *Physics Letters*, vol. 27A, pp. 264 - 265, 1968.

[85] J. C. Swihart, *Physical Review*, vol. 131, pp. 73 - 78, 1963.

[86] Y. Wada, *Physical Review*, vol. 135, pp. A1481 - A1497, 1964.

[87] J. C. Swihart, D. J. Scalapino, and Y. Wada, *Physical Review Letters*, vol. 14, pp. 106 - 108, 1965.

[88] L. Y. L. Shen, N. M. Senozan, and N. E. Phillips, *Physical Review Letters*, vol. 14, pp. 1025 - 1027, 1965.

[89] C. C. Sung and L. Y. L. Shen, *Physics Letters*, vol. 19, pp. 101 - 102, 1965.

[90] H. Suhl, B. T. Matthias, and L. R. Walker, *Physical Review Letters*, vol. 3, pp. 552 - 554, 1959.

[91] J. W. Garland, *Physical Review Letters*, vol. 11, pp. 111 - 114, 1963.

[92] L. J. Vieland and A. W. Wicklund, *Physics Letters*, vol. 23, pp. 223 - 224, 1966.

[93] L. J. Vieland and A. W. Wicklund, *Physical Review*, vol. 166, pp. 424 - 431, 1968.

[94] J. C. F. Brock, *Solid State Communications*, vol. 7, pp. 1789 - 1792, 1969.

[95] F. J. Morin, J. P. Maita, H. J. Williams, R. C. Sherwod, J. H. Wernick, and J. E. Kunzler, *Physical Review Letters*, vol. 8, pp. 275 - 277, 1962.

[96] B. B. Goodman, *Physics Letters*, vol. 1, pp. 215 - 217, 1962.

[97] R. R. Hake and W. G. Brammer, *Physical Review*, vol. 133, pp. A719 - A723, 1964.

[98] F. Heiniger and J. Muller, *Physical Review*, vol. 134, pp. A1407 - A1409, 1964.

[99] L. P. Gor'kov, *Soviet Physics JETP*, vol. 10, pp. 998 - 1004, 1960.

[100] B. B. Goodman, *IBM Journal of Research and Development*, vol. 6, pp. 63 - 67, 1962.

[101] L. P. Gor'kov, *Soviet Physics JETP*, vol. 10, pp. 593 - 599, 1960.

[102] P. G. d. Gennes, *Physik der Kondensieren Materie*, vol. 3, pp. 79 - 90, 1964.

[103] K. Maki, *Physics*, vol. 1, pp. 21 - 30, 1964.

[104] K. Maki, *Physics*, vol. 1, pp. 127 - 143, 1964.

[105] E. Hefland and N. R. Werthamer, *Physical Review Letters*, vol. 13, pp. 686 - 688, 1964.

[106] E. Hefland and N. R. Werthamer, *Physical Review*, vol. 147, pp. 288 - 294, 1966.

[107] K. Maki and T. Tsuzuki, *Physical Review*, vol. 139, pp. A868 - A877, 1965.

[108] C. Caroli, M. Cyrot, and P. G. d. Gennes, *Solid State Communications*, vol. 4, pp. 17 - 19, 1966.

[109] G. Eilenberger, *Physical Review*, vol. 153, pp. 584 - 598, 1967.

[110] E. W. Collings, *Applied superconductivity, metallurgy and physics of titanium alloys. Volume 1. Fundamentals*, 1986.

[111] T. Kinsel, E. A. Layton, and B. Serin, *Review of Modern Physics*, vol. 36, pp. 105 - 109, 1964.

[112] R. Radebaugh and P. H. Keesom, *Physical Review*, vol. 149, pp. 217-231, 1966.

[113] W. A. Feitz and W. W. Webb, *Physical Review*, vol. 161, pp. 423 - 433, 1967.

[114] B. Serin, "Type II superconductors: Experiments," in *Superconductivity*, vol. 2, R. D. Parks, Ed.: Marcel Dekker, Inc., 1969, pp. 925 - 976.

[115] T. McConville and B. Serin, *Physical Review*, vol. 140, pp. A1169 - A1177, 1965.

[116] T. McConville and B. Serin, *Review of Modern Physics*, vol. 34, pp. 112 - 116, 1964.

[117] J. F. d. Silva, N. W. J. v. Duykeren, and Z. Dokoupil, *Physics Letters*, vol. 20, pp. 448 - 449, 1966.

[118] J. F. d. Silva, J. Scheffer, N. W. J. v. Duykeren, and Z. Dokoupil, *Physics Letters*, vol. 12, pp. 166, 1964.

[119] J. F. d. Silva, E. A. Burgemeister, and Z. Dokoupil, *Physics Letters*, vol. 25A, pp. 354 - 356, 1967.

[120] A. A. Melo and K. Mendelssohn, *Physics Letters*, vol. 30A, pp. 104 - 105, 1969.

[121] R. Ehrat and L. Rinderer, *Physics Letters*, vol. 32A, pp. 547 - 548, 1970.

[122] P. Zoller and J. R. Dillinger, *Physical Review*, vol. 172, pp. 390 - 392, 1968.

[123] C. Caroli, P. G. d. Gennes, and J. Matricon, *Physics Letters*, vol. 9, pp. 307 - 309, 1964.

[124] K. Maki, *Physical Review*, vol. 139, pp. A702 - A705, 1965.

[125] L. J. Vieland, *Physics Letters*, vol. 15, pp. 23 - 24, 1965.

[126] A. G. v. Vijfeijken, *Physics Letters*, vol. 21, pp. 140 - 141, 1966.

[127] J. Cors, D. Cattani, M. Decroux, A. Settler, and Ø. Fischer, presented at International conference on low temperature physics, Brighton, U.K., 1990.

[128] B. S. Chandrasekhar, *Applied Physics Letters*, vol. 1, pp. 7 - 8, 1962.

[129] A. M. Clogston, *Physical Review Letters*, vol. 9, pp. 266 - 267, 1962.

[130] Y. Shapira and L. J. Neuringer, *Physical Review*, vol. 140, pp. A1638 - A1644, 1965.

[131] K. Maki, *Physical Review*, vol. 148, pp. 362 - 369, 1966.

[132] N. R. Werthamer, E. Hefland, and P. C. Hohenberg, *Physical Review*, vol. 147, pp. 295-302, 1966.

[133] R. R. Hake, *Physical Review Letters*, vol. 15, pp. 865 - 868, 1965.

[134] R. R. Hake, *Physical Review*, vol. 158, pp. 356 - 376, 1967.

[135] L. J. Barnes and R. R. Hake, *Physical Review*, vol. 153, pp. 435 - 437, 1967.

[136] R. R. Hake, *Applied Physics Letters*, vol. 10, pp. 189 - 192, 1967.

[137] L. J. Neuringer and Y. Shapira, *Physical Review Letters*, vol. 17, pp. 81 - 84, 1966.

[138] R. A. Brand, presented at Low Temperature Physics, 1975.

[139] R. Odermatt, Ø. Fischer, H. Jones, and G. Bongi, *Jounal of Physics C : Solid State Physics*, vol. 7, pp. L13-L15, 1974.

[140] T. P. Orlando, E. J. McNiff, S. Foner, and M. R. Beasley, *Physical Review B*, vol. 19, pp. 4545 - 4561, 1979.

[141] T. P. Orlando and M. R. Beasley, *Physical Review Letters*, vol. 46, pp. 1598 - 1601, 1981.

[142] M. R. Beasley, *Advances in Cryogenic Engineering*, vol. 28, pp. 346 - 360, 1982.

[143] N. Schopohl and K. Scharnberg, *Physica*, vol. 107B, pp. 293 - 294, 1981.

[144] Ø. Fischer, *Helvetica Physica Acta*, vol. 45, pp. 331 - 397, 1972.

[145] R. Chevrel, M. Sergent, and J. Prigent, *Journal of Solid State Chemistry*, vol. 3, pp. 515-519, 1971.

[146] B. T. Matthias, M. Maerzio, E. Corenzwit, A. S. Cooper, and H. E. Barz, , 1972.

[147] Ø. Fischer, R. Odermatt, G. Bongi, H. Jones, R. Chevrel, and M. Sergent, *Physics Letters*, vol. 45A, pp. 87 - 88, 1973.

[148] S. Foner, E. J. McNiff, and E. J. Alexander, *Physics Letters*, vol. 49A, pp. 269-270, 1974.

[149] Ø. Fischer, H. Jones, G. Bongi, M. Sergent, and R. Chevrel, *Jounal of Physics C : Solid State Physics*, vol. 7, pp. L450-L453, 1974.

[150] O. Pena and M. Sergent, *Progress in Solid State Chemistry*, vol. 19, pp. 165-281, 1989.

[151] Ø. Fischer, A. Treyvaud, R. Chevrel, and M. Sergent, *Solid State Communications*, vol. 17, pp. 721-724, 1975.

[152] R. N. Shelton, R. W. McCallum, and H. Adrian, *Physics Letters*, vol. 56A, pp. 213 - 214, 1976.

[153] B. T. Matthias, H. Suhl, and E. Corenzwit, *Physical Review Letters*, vol. 1, pp. 92 - 94, 1958.

[154] B. T. Matthias, H. Suhl, and E. Corenzwit, *Physical Review Letters*, vol. 1, pp. 449 - 450, 1958.

[155] M. Ishikawa and Ø. Fischer, *Solid State Communications*, vol. 24, pp. 747 - 751, 1977.

[156] R. W. McCallum, D. C. Johnston, R. N. Shelton, W. A. Fertig, and M. B. Maple, *Solid State Communications*, vol. 24, pp. 501 - 505, 1977.

[157] O. Pena, C. Geantet, H. Schmitt, F. L. Berre, and C. Hamard, *Solid State Sciences*, vol. 1, pp. 577 - 584, 1999.

[158] K. Yvon and A. Paoli, *Solid State Communications*, vol. 24, pp. 41 - 45, 1977.

[159] D. G. Hinks, J. D. Jorgensen, and H. C. Li, *Physical Review Letters*, vol. 51, pp. 1911-1914, 1983.

[160] D. N. Zheng, A. B. Sneary, and D. P. Hampshire, presented at Applied Superconductivity Conference, Netherlands, 1997.

[161] M. Decroux, P. Sevlam, J. Cors, B. Seeber, Ø. Fischer, R. Chevrel, P. Rabiller, and M. Sergent, presented at Applied Superconductivity Conference, 1993.

[162] P. Selvam, D. Cattani, J. Cors, M. Decroux, P. Niedermann, S. Ritter, and Ø. Fischer, *Materials Research Bulletin*, vol. 26, pp. 1151 - 1165, 1991.

[163] P. Rabiller, M. Rabiller-Baudry, S. Even-Boudjada, L. Burel, R. Chevrel, M. Sergent, M. Decroux, J. Cors, and J. L. Maufras, *Materials Research Bulletin*, vol. 29, pp. 567 - 574, 1994.

[164] R. Horyn, O. Pena, C. Geantet, and M. Sergent, *Superconducting Science and Technology*, vol. 2, pp. 71-90, 1989.

[165] R. Horyn, O. Pena, A. Wojakowski, and M. Sergent, *Superconducting Science and Technology*, vol. 7, pp. 146-153, 1994.

[166] O. Pena, F. LeBerre, M. Sergent, R. Horyn, and A. Wojakowski, *Journal of Magnetism and Magnetic Materials*, vol. 140-144, pp. 1171-1172, 1994.

[167] P. Selvam, D. Cattani, J. Cors, M. Decroux, A. Junod, P. Niedermann, S. Ritter, Ø. Fischer, P. Rabiller, and R. Chevrel, *Journal of Applied Physics*, vol. 72, pp. 4232-4238, 1992.

[168] A. Gupta, M. Decroux, P. Sevlam, D. Cattani, T. C. Willis, and Ø. Fischer, *Physica C*, vol. 234, pp. 219 - 228, 1994.

[169] H. Yamasaki, M. Umeda, S. Kosaka, Y. Kimura, T. C. Willis, and D. C. Larbalestier, *Journal of Applied Physics*, vol. 70, pp. 1606 - 1613, 1991.

[170] B. Seeber, L. Erbuke, V. Schroeter, J. A. A. J. Perenboom, and R. Grill, *IEEE Transactions on Applied Superconductivity*, vol. 5, pp. 1205 - 1208, 1995.

[171] H. D. Ramsbottom and D. P. Hampshire, *Physica C*, vol. 274, pp. 295-303, 1997.

[172] Ø. Fischer, *Applied Physics*, vol. 16, pp. 1 - 28, 1978.

[173] R. Flukiger and R. Baillif, "Metallurgy and structural transformations in ternary molybdenum chalcogenides," in *Superconductivity in Ternary Compounds I*, Ø. Fischer and M. B. Maple, Eds., 1982, pp. 113 - 141.

[174] O. K. Andersen, W. Klose, and H. Nohl, *Physical Review B*, vol. 17, pp. 1209 - 1237, 1978.

[175] L. F. Mattheiss and C. Y. Fong, *Physical Review B*, vol. 15, pp. 1760 - 1768, 1977.

[176] D. W. Bullet, *Physical Review Letters*, vol. 39, pp. 664 - 666, 1977.

[177] D. C. Johnston and R. N. Shelton, *Journal of Low Temperature Physics*, vol. 26, pp. 561 - 572, 1977.

[178] M. Pelizzone, A. Treyvaud, P. Spitzli, and Ø. Fischer, *Journal of Low Temperature Physics*, vol. 29, pp. 453 - 465, 1977.

[179] R. Flukiger, R. Baillif, and E. Walker, *Materials Research Bulletin*, vol. 13, pp. 743 - 750, 1978.

[180] Ø. Fischer and M. B. Maple, "Superconductivity in ternary compounds I. Structural, electronic and lattice properties," . Berlin Heidelberg New York: Springer-Verlag, 1982.

[181] N. E. Alekseevskii, G. Wolf, N. M. Dobrovolskii, and C. Hohlfeld, *Journal of Low Temperature Physics*, vol. 38, pp. 253 - 264, 1980.

[182] L. D. Woolf, M. Tovar, H. C. Hamaker, and M. B. Maple, *Physics Letters*, vol. 74A, pp. 363 - 366, 1979.

[183] H. P. v. d. Meulen, J. A. A. J. Perenboom, T. T. J. M. Berendschot, J. Cors, M. Decroux, and Ø. Fischer, *Physica B*, vol. 211, pp. 269-271, 1995.

[184] D. Cattani, J. Cors, M. Decroux, B. Seeber, and Ø. Fischer, *Physica C*, vol. 153-155, pp. 461-462, 1988.

[185] N. E. Alekseevskii, *Cryogenics*, vol. 26, pp. 257 - 265, 1980.

[186] B. P. Schweiss, B. Renker, E. Schneider, and W. Reichardt, "Phonon spectra of A15 compounds and ternary molybdenum chalcogenides," in *Superconductivity in d- and f- band metals*, D. H. Douglass, Ed., 1976, pp. 189 - 207.

[187] S. D. Bader, S. K. Sinha, and R. N. Shelton, "Inelastic neutron scattering studies of the phonon spectra of Chevrel phase superconductors," in *Superconductivity in d- and f- band metals*, D. H. Douglass, Ed., 1976, pp. 209 - 221.

[188] W. L. McMillan, *Physical Review B*, vol. 167, pp. 331 - 344, 1968.

[189] P. B. Allen and R. C. Dynes, *Physical Review B*, vol. 12, pp. 905 - 922, 1975.

[190] M. Marezio, P. D. Dernier, J. P. Remeika, E. Corenzwit, and B. T. Matthias, *Materials Research Bulletin*, vol. 8, pp. 657 - 668, 1973.

[191] M. Sergent, R. Chevrel, C. Rossel, and Ø. Fischer, *Journal of the Less-Common Metals*, vol. 58, pp. 179 - 193, 1978.

[192] R. N. Shelton, "The effect of high pressure on superconducting ternary molybdenum chalcogenides," in *Superconductivity in d- and f- band metals*, D. H. Douglass, Ed.: Plenum Press, 1976, pp. 137 - 160.

[193] R. Chevrel, M. Sergent, and Ø. Fischer, *Materials Research Bulletin*, vol. 10, pp. 1169 - 1174, 1975.

[194] F. Y. Fradin, J. W. Downey, and T. E. Klippert, *Materials Research Bulletin*, vol. 11, pp. 993 - 998, 1976.

[195] V. Sankaranarayanan, G. Rangarajan, R. Srinivasan, A. M. Umarji, and G. V. S. Rao, *Cryogenics*, vol. 22, pp. 305 - 309, 1982.

[196] M. Sergent, Ø. Fischer, M. Decroux, C. Perrin, and R. Chevrel, *Journal of Solid State Chemistry*, vol. 22, pp. 87 - 92, 1977.

[197] A. A. Abrikosov and L. P. Gor'kov, *Soviet Physics JETP*, vol. 15, pp. 752 - 757, 1962.

[198] D. Rainer and G. Bergmann, *Journal of Low Temperature Physics*, vol. 14, pp. 501 - 519, 1974.

[199] P. Entel and M. Peter, *Journal of Low Temperature Physics*, vol. 22, pp. 613 - 621, 1976.

[200] Ø. Fischer, M. Decroux, S. Roth, R. Chevrel, and M. Sergent, *Jounal of Physics C : Solid State Physics*, vol. 8, pp. L474-L477, 1975.

[201] Ø. Fischer, M. Decroux, R. Chevrel, and M. Sergent, "On the upper critical fields of the ternary molybdenum chalcogenides," in *Superconductivity in d- and f-band metals*, D. H. Douglass, Ed. New York and London: Plenum Press, 1976.

[202] B. G. Pazol, D. J. Holmgren, and D. M. Ginsberg, *Journal of Low Temperature Physics*, vol. 74, pp. 133 -140, 1989.

[203] M. B. Maple and Ø. Fischer, "Superconductivity in ternary compounds II. Superconductivity and magnetism," . Berlin Heidelberg New York: Springer-Verlag, 1982.

[204] D. Cattani, J. Cors, M. Decroux, and Ø. Fischer, *Physica B*, vol. 165, pp. 1409 - 1410, 1990.

[205] M. Decroux, D. Cattani, J. Cors, S. Ritter, and Ø. Fischer, presented at International Conference on Low Temperature Physics, Brighton, 1990.

[206] T. Matsushita, K. Kajiyana, K. Yamafuji, K. Hamasaki, and T. Komata, *Japanese Journal of Applied Physics*, vol. 25, pp. 831 - 834, 1986.

[207] N. Cheggour, M. Decroux, Ø. Fischer, and D. P. Hampshire, *Journal of Applied Physics*, vol. 84, pp. 2181-2183, 1998.

[208] S. Even-Boudjada, V. Tranchant, R. Chevrel, M. Sergent, M.-P. Crosnier-Lopez, Y. Laligant, R. Retoux, and M. Decroux, *Materials Letters*, vol. 38, pp. 90 - 97, 1999.

[209] Y. Kubo, F. Uchikawa, S. Utsunomiya, K. Noto, K. Katagiri, and N. Kobayashi, *Cryogenics*, vol. 33, pp. 883 - 888, 1993.

[210] A. Junod, "Specific heat of high temperature superconductors: A review," in *Physical properties of high temperature superconductors II*, D. M. Ginsberg, Ed.: World Scientific, 1990, pp. 13 - 120.

[211] N. E. Phillips, R. A. Fisher, and J. E. Gordon, "The specific heat of high-$T_c$ superconductors," in *Progress in low temperature physics*, vol. 8, D. F. Brewer, Ed.: Elsevier Science Publishers, 1992, pp. 267 - 394.

[212] A. Junod, A. Erb, and C. Renner, *Physica C*, vol. 317 - 318, pp. 333 - 344, 1999.

[213] M. Roulin, A. Junod, and E. Walker, *Science*, vol. 273, pp. 1210 - 1212, 1996.

[214] C. Renner, B. Revaz, K. Kadowaki, I. Maggio-Aprile, and Ø. Fischer, *Physical Review Letters*, vol. 80, pp. 3606 - 3609, 1998.

[215] P. Weiss, *Journal de Physique*, vol. 6, pp. 661 - 690, 1907.

[216] L. Neel, *Annals of Physics*, vol. 10, pp. 5 - 105, 1932.

[217] L. Landau, *Phys Z Sowjet-Union*, vol. 4, pp. 675 - 679, 1933.

[218] W. Heisenberg, *Z. Physics*, vol. 49, pp. 619 - 634, 1928.

[219] H. R. Ott, G. Keller, W. Odoni, L. D. Woolf, M. B. Maple, D. C. Johnston, and H. A. Mook, *Physical Review B*, vol. 25, pp. 477 - 480, 1982.

[220] W. L. Bragg and E. J. Williams, *Proceedings of the Royal Society of London*, vol. A 145, pp. 699 - 730, 1934.

[221] H. A. Bethe, *Proceedings of the Royal Society of London*, vol. A150, pp. 552 - 575, 1935.

[222] C. Domb, *Advances in Physics*, vol. 9, pp. 149 - 361, 1960.

[223] L. J. d. Jongh and A. R. Miedema, *Advances in Physics*, vol. 23, pp. 1 - 260, 1974.

[224] M. E. Fisher, *Reports on Progress in Physics*, vol. 15, pp. 615 - 730, 1967.

[225] C. Domb and A. R. Miedema, "Magnetic transitions," in *Progress in low temperature physics. Vol. IV*, C. J. Gorter, Ed. Amsterdam, 1964, pp. 296 - 343.

[226] N. D. Mermin and H. Wagner, *Physical Review Letters*, vol. 17, pp. 1133 - 1136, 1966.

[227] M. Suzuki, B. Tsujiyama, and S. Katsura, *Journal of Mathematical Physics*, vol. 8, pp. 124 - 130, 1967.

[228] J. W. Stout and E. Catalano, *Journal of Chemical Physics*, vol. 23, pp. 2013 - 2022, 1955.

[229] C. Domb and M. F. Sykes, *Physical Review*, vol. 128, pp. 168 - 173, 1962.

[230] C. Domb and M. F. Sykes, *Physical Review*, vol. 108, pp. 1415 - 1416, 1957.

[231] C. Domb and M. F. Sykes, *Journal of Mathematical Physics*, vol. 2, pp. 63 - 67, 1961.

[232] G. A. Baker, *Physical Review*, vol. 124, pp. 768 - 774, 1961.

[233] G. A. Baker, *Physical Review*, vol. 129, pp. 99 - 102, 1963.

[234] J. W. Essam and M. F. Sykes, *Physica*, vol. 29, pp. 378 - 388, 1963.

[235] M. F. Sykes, J. L. Martin, and D. L. Hunter, *Proceedings of the Physical Society*, vol. 91, pp. 671 - 677, 1967.

[236] D. S. Gaunt and C. Domb, *Jounal of Physics C : Solid State Physics*, vol. 1, pp. 1038 - 1045, 1968.

[237] C. Domb and N. W. Dalton, *Proceedings of the Physical Society*, vol. 89, pp. 859 - 871, 1966.

[238] R. F. Wielinga, H. W. J. Blote, J. A. Roest, and W. J. Huiskamp, *Physica*, vol. 34, pp. 223 - 240, 1967.

[239] J. D. Cashion, A. H. Cooke, T. L. Thorp, and M. R. Wells, *Jounal of Physics C : Solid State Physics*, vol. 1, pp. 539 - 541, 1968.

[240] H. E. Meissner and W. P. Wolf, *Journal of Applied Physics*, vol. 40, pp. 1038, 1969.

[241] H. W. J. Blote and W. J. Huiskamp, *Physics Letters*, vol. 29A, pp. 304 - 305, 1969.

[242] J. C. Wright, H. W. Moos, J. H. Colwell, B. W. Mangum, and D. D. Thornton, *Physical Review B*, vol. 3, pp. 843 - 858, 1971.

[243] M. F. Sykes, D. L. Hunter, D. S. McKenzie, and B. R. Heap, *Journal of Physics A: General Physics*, vol. 5, pp. 667 - 673, 1972.

[244] F. J. Dyson, *Physical Review*, vol. 102, pp. 1217 - 1230, 1956.

[245] F. J. Dyson, *Physical Review*, vol. 102, pp. 1230 - 1244, 1956.

[246] G. S. Rushbrooke and P. J. Wood, *Proceedings of the Physical Society*, vol. A68, pp. 1161 - 1169, 1955.

[247] G. S. Rushbrooke and P. J. Wood, *Molecular Physics*, vol. 1, pp. 257 - 283, 1958.

[248] G. S. Rushbrooke and P. J. Wood, *Molecular Physics*, vol. 6, pp. 409 - 421, 1963.

[249] N. W. Dalton and D. W. Wood, *Physical Review*, vol. 138, pp. A779 - A792, 1965.

[250] G. A. Baker, H. E. Gilbert, J. Eve, and G. S. Rushbrooke, *Physical Review*, vol. 164, pp. 800 - 817, 1967.

[251] J. Callaway and D. C. McCollum, *Physical Review*, vol. 130, pp. 1741 - 1742, 1963.

[252] D. T. Teaney, B. J. C. v. d. Hoeven, and V. L. Moruzzi, *Physical Review Letters*, vol. 20, pp. 722 - 724, 1968.

[253] C. Domb and R. G. Bowers, *Jounal of Physics C : Solid State Physics*, vol. 2, pp. 755 - 758, 1969.

[254] A. R. Miedema, R. F. Wielinga, and W. J. Huiskamp, *Physica*, vol. 31, pp. 1585 - 1598, 1965.

[255] A. J. Henderson, G. R. Brown, T. B. Reed, and H. Meyer, *Journal of Applied Physics*, vol. 41, pp. 946 - 947, 1970.

[256] D. T. Teaney, *Physical Review Letters*, vol. 14, pp. 898 - 900, 1965.

[257] D. T. Teaney, V. L. Moruzzi, and B. E. Argyle, *Journal of Applied Physics*, vol. 37, pp. 1122 - 1123, 1966.

[258] D. G. Onn, H. Meyer, and J. P. Remeika, *Physical Review*, vol. 156, pp. 663 - 670, 1967.

[259] F. L. Lederman, M. B. Salamon, and L. W. Shacklette, *Physical Review B*, vol. 9, pp. 2981 - 2988, 1974.

[260] V. L. Ginzburg, *Soviet Physics JETP*, vol. 4, pp. 153-160, 1957.

[261] A. A. Abrikosov and L. P. Gor'kov, *Soviet Physics JETP*, vol. 12, pp. 1243 - 1253, 1961.

[262] B. T. Matthias, E. Corenzwit, J. M. Vandenberg, and H. E. Barz, *Proceedings of the National Academy of Science (USA)*, vol. 74, pp. 1334 - 1335, 1977.

[263] Ø. Fischer, "Magnetic Superconductors," in *Ferromagnetic materials*, vol. 5, K. H. J. Buschow and E. P. Wohlfarth, Eds., 1990, pp. 465-550.

[264] R. Nagarajan, C. Mazumdar, Z. Hossain, S. K. Dhar, K. V. Gopalakrishnan, L. C. Gupta, C. Godart, B. D. Padalia, and R. Vijayaraghavan, *Physical Review Letters*, vol. 72, pp. 274-277, 1994.

[265] K. Machida, *Applied Physics*, vol. A35, pp. 193 - 217, 1984.

[266] V. Jaccarino and M. Peter, *Physical Review Letters*, vol. 9, pp. 290-292, 1962.

[267] W. A. Fertig, D. C. Johnston, L. E. DeLong, R. W. McCallum, M. B. Maple, and B. T. Matthias, *Physical Review Letters*, vol. 38, pp. 987 - 90, 1977.

[268] M. Ishikawa and Ø. Fischer, *Solid State Communications*, vol. 23, pp. 37 - 39, 1977.

[269] G. W. Crabtree, F. Behroozi, S. A. Campbell, and D. G. Hinks, *Physical Review Letters*, vol. 49, pp. 1342 - 1345, 1982.

[270] M. Giroud, J. L. Genicon, R. Tournier, C. Geantet, O. Pena, R. Horyn, and M. Sergent, *Physica B*, vol. 148, pp. 113 - 116, 1987.

[271] M. Tachiki, H. Matsumoto, and H. Umezawa, *Physical Review B*, vol. 20, pp. 1915 - 1927, 1979.

[272] K. E. Gray, *Physical Review B*, vol. 27, pp. 4157 - 4160, 1983.

[273] J. W. Lynn, G. Shirane, W. Thomlinson, and R. N. Shelton, *Physical Review Letters*, vol. 46, pp. 368 - 371, 1981.

[274] D. E. Moncton, D. B. McWhan, P. H. Schmidt, G. Shirane, W. Thomlinson, M. B. Maple, H. B. MacKay, L. D. Woolf, Z. Fisk, and D. C. Johnston, *Physical Review Letters*, vol. 45, pp. 2060 - 2063, 1980.

[275] S. K. Sinha, G. W. Crabtree, D. G. Hinks, and H. Mook, *Physical Review Letters*, vol. 48, pp. 950 - 953, 1982.

[276] L. N. Bulaevskii, A. I. Buzdin, M. L. Kulic, and S. V. Panjukov, *Advances in Physics*, vol. 34, pp. 175 - 261, 1985.

[277] E. I. Blount and C. M. Varma, *Physical Review Letters*, vol. 42, pp. 1079 - 1082, 1979.

[278] H. Matsumoto, H. Umezawa, and M. Tachiki, *Solid State Communications*, vol. 31, pp. 157 - 161, 1979.

[279] J. L. Genicon, J. P. M. Danon, R. Tournier, O. Pena, R. Horyn, and M. Sergent, *Journal de Physique: Letters*, vol. 45, pp. L1175 - L1181, 1984.

[280] P. Burlet, A. Dinia, S. Quezel, W. A. C. Erkelens, J. Rossat-Mignod, R. Horyn, O. Pena, C. Geantet, M. Sergent, and J. L. Genicon, *Physica B*, vol. 14, pp. 99 - 105, 1987.

[281] W. Baltensperger and S. Strassler, *Physik der Kondensieren Materie*, vol. 1, pp. 20 - 26, 1963.

[282] D. E. Moncton, G. Shirane, W. Thomlinson, M. Ishikawa, and Ø. Fischer, *Physical Review Letters*, vol. 41, pp. 1133 - 1136, 1978.

[283] M. B. Maple, L. D. Woolf, C. F. Majkrzak, G. Shirane, W. Thomlinson, and D. E. Moncton, *Physics Letters*, vol. 77A, pp. 487 - 489, 1980.

[284] N. E. Alekseevskii, G. Wolf, V. N. Narozhnyi, A. S. Rudenko, and H. Holfeld, *Soviet Physics JETP*, vol. 62, pp. 617 - 620, 1985.

[285] H. C. Hamaker, L. D. Wolf, H. B. MacKay, Z. Fisk, and M. B. Maple, *Solid State Communications*, vol. 31, pp. 139 - 144, 1979.

[286] C. F. Majkrzak, D. E. Cox, G. Shirane, H. A. Mook, H. C. Hamaker, H. B. MacKay, Z. Fisk, and M. B. Maple, *Physical Review B*, vol. 26, pp. 245 - 249, 1982.

[287] G. Hilscher and H. Michor, *Studies of high Temperature Superconductors*, vol. 26-27, TBP.

[288] H. Eisaki, H. Takagi, R. J. Cava, B. Batlogg, J. J. Krajewski, W. F. Peck, K. Mizuhashi, J. O. Lee, and S. Uchida, *Physical Review B*, vol. 50, pp. 647-650, 1994.

[289] P. C. Canfield, S. L. Bud'ko, and B. K. Cho, *Physica C*, vol. 262, pp. 249 - 254, 1996.

[290] F. W. Sears and G. L. Salinger, *Thermodynamics, kinetic theory and statistical thermodynamics*, Third ed: Addison-Wesley, 1986.

[291] A. Hirt, D. Gerion, I. M. L. Billas, A. Chatelain, and W. A. d. Heer, *Zeitschrift Fur Physik D*, vol. 40, pp. 160-163, 1997.

[292] D. Sanchez, A. Junod, J. Y. Genoud, T. Graf, and J. Muller, *Physica C*, vol. 200, pp. 1 - 11, 1992.

[293] S. Ali, "Specific heat measurements using the a.c. technique on the Chevrel phase superconductor $Pb_{1-x}Gd_xMo_6S_8$ in high magnetic fields," in *Department of Physics*. Durham: University of Durham, 1996.

[294] R. Bachmann, F. J. DiSalvo, T. H. Geballe, R. L. Greene, R. E. Howard, C. N. King, H. C. Kirsch, K. N. Lee, R. E. Schwall, H. U. Thomas, and R. B. Zubeck, *Review of Scientific Instruments*, vol. 43, pp. 205 - 214, 1972.

[295] P. F. Sullivan and G. Seidel, *Physical Review*, vol. 173, pp. 679-685, 1968.

[296] D. L. Martin, "Calorimetry in the range 0.3 - 30 K," in *Specific heat of solids*, A. Cezairliyan, Ed. New York: Hemisphere Publishing Corporation, 1988, pp. 113 - 152.

[297] R. L. Fagaly and R. G. Bohn, *Review of Scientific Instruments*, vol. 48, pp. 1502 - 1504, 1977.

[298] E. M. Forgan and S. Nedjat, *Review of Scientific Instruments*, vol. 51, pp. 411 - 417, 1980.

[299] H. D. Ramsbottom, S. Ali, and D. P. Hampshire, *Cryogenics*, vol. 36, pp. 61 - 63, 1996.

[300] G. E. Childs, L. J. Ericks, and R. L. Powell, *Thermal conductivity of solids at room temperature and below*: U.S. Department of Commerce, National Bureau of Standards, 1973.

[301] D. W. Osbourne, H. E. Flotow, and F. Schreiner, *Review of Scientific Instruments*, vol. 38, pp. 159 - 168, 1967.

[302] R. C. Weast, "CRC handbook of chemistry and physics: 69th Edition," . Florida: CRC Press Inc., 1988.

[303] J. C. Ho, Y. Y. Chen, Y. D. Yao, W. S. Huang, S. R. Sheen, J. C. Huang, and M. K. Wu, *Physica C*, vol. 282-287, pp. 1403-1404, 1997.

[304] R. J. Corruccini and J. J. Gniewek, "Specific heat and enthalpies of technical solids at low temperatures," United States Department of Commerce. National Bureau of Standards Monograph 21. 1960.

[305] J. T. Heessels, *Cryogenics*, vol. 11, pp. 483 - 484, 1971.

[306] W. Schnelle, J. Engelhardt, and E. Gmelin, *Cryogenics*, vol. 39, pp. 271 - 275, 1999.

[307] D. F. Brewer, D. O. Edwards, D. R. Howe, and T. E. Whall, *Cryogenics*, vol. 6, pp. 49 - 51, 1966.

[308] D. A. Ditmars, S. Ishihara, S. S. Chang, G. Bernstein, and E. D. West, *Journal of Research of the National Bureau of Standards*, vol. 87, pp. 159 - 163, 1982.

[309] Goodfellow, "Catalogue," 1996.

[310] D. L. Martin, *Physical Review B*, vol. 8, pp. 5357 - 5360, 1973.

[311] J. C. Holste, T. C. Cetas, and C. A. Swenson, *Review of Scientific Instruments*, vol. 43, pp. 670 - 676, 1972.

[312] G. Ahlers, *Review of Scientific Instruments*, vol. 37, pp. 477 - 480, 1966.

[313] D. L. Martin, *Review of Scientific Instruments*, vol. 58, pp. 639-646, 1987.

[314] H. J. Niu, N. A. Morley, and D. P. Hampshire, *IEEE transactions on Applied Superconductivity*, vol. 11, 2001.

[315] H. J. Niu, , 2000.

[316] R. Flukiger, A. Junod, R. Baillif, P. Spitzli, A. Treyvaud, A. Paoli, H. Devantay, and J. Muller, *Solid State Communications*, vol. 23, pp. 699 - 702, 1977.

[317] B. P. Schweiss, B. Renker, and R. Flukiger, presented at Proceedings of the Conference on Ternary Superconductors, Lake Geneva, 1980.

[318] A. Junod, T. Jarlborg, and J. Muller, *Physical Review B*, vol. 27, pp. 1568 - 1585, 1983.

[319] U. Poppe and H. Wuhl, *Journal de Physique*, vol. 39, pp. C6 361 - 362, 1978.

[320] U. Poppe and H. Wuhl, *Journal of Low Temperature Physics*, vol. 43, pp. 371 - 382, 1981.

[321] F. Marsiglio and J. P. Carbotte, *Physical Review B*, vol. 33, pp. 6141 - 6146, 1986.

[322] R. Odermatt, M. Hardiman, and J. v. Meijel, *Solid State Communications*, vol. 32, pp. 1227 - 1231, 1979.

[323] B. Mitrovic, H. G. Zarate, and J. P. Carbotte, *Physical Review B*, vol. 29, pp. 184 - 191, 1984.

[324] D. N. Zheng, H. D. Ramsbottom, and D. P. Hampshire, *Physical Review B*, vol. 52, pp. 1-8, 1995.

[325] I. J. Daniel, "The fabrication of Chevrel phase superconductors and the origin of the irreversibility field.," in *Physics*: Durham University, 1999.

[326] D. N. Zheng, A. B. Sneary, N. R. Leigh, C. Eastell, M. Goringe, C. Dong, and D. P. Hampshire, , TBP.

[327] N. A. Morley, N. R. Leigh, H. Niu, and D. P. Hampshire, *IEEE transactions on Applied Superconductivity*, vol. 11, pp. 3599 - 3602, 2001.

[328] N. E. Alekseevskii, G. Wolf, S. Krautz, and V. I. Tsebro, *Journal of Low Temperature Physics*, vol. 28, pp. 381 - 389, 1977.

[329] D. N. Zheng, S. Ali, H. A. Hamid, C. Eastell, M. Goringe, and D. P. Hampshire, *Physica C*, vol. 291, pp. 49-58, 1997.

[330] H. P. v. d. Meulen, J. J. M. Franse, Z. Tarnawski, K. Kadowaki, J. C. P. Klaasse, and A. A. Menovsky, *Physica C*, vol. 152, pp. 65 - 71, 1988.

# Appendix 1. Publications

1. The upper critical field of the Chevrel phase superconductor lead-molybdenum-sulphide doped with gadolinium.
   Leigh NR, Zheng DN, Hampshire DP
   *IEEE Transactions on Applied Superconductivity* **9** (2) 1739 – 1742 (1999).

2. The upper critical field of the Chevrel phase superconductor tin-molybdenum-sulphide doped with europium.
   Leigh NR, Daniel IJ, Zheng DN, Hampshire DP
   *IEEE Transactions on Applied Superconductivity* **11** (1) 3599 – 3602 (2000).

3. Calculating the Ginzburg-Landau parameter in magnetic superconductors from heat capacity measurements.
   Leigh NR, Hampshire DP
   *To Be Published, Physical Review B or Physical Review Letters* (2002).

# Appendix 2. Conferences and Courses

## Conferences Attended

| | | |
|---|---|---|
| December 1997 | University of Exeter | CMMP 1997 |
| April 1998 | University of Birmingham | Superconductivity Meeting |
| September 1998 | Palm Springs, California | ASC' 98 |
| April 1999 | University of Birmingham | Superconductivity Meeting |
| September 1999 | Sitges, Barcelona | EUCAS' 99 |
| December 1999 | University of Leicester | CMMP 1999 |
| April 2000 | University of Birmingham | Superconductivity Meeting |

## Courses Attended

| | |
|---|---|
| 1997 | Low temperature techniques course (Aston University) |
| 1998 | Mechanical workshop course (Durham University) |
| 1998 | Maple V for beginners (Durham University ITS) |
| 1999 | CRAC Research Councils' Graduate Schools Programme (Manchester) |

# Appendix 3. Computer Programs

## Maple V

Ferro.mws

Calculates the magnetisation, Gibbs free energy and specific heat of a ferromagnetic material as a function of temperature and applied field.

AFerro.mws

Calculates the magnetisation, Gibbs free energy and specific heat of an antiferromagnetic material as a function of temperature and applied field.

Param.mws

Calculates the magnetisation, Gibbs free energy and specific heat above the ordering temperature as a function of temperature and applied field.

## ASYST specific heat programs

relax1.nl

Runs a relaxation measurement of the specific heat as a function of temperature.

relax2.nl

The magnet power supply control program for relax1.nl.

hpulse.nl

Runs a heat pulse measurement of the specific heat as a function of temperature and applied field.

acgo.nl

Runs an ac measurement of the specific heat as a function of temperature and applied field.